UNIVERSITI TEKNOLOGI MARA

EFFECT OF GRAPHENE OXIDE IN BLENDED MORTAR FOR MECHANICAL PERFORMANCE, MICROSTRUCTURE AND MASS LOSS PROPERTIES

KHAIRUL NAZHAN BIN KHAIRUL IZWAN

PhD

August 2026

UNIVERSITI TEKNOLOGI MARA

EFFECT OF GRAPHENE OXIDE IN BLENDED MORTAR FOR MECHANICAL PERFORMANCE, MICROSTRUCTURE AND MASS LOSS PROPERTIES

KHAIRUL NAZHAN BIN KHAIRUL IZWAN

Thesis submitted in fulfilment
of the requirements for the degree of
Doctor of Philosophy
(Civil Engineering)

Faculty of Civil of Engineering

August 2026

CONFIRMATION BY PANEL OF EXAMINERS

I certify that a Panel of Examiners has met on 10th June 2026 to conduct the final examination of Khairul Nazhan bin Khairul Izwan on his Doctor of Philosophy thesis entitled "Effect of Graphene Oxide in Blended Mortar for Mechanical Performance, Microstructure and Mass Loss Properties" in accordance with Universiti Teknologi MARA Act 1976 (Akta 173). The Panel of Examiners recommends that the student be awarded the relevant degree. The Panel of Examiners was as follows:

Abdul Samad Abdul Rahman, PhD
Associate Professor
Faculty of Civil Engineering
Universiti Teknologi MARA
(Chairman)

Oh Chai Lian, PhD
Senior Lecturer
Faculty of Civil Engineering
Universiti Teknologi MARA
(Internal Examiner)

Taksiah. A. Majid, PhD
Professor
School of Civil Engineering
Universiti Sains Malaysia
(External Examiner)

PROFESSOR DR HJH ZURAEDA BINTI IBRAHIM
Dean
Institute of Postgraduates Studies
Universiti Teknologi MARA

Date: 17 August 2026

AUTHOR'S DECLARATION

I declare that the work in this thesis was carried out in accordance with the regulations of Universiti Teknologi MARA. It is original and is the results of my own work, unless otherwise indicated or acknowledged as referenced work. This thesis has not been submitted to any other academic institution or non-academic institution for any degree or qualification.

I, hereby, acknowledge that I have been supplied with the Academic Rules and Regulations for Postgraduate, Universiti Teknologi MARA, regulating the conduct of my study and research.

Name of Student	:	Khairul Nazhan bin Khairul Izwan
Student ID. No.	:	2023988879
Programme	:	Doctor of Philosophy (Civil Engineering) – CEEC 950
Faculty	:	Civil Engineering
Thesis Title	:	Effect of Graphene Oxide in Blended Mortar for Mechanical Performance, Microstructure and Mass Loss Properties
Signature of Student	:	
Date	:	August 2026

ABSTRACT

The application of Graphene Oxide (GO) has gained significant traction in recent years due to its ability to provide substantial enhancements to cementitious-based materials. Despite this widespread exploration, a critical gap exists in the literature regarding the comprehensive corrosion assessment of GO-blended mortars. Current studies often limit their corrosion evaluation to basic methods, such as the Rapid Chloride Penetration Test (RCPT) and the Half Cell Potential Test (HCP). This omission leaves a specific area of study untouched: the quantification of Mass Loss, which is essential for defining GO's role as a protective barrier within the cement matrix. Therefore, this study was initiated with the primary focus on evaluating the corrosion protective resilience of GO within a blended mortar system. The blended mortar formulation was established through a preliminary testing phase that compared the physical, mechanical, and durability properties of two Supplementary Cementitious Materials (SCMs), specifically Fly Ash and GGBS at fixed replacement rates (0%, 10%, 20%, 30%). The resulting optimal binder formulation then became the base for the main phase named as binder modification, which involved a deeper investigation into various GO dosages as additives. A comprehensive mechanical and microstructural assessment were conducted across these GO modified mixes. The final, critical phase of the study involved verifying the binder modification results through calculated mass loss determined via Faraday's Law. The experimental data strongly indicated that the optimal Mix 30SG2 (0.02% GO) achieved an 88.24% reduction in mass loss with an extended service life up to 86 days under normal conditions. This superior performance significantly demonstrates how GO can be fully engaged in its protective mechanism, acting through four key synergistic effects: the filling effect, nucleation effect, bonding effect, and the labyrinth effect. This robust methodology ultimately provides the necessary quantitative support to advance the understanding of GO's potential as a reliable durability additive.

ACKNOWLEDGEMENT

First and foremost, all praise and thanks belong to Allah (SWT) for the strength, health, and perseverance bestowed upon me throughout this demanding academic journey.

My deepest gratitude is reserved for my primary supervisor, Dr. Nazirah Mohd Apandi. Her exemplary mentorship, profound wisdom, and constant encouragement served as my steady anchor through every phase of this research. Her meticulous guidance, rigorous technical insights, and unwavering patience kept me grounded during moments of deep academic uncertainty. I am truly honoured to have conducted my research under her direction. I also express my sincere appreciation to my co-supervisors, Assoc. Prof. Ir. Ts. Dr. Mohd Khairul Kamarudin and Prof. Dr. Hamidah Mohd Saman @ Haji Mohamed, for their invaluable advice and continuous support.

I extend my heartfelt appreciation to Universiti Teknologi MARA (UiTM) for providing state-of-the-art laboratory facilities and a collaborative environment that proved instrumental in completing this work. Special thanks go to my cherished circle of friends from my childhood companions who kept me grounded, to my diploma, degree and postgraduate peers whose shared academic struggles and technical exchanges enriched this path. To my dear wife, thank you for your unconditional love, infinite patience, and personal sacrifices. Above all, thank you for waiting for me so selflessly and believing in my passion throughout this long journey. Your constant presence was my peaceful haven.

Above all, this achievement belongs to my family, who remain the absolute centre of my life and my ultimate pillar of strength. To my beloved father and brothers, thank you for your sacrifices, wisdom, steadfast support, and total faith in me. I am forever grateful to my father, who stood remarkably strong and carried our family forward as a steadfast pillar after my mother was gone. His courage continues to inspire me daily. Most of all, I honour the deeply cherished memory of my late mother, . Losing her to cancer during my first semester was a devastating blow, yet her enduring spirit, gentle teachings, and the echoes of her daily dua provided the resilience I needed to persevere. Though she is not here physically to witness this milestone, her love was the quiet force behind every page written. This victory is for you, Mama.

Al-Fatihah.

TABLE OF CONTENTS

		Page
CONFIRMATION BY PANEL OF EXAMINERS		**ii**
AUTHOR'S DECLARATION		**iii**
ABSTRACT		**iv**
ACKNOWLEDGEMENT		**v**
TABLE OF CONTENTS		**vi**
LIST OF TABLES		**xi**
LIST OF FIGURES		**xiii**
LIST OF ABBREVIATIONS		**xvii**
LIST OF NOMENCLATURES		**xix**
CHAPTER 1 INTRODUCTION		**1**
1.1	Research Background	1
1.2	Problem Statement	2
1.3	Research Objective	4
1.4	Scope & Limitation of Study	5
1.5	Significance of Study	7
CHAPTER 2 LITERATURE REVIEW		**9**
2.1	Introduction to Graphene Oxide	9
2.2	Comparative Analysis of Graphene Oxide and Graphene	12
2.3	Approaches for Synthesis of Graphene Oxide	16
	2.3.1 The Brodie's Method	18
	2.3.2 The Staudenmaier's Method	19
	2.3.3 The Hoffman's Method	19
	2.3.4 The Hummer's Method	20
2.4	Dispersion of Graphene Oxide	21
	2.4.1 Graphene Oxide Combination	21
	2.4.2 Physical Dispersion Techniques	22

2.4.3 Chemical Modification Techniques 22
2.5 Behaviour of Graphene Oxide as Cementitious Material 23
2.5.1 Filling Effect 23
2.5.2 Bonding Effect 24
2.5.3 Nucleation Effect 25
2.6 Physicomechano-Tribological Properties 26
2.6.1 Influence of Graphene Oxide on Hydration Process 27
2.6.2 Influence of Graphene Oxide on Physical Properties of Cement 29
2.6.3 Influence Of Graphene Oxide on the Mechanical Performance of Cement 34
2.6.4 Influence of Graphene Oxide on Durability Properties of Cement 53
2.6.5 Improvement of the Interface Structure Cement 57
2.6.6 Crystallographic Structure of GO 63
2.7 GO Mechanism Against Corrosion 66
2.7.1 Introduction of Corrosion 66
2.7.2 The Phase of Corrosive Deterioration 68
2.7.3 Graphene Oxide as Corrosion Resistance 70
2.7.4 Rapid Chloride Penetration Test (RCPT) 72
2.7.5 Depassivation of Half Cell Potential (HCP) 72
2.7.6 Quantitative Corrosion Corelation of Mass Loss 73
2.8 Research Gap 74

CHAPTER 3 RESEARCH METHODOLOGY 77
3.1 Introduction 77
3.2 Research Framework 79
3.3 The Simplified Hummer's Method Synthesis 89
3.4 Characterisation of Raw Materials 90
3.4.1 X-ray Fluorescence (XRF) 90
3.4.2 Elemental Analyser (EA) 91
3.4.3 Energy-Dispersive X-ray Spectroscopy (EDX) 91
3.4.4 X-ray Diffraction (XRD) 91
3.4.5 Scanning Electron Microscopy (SEM) 92
3.4.6 Field Emission Scanning Electron Microscopy (FESEM) 93
3.5 Properties of Blended Mortar and GO-Blended Mortar 93

3.5.1 Mix Proportion of Blended Mortar (Binder Formulation) 94
3.5.2 Mix Proportion of GO-Blended Mortar (Binder Modification) 95
3.5.3 Preparation of Binder Formulation and Binder Modification 97
3.6 Physical Properties of Blended Mortar 99
3.6.1 Density Test 99
3.7 Mechanical Properties of Blended Mortar 99
3.7.1 Compressive Strength Test 99
3.7.2 Split Tensile Strength Test 101
3.8 Durability Properties of Blended Mortar 101
3.8.1 Water Absorption Test 101
3.9 Corrosion Assessment of GO-Blended Mortar 103
3.9.1 Rapid Chloride Resistance Test (RCPT) 103
3.9.2 Half Cell Potential Test (HCP) 104
3.10 Porosity and Microstructure Properties 106
3.10.1 Mercury Intrusion Porosimetry (MIP) 107
3.10.2 Scanning Electron Microscopy (SEM) 108
3.10.3 X-ray Diffraction (XRD) 108
3.11 Mass Loss of Faraday's Law 109

CHAPTER 4 RESULT AND ANALYSIS 110
4.1 Introduction 110
4.2 Characterisation of Raw Material 110
4.2.1 X-ray Fluorescence (XRF) 110
4.2.2 Elemental Analyser (EA) 113
4.2.3 X-ray Diffraction (XRD) Analysis 114
4.2.4 Scanning Electron Microscopy (SEM) Analysis 120
4.2.5 Energy Dispersive X-ray (EDX) Analysis 126
4.2.6 Field Emission Scanning Electron Microscopy (FESEM) 131
4.3 Properties Binder Formulation 133
4.3.1 Physical Properties 133
4.3.2 Mechanical Properties 134
4.3.3 Durability Properties 137
4.4 Summary of Binder Formulation 138
4.5 The Properties of Binder Modification 139

4.5.1 Physical Properties 139
4.5.2 Mechanical Properties 140
4.5.3 Durability Properties 144
4.6 Corrosion Assessment of GO-Blended Mortar 145
4.6.1 Rapid Chloride Penetration Test (RCPT) 145
4.6.2 Half Cell Potential (HCP) 148
4.7 Porosity and Microstructure Properties 150
4.7.1 Scanning Electron Microscopy (SEM) 150
4.7.2 Mercury Intrusive Porosimetry (MIP) 155
4.7.3 X-Ray Diffraction (XRD) Analysis for GO-Blended Mortar 158
4.8 Summary of Binder Modification 162

CHAPTER 5 MASS LOSS CALCULATION 163
5.1 Introduction 163
5.2 Time to Depassivation (T_{HCP}) 164
5.3 Active Corrosion Time (t) 166
5.4 Total Corrosion Current (I) 167
5.5 Mass Loss (m) 169
5.6 Average Nominal Area Loss, A_{loss} 171
5.7 Comprehensive Discussion 174
5.7.1 Mass Loss in Normal Condition 174
5.7.2 Mass Loss in Saltwater Condition 176
5.7.3 Average Nominal Area Loss 178

CHAPTER 6 CONCLUSION & FUTURE RECOMMENDATION 180
6.1 General Conclusion 180
6.1.1 Characterisation of Blended Material and Graphene Oxide, and to Evaluate Their Influence on the Physical, Mechanical, And Durability Properties for Binder Formulation 180
6.1.2 Investigation on the Optimum Ratio of Graphene Oxide in Producing Nano-Composite Mortar Under Physical, Mechanical and Durability Properties for Binder Modification 181
6.1.3 Evaluation of the Microstructure and Durability of GO-Blended Mortar Against Corrosion Resistance 182

6.1.4 Investigation of the Mass Loss of the Steel Rebar Within The GO-Blended Mortar Using Faraday's Law Equation 182
6.2 Future Recommendation 183

REFERENCES **184**

AUTHOR'S PROFILE **198**

LIST OF TABLES

Tables	Title	Page
Table 2.1	Definition and Properties of Graphite Derivatives	10
Table 2.2	Properties of Graphite Derived Nanomaterials (Akarsh et al., 2022)	16
Table 2.3	Slump Test of GO in Cement Matrix from Previous Research	33
Table 2.4	Compressive Strength of GO in Cement Matrix from Previous Research	38
Table 2.5	Tensile Strength of GO in Cement Matrix from Previous Research	45
Table 2.6	Flexural Strength of GO in Cement Matrix from Previous Research	49
Table 2.7	Modulus of Elasticity of GO in Cement Matrix from Previous Research	52
Table 2.8	EDX Spectra of Cement Mortar (Ganesh et al., 2023)	61
Table 2.9	Surface Area and Pore Volume of Mixers Sample of OPC and GO Composite Cement (Chintalapudi & Pannem, 2020)	63
Table 2.10	Research Gap of the Study	76
Table 3.1	Research Phases and Alignment with Research Objectives	77
Table 3.2	Physical Properties of Raw Materials	81
Table 3.3	Type of Testing Methods and Standards	88
Table 3.4	Mix Proportions of Binder Formulation (Phase 1)	95
Table 3.5	Mix Proportion of Binder Modification (Phase 2)	96
Table 3.6	Chloride Ion Penetrability Range (ASTM C1012-22)	104
Table 3.7	Corrosion Condition Related to Half Cell Potential (ASTM C876-15)	106
Table 4.1	XRF Analysis Data of OPC Composition	111
Table 4.2	XRF Analysis Data of Fly Ash Composition	111
Table 4.3	XRF Analysis Data of GGBS Composition	112
Table 4.4	XRF Analysis Data of GO Composition	113
Table 4.5	Elemental Analysis of Graphene and GO	113

Table 4.6	Rapid Chloride Test Results for GO-Blended Mortar	147
Table 4.7	Corrosion Condition According to Half Cell Potential (ASTM C876-15)	149
Table 4.8	Half Cell Potential Reading for GO-Blended Mortar	150
Table 4.9	Calculated Porosity Value for Each Samples Based on MIP Test Report	157
Table 5.1	Half Cell Potential Reading for GO-Blended Mortar	165
Table 5.2	Time to Depassivation, T_{HCP} For Every Mix in Normal and Saltwater Condition	166
Table 5.3	Active Corrosion Time (t) for Every Mix in Normal and Saltwater Condition	167
Table 5.4	Range of Corrosion Current Value Related to Corrosion Level (Matilla et al., 2024)	168
Table 5.5	Corrosion Current Density for Every Mix	168
Table 5.6	Mass Loss Variables for Mix 30SG2	170
Table 5.7	Derived Mass Loss (M) And Nominal Area Loss (A_{loss}) For GO-Blended Mortar in Normal Condition	173
Table 5.8	Derived Mass Loss (M) And Nominal Area Loss (A_{loss}) For GO-Blended Mortar in Saltwater Condition	173

LIST OF FIGURES

Figures	Title	Page
Figure 2.1	Molecular Structure of Various Derivatives of Graphene (Qureshi et al., 2019)	9
Figure 2.2	Schematic Structure of GO (Anwar et al., 2023)	13
Figure 2.3	Formation of σ and π-bonds with Electron Lopping in a Graphene Sheet (Akarsh et al., 2022)	14
Figure 2.4	The Geometric Pore Structure of Carbon-Based Material Graphene (Alvi et al., 2023)	14
Figure 2.5	Illustration of GO Network Formation Within Cement Composites (Xu et al., 2018)	15
Figure 2.6:	Schematic Process of GO Synthesis (Anwar et al., 2023)	17
Figure 2.7	Schematic Representation of Graphene, Graphene Oxide And Reduced Graphene Oxide (Akarsh et al., 2022)	17
Figure 2.8	Timeline For Graphene Oxide Synthesis By Past Researchers (Singh et al., 2016).	18
Figure 2.9	Schematic Diagram Of GO Synthesis And Fabrication (Anwar et al., 2023)	21
Figure 2.10	Schematic Illustration Of GO-Agglomeration In Concrete (Anwar et al., 2023)	24
Figure 2.11	Graphical Model Of The (a) Bonding Effect; (b) Mechanical Interlocking Mechanism; And (c) Pull-Out Simulation For The GO/GNS Reinforcement And C-S-H Structures (Kai et al., 2019)	25
Figure 2.12	Catalytic Mechanism of GO Forms a Water Transport Network During The Hydration Phase for Further the Hydrating Cement Particle (Lin et al., 2016)	26
Figure 2.13	Mechanism Of Cement Hydration Crystal With The Inclusion Of GO (Anwar et al., 2023)	28
Figure 2.14	SEM Images Of GO In Cement Hydration Crystals (Lv et al., 2014)	29

Figure 2.15	Normalized Compressive Strength of GO in Cementitious Matrix	42
Figure 2.16	Normalized Tensile Strength Of GO In Cementitious Matrix	47
Figure 2.17	Normalized Flexural Strength of GO in Cementitious Matrix	50
Figure 2.18	Normalized Modulus of Elasticity of GO in Cementitious Matrix	53
Figure 2.19	Chloride Migration Coefficient with Different GO Dosage (Hong et al., 2023)	54
Figure 2.20	Chloride Penetration Depth of Different Cement Mixes (Mohammed et al., 2015)	55
Figure 2.21	Water Absorption Coefficient with Different GO Content (Bheel et al., 2023)	56
Figure 2.22	SEM Image of Cement Composite with GO (Alla & Asadi, 2023)	58
Figure 2.23	Hydration Product of Cement Composite at SEM Image (Alla & Asadi, 2023)	58
Figure 2.24	Flower-like Crystal of GO in SEM Image (Hong et al., 2023)	59
Figure 2.25	Selected Area in Microstructure Analysis (Ganesh et al., 2023)	61
Figure 2.26	MIP Result for Different Cement Pastes Mixes (Li et al., 2017)	62
Figure 2.27	XRD Pattern of Graphite And GO (Zhao et al., 2020)	64
Figure 2.28	XRD Pattern of GO (Lee et al., 2019)	65
Figure 2.29	XRD Patterns Of 28 Days Hydrated GO Reinforced Mortar (Huang et al., 2021)	65
Figure 2.30	Corrosion Mechanisms Affecting Steel Embedded in Concrete (Firouzi et al., 2020)	67
Figure 2.31	Deterioration of Concrete Due to Corrosion in Building Component (Zhao et al., 2025)	67
Figure 2.32	Schematic Diagram of the Stages of Reinforced Concrete Damage Due to Chloride Ion Corrosion (Zhao et al., 2025)	69
Figure 2.33	SEM Images of Deteriorated Concrete Due to Corrosion (Yuvaraj et al., 2022)	69
Figure 2.34	Visual Representation of GO Bridging in Cement (Qureshi & Panesar, 2019)	71

Figure 2.35	Schematic Diagrams of the Labyrinth Effect GO Against Corrosive Penetration (Zhang et al., 2021)	71
Figure 3.1	Homogenize Process for Raw Materials Used in the Study	80
Figure 3.2	Characterisation of raw materials	83
Figure 3.3	Properties of Binder Formulation	83
Figure 3.4	Properties of Blended Mortar Incorporating with GO (binder modification)	85
Figure 3.5	Mass loss of GO-blended Mortar	86
Figure 3.6	A Comprehensive Research Framework	87
Figure 3.7	Schematic Diagram of Simplified Hummer's Method	89
Figure 3.8	XRF Apparatus at Faculty of Chemical in UiTM	91
Figure 3.9	Test Apparatus Used for Morphology Analysis Using SEM	92
Figure 3.10	Materials for Binder Formulation	94
Figure 3.11	Materials for Binder Modification	96
Figure 3.12	Preparation of Binder Formulation	97
Figure 3.13	Preparation of Binder Modification	98
Figure 3.14	Test Procedure of Compressive Strength Test	100
Figure 3.15	Test Procedure of Water Absorption Test	102
Figure 3.16	Test Procedure of Rapid Chloride Penetration Test	104
Figure 3.17	Test Procedure of Half Cell Potential Test	105
Figure 3.18	Schematic Diagram of Rebar GO-blended Mortar Specimens	106
Figure 3.19	Apparatus of Mercury Intrusion Porosimetry (MIP) in UiTM	107
Figure 3.20	SEM Machine at Faculty of Mechanical Engineering laboratory	108
Figure 4.1	XRD Pattern of OPC in X'pert Highscore	114
Figure 4.2	XRD Pattern of Fly Ash in X'pert Highscore	115
Figure 4.3	Peak Value for Fly Ash Pattern	116
Figure 4.4	XRD Pattern of GGBS in X'pert Highscore	117
Figure 4.5	Peak Value for GGBS pattern	118
Figure 4.6	XRD Pattern of GO in X'pert Highscore	118
Figure 4.7	Peak Value for GO Pattern	119
Figure 4.8	Peak Value for Graphene Pattern	119
Figure 4.9	SEM Image of OPC with Different Magnification Scale	121
Figure 4.10	SEM Image of Fly Ash with Different Magnification Scale	122

Figure 4.11	SEM Image of GGBS with Different Magnification Scale	124
Figure 4.12	SEM Image of GO with Different Magnification Scale	125
Figure 4.13	EDX Analysis for OPC	126
Figure 4.14	EDX Analysis for Fly Ash	127
Figure 4.15	EDX Analysis for GGBS	128
Figure 4.16	Selected Area and Spot of Graphene and GO for EDX analysis	129
Figure 4.17	EDX Analysis for Graphene and Graphene Oxide	131
Figure 4.18	FESEM Image of GO with Various Magnifications	132
Figure 4.19	Density of Binder Formulation	134
Figure 4.20	Compressive Strength of Binder Formulation	136
Figure 4.21	Tensile Strength of Binder Formulation	137
Figure 4.22	Water Absorption for Binder Formulation	138
Figure 4.23	Density of Binder Modification	140
Figure 4.24	Compressive Strength of Binder Modification	142
Figure 4.25	Tensile Strength of Binder Modification	143
Figure 4.26	Water Absorption for Binder Modification	145
Figure 4.27	Total Charged Passed in RCPT for GO-Blended Mortar	147
Figure 4.28	Influence of Various GO to Corrosion Probability in Blended Mortar	150
Figure 4.29	SEM Images of Cement Hydration Crystals in a Cementitious Matrix at Varying Dosages of GO at Different Magnification Level	153
Figure 4.30	Close-Up Magnification SEM Image of GO-Blended Mortar Samples	154
Figure 4.31	MIP Results for Various GO in Blended Mortar	156
Figure 4.32	Pore Structure of GO-Blended Mortar	158
Figure 4.33	XRD Pattern for GO-Blended Mortar Specimens	161
Figure 5.1	Framework for Mass Loss Calculation	164
Figure 5.2	Mass Loss and Time to Depassivation in Normal Condition	175
Figure 5.3	Mass Loss and Time to Depassivation in Saltwater Condition	177
Figure 5.4	Average nominal Area Loss for Both Conditions of Curing	179

LIST OF ABBREVIATIONS

Abbreviations

SCMs	Supplementary Cementitious Material
A_{loss}	Average Nominal Area Loss
A_{rebar}	Area of Steel Rebar
CVD	Chemical Vapour Deposition
EA	Elemental Analyser
EDX	Energy Dispersive X-ray
FESEM	Field Emission Scanning Electron Microscopy
HCP	Half Cell Potential Test
I	Total Corrosion Current
I_{corr}	Current Corrosion Density
L	Exposed Length
MIP	Mercury Intrusive Porosimetry
RC	Reinforced Concrete
RCPT	Rapid Chloride Permeability Test
SCMs	Supplementary Cementitious Materials
SEM	Scanning Electron Microscopy
t	Active Corrosion Time
T_{HCP}	Time to Depassivation
T_{total}	Total Exposure Time
vdw	Van Der Waals

XRD	X-ray Diffraction
XRF	X-ray Fluorescence
EA	Elemental Analyser

LIST OF NOMENCLATURES

Nomenclatures

A	Akermanite
Al_2SiO_3	Alumina
C	Carbon
Ca	Calcium
$CaCl_2$	Calcium Chloride
CaO	Calcium Oxide
C-S-H	Calcium Silicates Hydrates
CH	Calcium Hydroxide
CO_2	Carbon Dioxide
COC	Alkoxy
COOH	Carboxylic Acid
FA / F	Fly Ash
Fe_2O_3	Iron Oxide
G	Gehlenite
GGBS / S	Granulated Ground Blast Furnace Slag
GNPs	Graphene Nanoplatelets
GNT	Graphene Oxide Nanotube
GO	Graphene Oxide
H_2SO_4	Sulphuric Acid

HCl	Hydrochloric Acid
Mg	Magnesium
NaOH	Sodium Hydroxide
OH	Hydroxide
PCE	Polycarboxylate Ether
SiO_2	Silica Oxide

CHAPTER 1
INTRODUCTION

1.1 Research Background

In recent years, various have included nanomaterials in cementitious based material to enhance its mechanical properties as well as the durability performance. Nanomaterials own a very high surface area and reactivity which directly acts as nucleation sites for the hydration process (K. R. Singh et al., 2022). This significantly enhances the hydration product and pore structure refinement. This eventually shows the major benefits of advancement in nanomaterials to modify the microstructures of cement at the nanoscale (Anwar et al., 2020). The addition of nanomaterial in the cement matrix performs four primary functions of filler material, enhancing pozzolanic activity, microstructure refinement and facilitating the cement hydration process. However, several issues need to be overcome as incorporating nanomaterial as an additive in cement. By achieving a stable and uniform dispersion of nanomaterial in cement remains an elucidate. This can be explained as a non-uniform mixture usually due to the agglomeration product of nanomaterial within the cement matrix. The occurrence of nanomaterial agglomeration causes poor effectiveness of high surface area which eventually reduces the ability to react during cement hydration (Long, Li, et al., 2018). The agglomeration of nanomaterials occurs when small particles adhere to one another rather than remaining uniformly distributed. This leads to the ineffectiveness of the cement hydration product because there is a lack of interaction between the surface area of the nanomaterial and water and other reactants. In other words, the large surface area of the nanomaterial is wasted as the particles clump together within the cement matrix. This also leads to an ineffective cement hydration reaction, which consequently weakens the cementitious base itself. With the aid of an uncontrolled amount of nanomaterial in the cement matrix, it tends to cause greater attractive forces between the cementitious material and nanomaterials (Anwar et al., 2020). This eventually causes the formation of agglomerates. As the attractive forces start to strengthen, it decreases the possibility of separating them within the cement matrix.

Within the area of nanomaterial research, graphene oxide (GO) has been devoted as an encouraging additive and the focus of the study. The incorporation of GO has attracted significant attention in cementitious properties due to remarkable well, chemical and durability. GO, a two dimensional nanomaterial derived from chemical oxidation of graphite, contains many oxygen functional groups that interact with cement hydration products (Meng et al., 2021). The increased in surface area and aspect ratio enhances the microstructure refinement, bridging effect as well as acceleration of calcium silicate hydrate (CSH) gel. These abundant oxygen are covalently bonded to the surface of GO which consequently improves the dispersion rate of GO within the cement matrix and enhances its hydrophilic behaviour (Son et al., 2023).

Despite the promising mechanism of GO in cementitious materials, a critical perspective remain exists regarding its long-term durability against corrosion assessment. While current studies confirm the microstructural refinement and durability of GO, most of the research relies on basic corrosion indirect corrosion metrics such as the Rapid Chloride Penetration Test (RCPT) and the Half-Cell Potential Test (HCP). However, these tests failed to accurately measure the extent of structural damage caused by the steel rebar once corrosion is active (Asen & Dehestani, 2021). Therefore, a shift from indirect durability metrics to direct quantification of material loss is necessary. The calculation of mass loss using Faraday's Law is observed as one of the precise methods to quantify the total consumption of steel rebar over time, especially in high corrosion potential environments. Therefore, a comprehensive analysis of GO and its mechanism within blended cement matrix are included in the research. To provide more detail, this research also evaluates GO's overall performance as a nanomaterial additive against corrosion and the influence of oxygen functionalities of GO towards dispersion and microstructural refinement.

1.2 Problem Statement

Corrosion is one of the major forms of attack from the environment on reinforced concrete (RC), which can reduce the reliability and strength of the structure. In general, the concentration of corrosion products around the steel rebar created internal stresses, leading to cracking of the concrete (Firouzi et al., 2020). This enables the diffusion of moisture, oxygen and even chloride ions as it facilitates the rebar

corrosion process (Zhang et al., 2023). Initially, a passive protection film surrounded the steel rebar as primary protection against corrosive penetration. Nevertheless, once the passive film started to deteriorate, corrosion began and consequently reduced the load-bearing capacity as the area of the rebar was also being reduced over time (Kobayashi et al., 2025). It is also worth mentioning that the mass loss also reduced linearly with the area of rebar.

To overcome this issue, various methods have been introduced in past literature reviews to be conducted, such as corrosion inhibitors mortar, rebar surface coatings, cathodic protection and even rebar surface coatings (Johari et al., 2021). However, these methods have several major drawbacks, including ineffective protection and posing a continuous hazard to the environment. This usually can be seen as the structure shows a severe combination of calcium leaching and sulfate attack in marine conditions promotes porosity increase. This shall leads to the formation of expansive products like ettringite, which further deteriorates the material. This approach also often leads to failure in balancing the extraction of chloride ions and the corrosion resistance mechanism (Burgos et al., 2017).

Therefore, to reduce the corrosion influence on the reinforced steel embedded in concrete, a variety of concrete and cementitious-based materials have been explored, including nanomaterials. In recent years, nanomaterials have been introduced, providing numerous significant opportunities to raise the physical and mechanical performance. It has been identified that the utilisation of nanomaterial as filler material and partial substitute for binder in cementitious matrix material (Abdalla et al., 2022). Bhojaraju et al.,(2023) also emphasise that adding nanomaterial within the cementitious-based material provides a significant enhancement to the durability of the RC member. This shows how microstructure refinement of the cement matrix improved as well. Nevertheless, despite the research on nanomaterials as a corrosion resistance additive, graphene oxide remains unexplored in the literature review.

A significant shortage of knowledge also exists regarding the integration of GO with supplementary cementitious materials (SCMs) or blended cements. Meanwhile, most existing research focuses on ordinary Portland cement, leaving the interaction between GO and SCMs mostly unexamined (Divya et al., 2022). This is because SCMs are well known for its durability where it can enhance the microstructure of concrete, making it denser and less permeable. This reduces chloride penetration and calcium leaching, especially in aggressive environments like seawater. While GO holds

significant promise for improving material properties within the cementitious matrix, a critical knowledge gap remains in predicting long-term performance, specifically concerning corrosion resistance and structural mass loss. This deficiency is due to the lack of reliable and time-efficient methods to forecast how these advanced nanomaterials behave over a structural lifespan. Henceforth, this creates the urgency for this study to be conducted as it opens the possibility of providing a formulation of blended mortar with GO that ensures an effective resistance against ion ingress and long-term effectiveness against corrosion.

There are two main research questions that can projected in this study:

i. How do the complementary benefits of blended material (Fly Ash and GGBS) and GO influence the microstructural refinement and subsequent service life of the blended mortar?
ii. How does the percentages of GO influence the mass loss and what is the critical value associated with GO mechanism against corrosion penetration?

1.3 Research Objective

The aim of this study focussed on developing a nano-composite blended mortar incorporating graphene oxide as it can improve as corrosion resistance. Four objectives were designed to achieve the aim of the study which are:

i. To characterise blended material and graphene oxide, and to evaluate their influence on the physical, mechanical, and durability properties for binder formulation.
ii. To investigate the optimum ratio of graphene oxide in producing nano-composite mortar under physical, mechanical and durability properties for binder modification.
iii. To evaluate the microstructure and durability of GO-blended mortar against corrosion resistance.
iv. To investigate the mass loss of the steel rebar within the GO-blended mortar using Faraday's Law equation.

1.4 Scope & Limitation of Study

This study consists of three major phases, where the first phase focused on the raw material characterisation and properties of blended mortar, also known as binder formulation. The second phase is the properties of binder modification where it included GO-blended mortar, microstructural and comprehensive corrosion assessment. Finally, the final phase in the study focused on the specific area of study of mass loss as well as the average nominal area loss for normal and saltwater conditions. Hence, the experimental works and testing parameters are as follows:

i. The raw material characterisation in the study included several types of characterisation such as chemical, phase, physical and microstructure. To be more specific, the related tests are X-ray Fluorescence (XRF), Elemental Analyser (EA), Energy Dispersive X-ray (EDX), X-ray Diffraction (XRD), Scanning electron microscopy (SEM) and Field Emission Scanning electron microscopy (FESEM).
ii. A total of 126 blended mortar samples were prepared in the binder formulation in order to assess the physical, mechanical, and durability properties. The tests cover density, compressive strength, split tensile, and water absorption. Moreover, the supplementary cementitious material (SCMs) studied in this phase were Fly Ash (F) and GGBS (S).
iii. In the binder formulation phase, it involves a fixed cement replacement percentage of SCMs by 0%, 10%, 20% and 30%. This phase aimed to determine the optimal SCMs percentage replacement and type of SCMs before GO inclusion.
iv. The experiment continued with the binder modification phase, where the inclusion of GO as a nanomaterial additive at various dosages, 0.02%, 0.04%, 0.06%, 0.08%, 0.10% was performed in the blended mortar. A total of 162 GO-blended mortar samples were prepared in this phase, with a consistent water-cement ratio of 0.5.
v. A final series of 54 GO-blended mortars were prepared for the corrosion assessment testing, including the Half Cell Potential Test (HCP) and the Rapid Chloride Penetration Test (RCPT). Moreover, the microstructural testing, including Scanning Electron Microscopy (SEM) and Mercury

Intrusion Porosimetry (MIP), were performed in the study. Moreover, an additional XRD analysis for GO-blended mortar specimens were conducted in this phase.

vi. The final phase of study involved the determination of Mass Loss using an analytical assessment of Faraday's Law equation from HCP test under two curing environments of normal curing and saltwater curing (5% NaCl solution). This analytical assessment required several major parameters of Time to Depassivation (T_{HCP}), Active Corrosion Time (t) and Total Corrosion Current (I).

vii. The calculated mass loss was then used to derive the Average Nominal Area (A_{loss}), which was defined as the final structural failure assessment due to corrosion.

This research established a definitive baseline for the incorporation of Graphene Oxide (GO) within blended cementitious matrices. Nevertheless, several experimental boundaries must be explicitly delineated. First, the evaluation of microstructural development and mechanical governance was strictly confined to the specific mix design parameters governed by the testing framework. The mortar formulation was rigidly proportioned at a fixed binder-to-sand ratio of 1:3 and a water-to-cement ratio of 0.5 in strict compliance with ASTM C109 guidelines. Furthermore, the binder variations were restricted to fixed supplementary cementitious material (SCM) replacement thresholds of 10%, 20%, and 30% by weight of cement, while the GO dosage was varied between 0.02% to 0.10% per weight of the binder. Additionally, the incorporation of a polycarboxylate ether (PCE)-based superplasticizer was maintained at a constant dosage of 0.02% per weight of the binder across all experimental mixes. Because the fundamental mechanism of GO relies on providing optimal nucleation sites for hydration products, any deviation from these fixed ratios could significantly alter the spatial dispersion kinetics, rheological behaviour, and chemical hydration of the matrix.

Second, the reinforcement degradation assessment was intentionally restricted to an analytical approach to establish an electrochemical baseline rather than capturing physical macro-scale destruction. Specifically, steel reinforcement degradation was evaluated through Faraday's Law through continuous electrochemical monitoring

instead of executing physical mass loss gravimetric calculations on the extracted steel rebars.

1.5 Significance of Study

This research portrayed the significant value of nanomaterials by exploring a direct approach of graphene oxide (GO) within a practical construction material. This is because by including GO into the blended cement matrix, it addresses theoretical information as well as practical application challenges faced by real-world structures. Not only that, but this research can also deliver the unique properties of GO itself, such as high surface area and the protective barrier effect, which directly contributed towards the enhancement of durability against corrosion of the cementitious materials. Thus, the findings shall provide a comprehensive foundation for further research and application of GO as it is being devoted as one of the alternative nanomaterials for improving structural durability and longevity.

As in the research, the primary contributions lie in the innovative utilisation of GO as a corrosion resistance additive within the blended mortar. In contrast to conventional corrosion inhibitors such as zinc-rich oxide, GO offers a significant mechanism for mitigating a corrosion attack when exposed to the environment. By preventing the degradation process, GO can lead to a reduction in the frequency of maintenance of infrastructure. This research shall also provide practical and effective answers, as it offers new findings to forecast or predict the constant threat of corrosion to construction materials. Furthermore, the findings of the study also provide a comprehensive understanding of the involvement of GO in cementitious materials. This shall pave a new way towards new industry standards and guidelines specifically in the corrosion resistance context.

Finally, the research also focuses on approaching the objectives of Sustainable Development Goal 9: Industry, Innovation, and Infrastructure. This can be explained by revealing the effectiveness of GO as a corrosion resistance additive, which tends to contribute towards the development of more durable yet resilient structures. On top of that, the findings in this research shall also promote sustainable innovation materials used in the industry. By extending the possibility of service life structure, it can reduce the consumption of existing material and waste with frequent repairs or even replacement. This indirectly contributes to a more systematic and sustainable circular

economy growth. The findings in this study not only provide a new framework for the industry standards, but they also promote a greater quality of material within the structural aspect.

CHAPTER 2
LITERATURE REVIEW

2.1 Introduction to Graphene Oxide

Generally, GO stands as the most promising derivative within the expansive of graphite family which consist of graphene, graphene oxide, reduced graphene oxide and graphene nanoplatelets as shown in Figure 2.1. Generally, the history of GO started with a single layer of graphite described as graphene whereby is commonly known for strength enhancement as it can improve several performances with novel properties. To be more specific, graphene is a two-dimensional crystalline allotrope with a hexagonal lattice structure that is solely formed by carbon atoms (Singh et al., 2022). Graphene also is commonly exposed for its fascinating properties of containing high optical transparency as well as thermal conductivity at room temperature. In detail, the derivatives and properties of graphene oxide can be shown in Table 2.1.

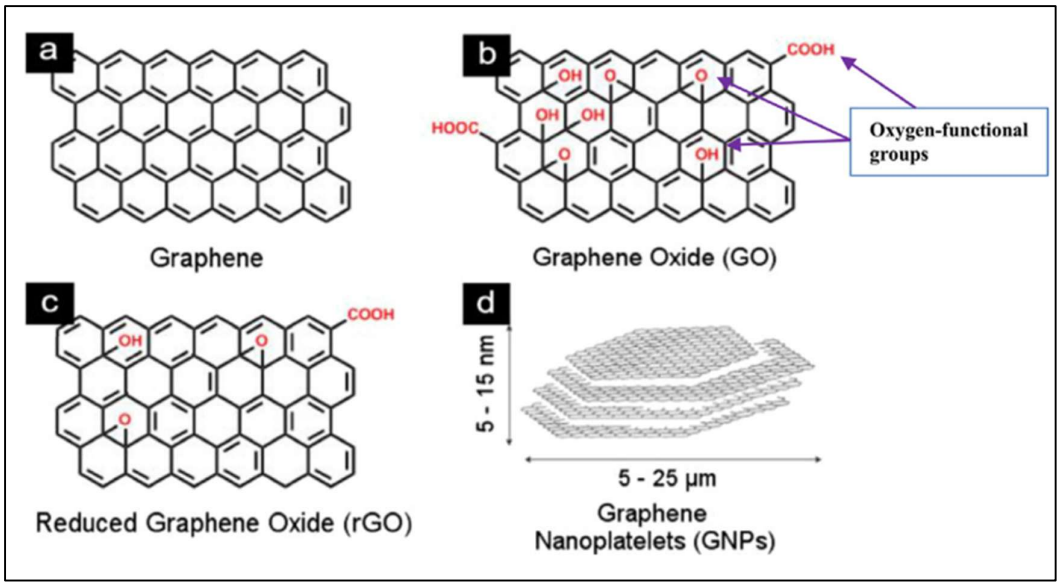


Figure 2.1 Molecular Structure of Various Derivatives of Graphene (Qureshi et al., 2019)

Table 2.1
Definition and Properties of Graphite Derivatives

No	Derivative	Definition	Properties
1	Graphite	An element of a crystalline allotrope of carbon with planar layered structures whereby each layer consists of carbon bonded covalently in a hexagonal array.	• Lighter than diamond, smooth and slippery to touch. • It is a good conductor of heat and electricity. • It is a crystalline solid. • Non-inflammable.
2	Graphene	A whole structure based on two-dimensional (2D) material is devoted as the first two-dimensional crystalline substance. One of the lightest materials ever found with an attached sheet of carbon atoms in a hexagonal shape.	• Transparent material and low-light absorbance. • High electrical conductivity. • Hydrophobic nature due to Due to the presence of attractive Van der Waals forces.
3	Graphene Oxide	A single layer of graphene with additional oxygen functionalities group on the material surface. It is generated by undergoing oxidative alteration on the basal plane due to the oxidation and exfoliation process during synthesis.	• Extensive amount of oxygenated functional group and high surface area. • Highly hydrophilic and easily dispersed in water due to the existence of oxygen functional groups on both basal planes and edges. • Stable and homogeneous colloidal suspensions in aqueous or polar organic solvents. • It may form a protective barrier against in a hazardous acidic environment. • High optical transparency and semi-conductivity at room temperature. • Flexible all within a strong nano-sized material.
4	Reduced Graphene Oxide	A derivatives of graphene that produced by the reduction method from GO as it includes thermal, chemical etc. in order to reduce the oxygenated functional groups. rGO is also devoted as one of the stable derivatives of graphene and higher	• A higher surface area due to the elimination of oxygen with a drawback of hydrophobic nature. • Low rate of dispersion in water.

		notable properties for other applications.	• Conductive composites with tailored electrical characteristics. • High electrical conductivity. • Good sensing abilities due to active surface and high surface area.
5	Graphene nanoplatelets (GNPs)	Graphene nanoplatelets (GNPs) are two-dimensional carbon structure materials attached with single or several layers of graphite plane. It also provides high electrical conductivity, modulus, strength, thermal conductivity and even surface area.	• Low weight of material with a high surface-to-volume ratio. • High electrical and thermal conductivity. • Improve mechanical strength. • Inexpensive and structures of planar form. • A higher magnitude order in electrical conductivity than graphene oxide. • Highly hydrophobic due to large-scale of oxygen reduction.

However, GO possess the most promising and preferable derivative among others as it shows a higher significant functional group of oxygen molecules. It is also can be considered a highly oxidized variant of graphene whereby it designed in 2-way dimensional nanomaterial. On top of that, GO also can be known as a primary precursor when it comes to cementitious composite using graphene. This is due to the attachment level with separate oxygen functional groups. Moreover, it is also due to the enormous surface area which eventually helps to provide a stronger reactivity with the cement during matrix interaction (Tay & Norkhairunnisa, 2021). From existing research, GO holds the potential to become the most convincing additive nanomaterial as in cementitious material. This is because present studies have addressed remarkable findings of GO particularly in mechanical performance with cementitious materials. Thus, a new introduction in the field of cementitious composites to utilize a two-dimensional material such as GO.

2.2 Comparative Analysis of Graphene Oxide and Graphene

A comparison of why GO is the preferred derivative in cementitious materials is due to the dispersion rate of GO itself. This can be discussed as a comparison between graphene and graphene oxide. Theoretically, GO can be described as a stronger derivative of graphene whereby it has been substantially oxidized into 2D material produced by a single layer and hybridized hexagonal linkage of carbon atoms. It also can be considered as an extensive amount of oxygen-based functional groups whereby it bonded covalently with the GO surface as it can enhance its dispersion in water (Babak et al., 2014; Singh et al., 2016). To put this into other words, it is an oxidized form of graphene laced with an oxygen-based group same as hydroxyl (−OH), alkoxy (C-O-C), carbonyl, the carboxylic acid (−COOH), and other oxygen-based functional groups at the surface of GO. This embedded the properties of having both hydrophobic (nonpolar) and hydrophilic (polar) regions in one molecule. Consequently, it improved water dispersal and enhanced its hydrophilic condition (Sai et al., 2025). This feature of hydrophilic shall allow GO to create and form stable colloids in water. Despite the formation of high colloidal stability in water along with various sets of mechanical, colloidal, and optical properties, the synthesis method that has been adopted for GO utilises strong oxidants. One of the most common oxidants used is potassium permanganate (KMnO4) which leads to signify a generous amount of defects in its crystalline network (Ghulam et al., 2022). It also contains a very high concentration of oxygen whereby the carbon to oxygen ratio (C/O) characterisation, is less than 3.0 and closer to 2.0**.** On top of that, GO also consists of the chemical composition of carbon, hydrogen, and oxygen molecules, which ultimately becomes inexpensive yet abundant.

Apart from that, due to the bigger surface availability, it contributes to a higher nanomaterial potential as well as novel behaviour. GO itself has a greater surface area of C-S-H nucleation owing to the 2-dimensional form which can lead to a higher reactivity (Liu et al., 2020). Thus, it can surely be affecting the strength obtained by cement as well the development of the adhesive property. This is because GO primary purpose in cement paste is to produce a substrate in its functional groups to react with cement hydration products such as C-S-H and $Ca(OH)_2$. To support this statement, GO is also a highly covalent bonded in the carboxylic groups on the boundaries due to a reaction concerning GO and calcium hydroxide (C-S-H). This can be visualised as Figure 2.2 in shows the Schematic structure of GO.

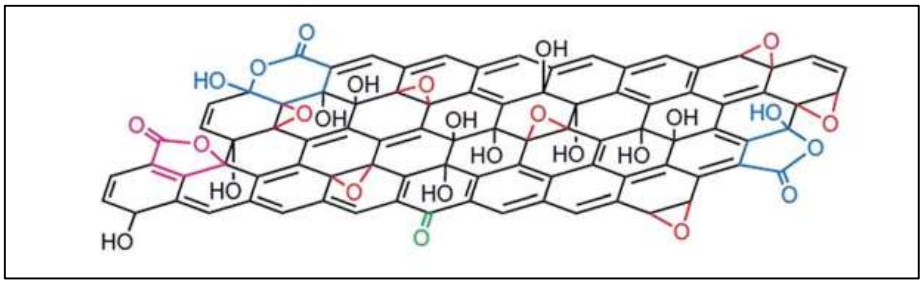


Figure 2.2 Schematic Structure of GO (Anwar et al., 2023)

Graphene however is also considered as a strong and stable form as each carbon atom is covalently bonded resulting in higher tensile strength and repulsion energy (Anwar et al., 2023). Consequently, the bonding configuration indicates tremendously strong σ-bonds and weak interplanar van der Waals (vdw) π –bonds (Janavika & Prakash Thangaraj, 2023). The σ-bonds help in holding the carbon atoms together which fundamentally contributes towards the strength of graphene. Meanwhile, π – bonds assist the ability of the graphene to slide over one another as shown in the Figure 2.3. However, this material has been categorized as inert and hydrophobic (Zhao et al., 2020). This causes difficulties in obtaining a proper homogenous bonding with any cement matrix interface. Not only that but it also has a poor dispersion which leads to the formation of agglomeration in the cement matrix or even a major hindrance in strength development (Zhao et al., 2020). This can be explained as the geometric pore size of Graphene is 0.064 nanometre (nm) which is particularly smaller in diameter of a molecule compared to hydrogen (0.314 nm) and helium (0.28 nm) as shown in the Figure 2.4. This is directly stagnant and forbidden for any molecule to pass through it.

In contrast, the existence of functional groups of oxygen attached to the surface of GO changes the van der Waals (vdw) interaction by extending the spacing of the layers within the range of 0.335 nm to 0.625 nm. This ultimately enhances water dispersal movement within the cementitious material as well as developing its hydrophilic behaviour (Lin & Du, 2020). To be more specific, a single layer of GO features a thickness between 0.7 nm to 1 nm, along with a side range of 100 nm and 100 micrometres. Therefore, by having these features also, it tends to enlarge the surface area within 700 to 1500 m^2/g and the aspect ratio of 1500 to 45000. Therefore, this explains concisely why GO spreads more easily in cement matrix than graphene or other nanomaterial as the hydrophilic behaviour significantly reduces the van der Waals forces between GO layers. Furthermore, due to the oxidation on the surface of GO, it

facilitates cement hydration as it refines the microstructures of the cement matrix leading to a reduction of porosity and permeability (Xu et al., 2018). This fundamentally helps in increasing the durability of the cement by mitigating any ingress of corrosive media such as water, chlorine, acid, and carbon dioxide or harmful substances from penetrating. Therefore, an illustration of GO network formation within cement composites can be shown in Figure 2.5.

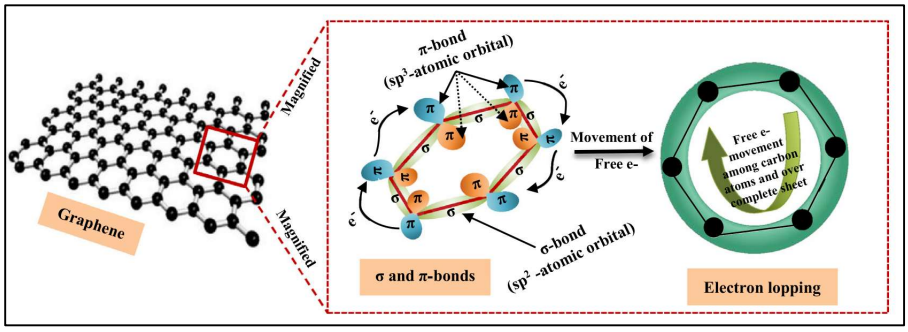


Figure 2.3 Formation of σ and π-bonds with Electron Lopping in a Graphene Sheet (Akarsh et al., 2022)

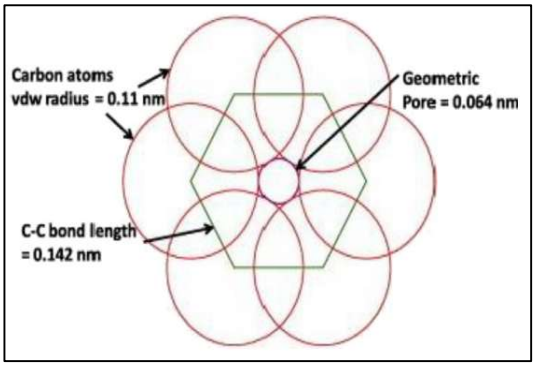


Figure 2.4 The Geometric Pore Structure of Carbon-Based Material Graphene (Alvi et al., 2023)

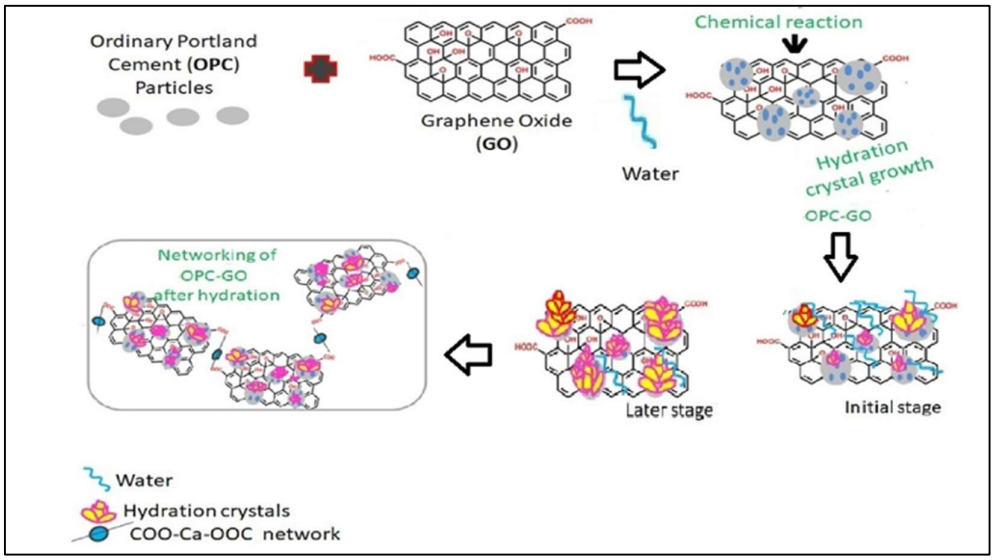


Figure 2.5 Illustration of GO Network Formation Within Cement Composites (Xu et al., 2018)

Moreover, graphene and GO also dominate superior properties in terms of physical and even mechanical compared to other nanomaterials. Based on Table 2.2, shows GO has lower physical attributes compared to graphene. Nevertheless, GO owns a major benefit from the attached oxygenated functional group whereby it fastens the reactivity pace and effortlessly disperses in the cement matrix (Susan Ja et al., 2023). Not only that but the mechanical properties in graphene also may be influenced by to existence of oxygenated functionalities groups which indicates GO sheets have second-fiddle in tensile strength and elastic modulus. This indicates why GO is one of the most promising nanomaterials that can exhibit significant performance with its novel properties in cement matrix material.

Table 2.2
Properties of Graphite Derived Nanomaterials (Akarsh et al., 2022)

Material	Surface area (m^2/g)	Thickness (nm)	Aspect Ratio	Density (kg/m^3)	Elastic Modulus (GPa)	Tensile strength (GPa)
Graphene	2600	~0.08	6000-600000	2200	1000	~130
CNTs	70-400	15-40	1000-10000	1330	950	11-63
Graphene Oxide	700-1500	~0.67	1500-45000	1800	23-42	~0.13
Carbon fibre	0.34	6000-20000	100-1000	1770	7-400	0.4-5
Polymeric fibre	0.225	18000-30000	160-1000	900	3-5	0.3-0.9
Steel fibre	0.02	50000-900000	45-80	7800	200	1.50
Glass fibre	0.3	5000-10000	600-1500	2540	72	3.45

2.3 Approaches for Synthesis of Graphene Oxide

To current knowledge, the synthesis of GO can be generated into two major approach of bottom-up and top-down. The bottom-up approach includes thermal pyrolysis and laser, epitaxial growth, chemical vapour deposition also known as CVD and direct organic synthesis from carbon precursors. Meanwhile, the top-down approach contain exfoliation, chemical oxidation as well and arc discharge which is normally used for low-cost production and viability for commercial purpose (Kumar et al., 2021).

As in the production of GO, the top-down approach has been the only method that includes a major oxidation and exfoliation process from graphite structures. Therefore, the schematic process of GO synthesis can be shown in the Figure 2.6. The oxidation process helps in introducing oxygen functional groups which generally reduce the bond strength of Van Der Waal between sheets of GO and consequently convert the material to become hydrophilic. Hydrophilicity is vital because it ensures uniform dispersion of GO sheets through electrostatic repulsion and provides oxygen-rich nucleation sites for C-S-H growth (Baomin & Shuang, 2019). In order to reduce the repulsion energy projected by the Van Der Waal interaction, oxygenated functional

groups tend to increase the interlayer spacing (Akarsh et al., 2022). This automatically leads higher dispersion rate and reactivity in the cement matrix compared to other derivates as it has lower repulsion energy. Furthermore, exfoliation tends to exfoliate the multilayer graphite oxide to a single or even several layers of GO using ultrasonication. In addition, GO also includes a slight hexagonal structure difference as it has a spare hydroxyl group connection towards the carbon community which can be depicted in Figure 2.7. It is also a single-layered of nano-material owning graphene sheet along with oxygen functionalities groups such as epoxy (-O-) and hydroxyl (O-H) on the GO's surface. Not only that but GO also consist of carboxyl (C-O-O-H) and carbonyl (C=O) which are located at the sheet edge for the surface. GO also can be considered as one of the most stable and strong graphene derivatives as it has been substantially oxidized into 2D material.

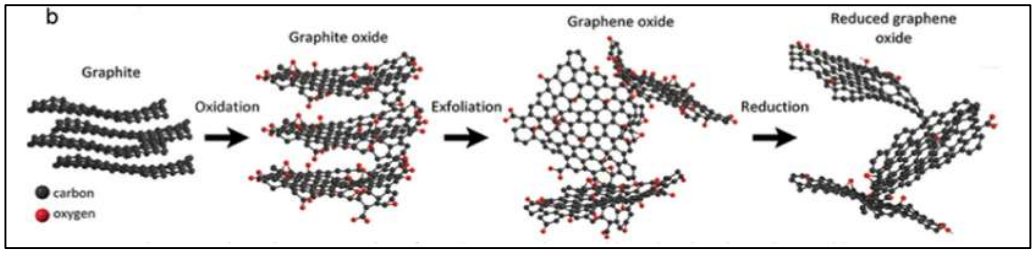


Figure 2.6: Schematic Process of GO Synthesis (Anwar et al., 2023)

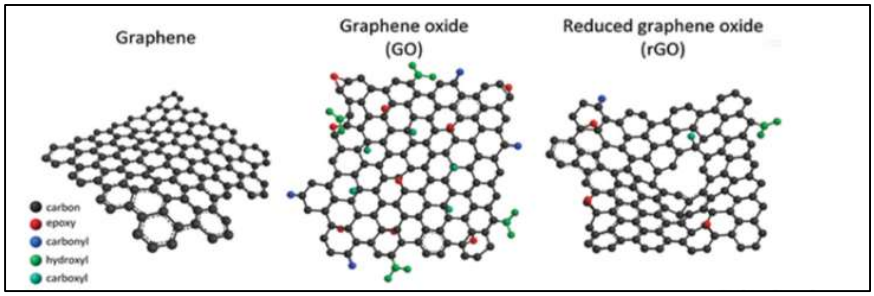


Figure 2.7 Schematic Representation of Graphene, Graphene Oxide And Reduced Graphene Oxide (Akarsh et al., 2022)

Nowadays, the urgency and need of producing GO are due to the noticeable ability of layered graphene to insert or position between existing layers of elements. To be more specific, it allows the active metal atoms along with several types of oxidation agents to penetrate between flat carbon layers of crystalline graphite. This shall influence the increasing of interlayer distance and altering surface layer chemically by bonded functional groups (Mashhadani & Pershin, 2020). Moreover, the presence of

suitable oxidation agents leads to a complete disassembling of graphitic crystals into separated carbon monolayers with modified surfaces chemically.

Theoretically, there are several methods of preparation when it comes to producing GO in previous research. They were named such as Brodie's, Staudenmaier's, and Hoffman's methods. However, one of the most common methods used was the Hummers-Offeman method whereby it uses a mixture of concentrated Sulfuric acid (H_2SO_4), Sodium nitrate ($NaNO_3$) as well as Potassium Permanganate ($KMnO_4$). The major reason why it is commonly used is that it provides less require time compared to other methods and even better yield (Dideikin & Vul', 2019). It can be concluded that different method carries different type of synthesis of the GO process using graphite, acids, and oxidizing chemicals. A detailed review of known methods of preparation GO by oxidation of graphite can be shown in Figure 2.8.

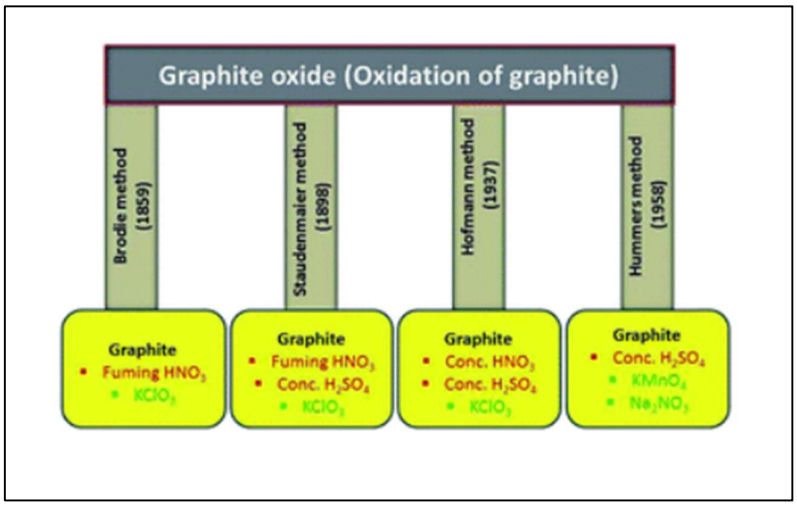


Figure 2.8 Timeline For Graphene Oxide Synthesis By Past Researchers (Singh et al., 2016).

2.3.1 The Brodie's Method

In the early year of 1859, Brodie managed to conduct the oxidation process with the presence of fuming nitric acid as well as potassium chlorate. Initially, he conducted a reaction of graphite powder with potassium chlorate ($KClO_3$) in concentrated fuming nitric acid (Kumar et al., 2021). Later on, he managed to obtain a new compound that consist of carbon, oxygen and hydrogen which eventually help in increasing the overall mass of graphite. He simply isolated the crystal of the material with one consequence

of not being able to measure the interfacial angles of the crystal lattice. Through a successful oxidative treatment, it increases the oxygen content and reached its limit after several reactions. In terms of the ratio of C:H:O percentage composition, it was determined as 61.04: 1.85: 37.11. The molecular formula was $C_{11}H_4O_5$, and he stated that the synthesized material can be considered as a dispersant in pure water but not in acidic media. Hence, along the way during this time, some groups of researchers used this method for graphene oxide production.

2.3.2 The Staudenmaier's Method

In 1898, there was one improvement idea on Brodie's work conducted by L. Staudenmaier himself by using an excess of the oxidizing agent along with the sulfuric acid that acts as an extra additive. He managed to improve the original Brodie's $KClO_3$-fuming HNO_3 preparation by adding generous aliquots of potassium chlorate ($KClO_3$) solution into the mixture during the reaction process. Not only that but he also added concentrated sulfuric acid (H_2SO_4) in order to increase the level of acidity in the mixture. Technically, these adjustments led to a highly oxidized graphite oxide in a single reaction vessel which simplified the GO synthesis process as a whole (Kumar et al., 2021). However, this method of preparation was stated to be time-consuming as well as hazardous as the additional potassium chlorate only lasted a week. On top of that, the chlorine dioxide also needed to be removed using inert gas as it has the tendency to explode on a certain level. Hence, despite it having been used during its time, a further study on better improvement methods was still under investigation.

2.3.3 The Hoffman's Method

As a further study conducted on the improvement method of GO synthesis, in 1937, Hoffmann managed to use concentrated sulfuric acid (H_2SO_4) along with concentrated nitric acid and potassium chlorate ($KClO_3$) for the oxidation of graphite. Potassium chlorate ($KClO_3$) is commonly known for its high level of oxidizing agent whereby it can oxidise the graphite powder in an acids solution. On top of that, it is also being used as the in-situ source of dioxygen where it acts as a reactive species element.

2.3.4 The Hummer's Method

Hummer's Method occupies the process of oxidation as well as exfoliation of graphite. On a crucial point, the condition of chemical oxidation of graphite is commonly found within a size of (< 10μm) as the initial size of the material particle. Besides that, intensive stirring or ultra-sonication is important to complete the chemical reaction fully along the process. This comes as a reason of large sized GO flakes can be controlled and even reduced. Thus, the mean size of particles of GO needed to be in the required size and not exceed the range. However, the properties of GO along with colligative properties of macroscopic structures rely on the mean size of the flakes. Hence, the increase in the size of synthesized GO particles still holds a gap and challenge for researchers to overcome over the years (Ghazizadeh et al., 2018). However, recent research managed to propose an improved GO preparation method whereby it focussed mainly on obtaining large and even ultra-large sized GO platelets known as LGO and ULGO (Dong et al., 2017). Basically, the main idea of this method is to split GO preparation into 2 major phase which is the soft chemical exfoliations of initial graphite into graphene flakes in liquid form. Later then it goes to the second phase of subsequent oxidation which results in the product being in mild conditions. To be more detailed, the interaction of crystalline graphite, chromium trioxide and hydrogen peroxide shall create the most effective exfoliated graphite at room temperature. On top of that, the subsequent oxidation in preparing the large graphene flakes will be at a reduced concentration of potassium permanganate whereby allows for obtaining a larger area uniform of GO flakes. This also shall prevent any formation of oxidation defects as shown in Figure 2.9. Moreover, the Hummers method was adopted for GO synthesis due to its superior safety, efficiency, and scalability compared to traditional oxidative techniques in this study. It is particularly advantageous for its ability to produce a high density of oxygen-containing functional groups without the risk of explosive chlorine dioxide gas, ensuring optimal chemical interaction within the cementitious matrix.

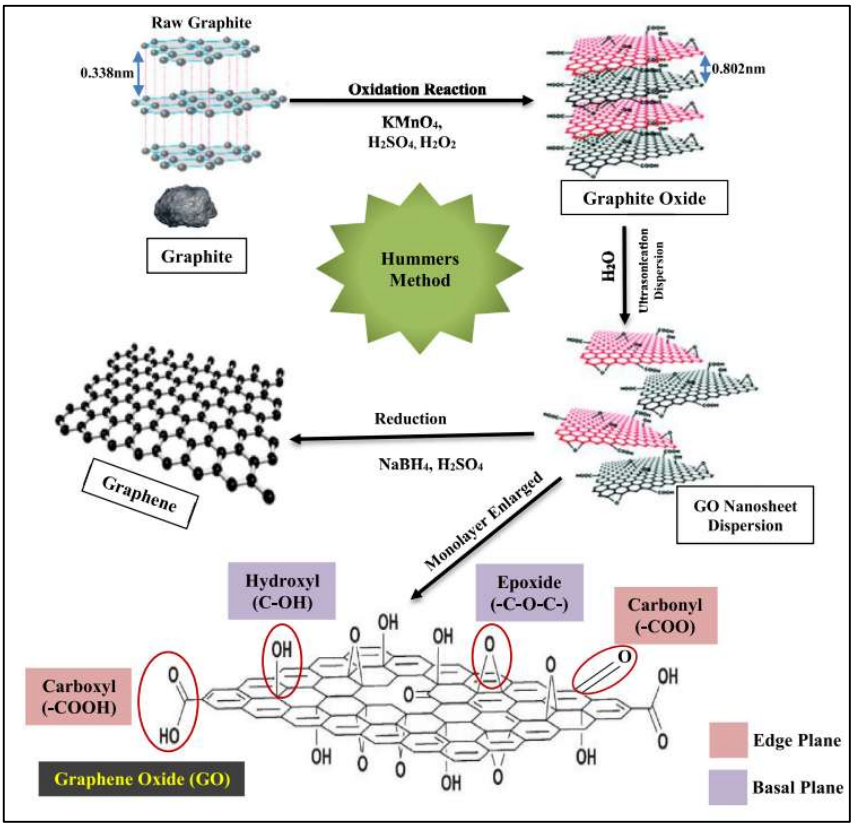


Figure 2.9 Schematic Diagram Of GO Synthesis And Fabrication (Anwar et al., 2023)

2.4 Dispersion of Graphene Oxide

With the aid of optimal content of GO, it tends to deliver an improvement and enhancement characteristic towards cement-based material as in mechanical and durability aspects. Nevertheless, GO also possesses the possibility of agglomeration in the preparation process due to strong van der Waals between layers and also high specific surface area. It also discussed that a higher concentration of GO does not significantly improve any performance of cement composite but instead creates a setback of agglomeration. Therefore, an excellent dispersion is crucial towards the successful usage of GO in cement-based materials (Liu, Chen, et al., 2021).

2.4.1 Graphene Oxide Combination

On notable preference, GO is devoted to its extensive amount of functional groups of oxygen. With the aid of this oxygen group located on the surface of GO, it tends to deliver a great dispersion rate due to its electrostatic repulsion and strong

hydrophilic. Therefore, it strongly facilitates an enhancement in the dispersion of GO in cement-based. On the other hand, as in cement pore solution, it has a strong alkaline solution whereby it has a significant amount of metal cations such as Ca^{2+}, K^{+} and Na^{+} (Zhao et al., 2018). As in previous research, GO is prone to agglomeration in cement and is mainly caused due to high calcium ion concentration and high alkalinity. On top of that, GO has a low tolerance to Ca^{2+} which indirectly causes the agglomeration process to occur by the bridging effect of Ca^{2+} when the concentration is too high.

2.4.2 Physical Dispersion Techniques

There are several most commonly used physical dispersion methods such as electromagnetic stirring, high-shear mixing as well as ultrasonic dispersion (Zhao et al., 2020). Technically, the physical dispersion acts upon the role of releasing mechanical energy by using ultrasonic waves and high-speed shear. In-depth, the extra energy tends to break the chemical interactions between nanomaterials by decreasing the van der Waals force and increasing the material dispersion (Liu, Chen, et al., 2021). This energy also can be known as repulsion energy whereby it can be defined as energy associated with the force that controls particles' distances. However, the physical dispersion also can be affected by the researcher's usage method and different functional equipment settings. As an example, the expansion of ultrasonic time can reduce the dispersion effect of GO when the ultrasonic strength is too low while excessive ultrasonic power has no significant effect to GO dispersion. This occurrence might interrupt the uniformity of GO particles and cause interlaminar slip movement (Lu & Ouyang, 2017). Similarly, it is noticeable finding that the physical dispersion method is restricted with significant limits and is only worthy of facilitating the GO dispersion in water (Cui et al., 2017). Therefore, physical dispersion is commonly required to be combined with chemical modification techniques.

2.4.3 Chemical Modification Techniques

Introducing the chemical modification technique allows GO to be transformed into its own structure with various application ways. It started as surfactants adsorb GO's surface, lowering the surface energy and distributing GO through electrostatic repulsion. Later then the oxygen functional groups were bonded onto the surface of the

GO and promoted the hydrophilic properties. There are major factors that contribute towards the dispersion effect which are the type of surfactant used and the compatibility of the surfactant with cement. As in a recent study, researchers suggested the utilization of superplasticizers that include amino sulfonic acid series, naphthalene series, polycarboxylic series as well as aliphatic series (Zhao et al., 2018). Hence, these findings revealed that each type of superplasticizer helps to enhance the dispersion of GO in cement-based materials. Nevertheless, polycarboxylate superplasticizer also known as PCE portrayed as the best dispersion enhancer in an alkaline environment along with good cement compatibility.

2.5 Behaviour of Graphene Oxide as Cementitious Material

As the most complex derivative of graphene, GO owns and possesses a Young's Modulus as well as a high specific area. In addition, GO's Young Modulus has a range of value between 210 to 470 GPa. Meanwhile, the specific area discovered is in the range of 1500 to 1700 m^2/g. Thus, due to these features, it is commonly stated that GO could be fully utilised as a nucleation seeding additive and even a reinforcing element in cement paste that suffers from a low tensile strength (Horszczaruk et al., 2015). On top of that, previous studies have discovered that adding GO to cement paste or mortars could improve the mechanical as well as physical performance of the material. Most of the studies managed to find the improvement of strength commonly found in Portland Cement (PC), alkali-activated slag as well as magnesium phosphate.

2.5.1 Filling Effect

The development of hydration products generally leads to pore refinement within the pores in the cement matrix. By saying this, it also reflects the stiffness properties of the cement as the ability for the final product (concrete) to withstand is higher due to compact and dense concrete. Other than that, GO is also able to conceal any crack formation during the cementitious development as well as preventing from a further crack which mainly happens because of substantial bonding with various oxygen functionalities (Ren et al., 2022). Not only that but due to the availability of a bigger surface area, GO managed to provide greater reactivity with cement constituents. However, the negative effect of this occurrence is it could lead to agglomeration of GO

as it may fill only larger pores along the mixing process. Theoretically, agglomeration can be defined as a process of accumulation of fine particles in a specific area which can be visualized in Figure 2.10. Thus, this shall reduce the composite behaviour as well as the overall strength of the cement matrix.

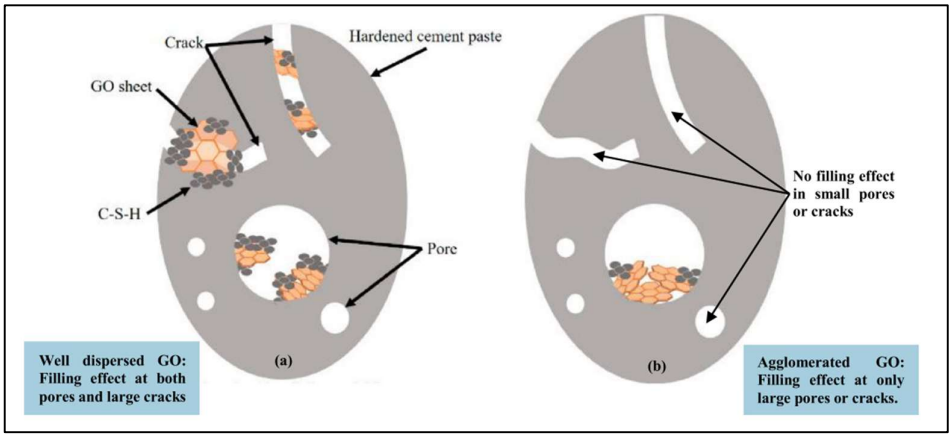


Figure 2.10 Schematic Illustration Of GO-Agglomeration In Concrete (Anwar et al., 2023)

2.5.2 Bonding Effect

Technically, the surface of GO consists of multiple oxygen functionalities such as –OH, –O–, -COOH, and -COO whereby it helps to form a strong interfacial bond with cement components known as C-S-H gel or -CH. To be more specific, the chemical interaction between GO and cement elements can be done in 2 major modes. First and foremost, it all started through the formation of ionic bonds among GO functional groups and C-S-H gel. Later, it goes through the development of hydrogen bonds between H_20 molecules and the cement components. The formation of hydrogen bonding in -OH groups revealed higher strength as well as stability compared to ionic bonds in the -COOH group (Baomin & Shuang, 2019). This can be explained as the -OH group bonding interaction enhancing the toughness surface of GO itself as it triggered the interlocking technique within atomic scales (Bellum et al., 2020). This leads to more powerful frictional resistance being pulled where eventually increasing the performance of the cement matrix overall.

Baomin & Shuang (2019) also stated that the reaction mechanism for GO with the cement constituents led to a high pH environment in the cement matrix which mainly provides Ca2+ ions. This reaction aligns with the formation of hydrogen

bonding with GO (Figure 2.11). The reaction itself triggers the production of GO-hydroxyl (GO-OH-) and GO-epoxide (GO-O) bonding effect whereby it helps to restrain any crack openings within dispersion. Not only that but it also helps to provide a more efficient load-transfer mechanism. The visualisation of these explanations can be shown in Figure 2.11 as it explains the graphical model of the bonding effect, mechanical interlocking mechanism as well as pull-out simulation of GO/GNS reinforcement and C-S-H structures formation (Figure 2.11b; 2.11c). However, due to the larger embedded depth contributed by GO-OH groups compare to the GO-O group, it provides a higher reinforcing effect as well as stronger interaction. Moreover, it also increases the coordination within Ca-O groups as well as the formation of hydrogen bonding.

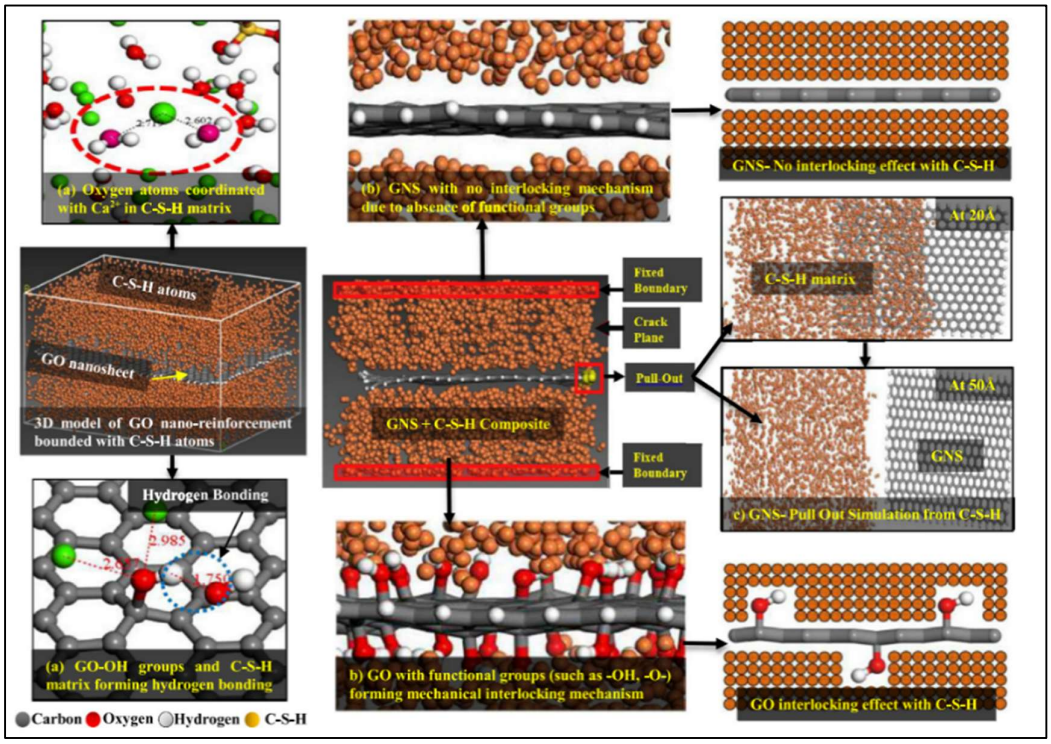


Figure 2.11 Graphical Model Of The (a) Bonding Effect; (b) Mechanical Interlocking Mechanism; And (c) Pull-Out Simulation For The GO/GNS Reinforcement And C-S-H Structures (Kai et al., 2019)

2.5.3 Nucleation Effect

The nucleation effect can be defined when oxygen-based functional groups on the surface of graphene interacted and the oxides or usually known as GO provide a

catalytic mechanism during the hydration reaction process. The GO-functional group consist of two crucial functions that include a sequence reaction mechanism with cement as well as developing an additional water transportation network for the hydration process of the cement matrix purpose (Raki et al., 2010). To be more specific, in the early stage of hydration, the functional group of GO adsorbed water molecules on their surface with a lower water-cement ratio and released after the hydration period. The process of water adsorption provides the novelty of GO's purpose to trigger the cement matrix's hydration mechanism as a whole. By promoting a rapid nucleation effect, GO not only facilitates the cement hydration process but also creates an individual curing process on its own, leading to the enhancement of the durability of the cement matrix. (B. Han et al., 2017). This can be concluded that it also helps to intensify the accumulation of C-S-H gel formation product and lead towards improvement of cement composite production. Furthermore, the GO itself consist of multiple oxygen-based functional groups that can be seen on the surface of GO. Figure 2.12 represents the catalytic mechanism of GO forms an additional water transport network during the hydration phase which enhances for further the hydrating cement particle.

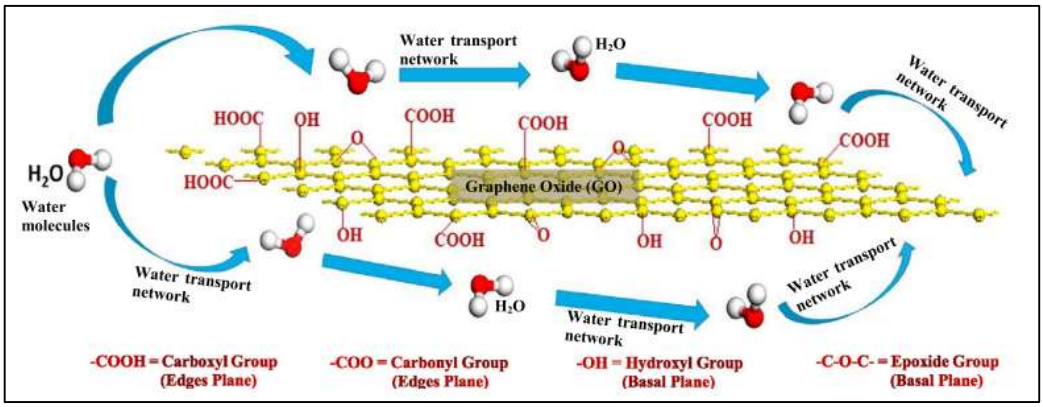


Figure 2.12 Catalytic Mechanism of GO Forms a Water Transport Network During The Hydration Phase for Further the Hydrating Cement Particle (Lin et al., 2016)

2.6 Physicomechano-Tribological Properties

Physicomechano-tribological performance is dictated by C-S-H maturity and the systematic refinement of hydration products. Unlike standard hydration where crystals such as ettringite (AFt) and calcium hydroxide (CH) form randomly, Graphene

Oxide (GO) leverages its large surface area and oxygen functional groups to act as a regulatory template for crystal growth (Meng et al., 2021). This controlled crystallization significantly increases matrix toughness and reduces brittle behaviour, ensuring a consistent and high-performance cementitious composite.

2.6.1 Influence of Graphene Oxide on Hydration Process

The hydration product of cement of C-S-H surely can influence the hardened as well as the maturity of the concrete. This is associated towards the physical and mechanical performance of the concrete. As in the inclusion of GO, it reported that GO significantly promotes the hydration product which leads to higher productivity of concrete's performance. Generally, during the hydration mechanism, every hydration products such as ettringite (AFt), mono sulfate (AFm) and Calcium Hydroxide (CH) under a complex reaction. These products lead to a formation of comprised needle and rod-shaped crystals which are located randomly, due to uncontrollable dispersion in the cement matrix. Nevertheless, as in the inclusion of GO in cement matrix composite, it tends to increase the toughness and eventually reduce the brittle behaviour of the cementitious material. This is because of GO's larger surface area and oxygen functional groups where it has greater influence in controlling the growth point and pattern of the hydration crystals. To be more precise, the oxygen functional groups react actively with a cement matrix material which directly enhances greater growth points at the GO's surface from the hydration reaction process (Lin et al., 2016; Xu et al., 2019). This also helps to provide a consistent hydration reaction which finally leads to the enlargement of hydration crystals into flower-like crystals or floral and thick polyhedral crystals. After the development from a column-shaped hydration crystal, it transforms into floral pattern hydration which is located in pores, cracks and any loose surface of cement composite. These floral crystals solely act as a filler preventing any microcrack development over time and manufactured a denser planar microstructure of composite. Figure 2.13 shows the mechanism of cement hydration crystal with the inclusion of GO.

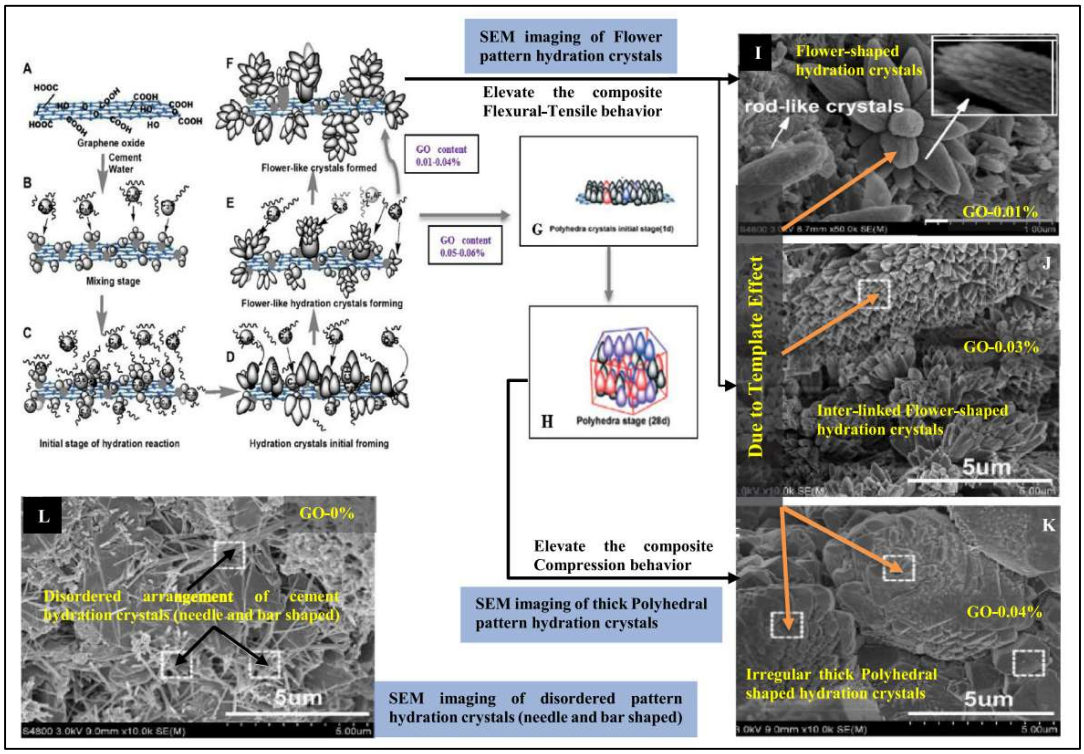


Figure 2.13 Mechanism Of Cement Hydration Crystal With The Inclusion Of GO (Anwar et al., 2023)

As in previous research, Lv et al., (2014) has concluded that with the aid of 0.04% of total binder GO, a formation of highly densified floral hydration crystal appeared. The floral hydration was stated to look like a polyhedron-pattern hydration crystal which indicates a denser microstructure as shown in Figure 2.14. In the architectural voids and capillary openings of the cement matrix, floral hydration crystals grow vigorously to establish a complex cross-connection structure. This interconnected formation facilitates a bridging effect, which serves as a micro-structural reinforcement mechanism by effectively stitching together the hydrated paste and filling internal cavities (Zhao et al., 2018). By transforming random crystalline growth into an organized network, this bridging action significantly enhances the overall mechanical strength and fracture toughness of the matrix. Furthermore, the introduction of Graphene Oxide (GO) optimizes this process; its oxygen functional groups act as high-energy templates that regulate these "floral" crystals, ensuring the bridging effect is more uniform and dense, which ultimately minimizes brittle failure and refines the pore structure (Ganesh et al., 2023).

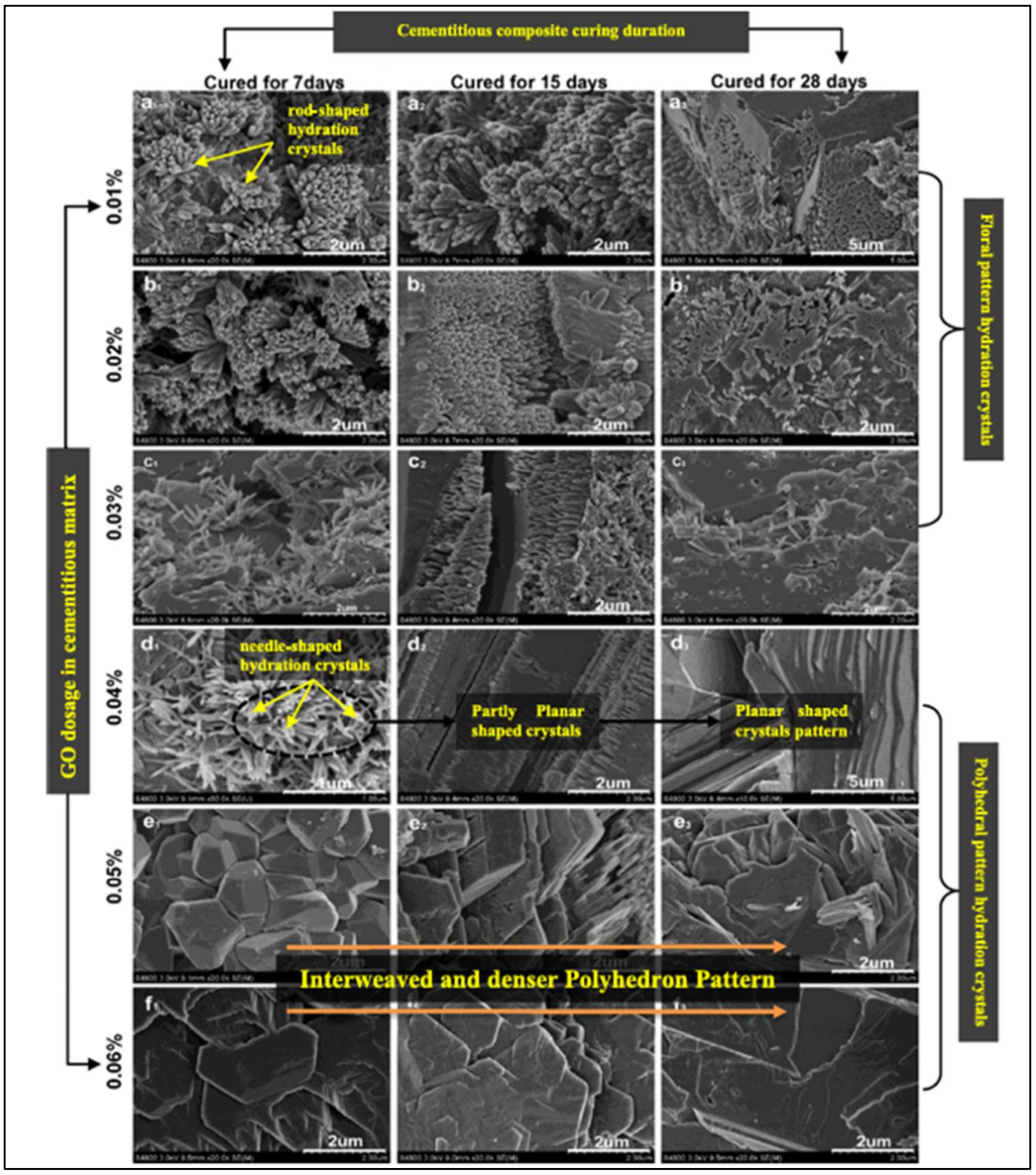


Figure 2.14 SEM Images Of GO In Cement Hydration Crystals (Lv et al., 2014)

2.6.2 Influence of Graphene Oxide on Physical Properties of Cement

GO retains the potential as one of the greatest nano-materials in enhancing the strength behaviour of cementitious material. The presence of oxygen functional groups on the surface of GO and high surface area indirectly affected the physical properties of the cement composite (Lin & Du, 2020). Not only that but it also comes with numerous novel mechanisms in cement composite that serve the main purpose of achieving certain strengths such as the filling effect. It tends to strengthen the cement composite by concealing any microcrack and even nano crack in the cement matrix resulting a higher

stiffness properties and load-bearing capacity. Nevertheless, as a result of the hydrophilic properties of GO itself, it holds great accountability in restoring water from the cement matrix. This leads to a decrease in water dosage which consequently affects the friction behaviour between cement particles and layers of GO. Therefore, due to the low fluidity rate of cement matrix has been found to be inevitably reduced over time. Henceforth, this sub-section discussed the physical properties of density and slump test for GO in cementitious material from past research.

2.6.2.1 Density

Hosseini et al., (2014) discovered that the increment of large quantities of nanoparticles has a higher probability of agglomeration occurrence in cement composite. Thus, this study concluded that a 0.5% addition of graphene increased the density of alkali-activated concrete. This happened due to the filling effect from the graphene itself whereby it refines the microstructure pores in the cement matrix. This automatically reduced the void in the concrete matrix and enhanced higher physical performance as it yielded greater density. Additionally, Li et al., (2006) reported that the density of cement mortar increased with the addition of alumina nanoparticles. This shows the relevancy of nanoparticles in cement matrix as it influenced the density aspect as a whole. In a nutshell, the incorporation of GO in the cement matrix certainly influenced the density. This is due to the filling effect attributed to GO as well as the great dispersion movement in the cement matrix which facilitates the reduction of porosity. This directly enhances the compactness and stiffness properties of the cement matrix itself. Nevertheless, exceeding the appropriate GO concentration leads to a reversal of this concept where it induces to the formation of agglomeration. Therefore, while GO often delivers promising results in density an adequate concentration of GO remains a crucial factor that needs to be observed.

2.6.2.2 Slump

Previous research has carried out a mini-slump test to observe the workability rate of GO in the cement matrix (Wei et al., 2021). The author observed that the lack of workability of cement paste reached 42% with GO dose used at 0.05% bwoc along with 0.5 of w/c ratio. The result indicated that due to the larger use of the surface area of GO,

more liquid is present in the cement paste. Moreover, Zhou et al., (2025) managed to observe the workability of GO in blended mortar whereby the author concluded the higher the GO content, the lower the workability indicating that GO had significant changes to the fluidity of the slurry. This statement is also in line with the results obtained by Gong et al. (2024) and Li et al. (2017). The author emphasized that the reduction of fluidity in the cement was due to the large surface of GO and the oxygen functional group attached to the surface of GO. This causes more free water to be adsorbed during the mixing process resulting in a decrease in the free water content of the cement. Not only that but it is also mainly due to the interaction of GO with other cementitious material where it flocculates a large content of water. This eventually leads to an increase in resistance between cement particles and a reduction of fluidity.

A finding from Wang et al. (2016) diverts a slight difference in the optimum percentage of GO in slump values as the study obtained 0.05% of GO inclusion in the cement paste. It has been concluded that when 0.05% of GO was added, the slump diameter was reduced approximately by 41.7%. This can be explained as to large surface area owned by GO decreases the water availability during mixing. Therefore, it is possible to speculate that GO modified the workability as in cement paste.

Apart from that, a similar pattern of optimum GO percentage was recorded as Pan et al. (2015) achieved 0.05% of GO in the related study of GO in mortar. The authors believed that the inclusion of GO enhanced the strength of mortar but also reduced the workability due to the high surface of GO. GO also managed to change the rheological properties of the mortar which resulted in a thickening effect.

A similar finding was discovered by Wu et al., (2019) as the authors observed that the value of the slump of concrete decreased with the increase of GO dosage from 0.02% to 0.08% by weight of cement under a water-cement ratio of 0.5. This might happen due to the large area surface area of the GO nanosheet which consequently affects the availability of water in the mix to be lower than normal. Thus, this explains the constant decline of slump concrete from 183mm to 154mm as the GO dosage increased. However, the authors also suggested that in order to improve the slump of conventional mixes, additional SCM material should be implemented such as fly ash and PCs.

However, the workability of the graphene composite can be improved and improvised by using a certain surfactant amount of plasticizer and even an ultrasonication treatment period. Du et al., (2016) managed to conduct a study on the

relationship between the dosage of plasticizer increased to 0.6%, 0.9%, 1.2% and 1.5% along with the GO dosage at 1.0%, 1.5%, 2.0% and 2.5%. The authors stated that the GO in cementitious material managed to flow as similarly as conventional concrete. Moreover, the flowability of a sample using the same GO content but with a variety dosage of plasticizers. In the end, the authors discovered that 1% of GO content cement paste is the optimum dosage to cement paste which can help the workability in general. In fact, the increase of superplasticizer also effectively increases the workability of the GO infused in the cement paste.

In conclusion, it can worth mentioning that the increasing amount of graphene has no significant changes towards the workability of the cement paste. Over and above that, a very low concentration of graphene or graphene with a low surface area shows a lesser amount of water required to saturate in cement paste which indirectly affected the flowability value. Henceforth, Table 2.3 indicated the slump test of GO in cement matrix from previous research.

Table 2.3
Slump Test of GO in Cement Matrix from Previous Research

Ref.	Optimum GO dosage	Application	Mix Design	Remarks
(Wei et al., 2021)	0.05%	Cement paste	• Ordinary Portland Cement • Fly ash class II • Polycarboxylic acid water reducer	The hydrophilic properties of GO tend to lower the workability of cement paste. Therefore, the utilization of Polycarboxylic is essential to increase a higher workability percentage.
(Zhou et al., 2025)	0.08%	Mortar	• Ultrafine cement • Fly ash • Silica Fume • Calcium lignosulfonate • Fine aggregate	GO high surface area and abundant of oxygen functional groups tends to adsorb more free water during mixing
(Wang et al., 2016)	0.05%	Cement paste	• Cement • Water reducing agent	The high surface of GO facilitates a greater reaction with cementitious material
(Pan et al., 2015)	0.05%	Cement paste	• Cement	GO high surface area reduces the water availability during mixing process

2.6.3 Influence Of Graphene Oxide on the Mechanical Performance of Cement

GO is categorised as a substance that has the ability to enhance and modify the strength behaviour of cement properties. This can be explained by the fact that oxygen functional groups from the GO surface itself are present and contribute to the cementitious material's solubility characteristics. Furthermore, it strengthens the composite cement's C-S-H crystal's nucleation impact. As previously stated, GO also helps facilitate the reaction during the cement hydration process. Furthermore, given specific modifications, it has a significant impact on the mechanical strength of cement composites generally. This will also have an impact on the cement composite's ability to reduce tiny cracks over time.

2.6.3.1 Compressive Strength

According to Bheel et al. (2023), the utilization of GO increased the overall mechanical performance of the cementitious material. The author managed to conduct research on the mechanical performance of concrete under various percentage content of GO like 0 %. 0.02 %, 0.04 %, 0.05 %, 0.06 %, 0.08 % and 0.10 %. As in compressive strength, the most optimum percentage content of GO is 0.05% which provides 25.24 MPa, 27.21 MPa and 37.53 MPa. Bheel et al., (2023) also explained that the increment in compressive strength is associated with the size of the GO itself which is nano-scale particles. This shall reflect the filler behaviour of GO in the cementitious matrix material. In terms of the nucleation effect of GO, the author also claimed that due to the improved hydration process, the molecular mechanics provide that the functional groups on the GO basal planes would create more substantial interfacial adhesion with Ca2+ ions from the C-A-S-A-H. This eventually leads to a stronger bond between the GO as well as other cement matrix materials.

Furthermore, Zhao et al., (2023) managed to observe that the compressive strength of concrete GO increased by 1.66%, 15.99%, and 20.62% respectively. This also can explain the due reinforcing mechanism of GO's nucleation effect. Besides that, the filler effect of GO also contributed to the compressive strength data as it refines the pore structure of the concrete denser than before. The improved mechanical properties and wrinkled morphology were due to the bonding effect between GO and cement

matrix materials. The author claimed that additional GO improved the compressive strength of concrete compared to the flexural strength.

According to Maglad et al., (2022), a study on the impact of adding GO to GBFS-fly ash-based geopolymer concrete was conducted as the study focussed on the inclusion of GO percentage content 0, 0.05, 0.15, 0.25 and 0.35 in concrete. There were 3 major mixes of M1, M2 and M3 in this study. For the M1, the result indicated that a low amount of GO shows a higher result of compressive strength at all curing ages. However, 0.25% of GO was considered as the reflection point as it displayed and visualised improved mechanical performance compared to other GO content. The compressive strength obtained was 55.74 MPa and 59.15 MPa at 56 and 90 days. The authors discovered that the increment of compressive strength was due to the wrinkled morphology and increased surface area of GO itself as it enhanced the interconnected mechanism within the mixture of geopolymer. A high surface area of GO acts as filler which fills the void located in this concrete and eventually improved the compressive strength. However, at 0.35% addition of GO, the authors observed a reduction of compressive strength that might happen due to agglomeration of GO in the geopolymer concrete because of the high surface area and hydrophilic nature.

Moreover, according to Yuan et al., (2022), the research discovered that the compressive strength of concrete increased linearly with the addition of GO. However, the compressive strength shows a steady decline in value when the GO content increased from 0% to 0.07% for 7 days, 14 days and 28 days. The author also managed to state that the peak value can be found with 0.03% of GO content as the compressive strength increased by 33.15%, 10.88%, and 17.72%, respectively, compared to that of ordinary concrete. As in the inclusion of fly ash, the compressive strength of mixed concrete with 30% of fly ash content was found to be greater compared to samples with 15% and 45% of fly ash. When fly ash was mixed at 15%, the compressive strength of the concrete at all ages increased with a relatively high GO dose (0.07%). Based on this study, it can be discussed that there was a tendency for compressive strength to decrease if the GO content used more than 0.03%. However, it still indicated a higher value compared to the control sample concrete which simply explains that GO does contribute to the mechanical performance of the concrete in general. The author also explained that the improvement of compressive strength was mainly due to numerous nanomaterials used which automatically enhance the C-S-H gel structure as well as the

pore structure in the cementitious material. This also applies towards other materials such as aggregate and mortar interface properties.

Considering previous research, the majority of the data depicted that the compressive strength increases linearly with the decrease in GO content. According to Chetty et al., (2022), the compressive strength of concrete and mortar with GO showed significant findings as for the concrete sample, the 0.1% and 0.2% PureGRAPH 50 samples obtained increment by 9.9% and 7.4% compared to the normal sample. A similar trend was also observed for mortar samples as the 0.07% and 0.15% PureGRAPH 50 gave a 19.8% and 7.5% increased value, respectively in comparison to the normal sample. However, as the PureGRAPH reached a usage of more than 0.1%, the compressive strength for both samples showed a gradual decline in data. Based on the result, it shows that determining an exact figure for the optimum dosage of GO to improve the mechanical characteristics of cement composite appears to be within the range of 0.02% and 0.1%. It has been concluded that a GO dosage of more than 0.1% can be considered as excessive due to GO aggregation formation which eventually can has an adverse effect towards the mechanical performance of cement composite.

Manikanta et al.,(2020) conducted a study on the addition of GO to high self-compacting concrete with the inclusion of fly ash as well as silica fume. In terms of mechanical performance, compressive strength was observed on all days of curing. The data measured presented the usage of cementitious materials has a higher tendency of achieving a higher strength at the of 90 days. However, the strength obtained at the end of 28 days was only around 45 to 50 MPa as the concrete containing SF and GO achieved lower strengths at the end of 28 days curing in fresh water.

A similar pattern of data was found in the study by Ganesh et al., (2023), the authors discovered that the compressive strength can be enhanced by the addition of GO as in mortar with both paste and powder. However, the most optimum GO content in this study was 0.03% as revealed in most of the mechanical performance results. As for the mortar, it can be shown that 0.03% GO paste indicated the highest compressive strength whereby the improvement of day 7 and day 28 increased by 51% and 41%, respectively compared to the control sample. Apart from that, the compressive strength of mortar with GO powder for day 7 and day 28 showed an increment of value by 23% and 21%. Nevertheless, the GO content of 0.04% and beyond indicated the reduction of compressive strength value which is even below the control sample. Generally, the mortar with the inclusion of GO powder has higher strength compared to GO paste at 7

and 28 days due to water-cement ratio differences. This is because GO powder has a lower water-cement ratio compared to GO paste as it also contains PCE superplasticizer. Along with that, the deviation of results between GO powder and GO paste was due to surface area whereby it is more difficult to attain a uniform mixing with powder. However, the strength development at the optimum level of GO can be concluded better for the mortar with paste rather than a mortar with powder. Moreover, Lv et al., (2016) discovered that even at a low concentration of 0.04% of GO, a significant improvement in compressive strength was observed in the study. This can be explained as 75.75 MPa managed to be obtained and dominated as the highest compressive strength value of GO cement paste. The author believes that due to the effectiveness of GO's filing effect, it tends to fill the voids and pores within the cement matrix, leading to a stiffer cement paste. Not only that but an adequate formation of C-S-H also offers a significant strength enhancement due to the nucleation effect of GO itself.

On top of that, with the same application of GO-modified cement paste, Zhou et al., (2025) managed to obtain 0.05% of GO as the optimal concentration as nanomaterial additive in the study. It has been concluded that the increment of compressive strength in the study achieved 64.66 MPa indicating a 15.8% increased value as overall data. This reasoning behind the data was similar to previous researchers as GO tends to promote the formation of C-S-H gels which are the major yet primary binding phase during cement hydration. This leads to a denser and greater strength of cement paste. Apart from that, Wang et al., (2016) investigated the effect of GO in cement paste under several mechanical performance tests. As in compressive strength, it has been determined that 0.04% of GO offers the highest value compared to other percentages as it achieved 92.8 MPa strength in 28 days. This can be explained as the presence of GO changes the rheological properties of cement paste which results in a significantly denser effect. This eventually enhanced the stiffness properties of the cement paste as it improved the load-bearing capacity of the cement paste.

In conclusion, the analysis from past research demonstrates a consistent impact on GO inclusion in cement matrices with various applications. The reviewed studies also managed to conclude the optimal range of GO concentration with exceptional discussion towards GO's mechanism within the cement. Thus, Table 2.4 presents the simplified compressive strength GO in cement matrix from previous research.

Table 2.4
Compressive Strength of GO in Cement Matrix from Previous Research

Ref.	Optimum GO dosage	Application	Mix Design	Compressive Strength					Remarks
				7 day	14 day	28 day	56 day	90 day	
(Bheel et al., 2023)	0.05%	Concrete	• Portland Cement (PC) • Fly ash • River sand • Polyvinyl alcohol (PVA) • Superplasticizer	25.24 (+5.44%)	27.21 MPa (+7.98%)	37.53 MPa (+25.1%)	NA	NA	• Pore refinement mechanism influenced by GO nano-scale particles. • Nucleation effect of GO improved the hydration process.
(Zhao et al., 2023)	0.05%	Cement mortar	• Cement • Coal-bearing metakaolin (CMK) • Sand • Superplasticizer	44 MPa (+15.99%)	NA	60 MPa (+20.62%)	NA	NA	• Reinforcing mechanism of GO's nucleation effect and nano-filler effect.
(Maglad et al., 2022)	0.25%,	Geopolymer concrete	• Granulated blast furnace slag (GBFS) • Fly ash • Coarse aggregate	27.8 MPa (+78.2%)	NA	43.9 MPa (+45%)	55.74 MPa (+39%)	59.15 MPa (+39.83%)	• The increment of GO surface area improved the interconnected mechanism of

			• Fine aggregate • Sodium hydroxide • Sodium metasilicate						geopolymer.
(Yuan et al., 2022)	0.03%	Modified-concrete	• Ordinary Portland Cement (OPC) • Calcareous gravel • River sand • Fly ash • Steel fiber • Superplasticizer	50.37 MPa (+33.15%)	52.03 MPa (+10.88%)	61.37 MPa (+17.72%)	NA	NA	• The usage of nanomaterials helps the improvement of C-S-H gel structure and pore refinement.
(Chetty et al., 2022)	0.1% 0.2%	Concrete	• Ordinary Portland Cement (OPC) • Manufactured sand • Coarse sand • Natural fine sand	50.37 MPa (+33.15%)	52.03 MPa (+10.88%)	61.37 MPa (+17.72%)	NA	NA	• The usage of nanomaterials helps the improvement of C-S-H gel structure and pore refinement.

	0.07% 0.15%	Mortar		NA	NA	55 MPa (+19.8%) 49 MPa (+7.5%)	NA	NA	
(Manikanta et al., 2020)	0.03%	High performance self-compacting concrete	• Ordinary Portland Cement • Fly ash class F • Silica fume • Poly-carboxylic • Crushed aggregate • River sand	47.33 MPa (+18.33%)	NA	61.50 MPa (+23.64%)	NA	NA	• Bigger specific area of GO helps to provide stiffer characteristic along with Fly Ash and Silica Fume.
(Ganesh et al., 2023)	0.03%,	Cement mortar	• UltraTech Ordinary Portland Cement (OPC) • River sand • Poly-carboxylic	27.81 MPa (+51%)	NA	36.46 MPa (+41%)	NA	NA	• A bigger specific area of GO helps to provide stiffer characteristics along with Fly Ash and Silica Fume.
(Wang et al., 2016)	0.05%	Cement paste	• Cement • Water-reducing agent	NA	NA	92.8 MPa (+40.3%)	NA	NA	• GO refined the rheological properties of the cement leading to the denser cement paste.

(Zhou et al., 2025)	0.05%	Blended cement paste	• Cement • Fly ash • Silica fume • Calcium lignosulfonate	42.79 MPa (+18.8%)	NA	64.66 MPa (+15.8%)	NA	NA	• GO promotes the hydration reaction of cement by forming an adequate quantity of C-S-H which helps in strengthening the mechanical properties of cement paste.
(S. H. Lv et al., 2016)	0.04%	Cement paste	• Cement • Poly-carboxylic	68.45 MPa (+18.8%)	NA	75.75 MPa (+32%)	NA	NA	• Enhanced the formation of flower-like crystals indicating the nucleation effect occurs in the cement matrix.

Based on Figure 2.15, shows the influence of GO in cement matrix on application cementitious material at 28 days of compressive strength. The normalized compressive strength of cementitious material can be calculated by dividing the compressive strength of cementitious application for each GO concrete by the compressive strength of control cementitious material. As an overall observation, it can be concluded that a low percentage of GO indicates a greater potential for compressive strength in cementitious material. Conversely, an excessive amount of GO concentration, results in inconsistency of compressive value as it scatters from the reference line. GO preserves the potential to provide enhancement of strength due to the presence of oxygen functional groups located at the surface of GO. This incredibly surges the solubility properties in cementitious solutions as well as unlocking the nucleation effect for C-S-H formation. However, the optimal dosage of GO can be different due to various applications of the cement matrix. On average range, the most optimum GO dosage in cement can be found within 0.01 to 0.10% as from the normalized compressive strength graph. Nevertheless, considering different applications, the GO dosage can increase drastically due to the complex composition and GO function.

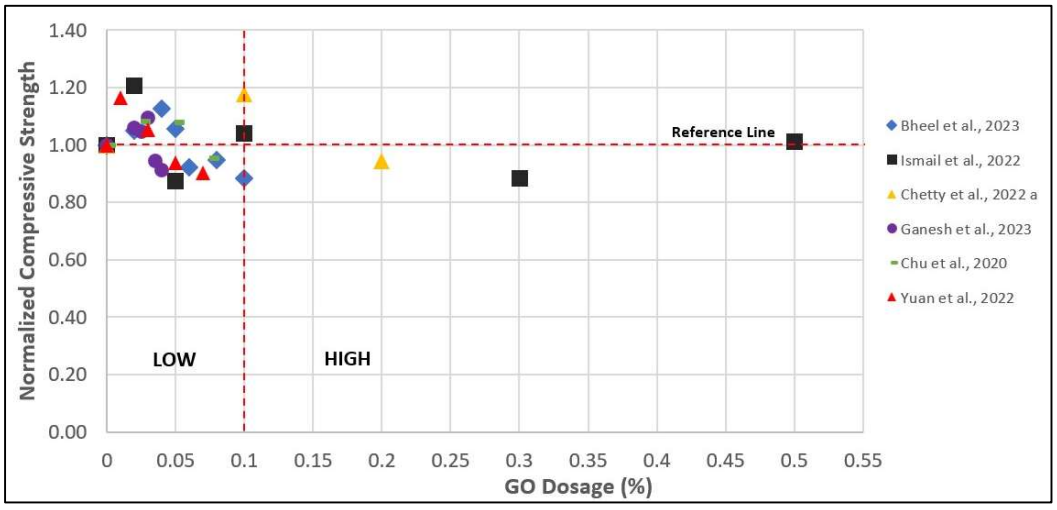


Figure 2.15 Normalized Compressive Strength of GO in Cementitious Matrix

2.6.3.2 Tensile Strength

According to Bheel et al., (2023), the highest tensile strength recorded by GO content of 0.02 %, 0.04 %, 0.05 %, 0.06 % and 0.08 % was 3.35 MPa, 3.71 MPa, 3.79 MPa, 3.60 MPa and 3.0 MPa which the usage of GO as a nanomaterial in concrete which more than control sample at 28 days. A similar finding is shown as the lowest tensile strength can be observed by 2.62 MPa at 0.10% as a nanomaterial in the concrete which is lower compared to the concrete without GO after 28 days. Thus, this concludes that the utilization of GO as nanomaterial has significantly improved the strength up to 0.08% in the concrete compared to the control sample. The enhancement in mechanical performance specifically in tensile strength can be associated with the surface area of GO itself as a nanomaterial. It aided the filler effect of the concrete as it seals the void left by other components which resulting an improvement in the transition zone. However, further addition of GO could lead to the reduction of tensile strength as it leads to agglomeration influenced by the uniform distribution of GO throughout the cement matrix. Specifically, the production rate for the C-A-H formation phase decreased with the increased of GO content which is due to uniform dispersion of GO in the cement matrix. Moreover, the delayed development of C-A-S-A-H gel due to the pozzolanic activity of fly ash particles. Lv et al. (2013) explored that 0.02% of GO achieved remarkable tensile strength compared solely to the presence of GO's nucleation effect. This can be explained as GO promotes the formation of C-S-H during the cement hydration process resulting in denser cement paste. Not only that but the author stated that the flower-like crystal formation generated in the holes reduces the void and crack within the cement matrix.

Moreover, Ganesh et al., (2023) discovered that the maximum splitting tensile strength of mortar with the inclusion of GO paste and GO powder can be seen at 0.03% of GO. Technically, the pattern of data acquired by tensile strength with GO percentages is similar to the compressive strength whereby the higher the percentage of GO content, the lower the strength obtained. In general, the addition of GO in powder or paste forms affects the strength development of the mortar. As for the tensile strength, mortar with GO paste increased by 84% at 0.03% concentration. Meanwhile, the mortar with GO powder indicated maximum strength of 62% with the same concentration. However, for comparison purposes, the peak tensile strength of mortar with GO powder is up to 50% higher compared to cement mortar with GO paste. Nevertheless, Kaur et al., (2020)

obtained 0.04% of GO as the optimum percentages as in cement mortar in the study. It has been stated that the inclusion of fly ash tends to provide an additional reaction of pozzolanic whereby it helps in increasing a long term strength and durability. As the spotlight of the study, GO managed to offer its nucleation effect for C-S-H growth in the cement matrix, resulting in reduction of voids and cracks. Further discussion of the result can be related to the properties of GO itself where it enhances the microstructure of cement-based material as well as the degree of cement hydration. This reflects the behaviour of GO as in the filler effect and the nucleation effect as in the cementitious matrix process. Therefore, this can concluded in Table 2.5 as it portrays overall tensile strength of GO in cement matrix from previous research.

Table 2.5
Tensile Strength of GO in Cement Matrix from Previous Research

Ref.	Optimum GO dosage	Application	Mix Design	Tensile strength			Remarks
				7 day	14 day	28 day	
(Bheel et al., 2023)	0.05%	Concrete	• Portland Cement (PC) • Fly ash • River sand • Polyvinyl alcohol (PVA) • Superplasticizer	NA	NA	3.79 MPa (+0.08%)	• Filler effect mechanism influenced by GO nano-scale particles. • Pozzolanic activity of FA particles delayed the CASAH development.
(Ganesh et al., 2023)	0.03%	Cement mortar	• UltraTech Ordinary Portland Cement (OPC) • River sand • Poly-carboxylic	NA	NA	GO paste 2.58 MPa (+84%) GO powder 3.55 MPa (+62%)	• Dispersion rate of GO • GO nanosheets act as a physical barrier that arrests the propagation of micro-cracks at the nanoscale. By bridging these nascent cracks, GO prevents them from coalescing into macro-cracks, thereby significantly enhancing the splitting tensile strength of the mortar
(Kaur et al., 2020)	0.04%	Cement mortar	• Cement • Fly ash class F • Sand	3.5 MPa` (+84.2%)	3.6 MPa (+85.7 %)	4.65 MPa (+88.0%)	• The high surface portrayed by GO tends to provide a greater reactivity for C-S-H development to prevent any crack

			• Poly-carboxylic				initiation in the cement matrix.
(Lv et al., 2013)	0.02%	Cement mortar	• Cement • Fine aggregate	NA	NA	78.6 MPa	• GO act as a nucleation effect resulting in denser microstructure in the cement matrix

Similarly with the compressive strength, the tensile strength of concrete with the inclusion of GO also significantly increases with low dosage as shown in Figure 2.16. Based on Figure 2.16, the data shows high dosage of GO leads to lower tensile strength. Meanwhile, a low dosage of GO indicates greater tensile strength compared to the normalized tensile strength reference. This can be explained as GO sheets within the cement matrix portray vital functions of bridging effect which eventually increase the coherence in cement. The increment of coherence in cement is due to the formation of covalent bonds produced by the hydration product (C-S-H).

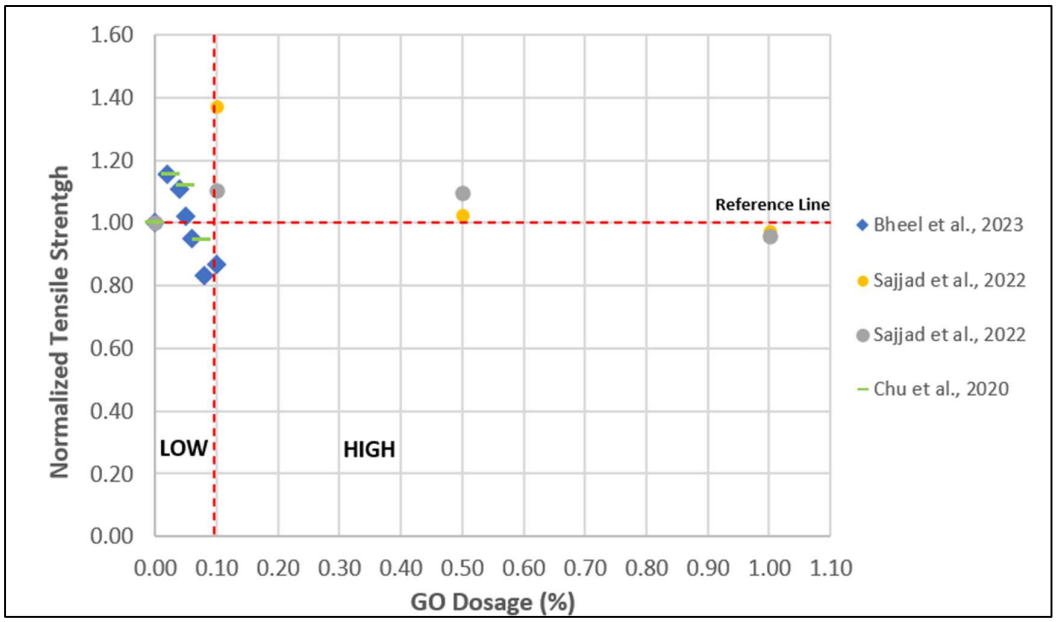


Figure 2.16 Normalized Tensile Strength Of GO In Cementitious Matrix

2.6.3.3 Flexural Strength

Ganesh et al., (2023) also confirmed a similar trend observed for mechanical properties in the study as in compressive as well as splitting tensile strengths. The authors discovered that the optimum GO percentage for flexural strength is the same as other mechanical performance which is 0.03% whether in paste or powder. It has been observed that the maximum strength increased by 44% for mortar with GO paste. Meanwhile, mortar with GO powder revealed a maximum strength increment of 80%. As mentioned previously for other strength parameters, the flexural strength of mortar with GO powder was perceived to be higher compared to the mortar with GO paste due to the presence of PCE superplasticizer as well as the difference in water cement ratio. As discussed earlier, the usage of GO powder was expected to be harder to attain a uniform mix compared to GO paste. Thus, it may varies the differences in the result are due to the consistency and dispersion of GO form in the cement matrix.

As in the cement paste application, Lv and Liu, et al., (2014) investigated the influence of GO with various percentages in cement paste. The authors contribute knowledge where 0.04% offers the best result in flexural strength by achieving 11.56 MPa with 67.1% increment percentages. The reasoning behind this finding was GO's nucleation effect as it reacts with cementitious material during cement hydration. This leads to a formation of polyhedral crystals in the cement matrix filling up every possible voids in the cement matrix leading to denser microstructure. The discussion has been confirmed by Lv et al. (2017) as the authors also believe that due to the nucleation of GO as well as the filing effect, it tends to refine the microstructure within the cement matrix greater than the control sample. This indicates that the presence of GO significantly increases the flexural strength of the cementitious material by embedding several crucial behaviours such as filing and nucleation effect. Table 2.6 indicates the flexural strength of GO in cement matrix from previous research.

Table 2.6
Flexural Strength of GO in Cement Matrix from Previous Research

Ref.	Optimum GO dosage	Application	Mix Design	Flexural strength			Remarks
				7 day	14 day	28 day	
(Ganesh et al., 2023)	0.03%	Cement mortar	• UltraTech Ordinary Portland Cement (OPC) • River sand • Poly-carboxylic	NA	NA	GO paste 9.66 MPa (+44%) GO powder 13.48 MPa (+80%)	• Data influenced by the difference of water cement ratio and presence of PCE superplasticizer. • Consistency and dispersion of GO at different form.
(Lv and Liu, et al., 2014)	0.04%	Cement Paste	• Cement • Poly-carboxylic	NA	NA	11.56 MPa (+67.1%)	• GO offers an exert influence towards cement hydration crystal within cement matrix.
(Lv et al., 2013)	0.05%	Cement mortar	• Cement • Sand • Carboxymethyl chitosan • Polycarboxylate superplasticizer	17.28 MPa (+50.7%)	NA	31.67 MPa (+60%)	• GO contributes in nucleation effect as the hydration crystal filled the void within the cement matrix

Figure 2.17 indicates the normalized flexural strength of GO in a cement matrix whereby the dosage of GO can be considered as low which is between 0.00 to 0.10%. It can be stated that the lesser to GO content, the higher the tendency of divergence in hydration products and the lesser the production of nucleation. However, excessive GO dosage also could lead to clusters or agglomeration in the cement matrix. As in the flexural strength of GO concrete, the development can be attributed to the higher bonding effect between GO and cementitious matrix. This interfacial bonding formed due to the combination of covalent bonding and mechanical bonding mechanisms.

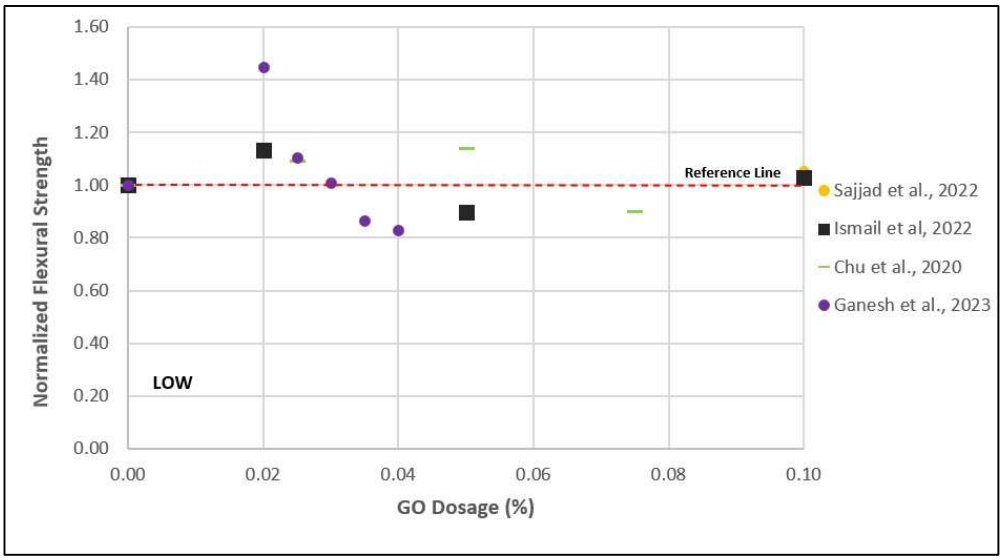


Figure 2.17 Normalized Flexural Strength of GO in Cementitious Matrix

2.6.3.4 Modulus of Elasticity

Maglad et al., (2022) also managed to conduct a study of the effect of GO on GBFS-fly ash-based geopolymer concrete. In this study, there were 3 major mixes of M1, M2 and M3 with different compositions and GO percentages of 0.05, 0.15, 0.25 and 0.35. As in the modulus of elasticity parameter, M1 samples after ambient curing for 56 days increased by 29.85 GPa, 30.39 GPa, 33.34 GPa, and 31.69 GPa, respectively compared to the reference elastic modulus of 27.81 GPa. Meanwhile, M2 samples managed to obtain 31.91 GPa, 32.67 GPa, 33.56 GPa, and 32.67 GPa and for reference mix of 28.72 GPa. Finally, for the M3 samples, it visualized data of 33.63 GPa, 34.16 GPa, 36.12 GPa, and 35.34 GPa, respectively with a reference mix of 29.13 GPa. Nevertheless, it can be concluded that the lower inclusion of GO had a more significant effect on the modulus of elasticity of GBFS-fly ash-based geopolymer concrete.

Horszczaruk et al. (2015) also managed to conduct a study of GO in cement mortar whereby the authors claimed that GO tends to show a very high increase in Young's modulus value. This can be explained as GO delivers a promising route towards mechanical properties enhancement within the cement matrix. This can be explained as GO's ability to refine the microstructure in the cement matrix leading to the reduction of porosity and the creation of a denser matrix. As in the filler effect provided by GO, it produces a denser interfacial transition layer in cement-based material which eventually enhances the resistance against elastic deformation. This ultimately enhances the bond with the cementitious material and hinders any crack propagation. This can be briefly displayed in Table 2.7 where includes the data on modulus of elasticity of GO in cement matrix from previous research.

Table 2.7
Modulus of Elasticity of GO in Cement Matrix from Previous Research

Ref.	Optimum GO dosage	Application	Mix Design	Modulus of Elasticity			Remarks
				7 day	28 day	56 day	
(Maglad et al., 2022)	0.25%	Geopolymer concrete	• Granulated blast furnace slag (GBFS) • Fly ash • Coarse aggregate • Fine aggregate • Sodium hydroxide • Sodium metasilicate	NA	NA	M1 33.34 MPa (+19.88%) M2 33.56 MPa (+16.85%) M3 36.12 MPa (+24%)	• Lower inclusion of GO had a more significant effect on the modulus of elasticity
(Horszczaruk et al., 2015)	0.5%	Cement mortar	• Cement • Sand	NA	NA	35.55 MPa (+17.87%)	• The improvement of the degree of cement hydration and microstructure refinement of the cement matrix. • Filler effect mechanism portrayed by GO. • GO's larger surface area and strong intermolecular forces lead to agglomeration.

As shown in Figure 2.18, a low dosage of GO contributes a greater modulus of elasticity properties compared to a higher dosage. This is due to the possession attributes towards compactness and densification from hydration crystal. On top of that, the strong covalent bonding between GO and cement matrix also helps towards this occurrence. To be more precise, the usage of GO as a nano-material in cement matrix hinders the formation and restricts the development of fine cracks which eventually increases the load-bearing capacity. This also leads to increased stiffness properties of GO concrete.

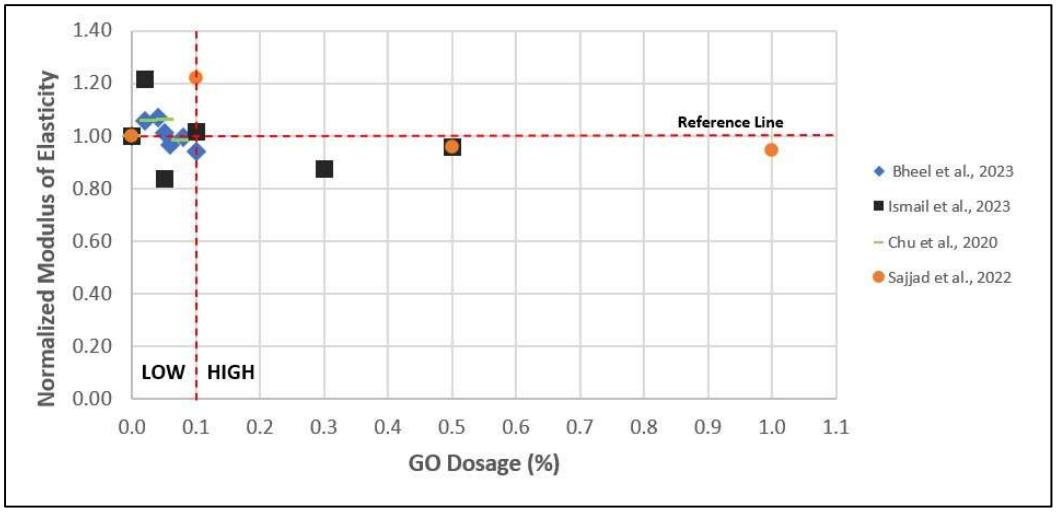


Figure 2.18 Normalized Modulus of Elasticity of GO in Cementitious Matrix

2.6.4 Influence of Graphene Oxide on Durability Properties of Cement

2.6.4.1 Chloride Ion Penetration

Theoretically, chloride penetration can be defined as the depth at which chloride ions from the environment react and penetrate into the concrete. This occurrence can lead to major and minor defects in concrete such as corrosion structures. Thus, it explains the urgency and courtesy of the presence of GO in concrete as it can provide good resistance against chloride penetration. Primary, the chloride ions act as a transport mechanism in a complex system whereby it tends to water diffusion, impregnation, and capillary absorption (Zhang et al., 2022). Fortunately, reported in considerable previous studies that the usage of nanomaterial and nanofiber is effective in terms of improving pore structure as well as forming the bridging micro-cracks of a cement-based material

(Han et al., 2023). This holds the possibility for a better impermeability of concrete and reduces any possibility of corrosion in the concrete.

In terms of chloride ion penetration, Hong et al., (2023) reported that incorporating GO content in lightweight concrete obtained a lower chloride-ion migration coefficient compared to samples without GO. This automatically concludes that the inclusion of GO in cementitious material promotes chloride-ion resistance. Based on Figure 2.19, the graph described that the increment of GO content leads to a non-linear trend of decreasing and then increasing. On top of that, 0.05% of GO content indicates the optimum dosage with significant data on the chloride-ion coefficient.

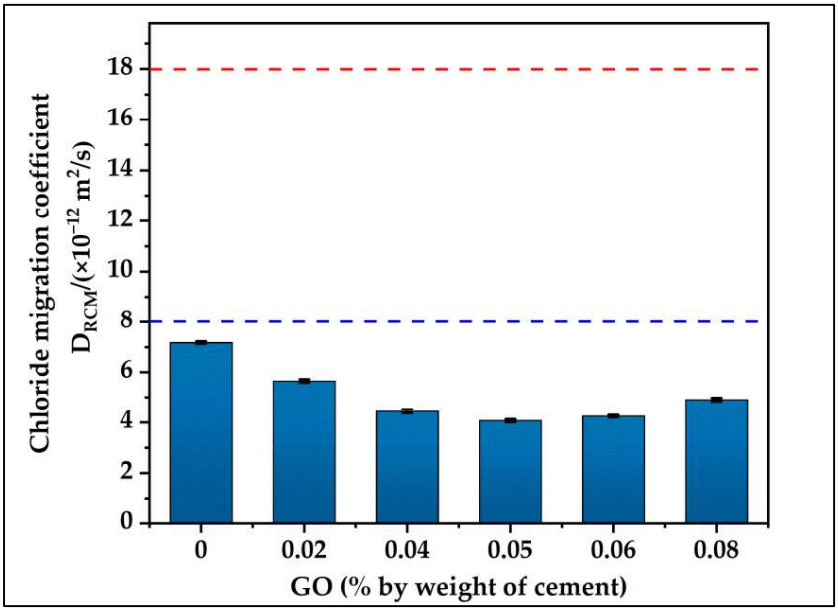


Figure 2.19 Chloride Migration Coefficient with Different GO Dosage (Hong et al., 2023)

To show the relevancy of GO in cementitious material also, Zhang et al., (2022) reported a study of GO incorporated with concrete under chloride ion corrosion. There were two different concentrations of silver nitrate (0.014 and 0.1002 mol/L) used in this study. Furthermore, the soaking time of each sample was decided for 40, 80, 120, and 240 days as the authors wanted to observe the permeability rate of concrete without GO and with GO. The findings indicating a significant reduction of chloride penetration portrayed by GO in cementitious materials compared to normal sample. This happened due to the filling effect by the GO which refine available pores in the concrete. The authors also claimed that this is probably due to the barrier property of the GO itself which makes the transportation path for the chloride ions more difficult compared to

OPC. As mentioned before in previous research, concrete GO is denser due to lesser void compared to normal concrete. Thus, this automatically enhances the resistance against chloride ion penetration even better and stronger.

Not only that but Mohammed et al. (2015) also concluded that GO reduces the rate of permeability within the cement matrix against chloride ion penetration. To be more specific, 0.01% concentration of GO delivers the lowest chloride ion penetration in the study. This can be shown in the Figure 2.20 as it portrays the chloride penetration depth of different cement mixes. The author claimed that this could be linked with the layer structure of GO as shapes a similar structure to a sponge structure. This finding also can be confirmed as Qureshi et al. (2019) found that when GO is added to cement, it develops a spongy formation layered with interlined structural characteristics within the cement matrix. This shall effectively retain any penetration of chloride ions and directly improve the cement permeability.

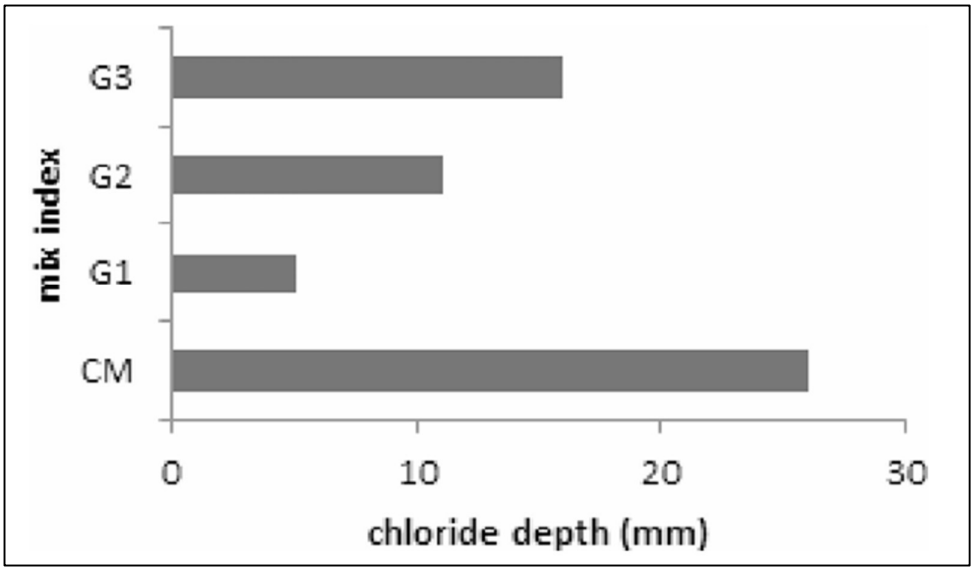


Figure 2.20 Chloride Penetration Depth of Different Cement Mixes (Mohammed et al., 2015)

2.6.4.2 Water Absorption

Theoretically, the durability of the concrete solely depends on the fluid penetration capacity of the concrete's microstructure. This refers to the permeability aspect of the concrete. The rate of permeability of concrete influenced several effects of durability. This can be explained as the low permeability of concrete could improve various resistance against penetration of chloride ions, alkali ions, water, and other chemical substance attacks (Han et al., 2023). Thus, this section explains the vulnerability of GO in cementitious material as in water absorption.

Bheel et al., (2023) examined the effect of GO in cementitious composite with Fly Ash and polyvinyl alcohol fiber. As in the durability aspect of water absorption, the maximum water absorption recorded was 3.88% of control. Meanwhile, the lowest water absorption was observed by 1.28% with 0.10% GO content as a nanomaterial in the concrete. Based on Figure 2.21, the water absorption of concrete gradually decreases as the increase of GO content.

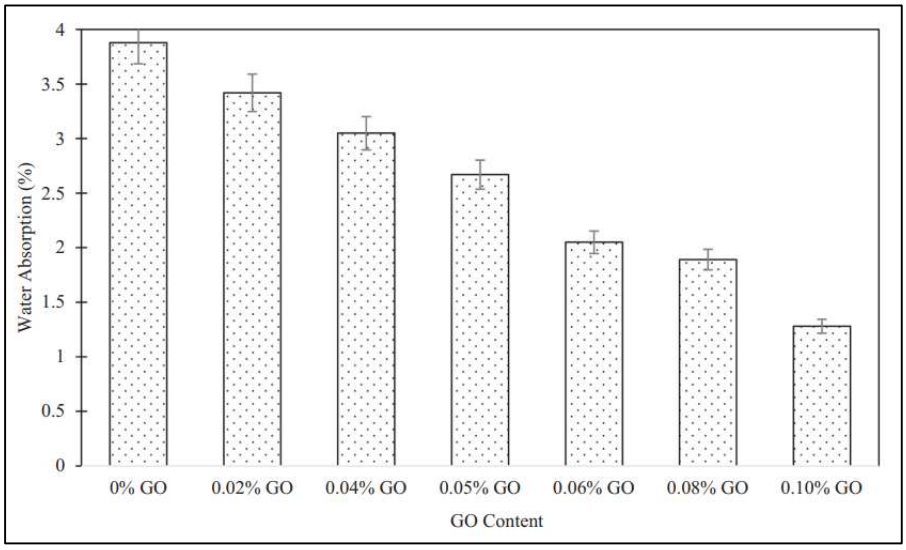


Figure 2.21 Water Absorption Coefficient with Different GO Content (Bheel et al., 2023)

This indicates that the improvement of water absorption can be related to the nanoscale of GO particles which fill every available void in the concrete mixture. Zhang & Zong, (2014) also reported that pore structure mainly involves the volume as well as the size of interconnected capillary pores. Thus, it also defines the filling effect

behaviour of GO. The improvement of the water absorption resistance can be related to the tortuosity of the pore structure. The tortuosity in pore structure can be defined as the path length for fluid or any sort of penetration element that needs to traverse compared to a straight line distance to the material's surface (Jena & Philip, 2022). Therefore, GO tends to create a high tortuosity making it harder for any fluids to penetrate directly into the cement matrix. Technically, GO directly refined the pore structure of the cement matrix which eventually created a higher water absorption resistance for the cementitious material.

2.6.5 Improvement of the Interface Structure Cement

2.6.5.1 Scanning Electron Microscope (SEM)

The mechanical performance and behaviour of concrete with the inclusion of GO are primarily examined by the microstructural analysis. GO consist of a high surface area as well as specific functional groups of oxygen. These are two major noteworthy aspects of two-dimensional GO itself. Thus, it is clear that GO act as competent reinforcing addictive which is not only applicable to technologies industries but also construction. As in the application of cementitious material, GO performs significantly as the microstructural surface properties can enhance the physicochemical properties of the cementitious matrix.

According to Alla & Asadi, (2023), the inclusion of GO in cementitious material does affect the microstructure in a certain way. The study examined the cured composite cement of GO with using a scanning electron microscope (SEM). Based on Figure 2.22, shows the ordinary hardened mix control specimen of OPC which the mix micrograph shows huge voids and tiny fractures.

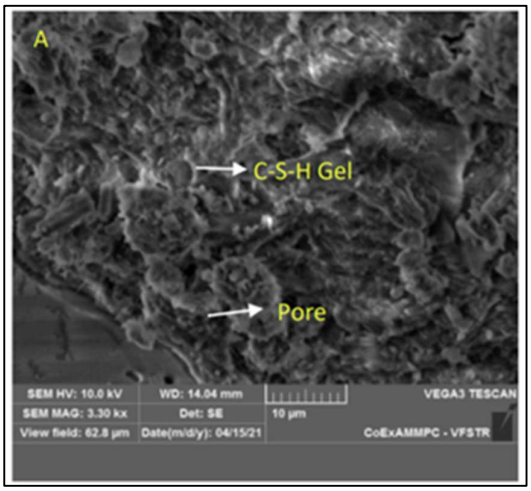


Figure 2.22 SEM Image of Cement Composite with GO (Alla & Asadi, 2023)

However, with the addition of GO, the cement composite produced a denser and more compact microstructure as shown in the Figure 2.23. This may happen due to a higher pozzolanic nature reaction from snail shell powder and the inclusion of GO itself, which caused the formation of hydration crystals perfectly (Calcium Silicate Hydrate gel (C–S–H), Calcium Hydroxide (Ca(OH)2, CH), calcium tri-sulfoaluminate (Ca6Al2(SO4)3 (OH)12·26H2O) also known as ettringite (AFt) and calcium mono-sulfoaluminate (AFm)) as shown in Figure 2.23.

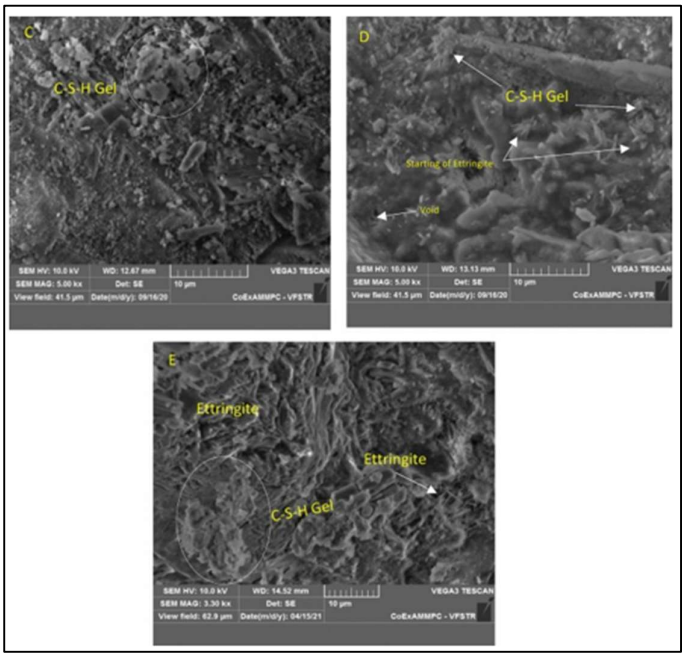


Figure 2.23 Hydration Product of Cement Composite at SEM Image (Alla & Asadi, 2023)

Moreover, the hardened specimens indicated greater binding centres which eventually improved the hydraulic capabilities of the cement composite specimens. In the scope of GO's behaviour, the nucleation effect assists the hydration process on nanoparticles which fasten and accelerate the cement hydration as well as the mechanical performance properties (Xu et al., 2019). Thus, it contributes to a denser structure which is responsible for the improved properties in durability and mechanical properties.

Similarly, Hong et al., (2023) examined the effect of GO on high self-weight concrete on mechanical properties as well as the durability properties. Based on the microstructure analysis, the SEM image obtained crystals formation which is quite similar produced by hydration reactions in cement mortar such as sheet-like crystals and rod-like crystals. This formations of crystal consist of the composite formed by AFt, AFm, and CH. Not only that, but the authors also claimed that this process was also followed by the formation of microcracks and nanoscale voids. Technically, Figure 2.24 shows the growth and formation of the flower-like crystal can only be observed from samples that contain GO. When the GO content increased within the range of 0.04% to 0.06%, the petals formation of the flower-like crystal gradually matured and grew stronger. However, when the content of GO reached 0.08%, the flower-like crystal began to static with a reduced number of flower crystals.

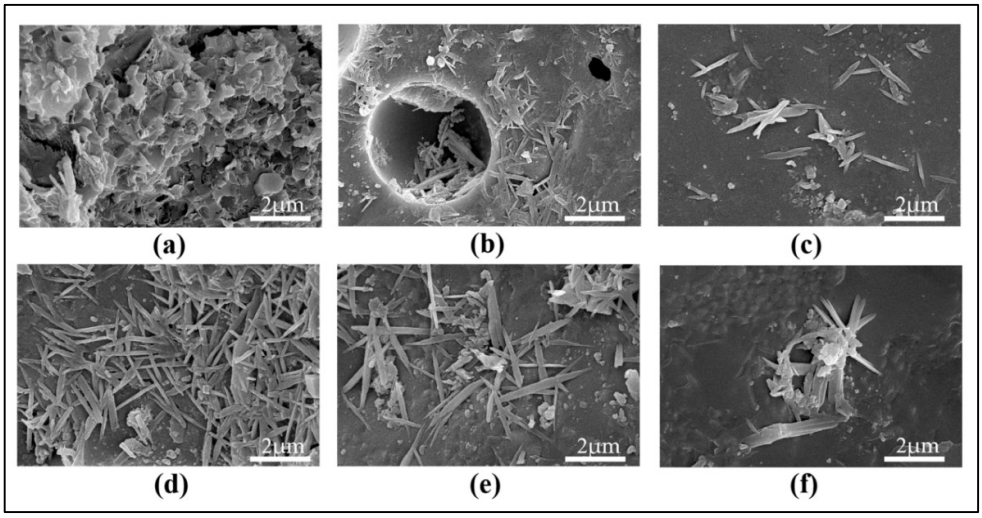


Figure 2.24 Flower-like Crystal of GO in SEM Image (Hong et al., 2023)

Chuah et al., (2014) also confirmed the inclusion of GO in the hydration reaction produces a significantly unique and firm flower-like crystal. Similarly, Xie et al., (2020) also reported that high dosages such as 0.03% of GO formed needle-like crystals compared to 0.01% of GO with the inclusion of cementitious materials. On top of that, Vantadori et al., (2022) also reported that the formation of flower-like crystals was crucial in improving the mechanical performance and durability of concrete.

2.6.5.2 Energy Dispersive X-Ray (EDX)

Generally, EDX microanalysis defines as a method of elemental analysis whereby it is based on the generation of X-rays characteristic in atoms form of the specimen with the help of beam electrons. To put it differently, it is a technique for obtaining elemental composition approached the elemental composition study of the inclusion of GO in cement mortar (Zaid et al., 2022). The authors reported different compositions referring to different dosages of GO content in mortar. The discussion regarding the location of Area 1 and Area 2 can be shown in the SEM images obtained from the study. Based on Figure 2.25, Area 1 comprised a needle-like structure of Ca by 38.4% of the atomic percentage. Meanwhile, area 2 portrayed a cotton-like morphology with a 19.12% of Ca atomic percentage. To be precise, the difference in Ca percentage indicates the chemical formula of the needle-like morphology is Ettringite, and that of cotton-like morphology is C-S-H. As for the EDX spectra, the data were collected from three located areas with the inclusion of 0.02% in cement mortar. Area 1 obtained the highest SiO_2 by the atomic percentage of 30.64% next to oxygen. On top of that Area 2 and Area 3, represent Ettringite and C-S-H whereby the data indicates a high alumina content found in Ettringite compared to C-S-H. This study claimed that the presence of GO acts as a nucleation site due to the "pulling effect" as well as C-S-H on GO. Technically, the control sample displayed the highest amount of Ettringite by producing thin-rod crystals on C-S-H. In contrast, 0.02% inclusion of GO showed lesser crystal rods and C-S-H. Meanwhile, 0.03% of GO showed no sight of thin-rod crystal with Tibermorite C-S-H and 0.04% of GO led to the disrupted matrix of fibrous C-S-H. To conclude, the presence of tobermorite C-S-H is essential for a strong performance with 0.03% GO while Ettringite and fibrous C-S-H cause a reduction of strength. Not only that but, 0.03% GO also had higher C-S-H on the surface of sand which helps to increase the thickness of the zone. This eventually improves a

higher resistance against load and the mechanical strength. This can be proved as Table 2.8 shows the EDX spectra of the control cement mortar taken at Areas 1 and 2.

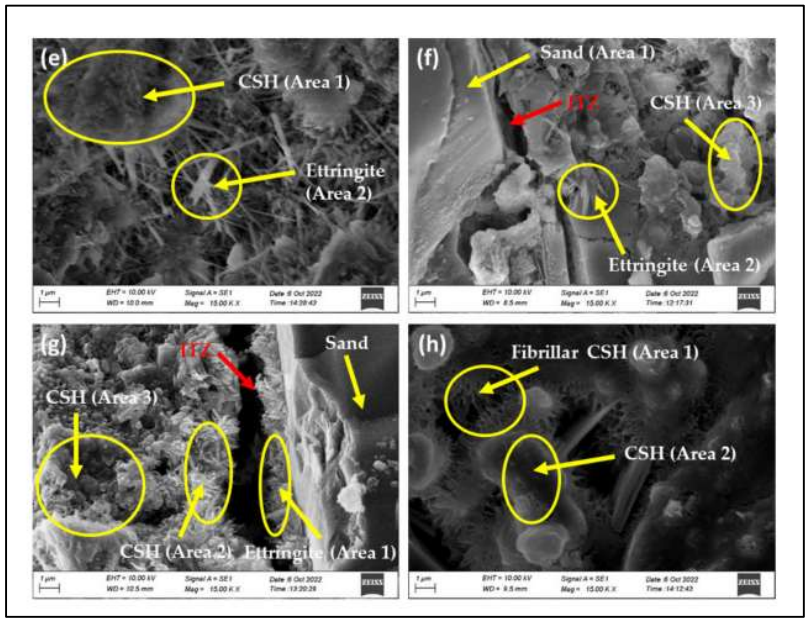


Figure 2.25 Selected Area in Microstructure Analysis (Ganesh et al., 2023)

Table 2.8
EDX Spectra of Cement Mortar (Ganesh et al., 2023)

Figure and Areas	Atomic percentage (%)									
	C	O	Na	Mg	AI	Si	Mo	K	Ca	Fe
8(e), Area 1	6.61	65.64	-	0.36	1.54	5.66	0.27	-	19.12	0.80
8(e), Area 2	0.04	51.84	-	-	1.76	4.78	0.70	0.42	38.24	2.22
8(f), Area 1	-	67.81	-	-	0.45	30.64	-	-	1.10	-
8(f), Area 2	6.08	63.35	-	-	1.34	4.69	0.75	-	23.80	-
8(f), Area 3	5.05	59.91	-	-	0.73	4.52	-	-	29.79	-
8(g), Area 2	-	27.70	0.85	-	6.65	31.71	-	4.35	25.29	3.45
8(g), Area 3	-	47.63	0.56	-	3.22	13.65	-	2.23	30.47	2.15
8(g), Area 1	-	63.74	0.85	-	1.90	4.34	-	0.90	27043	0.84
8(h), Area 1	0.05	40.73	-	-	0.96	9.76	0.38	0.72	46.42	0.98
8(h), Area 2	0.03	62.95	-	0.47	1.40	7.55	-	0.48	26.40	0.72

2.6.5.3 Porosity

Due to the filling effect and nucleation effect portrayed by GO, it also affected the porosity as well as the void located in the cementitious material. Li et al. (2017) concluded that the pore structure and porosity within the cement matrix are some of the most crucial aspects of hydrated cement performance. The author also identified that a 0.02% of GO (CG2) in the cement paste can refine the pore structure by reducing its critical pore size structure and even the macropore volume. This can be shown in the Figure 2.26 as it visualised CG2 (0.02% of GO) has the lowest pore diameter compared to other cement paste in the MIP results of the study. These findings have been influenced by the filing effect of GO itself as it provides an extensive mechanism of pore refinement. Not only that but one of the major factors of this occurrence is the nucleation effect of GO, which enhances cement hydration to generate even more hydration products. As a result, GO has been proven to be effective in improving the durability and mechanical properties of cementitious material.

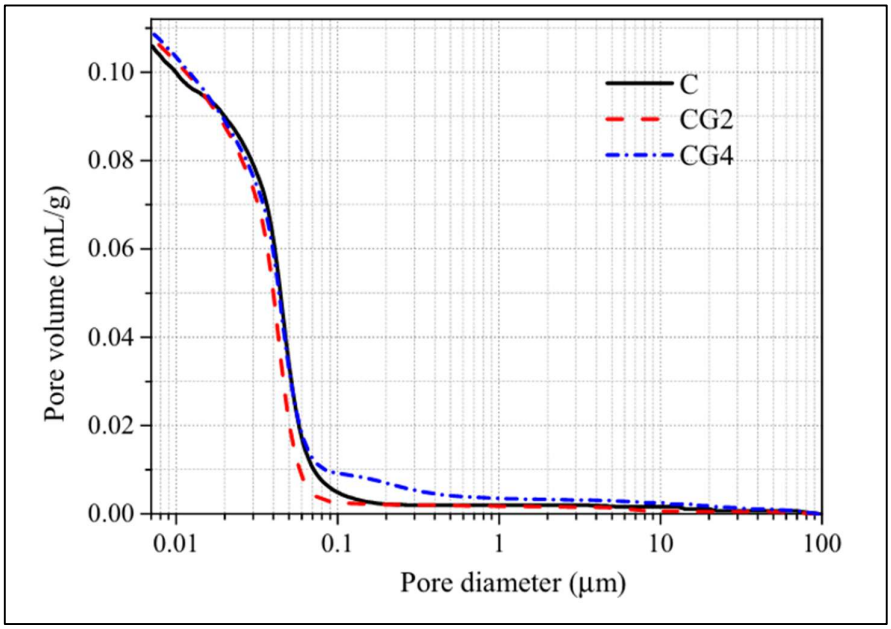


Figure 2.26 MIP Result for Different Cement Pastes Mixes (Li et al., 2017)

As in the pore refinement effect, GO also compliment well with the cementitious matrix as Pan et al., (2015) reported that the addition of GO has gradually increased the surface area measured from 27.3 m^2/g to 64.9 m^2/g. It is commonly accepted that almost

the majority of the total surface area of cement paste produced from C-S-H gel development is directly related to the porous phase in the matrix. Chintalapudi & Pannem, (2020) claimed that cement paste portrayed a very high surface area of microstructure parallel with a high degree of hydration. Thus, this indicates the relevancy of the increase of surface area along with hydration rate due to the addition of GO. Based on the Table 2.9, it indicates that the increment of GO increases the pore volume of the total composite in the pore diameter range of 1-80 nm. Technically, the higher the pore diameter, the lower the difference in pore volume. Therefore, a high proportion of gel pores can act as an indicator that the addition of GO promotes the hydration process. This also reflects towards the nucleation effect embraced by the GO itself in the cementitious matrix material.

Table 2.9
Surface Area and Pore Volume of Mixers Sample of OPC and GO Composite Cement (Chintalapudi & Pannem, 2020)

Sample	Surface area (m^2/g)	Total intruded vol (1 nm < d < 80 nm) (ml/g)	Intruded vol (1 nm < d < 10 nm) (ml/g)	Intruded vol (10 nm < d < 45 nm) (ml/g)	Intruded vol (45 nm < d < 80 nm) (ml/g)
OPC	27.3 ± 3.1	0.049 ± 0.003	0.020 ± 0.001	0.018 ± 0.001	0.011 ± 0.001
GO/cement	64.9 ± 5.2	0.101 ± 0.007	0.046 ± 0.002	0.042 ± 0.002	0.013 ± 0.001

2.6.6 Crystallographic Structure of GO

X-ray diffraction analysis (XRD) is a fascinating technique used in materials science to determine the crystallographic structure of a material. The purpose of XRD analysis is to provide a deep identification of materials based on their own diffraction pattern. XRD also provides notable information in detail towards the actual structure that deviates from the ideal one which includes any stresses, defects and internal.

Based on previous research, there have been similarities in data in terms of XRD analysis of GO over the years. Zhao et al. (2020) reported that after conducting the modified Hummer's method, GO has been produced from Graphite. The characterisation of XRD analysis can be seen in Figure 2.27 as the authors conducted the diffraction difference between GO and Graphite. XRD pattern shows variation of peak after oxidation, the interlayer space of GO significantly increases from 0.334 nm up to 0.769 nm. As in the graph, it can also be stated the peak of GO data is located

after 10° at 2θ. The major reason for this data is due to the introduction of the oxygen functional group.

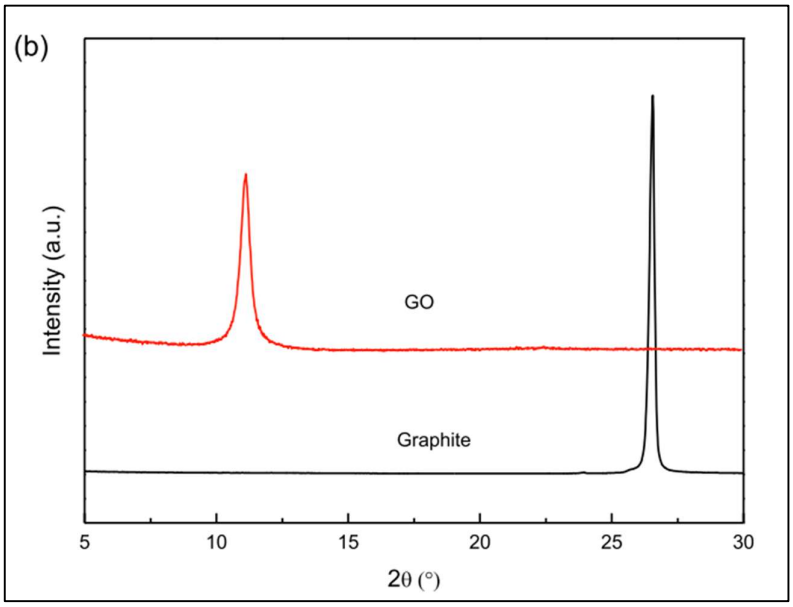


Figure 2.27 XRD Pattern of Graphite And GO (Zhao et al., 2020)

Furthermore, Anwar et al., (2020) also indicated that the diffraction angle of 2 θ of graphite decreases for the GO. The comparative study between graphite and GO was conducted to provide direct evidence of the oxidation occurrence specifically on the surface of the GO. The finding showed that graphite initially holds the highest peak of 26°. Meanwhile, GO depict the result of a diffraction angle between 9.45° - 10.7°. Figure 2.28 shows the XRD analysis data between graphite and GO in the study. A similar discussion has also been reported, in which during the oxidation process, the interlayer distance has increased from 0.34 nm to 0.94 nm. This is because of the presence of oxygen-functional groups during the synthesis process of GO. However, Lee et al., (2019) stated that there is the possibility of the low existence of GO in an amorphous phase instead of a crystalline phase. On top of that, the functional group also influenced in facilitating the reaction location which ultimately enhances a stronger bonding with C-S-H.

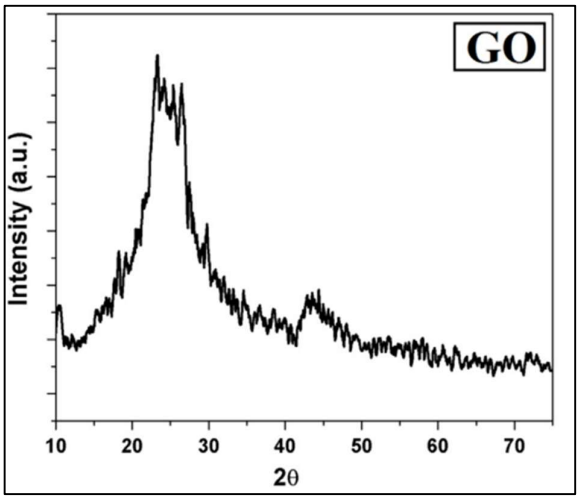


Figure 2.28 XRD Pattern of GO (Lee et al., 2019)

To add to the discussion, Huang et al., (2021) also demonstrated several characteristic peaks in the XRD pattern of GO in reinforced mortar shown Figure 2.29. The author believes that the obtained peaks refer to the abundant crystal structures that formed during cement hydration. The main components in the XRD peak managed are calcium hydroxide, C-S-H, C_2S and C_3S as in the remaining cementitious material. A detailed comparison observation has found that C_2S and C_3S peaks disappeared except in the control sample without GO. This explains the effectiveness of GO's nucleation effect where it rapidly enhances the cement hydration phase. In detail, the faster the process to form a hydration product, the weaker and broader XRD peak for C_2S and C_3S to appear.

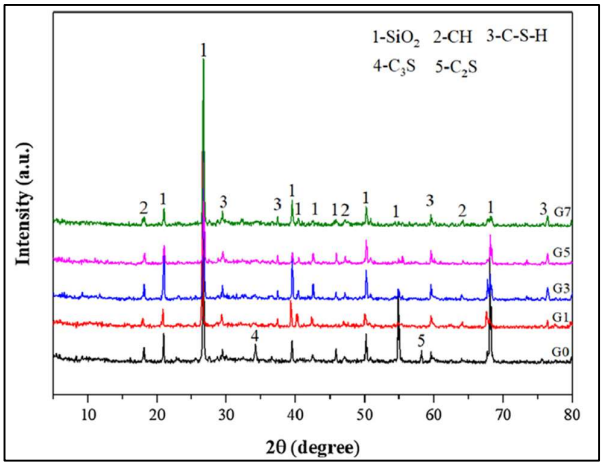


Figure 2.29 XRD Patterns Of 28 Days Hydrated GO Reinforced Mortar (Huang et al., 2021)

2.7 GO Mechanism Against Corrosion

2.7.1 Introduction of Corrosion

Generally, metals are famously known for their tendency to be affected by corrosion. The occurrence of corrosion happens due to contact with oxygen, water and chloride ions. There is no doubt that corrosion gradually destroys metal. Henceforth, the general equation of corrosion can be shown as:-

$$Fe + 2H_2O + O_2 \rightarrow 2\,Fe(OH)_2 \quad (2.1)$$

As in current construction development, more metal rebars are being used as reinforced concrete which also leads to a higher potential of corrosion. This extension of defect could directly lead to failure of the structure even reducing the mechanical performance of the reinforced concrete. Corrosion in steel reinforcement can be described as an electrochemical process in which metals undergo a chemical reaction on the reinforcement surface. The mechanism of corrosion can be depicted in the Figure 2.30. There is no doubt that corrosion can be categorized as a natural phenomenon of defects and deterioration which often happen through scattered metals or alloys (Jena & Philip, 2022). Corrosion also can be triggered by a few main aspects such as moisture, humidity, electrolytes and even the presence of oxygen. Due to these hazardous environments, it endures the performance of metal materials shortening the lifespan of infrastructures and even utilities. This shall eventually lead to various problems such as economic losses and even hazardous the industrial scope of work. In-depth corrosion, there are numerous damages have been reported such as premature failure of metals and other materials which consequently lead to pipeline leakage and eventually cause an excessive amount of soil or water pollution. Concrete is famously known for its vulnerability to environmental degradation due to its porous nature. This occurs when aggressive ions such as chlorides and sulphates penetrate into the concrete eventually destroying the passive layer of oxide on the concrete surface, leading to corrosion deterioration (Yuvaraj et al., 2022). In addition, concrete is primarily known for its porous properties with the existence of crystals within the microstructure pores to resist penetration. Nevertheless, it is crucial to understand that permeation of any corrosive media is notably facilitated by the presence of moisture content. This contributes deeply

to the corrosion deterioration of the concrete structures as it emphasizes the inseparable relationship between how corrosive media and permeability to the concrete structure (S. Li et al., 2024). Thus, a deterioration of concrete structure due to corrosion can be depicted in Figure 2.31. To be more specific, the formation of rust could extend up to 6 to 10 times more volume than the parent volume. This shall lead to lower stiffness properties of the concrete resulting in poor mechanical performance which leads to cracking and spalling to the surface of the concrete itself (Zhao et al., 2025).

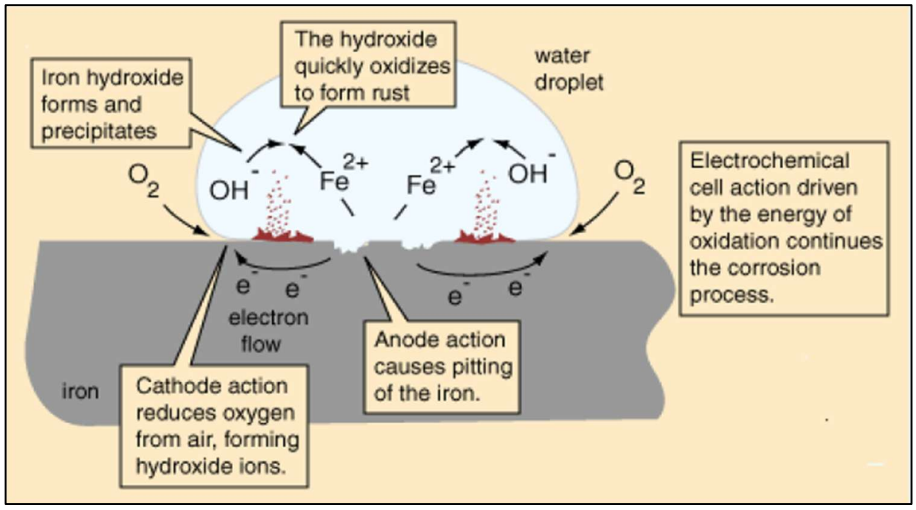


Figure 2.30 Corrosion Mechanisms Affecting Steel Embedded in Concrete (Firouzi et al., 2020)



Figure 2.31 Deterioration of Concrete Due to Corrosion in Building Component (Zhao et al., 2025)

2.7.2 The Phase of Corrosive Deterioration

The penetration of chloride ion corrosion gradually leads to reinforced concrete damage. This damage or deterioration can be categorized into four major phases which are the latent period, development period, acceleration period, and deterioration period as depicted in Figure 2.32. Generally, the latent period can be described as the initial phase whereby the degradation process occurs at the microstructural level. This latent period also can be precisely represent the Initiation Period (T_{HCP}). As the steel remains protected by its passive film, mass loss (m) is effectively zero as the structure maintains its nominal properties. Hence, the latent period, marked by the breakdown of the passive film, initiates the Propagation Period or known as Active Corrosion time (t). Later then, it leads to the development period whereby it starts to manifest damage and transition from microstructure to macroscopic scale and mass loss begins to accumulate. This is when the functional performance of the structures starts to decline gradually due to the underlying deterioration (Zhao et al., 2025). The period of deterioration continues to the acceleration period where the rate of damage eventually accumulates and increases the deterioration defect to the structure. Finally, the deterioration period represents the permanent phase of the critical or tipping point of structural failure. This period eventually led to total damage deterioration and poor structure integrity. Not only that, but the effect of the long-term corrosion current also influenced the reduction of mass loss (m) due to the reduction of the sectional area of the rebar.

As in chloride penetration process, the deterioration phase is initiated with a sequential process as in the latent period, external chloride ions started to invade by penetrating the interface of the steel bar from the surface of the structures. When the external chloride overlaps the internal chloride that mainly comes from cement, water and mortar, critical chloride ion concentrations have been achieved. This eventually leads to steel bar to corrode on its own. During the last period of the latent phase, the corrosion product will expand vigorously as it begins the squeeze all over the concrete to produce a crack right after the steel bar surface rusts (Schwarz et al., 2018). As the number of cracks begins to increase inside the concrete, it allows oxygen content to be added and leads to faster chloride ion erosion and corrosion range. As the concrete finally begins to damage, it enters the acceleration phase whereby it indicates the oxygen content inside the structure increases remarkably. This devoured concrete

spalling and ended up in a deterioration phase where the life structural life span capacity dropped tremendously over time until its being finally destroyed (Zhao et al., 2025).

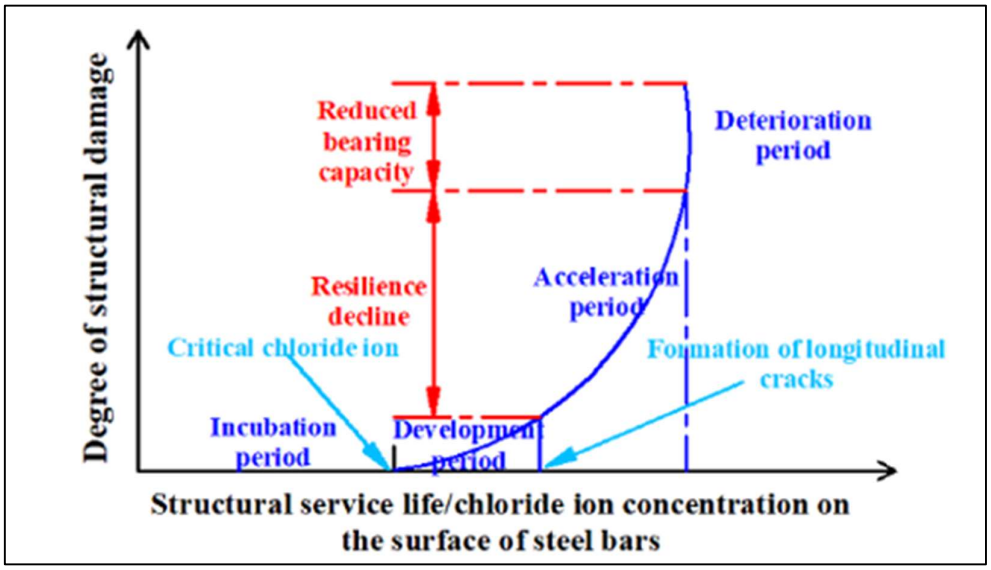


Figure 2.32 Schematic Diagram of the Stages of Reinforced Concrete Damage Due to Chloride Ion Corrosion (Zhao et al., 2025)

The deterioration of concrete due to corrosion caused by the penetration of ion chloride can be portrayed as a growing tumour within the concrete. It devours the concrete silently over time causing internal pressure within the concrete and eventually leading to cracking and spalling. This level of damage not only exposed the overview of the structure but also weakened the structure's integrity over time. Therefore, Figure 2.33 reveals the SEM images of the deteriorated surface of concrete due to corrosion exposed in real world environments.

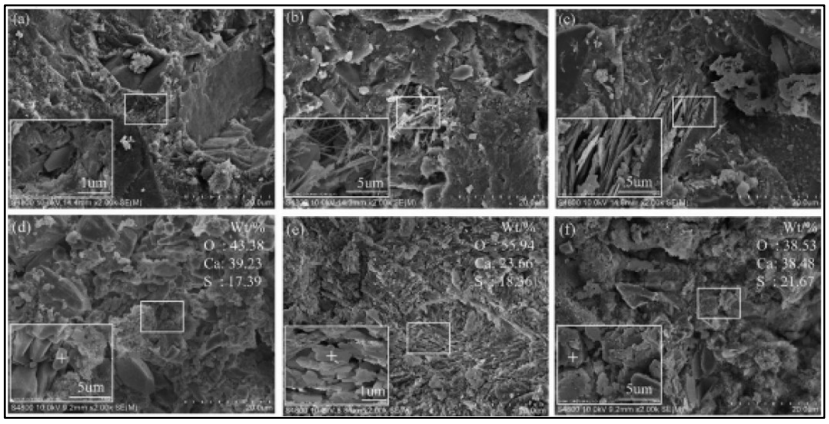


Figure 2.33 SEM Images of Deteriorated Concrete Due to Corrosion (Yuvaraj et al., 2022)

2.7.3 Graphene Oxide as Corrosion Resistance

Therefore, as an inclusion of GO in cementitious material, the expansion of GO tends to go through the corrosion resistance study. The mechanism of GO extends beyond just a protective barrier to the cement matrix. As mentioned before in the previous sub-section of this chapter, GO owns a significant role as a nucleation site where it helps in providing denser and uniform microstructure in the cement matrix. This pore refinement directly leads to the reduction of permeability of the cementitious material resulting in more challenges for any penetration to be done. This penetration specifically includes corrosive media such as chloride ions, dissolved oxygen and even sulfates. Therefore, the cracks and voids are the primary effects due to the penetration of the corrosive media within the cementitious material. Apart from that, compared to the mechanical properties of GO in cementitious material, the durability of GO remains largely unexplored. This durability issue in cementitious material stretches many areas, including corrosion which is mainly caused by chloride, carbonation and many more (Tong et al., 2016). This shows a correlation of GO with corrosion resistance to be studied. This can be explained as Mohammed et al. (2015) explored that GO tends to reduce the chloride ion penetration as the inter-connected design of GO layers acted as a protective barrier to capture the chloride. In another study, it was stated that 24.8% sorptivity coefficient with 0.06% of GO inclusion in the cement matrix (Qureshi & Panesar, 2019). The sorptivity coefficient can be defined as the capacity of the material to absorb and transmit water to the capillary pores. These findings and discussion also can be confirmed by Long, Gu, et al. (2018) as the authors believed that GO could reduce the sorptivity coefficient within the cementitious material. Lv et al. (2016) identified that GO could reduce the rate of permeability depth approximately by 72% and improve the modulus of elasticity by up to 78%. The author also stated that GO helps to reduce the carbonation depth of the cementitious material by 66% at 28 days. This is due to the formation of polyhedral crystals from the hydration process which filled the un-left void and cracks within the cement matrix.

Within the same context of the corrosion resistance of GO, it is worth stating that the "bridging effect" of GO plays a crucial role in enhancing the durability properties of the cementitious material. Figure 2.34 visualized the GO's bridging effect in cement mortar. This can be described as a uniform dispersion of GO within the cement matrix act a nanoscale bridge that builds across cracks which is mainly caused

by applied load and exposed penetration (Qureshi & Panesar, 2019). This shall prevent and restrict any further crack propagation which eventually enhances the structural integrity of the structure. Not only that but it also reduces the potential for any ingress or penetration of corrosive media. GO is also famously known for its bonding and nucleation effect where it facilitates the cement hydration product of C-S-H (Zhang et al., 2021). Therefore, with an enormous quantity of C-S-H being produced, it tends to create a denser cement matrix. This also helps create a tortuous diffusion path or also known as the Labyrinth Effect which significantly hinders the rate of corrosive media penetrating into the cement matrix as shown in Figure 2.35. Nevertheless, there have been limited studies in the corrosion effect towards GO in the cementitious material. Particularly, in limited studies focused on analysing the theoretical understanding and behaviour mechanism of GO within these durability issues.

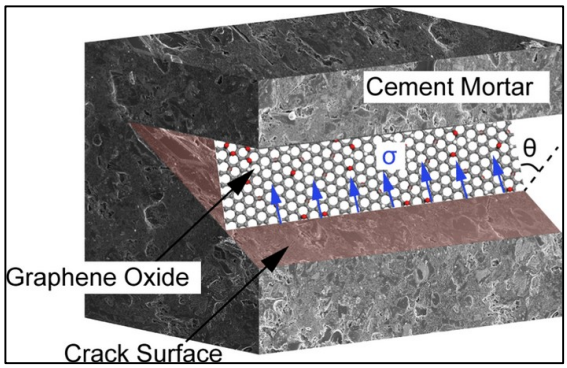


Figure 2.34 Visual Representation of GO Bridging in Cement (Qureshi & Panesar, 2019)

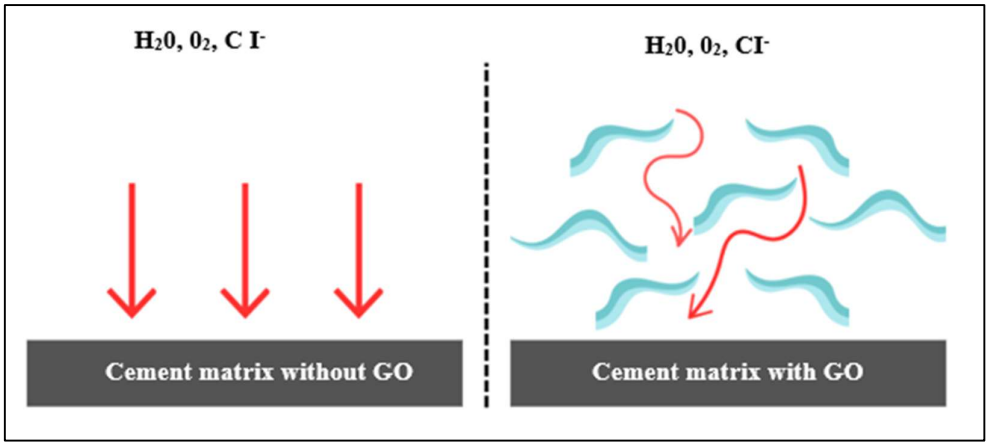


Figure 2.35 Schematic Diagrams of the Labyrinth Effect GO Against Corrosive Penetration (Zhang et al., 2021)

2.7.4 Rapid Chloride Penetration Test (RCPT)

Generally, the Rapid Chloride Permeability Test (RCPT) can be described as the accelerated electrochemical method which used to evaluate the resistance of cementitious materials to chloride ion penetration. This test focussing on the electrical conductance of a saturated specimen by measuring the total charge passed known as Coulombs over six hour period according to ASTM C1012. Therefore, as in the context of GO in cementitious based materials, the RCPT is primarily to quantify the efficiency of GO in pore refining mechanisms within the cementitious based materials. The presence of GO justifies the development of more torturous capillary network that obstruct the migration of aggressive ions. This can be proved by one of previous study conducted by Anish et al., (2025) where GO recorded a significant enhancement as corrosion resistance of reinforced concrete. This study found that the concrete containing 0.05% of GO by weight of cement exhibited approximately 70% reduction in chloride ion permeability. This leads to an improved resistance to chloride induced corrosion as GO tends to reduce the porosity and pore size due to the filling effect mechanism. Similar discussion found in Bellum et al., (2020) study where the incorporation of GO within the geopolymer concrete resulted in a 65.44% reduction in chloride ion permeability. Moreover, GO-modified concrete also managed to show a reduction in chloride permeability by 35.3% when 0.25 wt. GO was added, alongside increases in compressive strength and modulus of elasticity (Maglad et al., 2022). This happened due to the contribution of GO where it promotes the formation of high density calcium silicate hydrate which further improves the pore structure and reduces permeability (Guo et al., 2019). This eventually leads to a denser microstructure by refining the pore size distribution and reducing porosity.

2.7.5 Depassivation of Half Cell Potential (HCP)

The corrosion risk associated with GO in cementitious based materials corelates with the usage of Half Cell Potential (HCP) testing. The primary importance of HCP lies in its ability to provide a rapid corrosion risk assessment, allowing for the detection of possibility active corrosion zones before visible physical deterioration, such as cracking or spalling, occurs on the concrete surface. Previous research managed to explore the effects of combining GO with supplementary cementitious materials,

specifically Ground Granulated Blast-furnace Slag (GGBS). A landmark study by Bhojaraju et al., (2023) investigated the corrosion resistance of GGBFS-blended composites from 15% to 45% cement replacement reinforced with GO at dosages of 0.03% and 0.06%. Their findings indicated that the integration of 0.03% GO with 45% GGBFS yielded the most superior performance in aggressive saltwater environments. The study demonstrated that GO acts as a nucleation site that accelerates the hydration of slag particles, leading to a significantly denser blended mortar and higher electrical resistivity compared to plain GGBS mortar. This can be explained as the half-cell potential confirmed that GO effectively delays the depassivation of the steel reinforcement by creating a more complex and refined pore structure (Firouzi et al., 2020; Zhang et al., 2021). Nevertheless, research regarding the use of half-cell potential testing for GO in cement-based materials remains limited. Most studies prioritize strength and microstructural changes, leaving a gap in the understanding of when corrosion actually begins. This starting point, known as the time to depassivation, is rarely explored in GO-modified systems. Understanding this initiation period is critical to determining the duration of protection provided by GO. Without such data, the exact delay in the start of corrosion caused by GO is difficult to quantify. Therefore, further investigation is needed to track the time required for the steel to lose its protective layer and begin the corrosion process.

2.7.6 Quantitative Corrosion Corelation of Mass Loss

Corrosion in reinforced concrete leads to the physical reduction of steel, which is commonly measured as mass loss. This metric provides a direct indication of the structural damage occurring at the reinforcement level. Faraday's Law serves as the mathematical tool used to calculate this loss by converting electrochemical data into physical weight. By relating the total electrical charge passed over time to the amount of metal consumed, this law allows for a precise determination of the corrosion rate. As for the context of GO in cementitious based material against mass loss of steel rebar, there are very limited area of knowledge that has been explored. One of the finding can be found in Nascimento et al., (2024) study where the addition of GO to concrete has been shown to significantly enhance the corrosion resistance of steel rebar. For instance, a study demonstrated that incorporating 0.03 wt. GO in concrete improved the corrosion inhibition efficiency by 79.3% in a saline medium. This suggests a substantial reduction

in the mass loss of steel rebar due to corrosion. In addition, Anish et al., (2025) highlighted that 0.05 wt.% of GO in reinforced concrete lowered the mass loss of steel rebar due to a reduction of chloride ion permeability up to 70% compared to control sample. This can be discussed as the formation of stable hydration products and the refinement of pore structure due to GO addition also contribute to the enhanced durability and reduced mass loss of steel rebar (Zhang et al., 2024). Not only that but within a cementitious system, GO functions as nano-scale protective barrier, utilizing its high surface area and tortuous molecular structure to create a labyrinth effect (Zhang et al., 2021). This physical obstruction significantly impedes the migration of chloride ions and moisture, thereby suppressing the corrosion current at the steel-concrete interface. Existing literature has predominantly focused on the microstructural and mechanical enhancements of GO-modified composites. However, the influence of GO on the mass loss aspect of reinforcement remains an unexplored topics. While previous studies have documented reductions in porosity and increases in strength, a significant gap exists regarding the direct, quantitative correlation between GO integration and mass loss. Utilizing Faraday's Law to calculate the analytical mass loss addresses this research void, transforming qualitative observations into precise numerical evidence of the material protective efficiency.

2.8 Research Gap

The analysis of the literature review revealed that the utilisation of GO in the cement matrix has provided a generous amount of enhancement for the past few years. On top of that, GO also represents an exceptional yet notable performance in delivering three major mechanisms which are the filling effect, bonding effect, and nucleation effect. Not only that but GO also dominated the cementitious industries for various types such as geopolymer, blended, and high performance self-compacting concrete. Nevertheless, a persistent and critical gap in terms of corrosion assessment provided by this carbon-rich nanomaterial remains unexplored. The influence of GO successfully documented the microstructural enhancement and strength, but it falls significantly short in providing a conclusive structural performance on the corrosion aspect. The existing research is typically limited to insufficient quantitative measures, which eventually reduces the potential of long-term structural degradation prediction. This leaves a critical void in understanding how GO would work as a protective barrier

against the corrosive penetration. Based on previous sub sections, it can be concluded that Rapid Chloride Permeability Testing (RCPT) serves as a vital indicator for determining the resistance of the matrix to ion ingress. This measurement is crucial for evaluating the corrosion current density, as it reflects how effectively GO-modified pores restrict the movement of aggressive agents. Moreover, the Half Cell Potential also provides a crucial data identify the Initiation Period of corrosion or known Time to Depassivation (T_{HCP}). Previous research lacks sufficient detail on this initiation period in GO blended cementitious system which leaves a gap in understanding when the steel rebar protective layer started to fail. Finally, the Mass loss represents the final outcome of the corrosion process and serves as the ultimate metric for structural degradation. While microstructural and mechanical properties are well studied, the quantitative link between GO integration and physical metal loss remains largely unexplored. Correlating RCPT and HCP findings with mass loss results provides the evidence needed to validate GO as a functional protective barrier against long-term material degradation. Therefore, Table 2.10 indicates the research gap of GO within the cement-based material for specific analysis and the present study for this thesis, as in the corrosion aspect.

Table 2.10
Research Gap of the Study

Nanomaterial					Type of cement		Analysis			Remarks	Reference
SiO_2	TiO_2	CNT	Graphene	GO	OPC	Blended	HCP	RCPT	Mass Loss		
			✓	✓		✓	✓			An adequate percentage of GO influenced to lower value of current corrosion density values.	(Bhojaraju et al., 2023)
		✓			✓		✓			Significantly reduced the corrosion rate by 60%. However, the mass loss was not calculated in the study.	(Konsta-Gdoutos et al., 2017)
✓	✓				✓			✓	✓	The data exhibited a reduction of pore size which delivers the filling effect role of nanomaterials.	(Vitharana et al., 2020)
				✓		✓		✓		GO offers a promising, lower-carbon route to durable, chloride-resistant concrete for marine environments.	(Rezakhani et al., 2023)
			✓		✓			✓		The protective barrier mechanism of graphene increased tremendously with the increase of dosage.	(Q. Liu et al., 2016)
			✓	✓				✓		Graphene derivatives tend to provide a protective layer to the cementitious due its high surface area.	(Ying et al., 2021)
				✓		✓	✓	✓	✓	Present studies	-

CHAPTER 3
RESEARCH METHODOLOGY

3.1 Introduction

This chapter summarily presents the sequence for the research along with the related methods used in the study. Generally, this study has been constructed into three major phases whereby it had been designed towards achieving research objectives as shown in Table 3.1. Phase 1 focuses on the characterisation and properties of raw materials used in the study and addresses the binder formulation as in the properties of blended mortar. Furthermore, Phase 2 projects the binder modification and determines the corrosion resistance test. The study eventually ended with Phase 3 whereby it identifies the mass loss of steel rebar to prove the protective barrier role of GO as nanomaterial additive in the blended mortar.

Table 3.1
Research Phases and Alignment with Research Objectives

Phase	Research Objective	Testing	Output
Phase 1	Objective 1 To characterise blended material and graphene oxide, and to evaluate their influence on the physical, mechanical, and durability properties for binder formulation.	Raw material characterisation:- • X-ray Fluorescence • Elemental Analyser • Energy-Dispersive X-ray Spectroscopy • X-ray Diffraction • Scanning Electron Microscopy • Field Emission Scanning Electron Microscopy Properties of binder formulation:- • Density • Compressive strength • Split Tensile strength • Water absoprtion	Provide an extensive characterisation data of raw materials in the study as well as their influence towards physical, mechanical, and durability properties of Ordinary Portland Cement.
Phase 2	Objective 2 To investigate the optimum ratio of graphene oxide in producing nano-	Properties of binder modification:- • Density • Compressive strength • Split Tensile strength	This phase determined the optimum ratio of GO in blended mortar as evaluation in physical, mechanical and durability

	composite mortar under physical, mechanical and durability properties for binder modification. Objective 3 To evaluate the microstructure and durability of GO-blended mortar against corrosion resistance.	• Water absoprtion • Mercury Intrusive Porosimetry (MIP) • Scanning Electron Microscopy (SEM) • Rapid Chloride Permeability Test (RCPT) • Half Cell Potential (HCP) • X-ray Diffraction (XRD)	performance. Through the evaluation of optimum GO in binder modification, it continues determined the durability parameters and microstructural properties against corrosion resistance.
Phase 3	Objective 4 To investigate the mass loss of the steel within the GO-blended mortar using Faraday's Law.	• Time to Depassivation • Active Corrosion Time • Total Corrosion Current • Mass Loss	The final phase was to quantify the structural degradation of mass loss of the steel embedded in GO-blended mortar by corrosive attack in normal and saltwater conditions.

Phase 1: Raw Material Characterisation and Blended Mortar Properties

This phase focussed on characterisation of each material before conducting binder formulation and modification. The experimental work was conducted in this phase as it requires an optimum percentage of supplementary cementitious materials as cement replacement of OPC. This phase was also intended to evaluate engineering properties of binder as it achieves research objective 1.

Phase 2: Properties of Blended Mortar Incorporating with GO Against Corrosion

A comprehensive experimental work continued with the optimal performance of supplementary cementitious materials (SCMs) and various of GO percentages was obtained. This phase also indicates optimal GO performance as it was carried out to achieve research objective 2 and objective 3.

Phase 3: Mass Loss of GO-blended Mortar

This last phase concluded experimental data and calculated mass loss of steel rebar within the GO-blended mortar. Not only that but this phase also determined

several parameters such as Time to Depassivation (T_{HCP}), Active corrosion time (t), Total Corrosion Current (I) as well as the Average Nominal Area Loss (A_{loss}). The Faraday's Law was calculated to achieve the last objective in this study.

3.2 Research Framework

The study begins with selection of raw materials which includes OPC, fly ash, GGBS and GO. The Ordinary Portland Cement (OPC) employed in this study was Tasek Buaya OPC, which was acquired from the local, Tasek Corporation Berhad. It acts as the primary binder throughout the study.

Meanwhile, fly ash and GGBS are commonly used as supplementary cementitious materials (SCMs) in cement replacement. The main purpose of these SCMs was to enhance both the performance and sustainability of the mortar. Therefore, the fly ash was obtained from the Kapar Energy Ventures (KEV) Power Station located in Klang with particle sizes ranging from 10-20 micrometres (μm). This suits the general size of the cement replacement application in the study. Moreover, the GGBS was supplied by Macro Dimension Concrete (MDC) and was finely processed with a particle size below 15 micrometres. Additionally, the original form of GO, which is graphene, was supplied by the Petronas Research Team. As the study continued, the graphene was synthesised using the Simplified Hummer's Method to produce the graphene oxide. The raw material of GO was produced in a powder form, with vertical, lateral sizes and the specific surface area evaluated through nano size analyser by third party testing at SIRIM.

Moreover, a constant size of fine aggregate or sand also was used throughout the study where it was collected from CEN Standard Sand, complying with the EN 196-1 standards. It is distributed in a consistent pack of 0.08 mm size of fine aggregate. Nevertheless, in order to evaluate a proper and homogenize filler size, a sieve shaker was used throughout the study for the raw materials except GO. The procedure of sieve shaker follows as shown in Figure 3.1. Moreover, the proper properties of raw material in the study can be shown in Table 3.2.



(i) (ii)

Figure 3.1 Homogenize Process for Raw Materials Used in the Study

i. Raw materials were processed through a sieve shaker using a stack consisting of 300 µm, 150 µm, and 75 µm mesh sizes, ending with a collection pan.
ii. The shaking process was timed precisely for 7 minutes.
iii. Material retained on each sieve was brushed to ensure all undersized particles passed through to the next level.
iv. The collected material for each sieve was recorded and labelled properly.

Table 3.2
Physical Properties of Raw Materials

Material	OPC	Fly Ash	GGBS	Sand	GO
Purpose	Primary binder	Cement replacement	Cement replacement	Filler	Nanomaterial additive
Colour	Grey	Yellowish	Off White	Grey	Black
					
Size	< 75 µm	< 75 µm	< 75 µm	0.08 mm	• 0.8 to 1.2 nm (vertical size) • 73.0 to 89.0 µm (lateral size) • 530 m^2/g to 1050 m^2/g
Particle Shape	Irregular and angular	Spherical and glassy	Sharp and angular edges	Angular	Wrinkled surface
Sources	Tasek Corporation Berhad	Kapar Energy Ventures (KEV)	Macro Dimension Concrete (MDC)	CEN Standard Sand	Petronas Research Team

A comprehensive characterisation of these raw materials was performed various testing which are, chemical characterisation analysis under XRF, EA and EDX; phase characterisation through XRD; and finally microstructural investigation using SEM and FESEM. This characterisation analysis determines of each material's properties which are consequently being used as in blended mortar. This characterisation analysis for each material are used as in blended mortar as shown in Figure 3.2.

Figure 3.3 focused on research framework to optimize binder formulation by investigating the functionality and effect of partial replacement of Ordinary Portland Cement (OPC) with Fly Ash (F) and Ground Granulated Blast Furnace Slag (GGBS). The phase 1 covers evaluation of the physical, mechanical and durability properties of blended mortar with various percentages of SCMs (0%, 10%, 20%, 30%) for both materials. Therefore, the research flow begins with performing different binder mixes as a comparison where OPC with fly ash and OPC with GGBS as blended mortar. Each testing underwent a constant type of testing which includes density tests, mechanical properties through compressive and split tensile strength tests and durability property, specifically water absorption. Later, the data obtained from each test were analysed and compared to identify the optimum percentage of fly ash and GGBS that compromise overall performance as SCM in cement. This systematic approach is crucial to grip an understanding of fly ash and GGBS as cement replacement and consequently achieving objective 1 in the study.

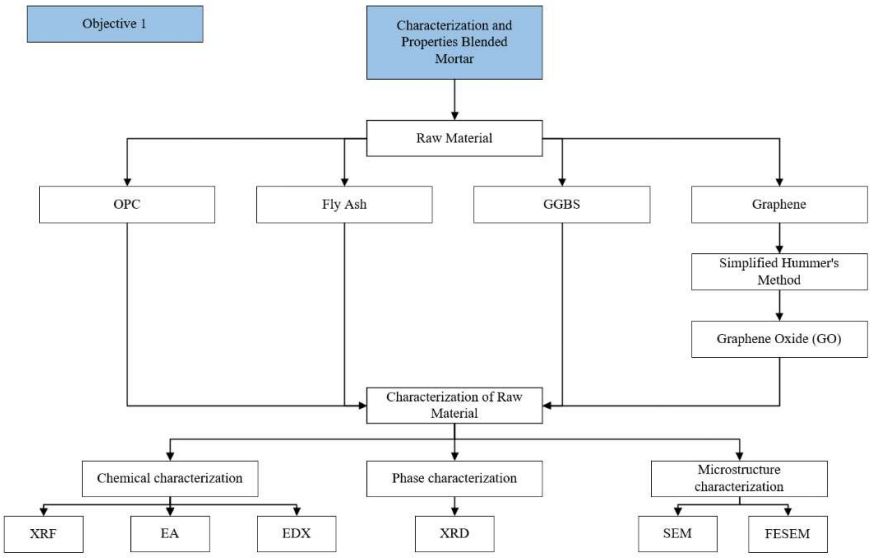


Figure 3.2 Characterisation of raw materials

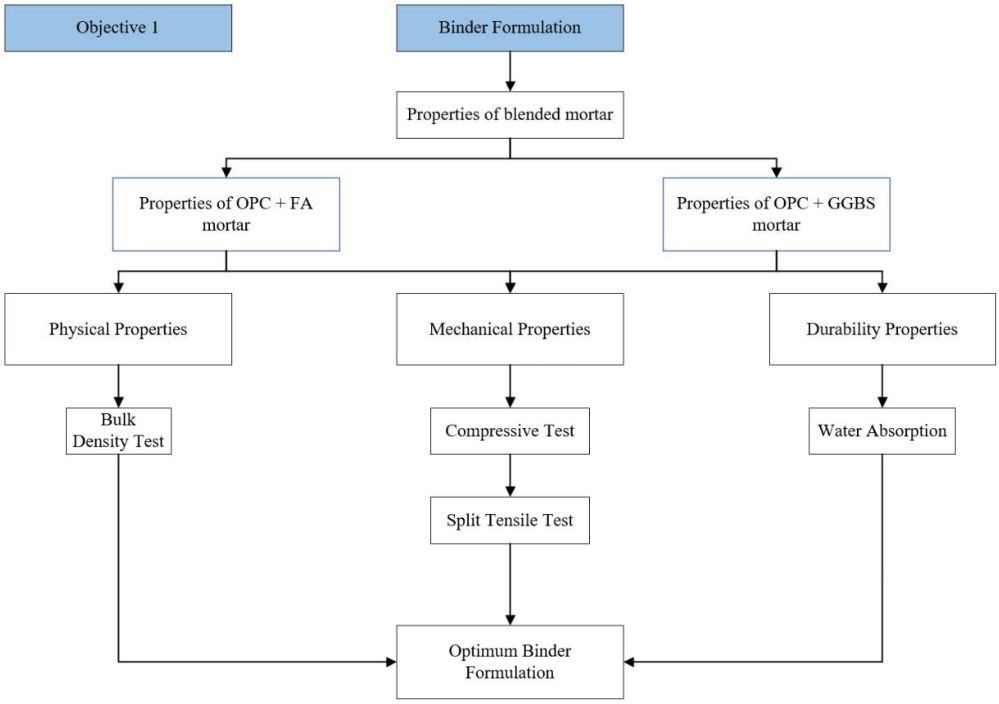


Figure 3.3 Properties of Binder Formulation

Based on the optimal percentage of SCMs obtained in binder formulation, the data was carried forward for the binder modification stage which includes the properties of blended mortar incorporated with a nanomaterial of graphene oxide (GO). Figure 3.4 indicates the research objective 2 as it undergoes similar testing as binder formulation whereby physical, mechanical and durability testing were conducted. Binder

modification started by incorporating GO into OPC with GGBS mortar with various dosages of 0.02%, 0.04%, 0.06%, 0.08%, and 0.10% by total weight of binder. The variety of dosages was designed to identify the most influential yet high impact of GO in blended mortar. Further investigation also covers corrosion resistance test whereby Rapid Chloride Penetration Test (RCPT) and Half Cell Potential Test (HCP). RCPT was conducted to assess the mortar resistance against penetration of chloride ion, meanwhile HCP tends to identify the probability of corrosion that might occur to the GO-blended mortar. On top of that, Mercury Intrusion Porosimetry (MIP) also being conducted to evaluate the pore structure of GO-blended mortar by identifying the total size pore volume, porosity and size distribution under mercury's pressure. Further investigations also include microstructure characterisation which was SEM to provide a greater resolution of samples tested. This leads to a detailed morphology and homogenous distribution of GO within the blended cement matrix. Finally, an analysis of X-ray diffraction (XRD) for each samples was conducted to observe the crystalline phase of the blended mortar influenced by GO. Every data was analysed with a selectively related discussion which led to the development of GO-blended mortar. This shall provide a comprehensive approach towards research objective 3 as the effect of GO modification in blended mortar in creating enhancement performance.

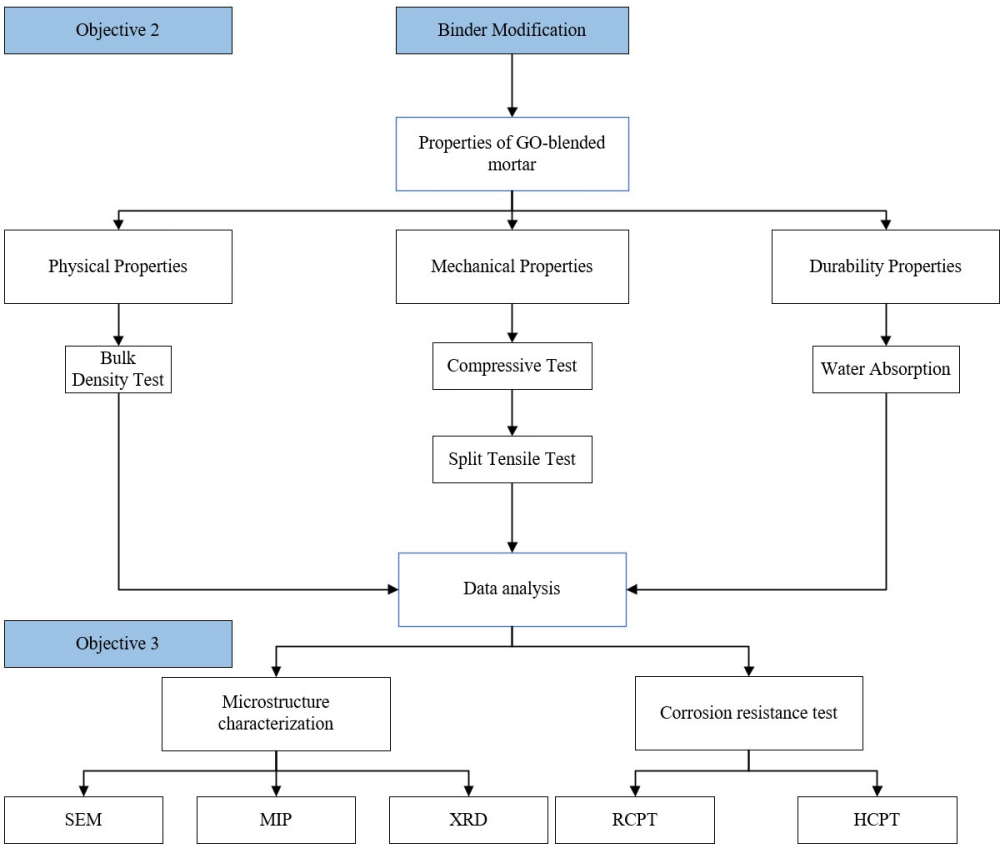


Figure 3.4 Properties of Blended Mortar Incorporating with GO (binder modification)

In the final phase of the study, the research framework employs a development research in mass loss as shown in Figure 3.5. The main purpose of this phase was to measure the durability performance of GO-blended mortar using analytical assessment of Faraday's Law equation, specifically as structural damage sustained by the rebar. This significantly leads to a better understanding of GO as an additive nanomaterial as a protective barrier against corrosive environment. Therefore, this phase focusses on the equation of mass loss with several parameters that required to be obtained such as Time to Depassivation (T_{HCP}), Active Corrosion Time (t) and Total Corrosion Current (I). Not only that but from the calculated mass loss for each sample also then serves as deriving an Average Nominal Area (A_{loss}). This step allows this study to move from general understanding of GO in cement matrix towards a specific structural assessment. Therefore, this research adopts an integrated framework, visually shown in Figure 3.6, which includes all phases of the study. Moreover, the overall type of testing and standard method can be visualized in Table 3.3.

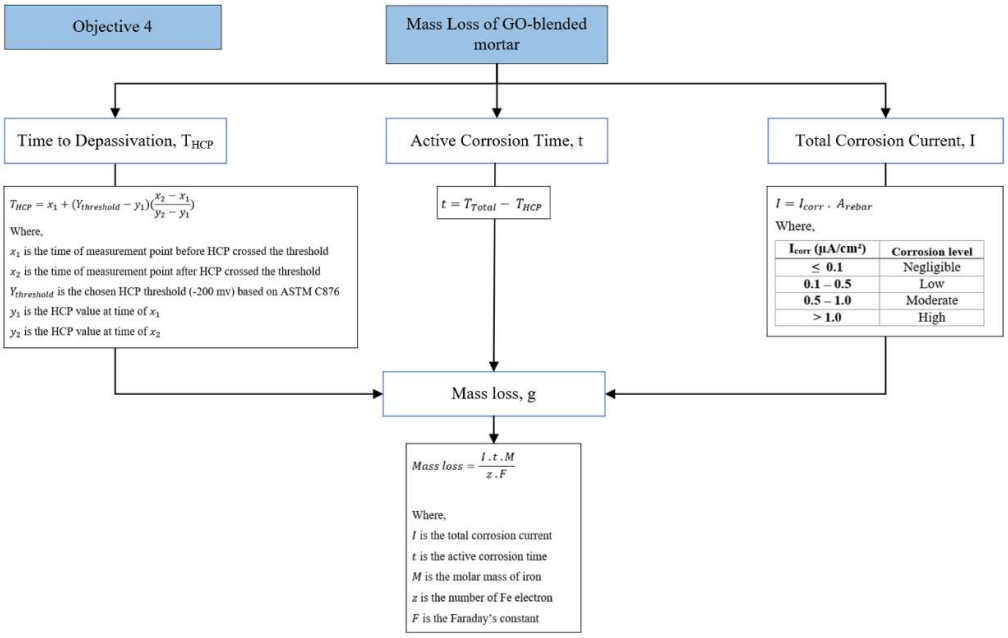


Figure 3.5 Mass loss of GO-blended Mortar

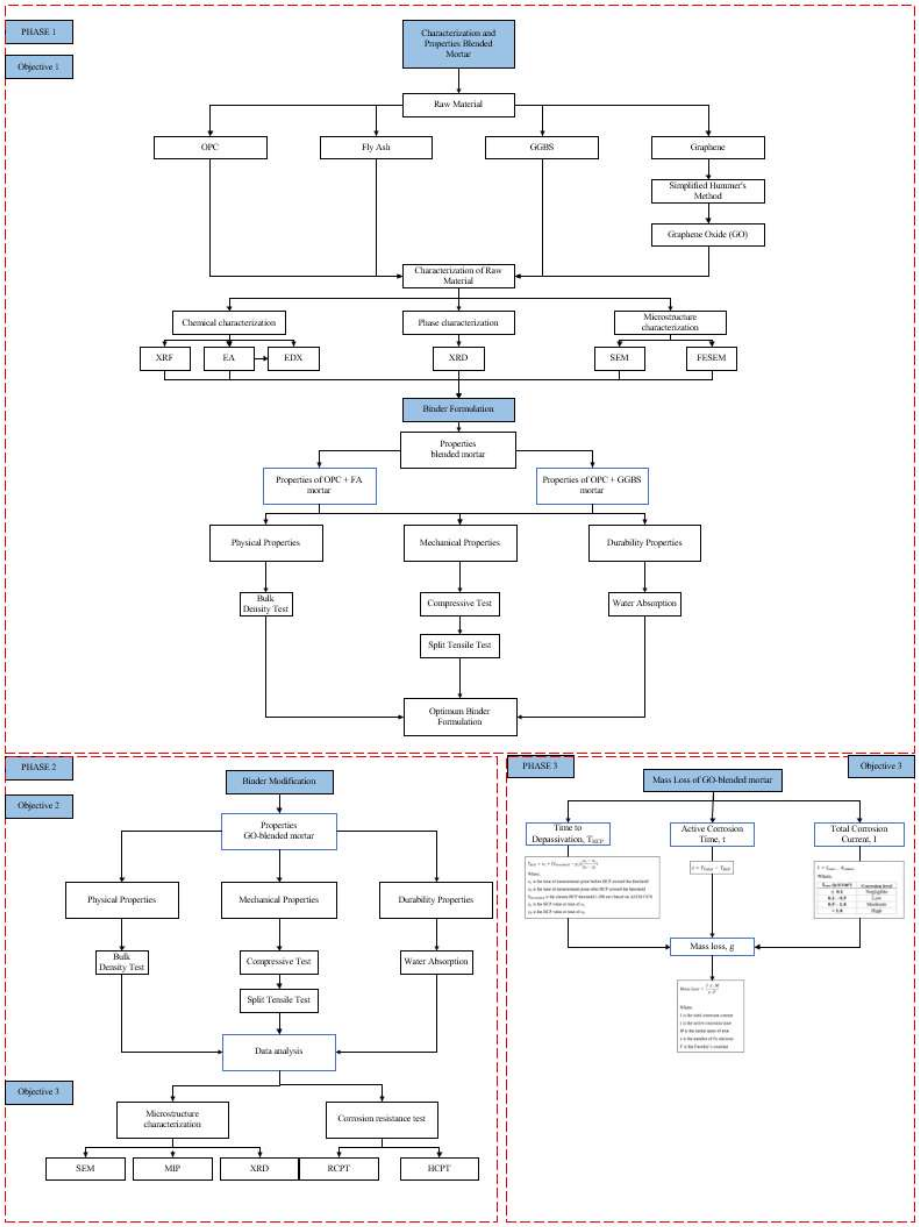


Figure 3.6 A Comprehensive Research Framework

Table 3.3
Type of Testing Methods and Standards

Properties	Type of Testing	Standard Method	No. of samples (s)
Phase 1 : Characterisation of Raw Material and Blended Mortar Properties			
Chemical Characterisation	XRF	PR	3
	EDX	PR	3
	EA	PR	2
Phase Characterisation	XRD	PR	4
Microstructure Characterisation	FESEM	PR	1
	SEM	PR	4
Physical Properties	Density	ASTM C138 (2017)	63
Mechanical Properties	Compressive Strength	ASTM C109 (2016)	63
	Tensile Strength	ASTM C496 (2017)	63
Durability	Water Absorption	ASTM C642 (2021)	63
Phase 2 : Properties of blended mortar incorporating with GO against corrosion			
Physical Properties	Density	ASTM C138 (2017)	54
Mechanical Properties	Compressive Strength	ASTM C109 (2016)	54
	Tensile Strength	ASTM C496 (2017)	54
Durability Properties	Water Absorption	ASTM C642 (2021)	54
Microstructure Characterisation	MIP	ASTM D4404 (2018)	5
	SEM	PR	5
	XRD	PR	6
Corrosion Resistance Test	RCPT	ASTM C1202 (2022)	18
	HCP	ASTM C876 (2015)	36
Phase 3 : Mass Loss of GO-blended mortar			
This phase was justified by mass loss equation via Faraday's Law.			

***Note: PR is referred to previous research of standard method**

3.3 The Simplified Hummer's Method Synthesis

Initially, the GO was primarily synthesise from its parent's derivative which is graphene where it was obtained from a high-quality petroleum coke which contains an enormous amount of carbon material, low sulphur, low porosity, and even low ash. However, as the requirement of the research, graphene needs to be synthesised into GO under detailed method. GO can be considered a non-conductive hydrophilic carbon-based material which relies on its degree of oxidation. Commonly, it is produced from Hummer's method or bottom-up methods whereby GO able to obtain chemical exfoliation of the root derivatives of graphene. However, despite the uncommon use of the bottom-up method due to high cost, it is still being implemented in the production of GO at laboratories. On the other side, Hummer's method has been famously known for using the top-down approach which gives higher oxidation results. This directly leads to a higher degree of oxidation on the GO surfaces and consequently compromises a better synthesis of oxygen-functional group-based material. Therefore, the simplified Hummer's method was used to produce GO with sufficient oxidation properties which could be worthy of attention as inclusion in cementitious matrix material. Thus, the procedure of Simplified Hummer's method can be shown Figure 3.7 and as follow:

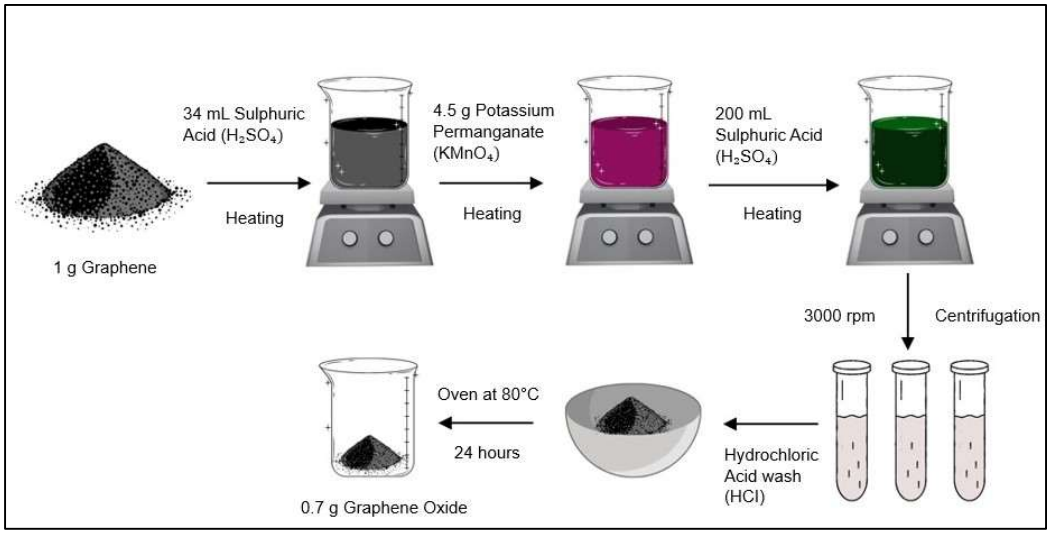


Figure 3.7 Schematic Diagram of Simplified Hummer's Method

i. 1 g of graphene is added to 34 mL of sulphuric acid and kept stirred for 30 minutes. Temperature is maintained below 5°C.

ii. 4.5 g potassium permanganate is added slowly to the mixture within 30 minutes while the temperature is kept maintained below 5°C.
iii. 200 mL of 5% sulphuric acid is slowly added to the mixture followed by 200 mL of 6% hydrogen peroxide to stop the reaction. The mixture was continued stirred for another 2 hours.
iv. Then, the mixture solution was washed three times using 10% of hydrochloric acid by centrifugation with speed 3000 rpm for 10 minutes.
v. The excess solution was removed, and the GO produced were collected. The GO was transferred to a petri dish and dried in oven for 24 hours at temperature 80°C.

3.4 Characterisation of Raw Materials

This section describes a crucial process known as material characterisation whereby it includes the microstructure of the raw material using a variety of techniques and analytical methods.

3.4.1 X-ray Fluorescence (XRF)

X-ray fluorescence (XRF) spectroscopy can be described as a non-destructive method which quantitively determines the elemental compositions of involved materials which were OPC, fly ash, GGBS, and graphene oxide (GO). This method helps to analyse the characteristic secondary of (fluorescent) X-rays emitted when these materials were radiated with a primary X-ray beam. This shall identify the element present in each material along with spectroscopic analysis conducted in Chemical Faculty of UiTM as shown in Figure 3.8. Nevertheless, XRF was stagnant in revealing crystalline phases within the raw materials, requiring further techniques such as XRD for structural information.



(i) (ii)

Figure 3.8 XRF Apparatus at Faculty of Chemical in UiTM

3.4.2 Elemental Analyser (EA)

The Elemental Analyser (EA) is a process of determining the quantitative presence of carbon (C), hydrogen (H), nitrogen (N), and oxygen (O) content. The main purpose of this analysis was to determine the elemental composition of carbon-based materials such as graphene and GO particularly in identifying the oxygen-to-carbon ratio in graphene oxide. This is crucial in proving the degree of oxidation during the synthesis of GO has been achieved. Not only that but it is valuable in understanding the fundamental structure and purity of these materials as it benefits the properties of blended mortar.

3.4.3 Energy-Dispersive X-ray Spectroscopy (EDX)

Energy-dispersive X-ray spectroscopy (EDX) can be described as a surface analytical technique that requires an electron beam projected to the samples and causes the formation of an electron-hole located in the electronic structure of the element. In relation to SEM, this test can provide insight of material composition as well as structures. It is also commonly used for early detection analysis and characterisation processes.

3.4.4 X-ray Diffraction (XRD)

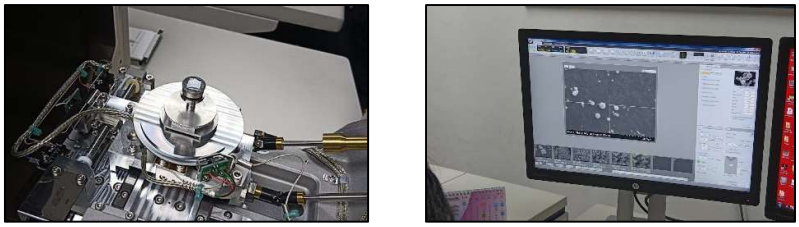
X-ray diffraction (XRD) can be defined as a rapid and powerful non-destructive technique used which helps to determine the crystalline phases of material. This test also could provide deeper information on the chemical composition, structural parameters as well as preferred crystal orientation. Therefore, there were four samples

prepared for the test for each material which were OPC, fly ash, GGBS and GO. Technically, the procedure for this test started with preparing a small amount of powder sample and placed on the diffractometer's holder. Next, the sample was scanned in the diffraction angle between 0° to 80° theta scale.

3.4.5 Scanning Electron Microscopy (SEM)

Scanning Electron Microscopy or known as SEM analysis is an instrument that provides high-resolution images using electrons beam in order to investigate the microstructure and chemistry of a range of materials. Not only that but the images obtained from SEM are useful for evaluating surface fractures, corrosion, shape as well as flaws of raw materials. Therefore, this study conducted SEM analysis on four materials of OPC, fly ash, GGBS and GO. The details of the test procedure are explained below with reference to Figure 3.9.

i. Samples were sowed onto double-sided adhesive and attached to metal stubs.
ii. Specimen preparation included a pre-coating process using a gold sputter coater.
iii. SEM analysis was performed to examine surface morphology, with magnification levels optimized for maximum detail.



(i) (ii)

Figure 3.9 Test Apparatus Used for Morphology Analysis Using SEM

3.4.6 Field Emission Scanning Electron Microscopy (FESEM)

Field emission scanning electron microscopy (FESEM) stands as a high-resolution microstructure analysis technique, offering superior image quality for material visualisation. Typically, FESEM has been conducted under a high vacuum to ensure minimum interference of gas molecules with the electron beam. Moreover, FESEM also operates by identifying secondary and backscattered electrons that have been emitted from the surface's sample upon beam radiation. The test procedure of FESEM was similar with the previous morphology testing of SEM but with the enhancement of a high-magnification image that reveals the detailed topography and surface morphology of the material. Therefore, FESEM was used to investigate the surface characteristics of GO.

3.5 Properties of Blended Mortar and GO-Blended Mortar

This study investigates the impact of a two-major approach on the properties of mortar which were binder formulation and subsequent binder modification. The binder formulation focussed on optimizing the selection of supplementary cementitious material (SCMs), particularly fly ash and GGBS, to create a blended mortar. This phase of the study demonstrates the enhanced performance and efficiency of SCMs in blended mortar. Moreover, the properties of these blended mortars were assessed differently in the replacement percentage (10%, 20% and 30%) and control in order to identify the optimum binder formulation that portrays desirable overall performance.

Based on the optimized binder formulation, binder modification involves the incorporation of graphene oxide (GO) at various percentages dosages to propose the GO-blended mortar. This phase investigates the potential of carbon-based materials such as GO to further the mechanical and durability performance of existing blended mortar. This shall reveal the behaviour of GO within the cementitious matrix due to its high surface area and other performance parameters. Henceforth, the subsection introduced the properties of both blended mortar that following developed through binder formulation and binder modification.

3.5.1 Mix Proportion of Blended Mortar (Binder Formulation)

The binder formulation of this study involved the development of blended mortars with supplementary cementitious material (SCMs) which were OPC, fly ash, GGBS and sand as shown in Figure 3.10. Therefore, the cement replacement varies at different percentages of total binder content, specifically at 0%, 10%, 20% and 30% per binder with a consistent water-cement ratio of 0.5 constant in all mixes. In addition, the binder sand ratio was 1:3 was used according to ASTM C109 throughout the study. Therefore, the Table 3.4 shows mix design and the involved materials for the binder formulation in the study.



(i) Ordinary Portland Cement



(ii) Ground Granulated Blast Furnace Slag



(iii) Fly Ash



(iv) Sand

Figure 3.10 Materials for Binder Formulation

Table 3.4
Mix Proportions of Binder Formulation (Phase 1)

Mixtures	Water	Cement	Fly Ash	GGBS	Sand
	(kg/m^3)	(kg/m^3)	(kg/m^3)	(kg/m^3)	(kg/m^3)
REF	800.0	1600	-	-	4800
10F	800.0	1440	160	-	4800
20F	800.0	1280	320	-	4800
30F	800.0	1120	480	-	4800
10S	800.0	1440	-	160	4800
20S	800.0	1280	-	320	4800
30S	800.0	1120	-	480	4800

3.5.2 Mix Proportion of GO-Blended Mortar (Binder Modification)

In the binder modification stage, graphene oxide (GO) was introduced as a nanomaterial additive to the optimized blended mortar. The formulation also utilized 30% GGBS (30S) as the primary binder replacement. This specific dosage was selected because, during the initial binder formulation phase, the 30S mix achieved the most superior results across all tested parameters compared to other replacement levels. Therefore, various percentages of GO specifically 0.02%, 0.04%, 0.06%, 0.08%, and 0.10% by weight of the binder and constant water-cement ratio of 0.5. The utilization of PCE-based superplasticizer from Sika also has been introduced with 0.02% per binder to smoothen the dispersion of GO within the blended mortar. The main purpose of the PCE usage was to enhance the dispersion of GO within the blended mortar, as it is recommended by previous researchers. Bhojaraju et al., (2023) suggested that the range of PCE used in GO's cementitious material is within the range of 0.02% and 0.06% per total binder. The adding of PCE also shall create a greater dispersion for GO when mixing with other cementitious based materials and reducing the tendency of agglomeration (Son et al., 2023). Moreover, the properties of these GO-blended mortars were evaluated based on different testing to determine the effectiveness of GO within the cementitious matrix. Therefore, the main material and mix proportion for the binder modification can be shown in Figure 3.11 and Table 3.5.



(i) Ordinary Portland Cement



(ii) Ground Granulated Blast Furnace Slag



(iii) Graphene Oxide



(iv) Sand



(v) PCE-based superplasticizer

Figure 3.11 Materials for Binder Modification

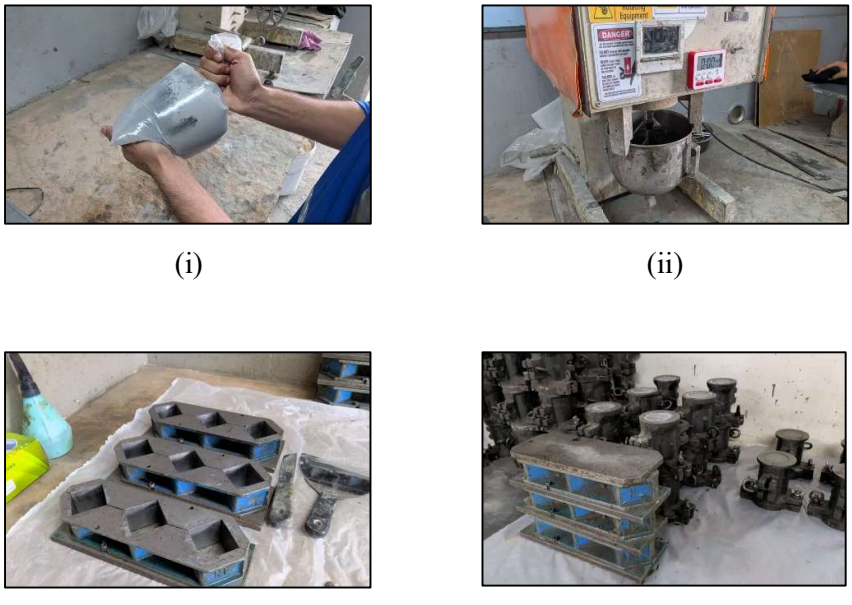
Table 3.5
Mix Proportion of Binder Modification (Phase 2)

Mixtures	Water	Cement	GGBS	Sand	PCE superplasticizer	Graphene Oxide
	(kg/m^3)	(kg/m^3)	(kg/m^3)	(kg/m^3)	(kg/m^3)	(kg/m^3)
30SG0	800	1120	480	4800	0.32	0.00
30SG2	800	1120	480	4800	0.32	0.32
30SG4	800	1120	480	4800	0.32	0.64
30SG6	800	1120	480	4800	0.32	0.96
30SG8	800	1120	480	4800	0.32	1.28
30SG10	800	1120	480	4800	0.32	1.60

3.5.3 Preparation of Binder Formulation and Binder Modification

The preparation of blended mortar was followed strictly by ASTM C595. There were two types of mixing in this study which included the binder formulation (Figure 3.12) and binder modification (Figure 3.13). As for the binder formulation, the preparation of specimens as follows:

i. The dry mix consisting Ordinary Portland Cement (OPC), selected SCMs, and fine aggregate was prepared and weighed according to desired mix proportion. Then, a short mix of 30 seconds was conducted to mix well the components of the binder.
ii. Then, design water was added to the bowl and mixed well with the dry mix binder with 3 minutes of control mixing to ensure a homogenous mixture.
iii. The preparation of moulds had been conducted beforehand, tightened, and cleaned under desirable conditions.
iv. Freshly blended mortar was poured into the mould and then compacted properly. The step was repeated three times until the mould was filled.



(i) (ii)

(iii) (iv)

Figure 3.12 Preparation of Binder Formulation

For the binder modification, the step to step preparation as follows:

i. The dry mix consisting Ordinary Portland Cement (OPC), GGBS, GO and fine aggregate was prepared and weighed according to desired mix proportion. Then, a short mix of 30 seconds was conducted to mix well the components of the binder.
ii. Then, design water was added to the bowl with PCE-based superplasticizer and mixed well with the dry mix binder with 3 minutes of control mixing to ensure a homogenous mixture.
iii. The preparation of moulds had been conducted beforehand, tightened, and cleaned under desirable conditions.
iv. Freshly GO-blended mortar was poured into the mould and then compacted properly. The step was repeated three times until the mould was filled.



(i)



(ii)



(iii)



(iv)



(v)

Figure 3.13 Preparation of Binder Modification

3.6 Physical Properties of Blended Mortar

The physical properties of blended mortar in this study can be obtained by conducting density test. The details of the test were briefly discussed and explained in the following paragraph.

3.6.1 Density Test

The density is described as mass per volume whereby the mass of blended mortar was measured by using a digital weighing scale. This parameter was measured followed the standard of ASTM C143. Therefore, the consistency of mortar production was measured from density and calculated by Equation 3.1:

$$\rho_c = \frac{W}{V} \tag{3.1}$$

W is the mass of cured mortar in gram (g)
V is the volume of cured mortar in cm^3

3.7 Mechanical Properties of Blended Mortar

The mechanical properties of blended mortar specimens in this research are achieved by conducting compressive and split tensile strength tests.

3.7.1 Compressive Strength Test

The compressive strength test was conducted based on the optimized blended mortar as well as the GO-blended mortar with various percentages of GO. Following the testing of 63 specimens for binder formulation and 63 specimens for binder modification cubes were tested on the mechanical performance according to ASTM C109 (2016). To be more precise, the compressive strength was calculated using Equation 3.2 with following test procedure in Figure 3.14:

$$F_c = \frac{F}{A} \tag{3.2}$$

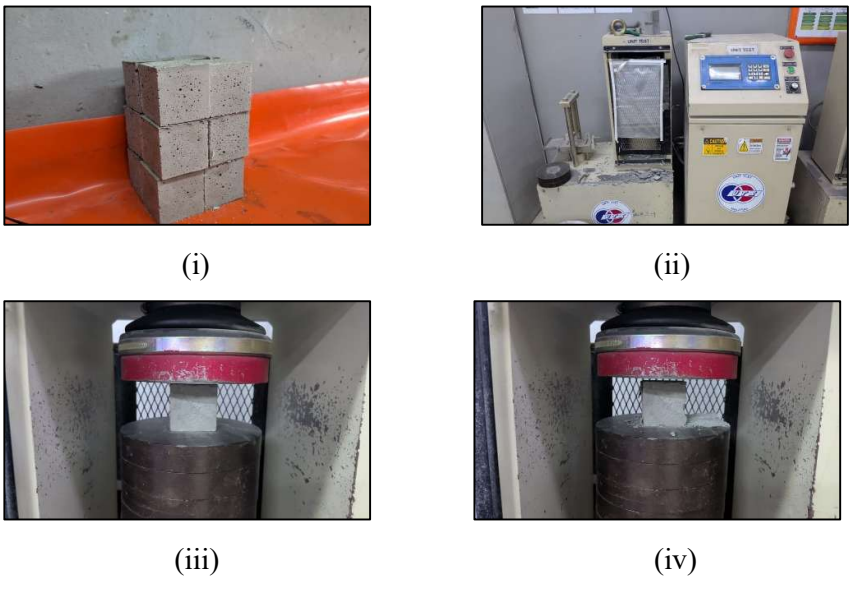
where,

F_c is compressive strength in MPa (N/mm^2)

F is maximum load in N; and

A is cross section of specimen in mm^2

i. The cubes of specimens with dimensions of 50 mm x 50 mm were prepared.
ii. The top and bottom surfaces of the cube were cleaned before being tested in the compression machine.
iii. Each specimen was placed centrally between the upper and lower bearing platens of the compression testing machine.
iv. A consistent rate of compressive load was applied to the specimens within the specified range of 2.0 kN/s as per advised in ASTM C109 (2016).
v. The average compressive strength was recorded and presented in the next chapter.



(i) (ii)

(iii) (iv)

Figure 3.14 Test Procedure of Compressive Strength Test

3.7.2 Split Tensile Strength Test

The tensile strength performance was evaluated through a split tensile test adapted from the standard of ASTM C496 (2017). In this study, a total of 63 specimens during binder formulation (Phase 1) and 63 specimens from binder modification (Phase 2) were assessed. This section presents the data on how the inclusion of blended mortar and GO affected the mortar's resistance against cracking when indirect tension is applied. To validate the data, an Equation 3.3 for split tensile strength was used;

$$f = \frac{2F}{\pi DL} \tag{3.3}$$

where,

f is splitting tensile strength in MPa

F is maximum load N

π is equal to 3.142

D is diameter of specimens in mm (50 mm) ; and

L is length of specimens in mm (100 mm)

i. The cured cylindrical specimens with dimensions of 50 mm in diameter and 100 mm were prepared.
ii. The test was conducted with a rated load of 2.0 kN/s.
iii. The tensile strength was calculated using Equation 3.3 as follows.
iv. The mode of failure was observed, and the data was recorded for further analysis.

3.8 Durability Properties of Blended Mortar

3.8.1 Water Absorption Test

The purpose of this test to determine the vulnerability of mortar against the penetration of water. Water absorption can be linked directly to porosity which eventually leads to the deterioration effect of mortar. Therefore, the test procedure was followed the specified in ASTM C642 (2021) as the detail of test procedure is:

i. The hardened blended mortar specimens were immersed in a water bath

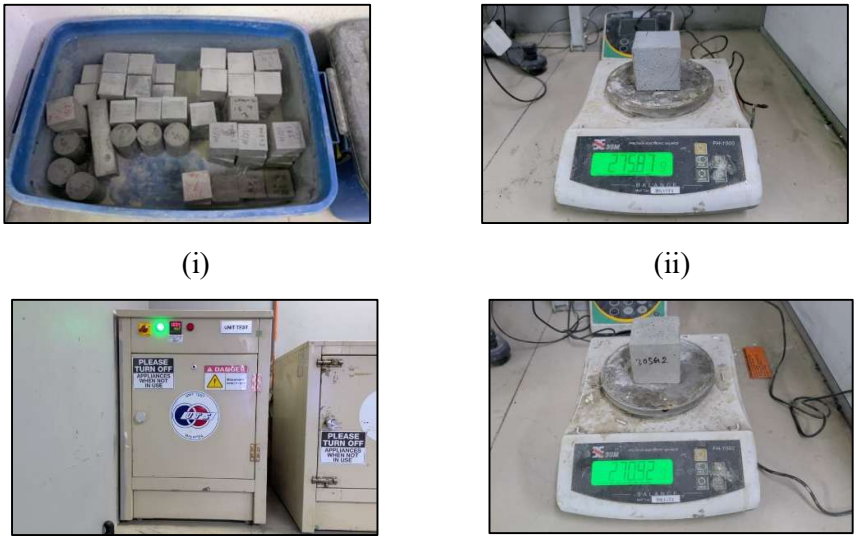
and kept submerged for 24 hours.

ii. After 24 hours, the wet specimens were drained and dried to every surface or known as surface-dried specimens as shown in Figure 3.15.

iii. The weight of specimens was recorded and labelled as B.

iv. The specimens were placed into the oven with a set temperature of 100 °C for 24 hours. Then, the weight of the specimens was recorded again after being taken out from the oven. Later then, the oven-dried mass specimens were designed as A.

v. The water absorption of the specimens was calculated using the formula in Equation 3.4.



(i) (ii)

(iii) (iv)

Figure 3.15 Test Procedure of Water Absorption Test

$$\text{Absorption} = \frac{B-A}{A} \times 100\% \quad (3.4)$$

where,

A is a mass of oven-dried specimens in g; and

B is a mass of surface-dried specimens after immersion in g

3.9 Corrosion Assessment of GO-Blended Mortar

The following sub-section will present the procedure and method for RCPT and HCP measurement of GO-Blended mortar.

3.9.1 Rapid Chloride Resistance Test (RCPT)

The main purpose of RCPT on hardened blended mortar specimens was to identify the capacity of chloride ions to penetrate the specimens. This test also evaluates the rapid indication of the blended mortar's permeability against chloride ions by allowing a comparative assessment of durability performance for each mix design. Thus, the results obtained for this test were used as a reference to the long-term durability characteristics and properties of the GO-blended mortar specimens. This test was conducted based on ASTM standard C1202-22 which provides a guideline procedure for measuring the electrical flow of mortar which is ultimately related to chloride ion penetration resistance as shown in Figure 3.16.

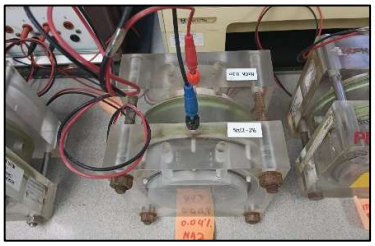
i. A total of 18 blended mortar specimens were cast in a cylindrical mould with a diameter of 100 mm of diameter and 50 mm of height based on ASTM C1202 (2022). The specimens were placed in water curing and prepared for testing.
ii. A 50 mm thick slice of each specimens was obtained and coated with an epoxy to prevent current flow and thus chloride ions through any other surface than the circular faces.
iii. The test setup consisted of two major compartments where one compartment was filled with a 3.0 sodium chloride (NaCl) solution. The other compartment was filled with 0.3N of sodium hydroxide (NaOH) solution.
iv. The specimens were placed in between those two compartments with a tight seal to ensure zero leakage of the solutions.



(i)



(ii)



(iii)

Figure 3.16 Test Procedure of Rapid Chloride Penetration Test

Based on ASTM C1202 (2022), a 60 V DC potential difference was applied for each specimens with an interval of 30 minutes for electrical current passing measurement of an overall 6-hour test duration. The total charge passed obtained was a primary indicator of the blended mortar's resistance against chloride ion penetration. Henceforth, the results were analysed based on chloride ion penetrability range provided in ASTM C1202 (2022) as shown in Table 3.6.

Table 3.6
Chloride Ion Penetrability Range (ASTM C1012-22)

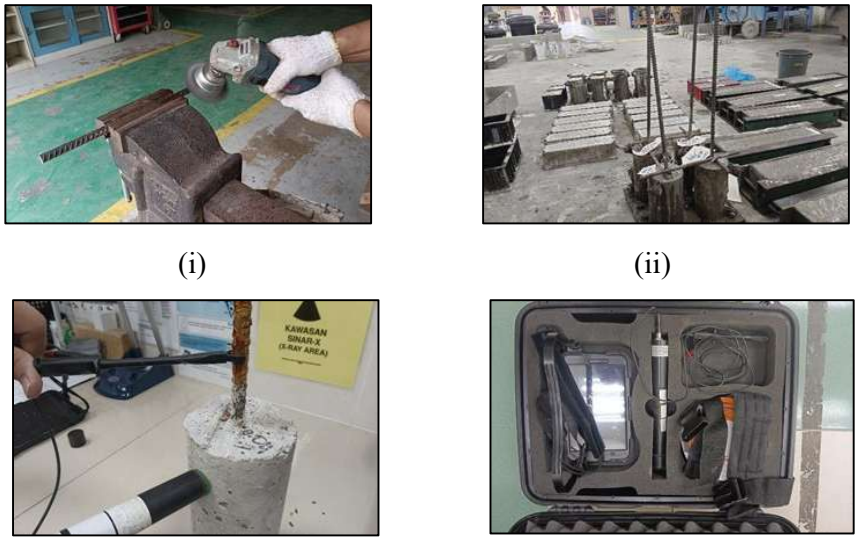
Charge passed (Coulombs)	Chloride Ion Penetrability
> 4000	High
2000 – 4000	Moderate
1000 – 2000	Low
100- 1000	Very Low
< 100	Negligible

3.9.2 Half Cell Potential Test (HCP)

The primary purpose of the Half Cell Potential Test (HCP) was to evaluate the corrosion activity towards the reinforcing steel embedded within the GO-blended mortar specimens. This test provides insightful information on the electrochemical condition of the reinforced steel which directly indicates the durability properties of the GO-blended mortar. The HCP was conducted based on the followed standard of ASTM

C876-15 as it provides a standardized procedure of electrical potential measurement as shown in Figure 3.17.

i. The steel rebar was polished using a steel grinder disc to remove existing corrosion and smooth the surface.
ii. A total of 36 GO-blended mortar specimens were cast in 100 mm diameter x 200 mm with an embedded steel bar of 12 mm diameter and 305 mm of length as shown in the schematic diagram of Figure 3.18. The specimens were then cured in two curing condition of normal curing and 5% NaCl solution of saltwater curing adapted from ASTM C1012. The specimens were set to be tested for 30, 60 and 90 days of curing.
iii. The test setup consisted of a copper sulphate electrode, connecting wires and a high-impedance voltmeter. The voltmeter was later connected between the electrode and the connection to the reinforcing steel.
iv. The reference electrode was placed at random locations on the surface of the blended mortar specimens as each location provided readings of the half-cell potential (HCP).
v. The readings were recorded and organised for results and discussion.



(i) (ii)

(iii) (iv)

Figure 3.17 Test Procedure of Half Cell Potential Test

The half-cell potential readings were analysed based on

Table 3.7 in accordance with ASTM C876-15. Therefore, following this procedure, it tends to provide crucial data for durability and performance assessment of GO-blended mortar against corrosion activity.

Table 3.7
Corrosion Condition Related to Half Cell Potential (ASTM C876-15)

E_{corr} vs CSE	Corrosion Condition
$E_{corr} > -200$	Low (10% of risk corrosion)
$-200 > E_{corr} > -350$	Intermediate corrosion risk
$-350 > E_{corr} > -500$	High (<90% of risk corrosion)
$E_{corr} < -500$	Severe Corrosion

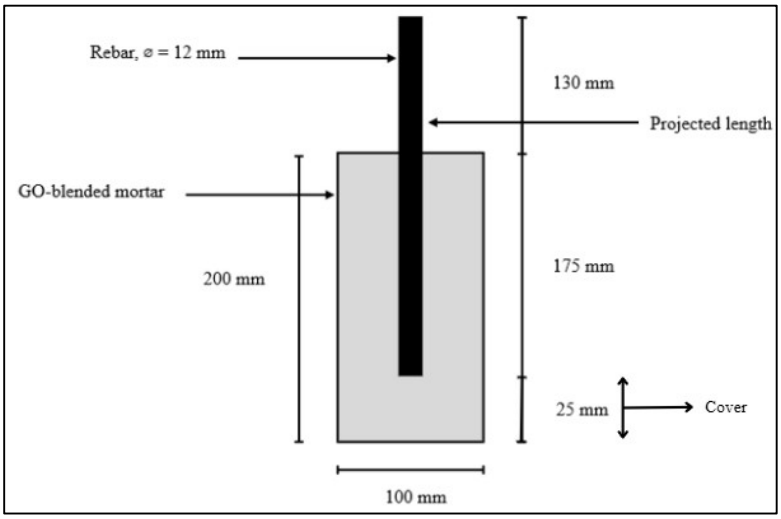


Figure 3.18 Schematic Diagram of Rebar GO-blended Mortar Specimens

3.10 Porosity and Microstructure Properties

The microstructure properties of GO-blended mortar specimens were studied under Mercury Intrusion Porosimetry (MIP) and Scanning Electron Microscopy (SEM). The details for each test were explained in the following sub-section.

3.10.1 Mercury Intrusion Porosimetry (MIP)

Mercury Intrusion Porosimetry (MIP) can be defined as a method to study the pore characteristics of materials by injecting mercury into the pores under certain pressure. This shall help to provide an understanding of the pore size distributions, porosity and even total pore volume which are significantly related to the durability properties of the blended mortar specimens. The standard used for this test was based on ASTM D4404 (2018) which outlines the related guideline for finding the pore volume and distribution in soil and rock, but it can also be used for mortar.

i. The sample preparation for this test requires small pieces from each sample within 5 mm in size. The samples were also required to be between 3.5 and 4.5 g.
ii. The samples were dried to remove any excess moisture on the surface and placed in a special holder called a penetrometer.
iii. A thin layer of grease was applied to the flange of the penetrometer and sealed.
iv. The weight of the sample and penetrometer was recorded using a balance.
v. Then, mercury was introduced through the funnel as the pressure gradually increased into the MIP instrument as shown in Figure 3.19.
vi. As the pressure increases, the mercury tends to enter smaller and smaller pores into the mortar. Once completed, the penetrometer was removed from the holder.
vii. The data was recorded for further analysis and discussion.



Figure 3.19 Apparatus of Mercury Intrusion Porosimetry (MIP) in UiTM

Moreover, based on the MIP test report, a porosity value can also be achieved for every sample with skeletal density and total intrusion volume. The calculation for the porosity used the following Equation 3.5:

$$\Phi = \frac{Vintrusion\ x\ P}{1+Vintrusion\ x\ P}\ x\ 100\% \tag{3.5}$$

where,

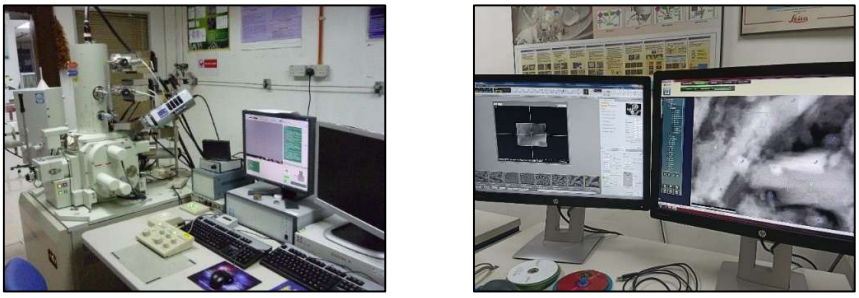
Φ is the total porosity value in %;

$Vintrusion$ is the total intrusion volume in mL/g; and

P is the skeletal density in g/mL

3.10.2 Scanning Electron Microscopy (SEM)

Following the completion of the Mercury Intrusion Porosimetry (MIP) analysis, the selected crushed mortar samples were further ground into finer sizes to ensure a clear representative image when subjected to SEM. Therefore, samples were collected and tested in UiTM facilities as shown in Figure 3.20.



(i) (ii)

Figure 3.20 SEM Machine at Faculty of Mechanical Engineering laboratory

3.10.3 X-ray Diffraction (XRD)

To validate the occurrence of cement hydration and characterize the resulting phase transformations, X-ray diffraction (XRD) analysis was systematically conducted on every specimen of the GO-blended mortar.

3.11 Mass Loss of Faraday's Law

This final phase of the study measures the parameters required to calculate mass loss (m) via Faraday's Law to quantify structural corrosion damage. The time to depassivation (HCP) is derived from Half-Cell Potential (HCP) data, which defines the non-corroding initiation period. This initiation period is then used to establish the active corrosion time (t) for each sample. Finally, mass loss (m) is determined by integrating the active corrosion time (t) and the total corrosion current (I), serving as the definitive measure of structural damage. Therefore, the mass loss was a direct consequence of the electrochemical reaction, which was quantified using Faraday's Law as shown in Equation 3.6:

$$Mass\ loss = \frac{I\ .t\ .M}{z\ .F} \tag{3.6}$$

where,

I is the total corrosion current

t is the active corrosion time

M is the molar mass of iron

z is the number of Fe electron

F is the Faraday's constant

CHAPTER 4
RESULT AND ANALYSIS

4.1 Introduction

This chapter outlines the findings and subsequent analysis of the experimental work, encompassing the fulfilment of each objective specified within the study.

4.2 Characterisation of Raw Material

This sub-section discussed on comprehensive characterisation of raw material in the study.

4.2.1 X-ray Fluorescence (XRF)

4.2.1.1 OPC

Regarding the XRF analysis for Ordinary Portland Cement (OPC), the chemical composition was analysed and determined by conducting XRF as depicted in Table 4.1. The main purpose of OPC acted as the primary cementitious materials during mortar hydration process. According to 36.65% of the total composition owned by CaO. This high concentration of CaO was crucial for the formation of Calcium Silicate Hydrate (C-S-H) gels, which represent the main product of mortar matrix strength and biding properties. On top of that, the second composition identified as Silica (SiO_2) and Alumina (Al_2SiO_3) at concentrations of 4.36% and 1.43%, respectively. Last but not least, the recorded presence of Iron Oxide (Fe_2O_3) and Magnesia (MgO) assisted in maintaining the chemical stability of the binder.

Table 4.1
XRF Analysis Data of OPC Composition

Chemical Composition	Percentage %
Silica (SiO_2)	4.36
Alumina (AI_2O_3)	1.43
Calcium Oxide (CaO)	36.65
Iron Oxide (Fe_2O_3)	1.78
Magnesia (MgO)	1.72

4.2.1.2 Fly Ash

As for the XRF analysis for fly ash, this fly ash was classified as fly ash Class F according to ASTM C618. Technically, the utilization of fly ash as supplementary cementitious material can be considered a worldwide material due to the pozzolanic reaction provided during the mixing process. As mentioned in the Table 4.2, it is worth stating that the composition of fly ash indicates that there are 2 dominant reading which was Silica (SiO_2) by 59.49% and Alumina (Al_2SiO_3) by 20.00% content which complement well with OPC. On top of that, high silica (SiO_2) could potentially help in providing a greater interlocking mechanism in the cement matrix. Meanwhile, Alumina (Al_2SiO_3) plays a significant role towards the fast setting of the cement matrix.

Table 4.2
XRF Analysis Data of Fly Ash Composition

Chemical Composition	Percentage %
Silica (SiO_2)	59.49
Alumina (AI_2O_3)	20.00
Calcium Oxide (CaO)	8.74
Iron Oxide (Fe_2O_3)	4.13
Magnesia (MgO)	2.94

4.2.1.3 GGBS

Based on the XRF analysis in Table 4.3, it has been proved that GGBS consist of similar important composition which can act as substitute material in cement which was Silica (SiO_2), Alumina (Al_2SiO_3), Calcium Oxide (CaO) and Iron Oxide (Fe_2O_3). Nevertheless, it can be seen that GGBS has the highest reading on Calcium at 37.22% followed by Silica at 35.85%. Basically, the role of calcium in cement matrix was to introduce a greater strength during the hydration process. The major hydration product in Ordinary Portland Cement (OPC) was calcium silicate hydrate (C–S–H) whereby calcium preferentially chemically binds with the silicate during the reaction of Silica and water (Munjal et al., 2021). This eventually produces a form of stable C-S-H products and dictates the hardening process of the material itself. Therefore, this differentiates the chemical composition between GGBS and fly ash in this study even though they carried the same purpose of SCMs in the cement matrix.

Table 4.3
XRF Analysis Data of GGBS Composition

Chemical Composition	Percentage %
Silica (SiO_2)	35.85
Alumina (AI_2O_3)	14.90
Calcium Oxide (CaO)	37.22
Iron Oxide (Fe_2O_3)	7.77
Magnesia (MgO)	3.55

4.2.1.4 Graphene Oxide

The XRF analysis in Table 4.4 shows the chemical composition of GO. It can be stated that GO consists of a major element in cement which can contribute to the strength development in a certain way. Based on the data, the highest reading can be found for Silica oxide (SiO_2) as it shows 62.93% followed by Calcium Oxide (CaO) by 11.71%. Therefore, an adequate amount of these compounds shall lead to a greater hydration reaction which eventually leads to a perfectly form hydration product.

Table 4.4
XRF Analysis Data of GO Composition

Chemical Composition	Percentage %
Silica (SiO_2)	62.93
Alumina (AI_2O_3)	0.81
Calcium Oxide (CaO)	11.71
Iron Oxide (Fe_2O_3)	0.39
Magnesia (MgO)	10.01

4.2.2 Elemental Analyser (EA)

This elemental analysis serves as primary evidence for the successful synthesis of GO using the simplified Hummer's method. The comparison between the two materials reveals a significant chemical addition which notably introduced of oxygen elements as shown in Table 4.5. The synthesized GO exhibited an oxygen content of 21.22%, with carbon remaining the major element at 48.80%. This high carbon to oxygen ratio indicated 2.3 ratio which defines a significant oxidation process created to the surface of the GO. In addition, the hydrogen element also increased from 0.47% 1.07%, confirming the attachment of oxygen functional groups to the carbon element. These oxygen molecules tend to occupy the spaces in between the carbon molecules, resulting in increase of interplanar spacing (Suo et al., 2022).

Table 4.5
Elemental Analysis of Graphene and GO

Raw material	Carbon (%)	Oxygen (%)	Hydrogen (%)	Nitrogen (%)	Sulphur (%)
Graphene	36.98	-	0.47	0.03	0.14
GO	48.80	21.22	1.07	0.04	0.15

4.2.3 X-ray Diffraction (XRD) Analysis

4.2.3.1 OPC

The initial XRD data have been recorded and interpreted using Origin software. Origin is a computer program that helps with interactive scientific graphing and data analysis. Thus, the XRD data has been neutralised for noise reduction by using X'pert Highscore software, which is similar to Origin. However, X'pert Highscore's primary target is the phase identification of material, which also adds to the crystallographic analysis. Figure 4.1 managed to identify several key mineral phases, including Calcium Silicate (CS), Tricalcium Aluminate (TA), Calcite (CC), and Gypsum (G). The presence of CS was solid evidence by distinct peaks within 18° and 39° at 2θ, which represents a long-term strength development of the blended mortar. This reflects the results of XRF analysis, which indicates a Calcium (CaO) content of 36.65% and Silica (SiO_2) content of 4.36%. Moreover, the XRD pattern also reveals a significant peak for Calcite (CC) at 26°, followed by Gypsum, which was added to regulate the hydration alumina phases (Meng et al., 2021). Thus, these phases also confirmed that the OPC provides a chemically stable and highly alkaline environment.

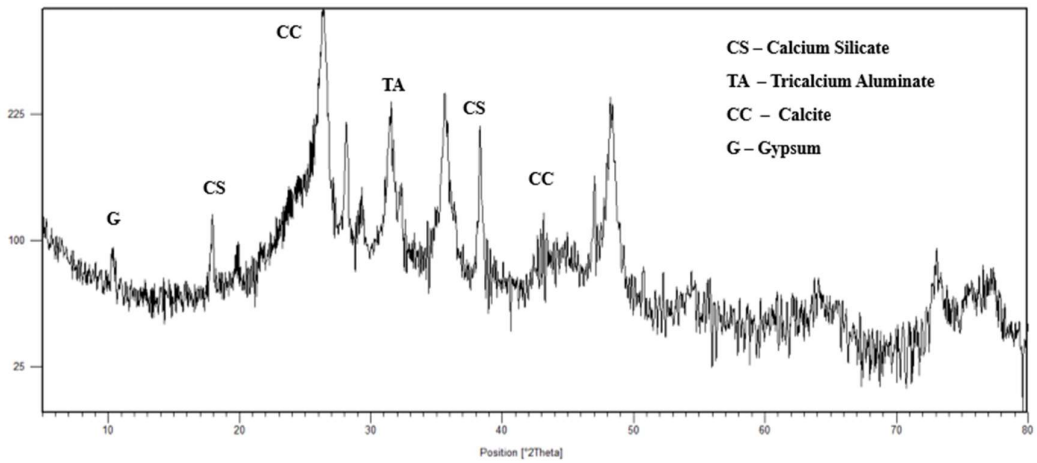


Figure 4.1 XRD Pattern of OPC in X'pert Highscore

4.2.3.2 Fly Ash

The XRD analysis for fly ash was also being interpreted by using X'pert Highscore, as it can reduce layers of noise from the original sources. As visualized in Figure 4.2, the fly ash exhibited a major crystalline phase as it was dominated by dominant presence of Quartz (Q) and Mullite (M). Theoretically, the existence of these mineral phases reflected the composition of fly ash itself, where it consists of Calcium Oxide (CaO), Silica (SiO_2), and Alumina (Al_2O_3). These chemical compositions are responsible for the formation of Calcium Silicate Hydrates (C-S-H) gel during the cement hydration process. Moreover, as in comparison to GGBS, the fly ash pattern showed a smaller amorphous indicating a lower glass content. This difference in amorphicity directly influences the reactivity of supplementary cementitious materials (SCMs) within the blended matrix.

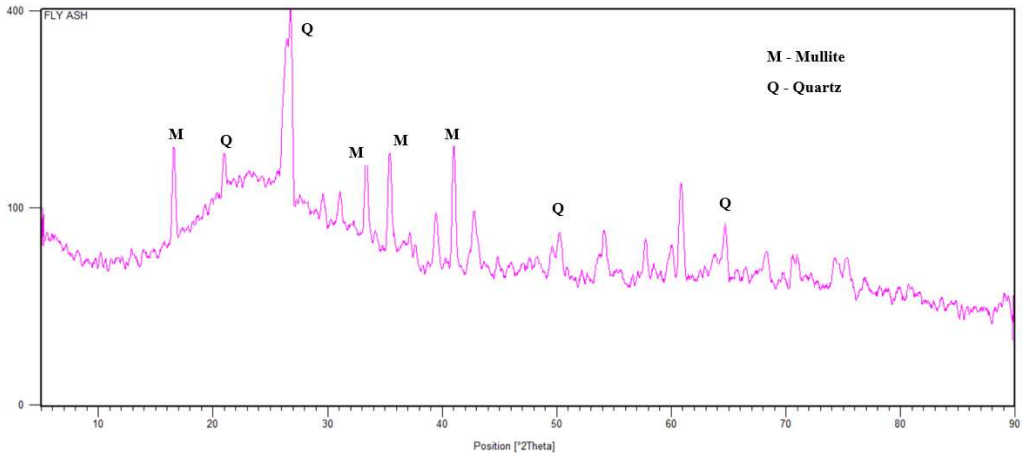


Figure 4.2 XRD Pattern of Fly Ash in X'pert Highscore

A high-magnification analysis of fly ash can be seen in Figure 4.3. As mentioned in the previous discussion, the crystalline phases peak was identified as Quartz (Q), located at 2θ= 26.79° along with spacing between the plane (d)= 3.32 A. This significantly represents a stable silica fraction in the dominant crystalline element. On top of that, the second-highest peak determined was Mullite (M), at 2θ= 33.38° with an interplanar spacing of 2.68 A. The existence of Mullite is a critical indicator of material's thermal as it forms during high temperatures due to combustion process of clay minerals.

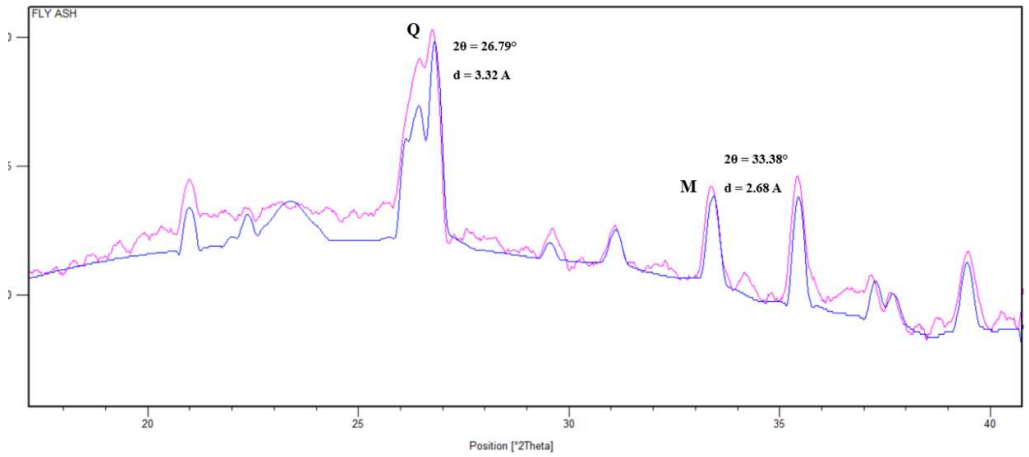


Figure 4.3 Peak Value for Fly Ash Pattern

4.2.3.3 GGBS

As computed by X'pert Highscore software, the XRD pattern for GGBS has been determined in this research. Based on Figure 4.4, it can be interpreted that GGBS primarily consist of an amorphous phase, specifically as in glassy features. This aligns with the finding reported by Siddique and Bennacer (2012) where the glassy nature of GGBS is responsible for the reaction with cementitious-based material. Nevertheless, GGBS also owns the crystalline phase, but the chemical energy is lower compared to the amorphous phase. The figure shows that the GGBS prominent peaks can be identified as Gehlenite (G) as well as Akermanite (A). Not only that, but the presence of Calcite (C) was also observed in the XRD analysis figure. Generally, these minerals mainly provide the essential Calcium Oxide (CaO), Silica (SiO_2), and Alumina (Al_2O_3) required for the cement hydration reaction as well as the pozzolanic reaction within the blended mortar matrix. Furthermore, the minerals in GGBS are primarily calcium-alumino-silicates, which play a direct role in producing the Friedel's salt compared to the crystalline silica obtained from the fly ash (Aydoğan et al., 2025).

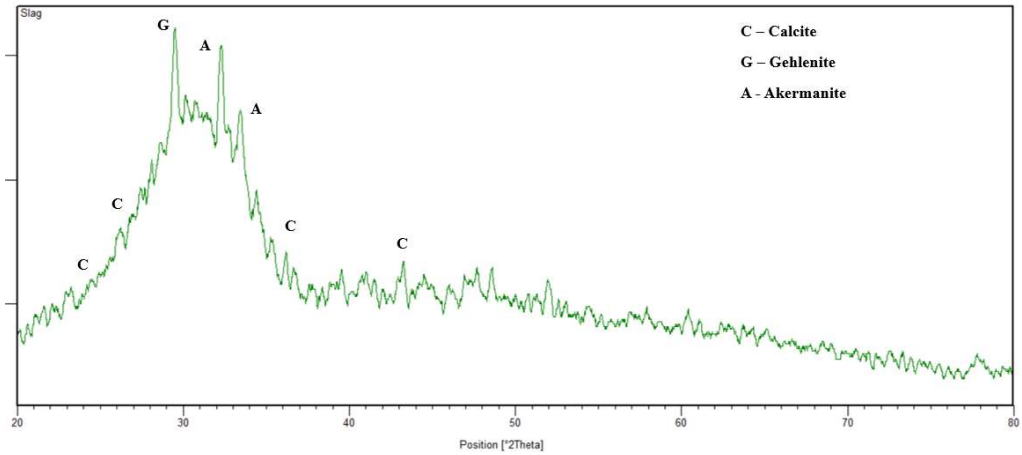


Figure 4.4 XRD Pattern of GGBS in X'pert Highscore

As illustrated close up XRD image of the GGBS in Figure 4.5, the primarily diffraction peak was identified as Gehlenite (G) located at 2θ= 29.43° with the spacing between the plane of 3.03 A. The second major peak indicates Akermanite (A), at 2θ= 32.30° with a d-spacing of 2.77 A. The concentration of calcium alumino silicates phase was profound as the solid answer towards calcium silicate hydrates (C-S-H) gel formation within the matrix. In addition, the XRD pattern also shows prominent glassy features or also known as the amorphous phase. This might have happened due to the rapid cooling rate of the molten slag during the production of the GGBS itself (Shahas et al., 2022).

In comparison with fly ash, both of these materials share a similar behaviour as they served the role as supplementary cementitious material (SCMs). Nevertheless, the GGBS mineral composition tends to have a higher amorphous phase compared to the fly ash, indicating a higher potential to provide denser secondary cement hydration when reacting with cement. This shall be the result of a more compact microstructure and lower porosity blended mortar.

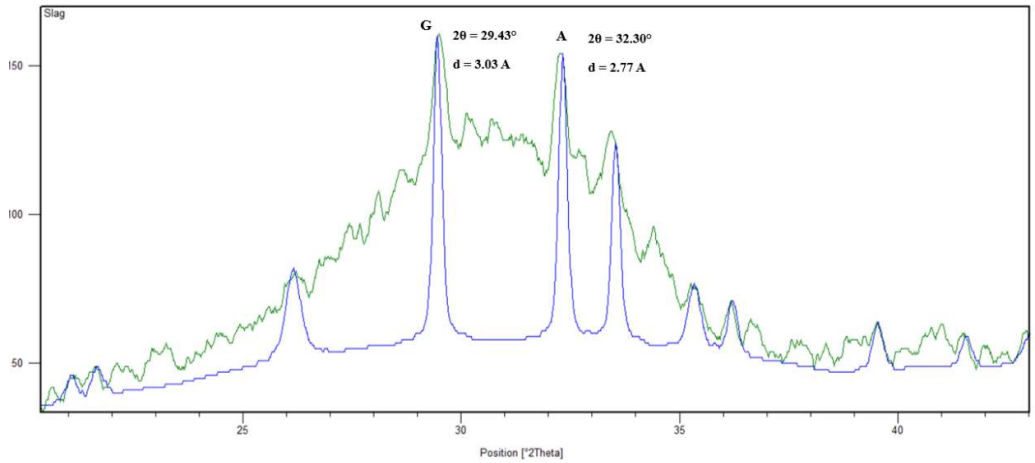


Figure 4.5 Peak Value for GGBS pattern

4.2.3.4 Graphene Oxide

Figure 4.6 depicted the XRD pattern of GO, providing a comprehensive mineralogical analysis of the synthesized nanomaterial. The analysis managed to identify the presence of Carbon (C) and oxygen integrated carbon (C,O2) as the main mineral phases within the GO. These identified phases indicate the successful formation of oxygen molecules and functional groups attached to the surface of the GO. Not only that but, but the presence of these mineral constituents ensures that the GO possesses the necessary chemical functionalization and high surface area required to interact effectively as a nucleation site during the hydration of the cementitious matrix.

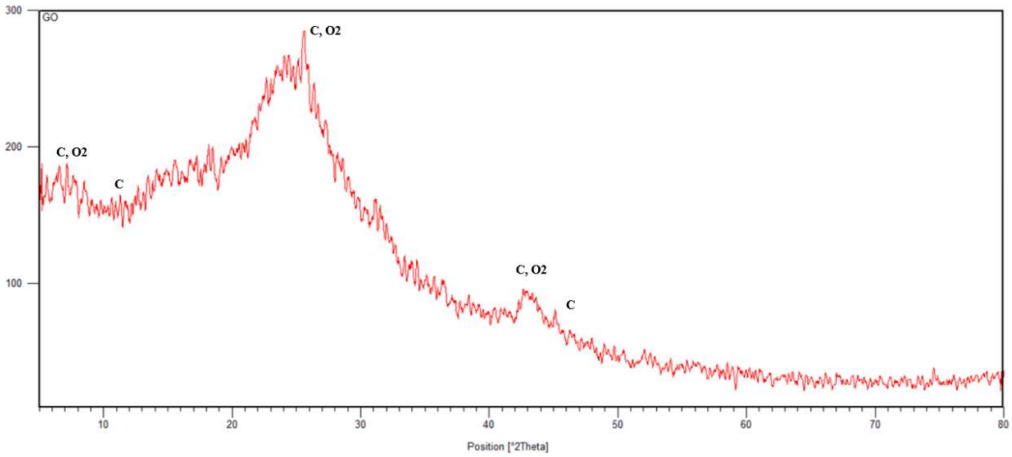


Figure 4.6 XRD Pattern of GO in X'pert Highscore

For a comparison purpose, a high magnification XRD pattern of graphene and GO has been determined. As shown in the closed-up XRD in Figure 4.7, the GO pattern

indicated a wide diffraction peak which started at 2θ = 7.09° with a corresponding interlayer d-spacing of 12.54 A. This represents a significant increase compared to the d-spacing of graphene, which was 4.49 A depicted in the Figure 4.8, which directly indicates the presence of oxygen-based functional groups and the presence of water molecules trapped in between the carbon element planes. This also confirmed the high degree of oxidation reported in the elemental analyser analysis in sub section 4.2.2. In detail, the broad diffraction peaks show that the material was a semi-crystalline material rather than purely crystalline or amorphous. This is because, as in nanomaterial studies, semi-crystalline peaks represent a high surface area and high density of material, which serves as active nucleation sites for the cement hydration process (Anwar et al., 2023). This directly enhances the purpose of GO, where it promotes the growth of calcium silicate hydrates (C-S-H) gel in cementitious-based matrix.

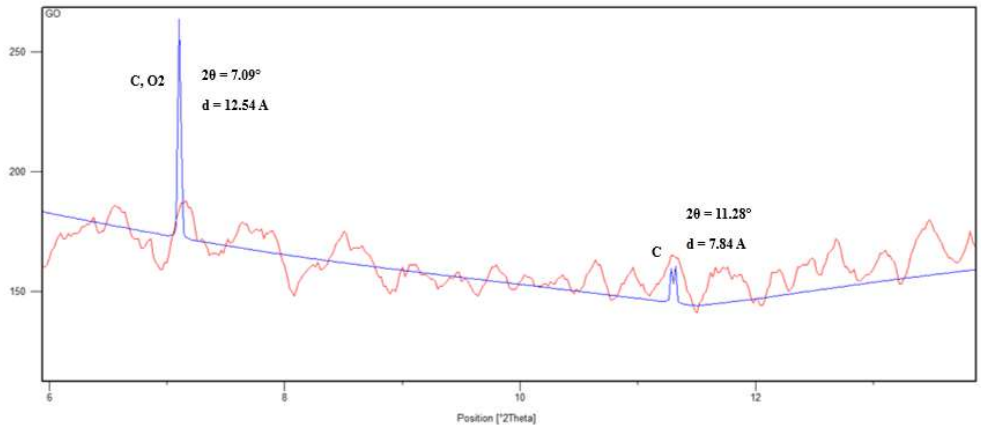


Figure 4.7 Peak Value for GO Pattern

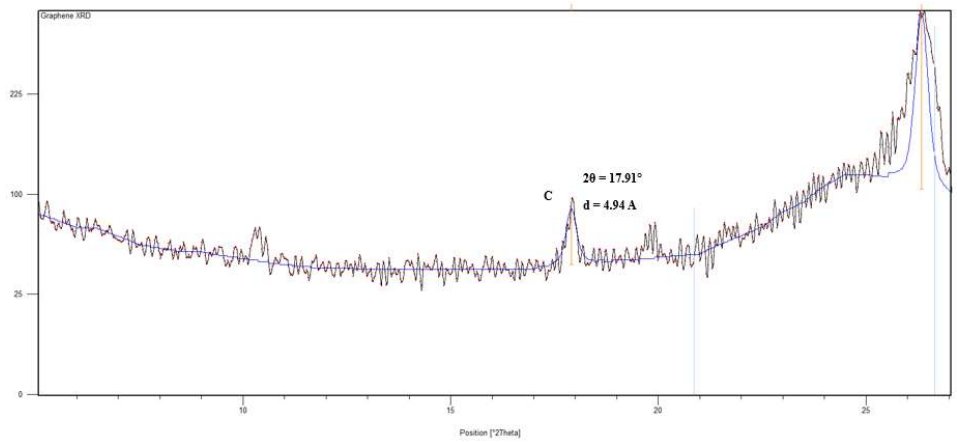
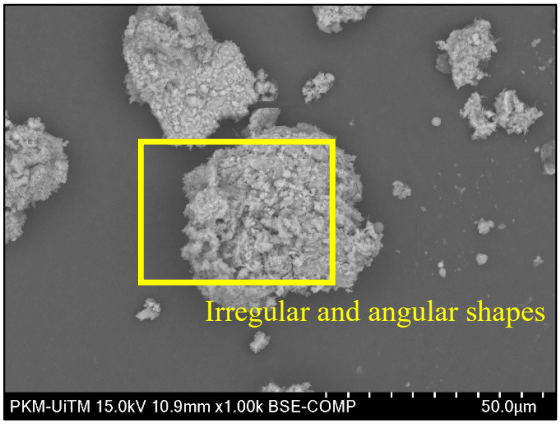


Figure 4.8 Peak Value for Graphene Pattern

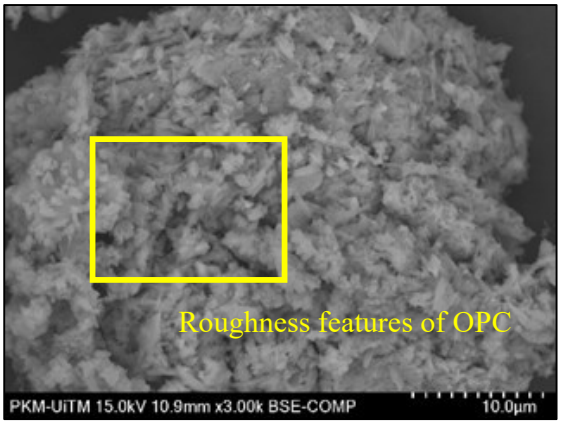
4.2.4 Scanning Electron Microscopy (SEM) Analysis

4.2.4.1 OPC

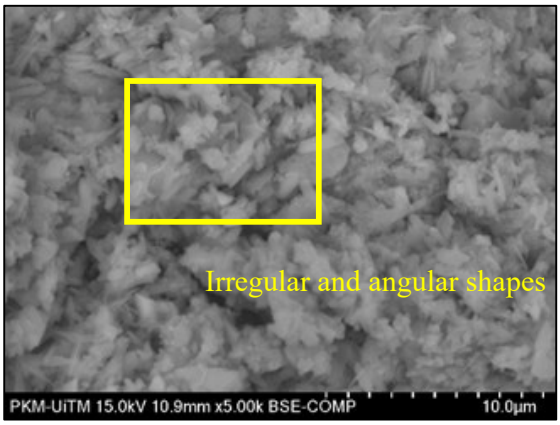
Figure 4.9 illustrates the SEM images of the OPC, which act as the main physical structure of the primary binder at various magnification levels. Technically, the SEM images reveal a predominantly irregular and angular geometry of particle shapes. Not only that, but OPC also possesses a rough yet crystalline surface texture, which is usually indicative of the mechanical grinding process used during production. Moreover, the roughness features also delivered a high degree of friction and contact area with other cementitious materials during the cement hydration process (Ying et al., 2021). This leads to initial stability and subsequent strength development in accordance with the curing time of the hydration process.



i) 1.00k magnification zoom in SEM



ii) 3.00k magnification zoom in SEM

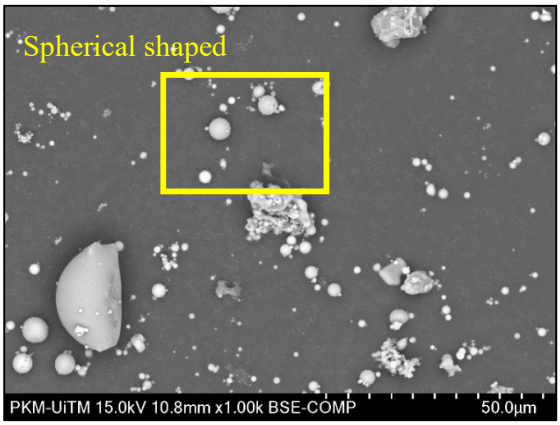


iii) 5.00k magnification zoom in SEM

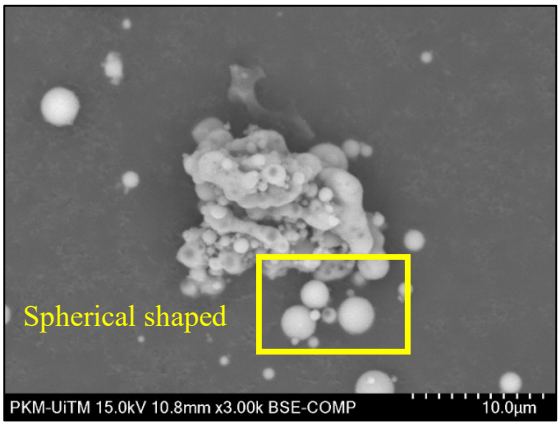
Figure 4.9 SEM Image of OPC with Different Magnification Scale

4.2.4.2 Fly Ash

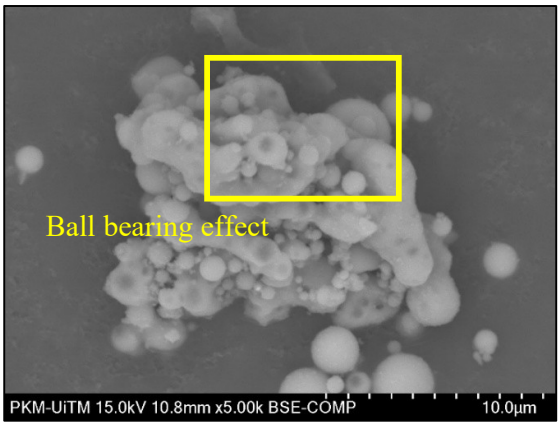
These SEM images were collected to obtain in-depth information on the morphology of fly ash Class F. Based on Figure 4.10, the images exhibited consistent shapes of solid spheres, mostly of a glassy and hollow, with irregular shape particles. Moreover, some of the larger particle sizes also were noticed through SEM images as the formation of larger particle sizes may be the end result of the collision of flame-borne particles during the furnace process. In other words, due to high surface tension and rapid cooling, perfectly spherical forms were created as visualized in the SEM image. Meanwhile, these spherical-shaped particles were portrayed by fly ash also known as miniature ball bearing which helps in terms of providing a lubricant effect (Alterary & Marei, 2021). This effect also provides an improved performance towards cement workability by reducing frictional losses which ultimately focuses on achieving the required workability rate. However, the presence of solid spheres can be seen to be dispersed over larger particles. Apart from that, it is also apparent and obvious that the surface of particles in fly ash refrains in smooth texture.



i) 1.00k magnification zoom in SEM



ii) 3.00k magnification zoom in SEM

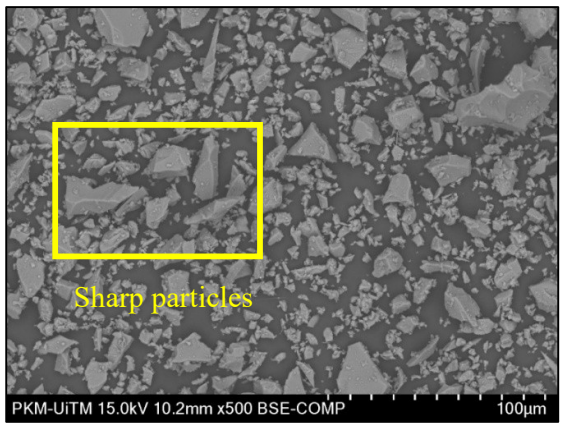


iii) 5.00k magnification zoom in SEM

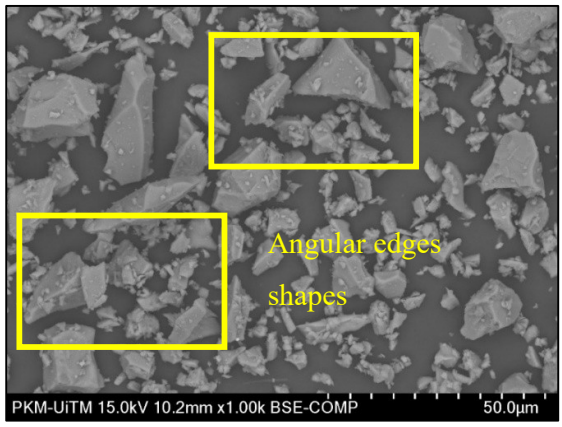
Figure 4.10 SEM Image of Fly Ash with Different Magnification Scale

4.2.4.3 GGBS

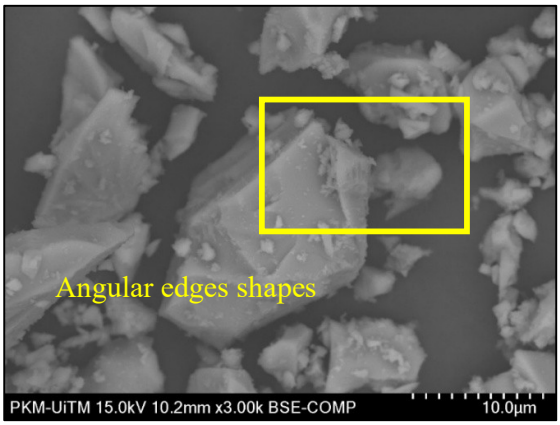
Figure 4.11 provides a detailed view of GGBS particles through SEM images. A primary observation can be determined where GGBS features sharp and angular edges of the GGBS particle due to crushing processes during the milling of GGBS. In detail, it also created a fracture to the GGBS, leaving well-defined edges rather than rounded ones (Munjal et al., 2021). Even though most of the particles share an overall similar morphology it still has distinct variations in their forms. This morphology was crucial as it influences during mixing process with other cementitious materials.



i) 500 magnification zoom in SEM



ii) 1.0k magnification zoom in SEM

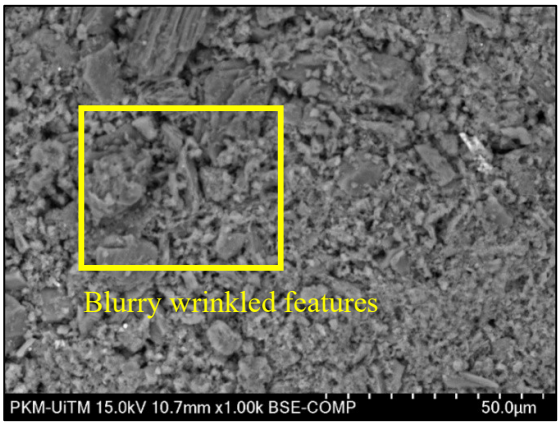


iii) 3.0k magnification zoom in SEM

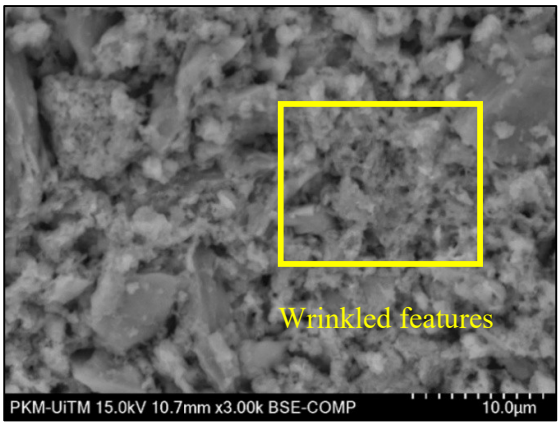
Figure 4.11 SEM Image of GGBS with Different Magnification Scale

4.2.4.4 Graphene Oxide

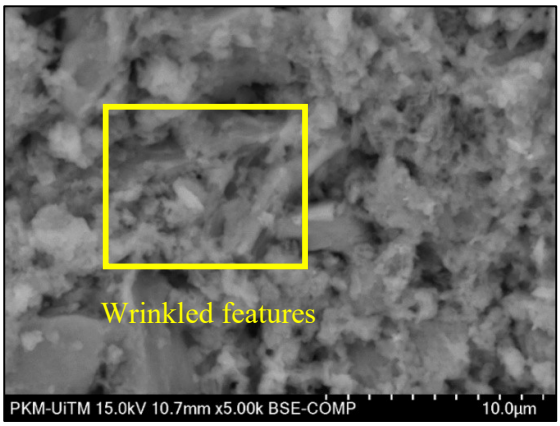
Figure 4.12 visually represents the morphology and properties of the synthesized GO. Based on the SEM images, GO tends to reveal the presence of plate-like structures and irregular shapes in consistent particles across the field. This can be attributed to the chemical reaction process during the synthesis method, which introduces the oxygen functional groups to the graphene layers (Anwar et al., 2023). Moreover, it also introduces visual evidence of the effectiveness of the oxidation process, resulting formation of GO. As a preliminary observations, a wrinkled surface of GO can be seen in the SEM images. Nevertheless, due to the nanoscale of GO, it presents a limitation for SEM imaging at higher magnifications. Thus, it leads to a decrease in image clarity and blurry features. Henceforth, to achieve a higher resolution and more detailed image, Field Emission Scanning Electron Microscopy (FESEM) analysis was conducted in this study.



i) 1.00k magnification zoom in SEM



ii) 3.00k magnification zoom in SEM



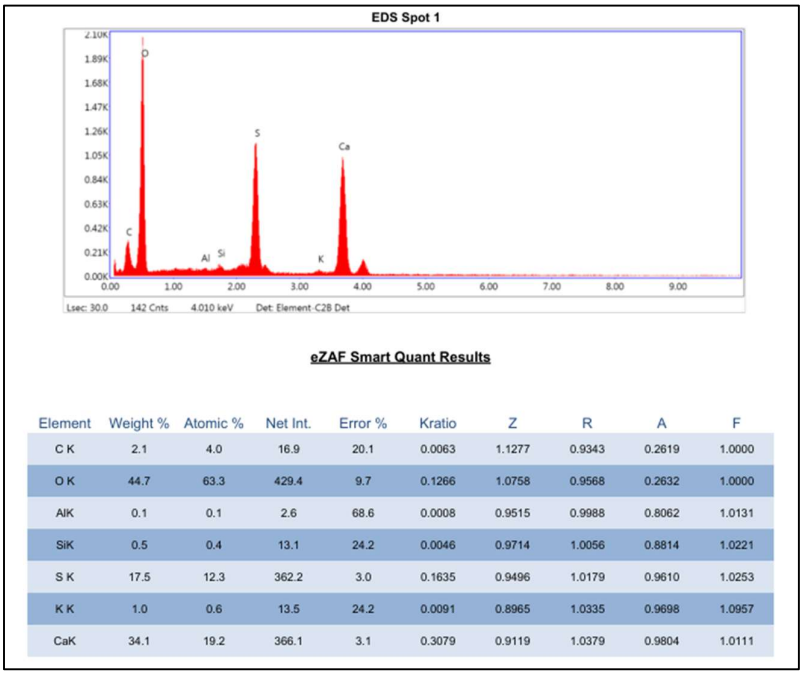
iii) 5.00k magnification zoom in SEM

Figure 4.12 SEM Image of GO with Different Magnification Scale

4.2.5 Energy Dispersive X-ray (EDX) Analysis

4.2.5.1 OPC

As shown in Figure 4.13, the OPC EDX results shown the two most dominant element were Oxygen (O) at 63.3% followed by Calcium (Ca) at 19.2%. The high concentration of oxygen was expected due to the existing cement components primarily in oxide forms, while calcium content confirmed due to the presence of Calcium silicate and Calcite during XRD phase analysis. Moreover, the presence of Sulphur (S) also was recorded at 12.3 wt%, which refers to the concentration of Gypsum (G) phase. The spectrum also identified a small amounts of Silica (Si) at 0.4 %, Alumina (Al) at 0.1%, and Potassium (K) at 1.0 wt%. Additionally, the detection of Carbon (C) at 4.0% supported the mineralogical identification of Calcite (CC) within the binder matrix. These elemental findings provided a comprehensive OPC chemical stability analysis.



eZAF Smart Quant Results

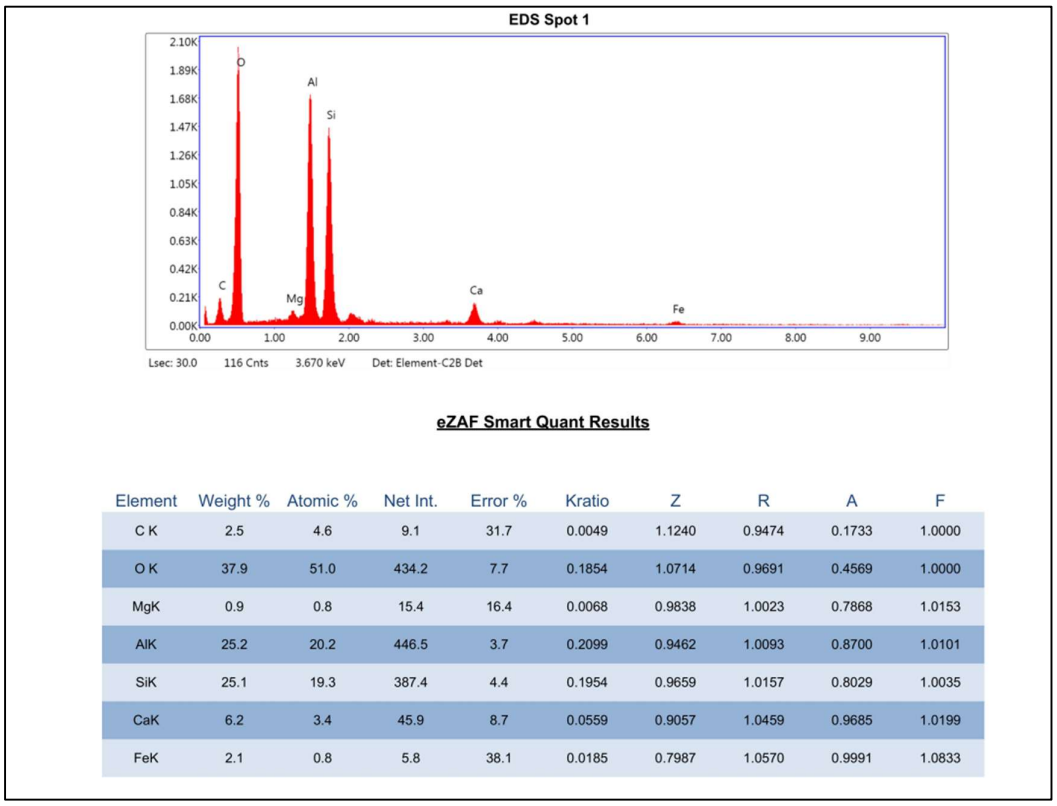
Element	Weight %	Atomic %	Net Int.	Error %	Kratio	Z	R	A	F
C K	2.1	4.0	16.9	20.1	0.0063	1.1277	0.9343	0.2619	1.0000
O K	44.7	63.3	429.4	9.7	0.1266	1.0758	0.9568	0.2632	1.0000
AlK	0.1	0.1	2.6	68.6	0.0008	0.9515	0.9988	0.8062	1.0131
SiK	0.5	0.4	13.1	24.2	0.0046	0.9714	1.0056	0.8814	1.0221
S K	17.5	12.3	362.2	3.0	0.1635	0.9496	1.0179	0.9610	1.0253
K K	1.0	0.6	13.5	24.2	0.0091	0.8965	1.0335	0.9698	1.0957
CaK	34.1	19.2	366.1	3.1	0.3079	0.9119	1.0379	0.9804	1.0111

Figure 4.13 EDX Analysis for OPC

4.2.5.2 Fly Ash

As indicated in the EDX results in Figure 4.14, the elemental properties of fly ash were dominated by Oxygen (O) at 51.0%, followed by Alumina (AI) and Silica (Si)

at 20.2 wt% and 19.3 wt%. respectively. Technically, the high percentage of Alumina reflected a specific role as a fast-setting time for the hardening process of the cement matrix. This also can also be confirmed by referring to existing XRF data where the Alumina was recorded at 20.00%. Not only that, but the silica content also shall provide a significant pozzolanic reaction during cement hydration. This leads to a proper and compact formation of Calcium Silicate Hydrate (C-S-H). The spectrum of EDX results indicated the presence of Calcium (Ca) at 3.4%, Carbon (C) at 4.6%, and Ferum (Fe) at 0.8%, alongside a minor amount of Magnesium (Mg) at 0.8%. The low percentage of calcium confirmed the classification of the material as fly ash class F according to ASTM C618.



eZAF Smart Quant Results

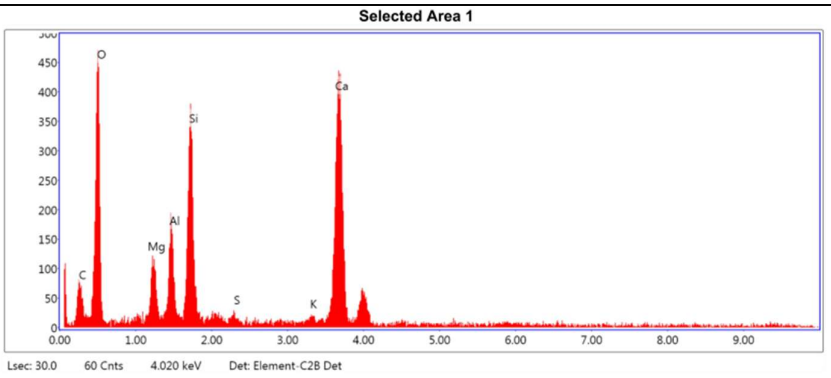
Element	Weight %	Atomic %	Net Int.	Error %	Kratio	Z	R	A	F
C K	2.5	4.6	9.1	31.7	0.0049	1.1240	0.9474	0.1733	1.0000
O K	37.9	51.0	434.2	7.7	0.1854	1.0714	0.9691	0.4569	1.0000
MgK	0.9	0.8	15.4	16.4	0.0068	0.9838	1.0023	0.7868	1.0153
AlK	25.2	20.2	446.5	3.7	0.2099	0.9462	1.0093	0.8700	1.0101
SiK	25.1	19.3	387.4	4.4	0.1954	0.9659	1.0157	0.8029	1.0035
CaK	6.2	3.4	45.9	8.7	0.0559	0.9057	1.0459	0.9685	1.0199
FeK	2.1	0.8	5.8	38.1	0.0185	0.7987	1.0570	0.9991	1.0833

Figure 4.14 EDX Analysis for Fly Ash

4.2.5.3 GGBS

According to the EDX result depicted in Figure 4.15, Calcium (Ca) recorded a high atomic percentages by 24.71%, followed by Oxygen (O) stood at 56.23%. This aligns with the high calcium percentages, where it acts as the foundation of C-S-H gel formation during the cement hydration process. Similarly with other cementitious

materials, Silica (Si) and Alumina (AI) were determined at 9.89% and 4.27%, respectively. These values were expected to observe for GGBS, supporting the role as a reactive supplementary cementitious material. Moreover, the results also trace low percentages of elements such as Magnesium (Mg) at 3.11%, Carbon (C) at 1.26%, Potassium (K) at 0.31%, and Sulphur (S) at 0.23%. By comparing these results to the fly ash data, a significantly higher calcium percentage difference established a distinct difference in terms of the rapid hardening process. This also indicates a strength development as well as the durability of the mortar.



eZAF Smart Quant Results

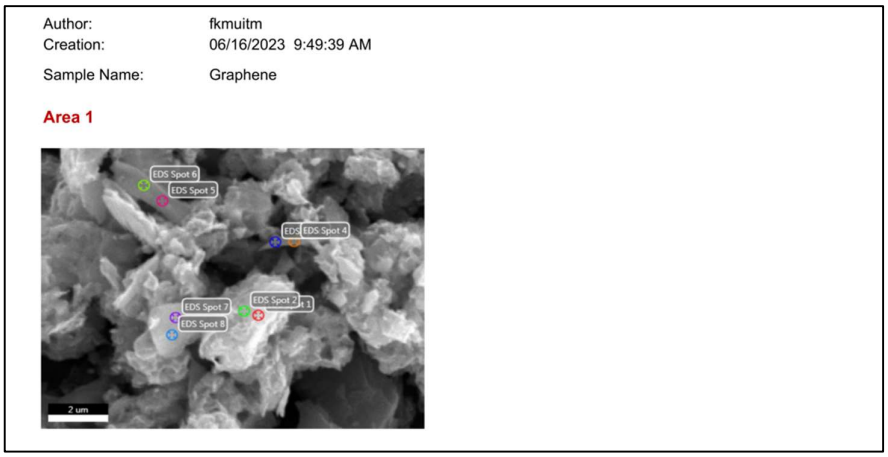
Element	Weight %	Atomic %	Net Int.	Error %	Kratio	Z	R	A	F
C K	0.63	1.26	1.77	82.09	0.0021	1.1395	0.9298	0.2936	1.0000
O K	37.59	56.23	95.64	11.29	0.0866	1.0873	0.9526	0.2119	1.0000
MgK	3.16	3.11	23.09	11.37	0.0210	0.9999	0.9877	0.6614	1.0080
AlK	4.82	4.27	37.06	8.66	0.0357	0.9620	0.9951	0.7604	1.0122
SiK	11.60	9.89	92.40	6.03	0.0949	0.9822	1.0020	0.8221	1.0128
S K	0.31	0.23	2.05	67.61	0.0027	0.9602	1.0146	0.8872	1.0349
K K	0.51	0.31	2.58	64.74	0.0051	0.9066	1.0306	0.9744	1.1361
CaK	41.38	24.71	154.64	3.77	0.3801	0.9222	1.0350	0.9855	1.0107

Figure 4.15 EDX Analysis for GGBS

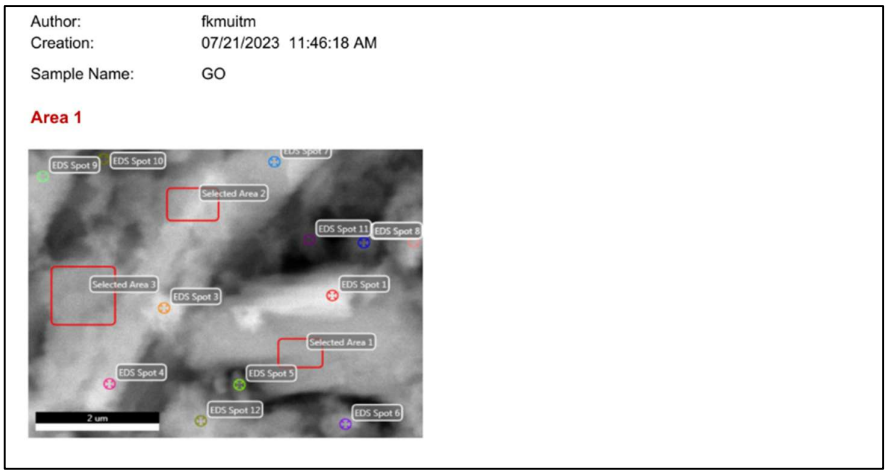
4.2.5.4 Graphene Oxide

The elemental constituents of both graphene and Graphene Oxide (GO) were evaluated through Energy Dispersive X-ray (EDX) analysis to quantify the chemical shifts occurring at the micro-scale. To ensure a representative characterisation, multiple localized spots and specific surface areas were selected for analysis, providing a detailed

map of the existing elemental distribution. Therefore, the Figure 4.16 depicts selected spots and areas for EDX analysis of graphene and GO. As for the previous preliminary data, obtained SEM image of GO, there were few pointed spots, and an area has been selected to reveal the existing composition. Therefore, the figure depicts selected spots and areas for EDX analysis of GO.



i) Selected area and spot for Graphene sample



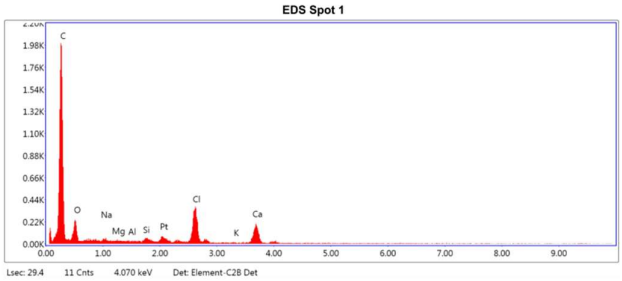
ii) Selected area and spot for GO sample

Figure 4.16 Selected Area and Spot of Graphene and GO for EDX analysis

Based on the EDX analysis shown in Figure 4.17, it can be confirmed that both of these materials are some of the greatest carbon-based materials in nanomaterial technology. This is because the carbon readings for both of them are significantly high with the atomic percentage of 78.4% for graphene and 64.0% for GO. Technically, the major elemental composition in both of these samples is Carbon (C) and also Oxygen (O). Nevertheless, there are noticeable changes in the oxygen level located in GO as it

increased tremendously compared to graphene. This indicates the presence of an oxygen functional group on the GO surface as the oxidation process takes place during the synthesis.

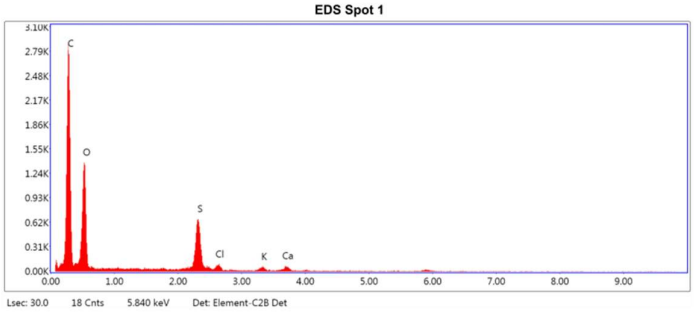
Theoretically, the most used graphene oxidation indicator is calculating the carbon to oxygen (C/O) atomic ratio. In other words, the degree of oxidation during GO preparation can be estimated from this ratio. Therefore, it is worth stating that the carbon-oxygen ratio for GO obtained was 2.19 as it aligns with recommended range of C/O ratio of 2.0 to 3.0 (Vantadori et al., 2022). This describes the GO as having a high density of oxygen functional groups attached to the surface. This ensures the hydrophilic features of GO, which enhance the dispersion within the cementitious-based material during the mixing process. To add to the bargain of well-oxidized graphene, during the preparation of GO, a yellowish colour appeared indicating the presence of oxygen reaction when it is dispersed in deionized water.



eZAF Smart Quant Results

Element	Weight %	Atomic %	Net Int.	Error %	Kratio	Z	R	A	F
C K	61.5	78.4	358.4	10.1	0.2211	1.0628	0.9661	0.3382	1.0000
O K	11.4	10.9	49.6	12.8	0.0240	1.0121	0.9864	0.2087	1.0000
NaK	0.9	0.6	9.3	21.0	0.0054	0.9144	1.0105	0.6595	1.0018
MgK	0.4	0.2	5.3	27.0	0.0026	0.9287	1.0174	0.7873	1.0030
AlK	0.3	0.2	4.0	39.0	0.0021	0.8931	1.0237	0.8757	1.0052
SiK	0.9	0.5	12.8	14.0	0.0073	0.9116	1.0296	0.9322	1.0076
PtM	2.3	0.2	15.1	18.8	0.0220	0.5733	1.4000	1.2580	1.3229
ClK	11.4	4.9	115.8	4.0	0.0963	0.8464	1.0449	0.9908	1.0081
K K	0.3	0.1	2.6	63.0	0.0028	0.8404	1.0531	0.9808	1.0180
CaK	10.7	4.1	66.5	5.5	0.0912	0.8547	1.0565	0.9900	1.0086

i) EDX data for Graphene sample



eZAF Smart Quant Results

Element	Weight %	Atomic %	Net Int.	Error %	Kratio	Z	R	A	F
C K	52.6	64.0	506.4	9.6	0.1971	1.0419	0.9797	0.3598	1.0000
O K	32.0	29.2	302.3	9.6	0.0927	0.9911	0.9989	0.2926	1.0000
S K	11.0	5.0	205.3	3.1	0.0964	0.8699	1.0490	0.9915	1.0127
Cl K	1.3	0.6	20.7	12.6	0.0110	0.8265	1.0533	0.9679	1.0160
K K	1.3	0.5	14.9	15.1	0.0104	0.8203	1.0607	0.9904	1.0270
Ca K	1.8	0.7	17.5	14.9	0.0153	0.8341	1.0638	0.9955	1.0248

ii) EDX data for GO sample

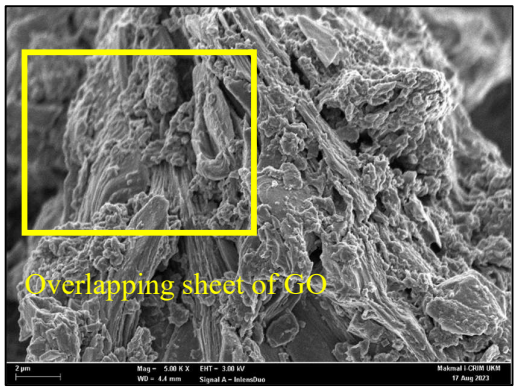
Figure 4.17 EDX Analysis for Graphene and Graphene Oxide

4.2.6 Field Emission Scanning Electron Microscopy (FESEM)

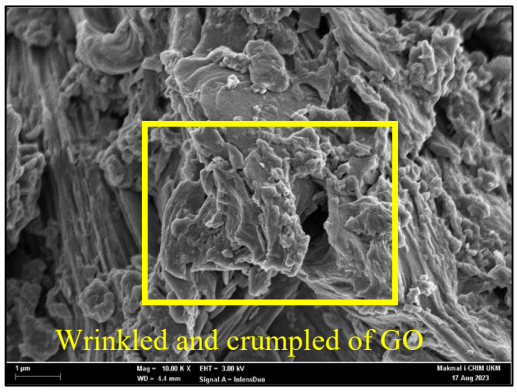
4.2.6.1 Graphene Oxide

This section discussed further investigation of the microstructure and morphology of GO at a higher resolution, which eventually overcame the limitations displayed by SEM. Figure 4.18 exhibits the FESEM images of GO at various magnification scales, revealing in-depth detail of morphology surface and visualization of surface features to the nano-meter. These high-quality images also directly provide a comprehensive assessment of the structural characteristics and exfoliation of GO's surface. In detail, these images illustrated a disorder solid structure where thin sheets are closely attached and often overlapping, indicating the presence of strong van der Waals forces. Not only that but the wrinkled and crumpled features of the GO sheets visualized the high surface area where it can be an advantageous tool as an efficient nucleation effect (Hulagabali et al., 2023). This can be explained as the larger the surface area, the higher the reactivity between GO and other cementitious material. In other words, it also helps to facilitate interaction with surrounding material during the cement hydration process leading to compact and denser microstructure refinement. Furthermore, the wrinkled layer on GO's surface also introduced the presence of oxygen

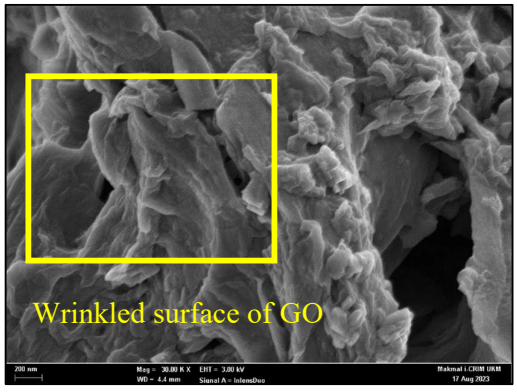
functional groups during oxidation synthesis as it tends to increase the interlayer spacing. These features also prove the intercalation success between graphene layers and the oxygen functionalities, leading to an increase in interlayer overlapping to the surface of the GO (Bheel et al., 2023). It is also worth noticing that the carbon framework remains in the GO structure with added oxygen-containing groups.



i) 5.0k magnification zoom in FESEM



ii) 10.0k magnification zoom in FESEM



iii) 30.0k magnification zoom in FESEM

Figure 4.18 FESEM Image of GO with Various Magnifications

4.3 Properties Binder Formulation

This section discussed the properties of the binder formulation, specifically focusing on two supplementary cementitious materials (SCMs) which were fly ash and GGBS. The primary goal was to evaluate and analyse the optimal dosage for each SCMs before modification with graphene oxide (GO). To achieve this, the physical, mechanical, and durability properties of the blended mortar were determined.

4.3.1 Physical Properties

4.3.1.1 Density

The graphs in the Figure 4.19, represent the density of binder formulation whereby it includes the replacement of fly ash and GGBS in the cement matrix. Moreover, the data collected refers to the mean density of specimens of various replacement percentages of 10%, 20% and 30%. The density recorded for fly ash were 1.90 g/cm^3, 1.91 g/cm^3 and 1.92 g/cm^3. Meanwhile, the density for GGBS in blended mortar managed to record 1.97 g/cm^3, 1.98 g/cm^3 and 1.99 g/cm^3. It can be stated that a consistent trend of increasing cement replacement to density. Nevertheless, GGBS managed to reveal a higher density at all replacement levels with the most significant increase of 30% replacement. This may be attributed to the pozzolanic nor filler effect of both materials, with GGBS ahead potential of more significant filler fact. This may happened due to particle characteristics, forming a denser mortar.

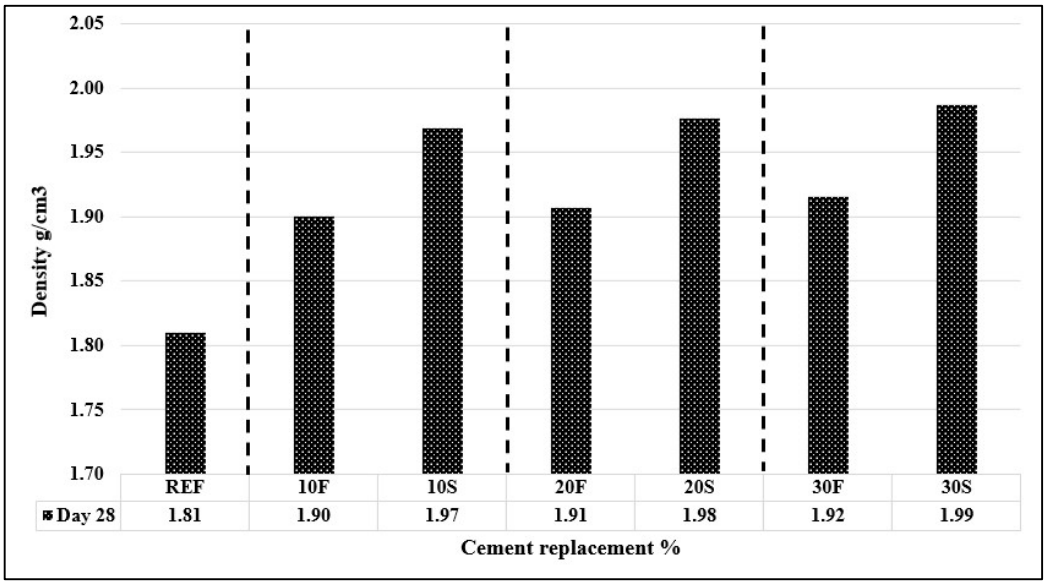


Figure 4.19 Density of Binder Formulation

4.3.2 Mechanical Properties

4.3.2.1 Compressive Strength

The compressive strength development of the blended mortar specimens, incorporating various percentages of fly ash (F) and ground granulated blast-furnace slag (S) as cement replacements, is illustrated in Figure 4.20. A general observation of the data indicates that the overall results for cement replacement followed a trend of increasing strength parallel with the added dosage when compared to the control specimen. The reference specimen established the baseline performance, achieving compressive strengths of 19.99 MPa, 27.67 MPa, and 30.44 MPa at 7, 14, and 28 days, respectively.

At 10% of cement replacement, the compressive strength for both materials (10F and 10S) revealed an increment gradually. At day 7, a compressive strength of 20.07 MPa was shown by 10F, followed by 21.08 MPa recorded by 10S. This can be explained as GGBS consisting of a higher alumina content which is crucial in providing early strength. As the curing days progressed to 14 days, 10F recorded 27.79 MPa and 10S achieved 29.18 MPa. Moreover, by 28 days, the strength further increases as it reaches 30.57 MPa and 32.10 MPa for 10F and 10S. The discussion furthers to 20% of cement replacement, at day 7, 20F exhibited a compressive strength of 21.26 MPa which is slightly higher than 10F. This might happened due to a higher pozzolanic reaction availability portrayed by 20% of fly ash. In contrast, 20S shows 22.97 MPa revealing

its dominance over 20F and even 10S. As the curing days further to 14 days, 20S achieved 31.81 MPa and 20F 29.44 MPa. Thus, on day 28, 20S shows an impressive strength of 34.49 MPa putting a notch compared to fly ash at a 20% replacement level. Finally, at 30% cement replacement, it can be seen that 30F recorded 21.00 MPa, showing a decrease in strength compared to 20F which could be attributed towards a slower pozzolanic reaction of fly ash. Nevertheless, 30S demonstrated a consistently high strength by achieving 32.35 MPa and 35.59 MPa on days 14 and 28 of curing. This constitutes a substantial 16.92% increase over the reference specimen, representing the highest overall strength gain observed in this study.

Across all replacement percentages, it can be observed that GGBS (S) managed to obtain a higher compressive strength compared to fly ash (F). This can be explained as GGBS reactivity as latent hydraulic material produces C-S-H gel, similar to cement. This helps in generating a greater amount of C-S-H as it helps in providing early and late strength enhancement. This can be discussed as due to the presence of Silica (SiO_2), it devoted the features of pozzolanic reaction towards calcium hydroxide in the hydration process. This contributes to the strength of the blended mortar as a whole. On top of that, what differs from the compressive strength of fly ash and GGBS blended mortar was the calcium oxide percentage whereby GGBS possesses a higher value compared to fly ash. The existence of calcium oxide in the GGBS provides even greater strength to the blended mortar as it quickens the hydration process. This leads to a greater strength as the hydration product of C-S-H is higher compared to fly ash blended mortar. At 30% replacement, an adequate GGBS replacement also managed to allow extensive hydration and pozzolanic reaction for optimal strength enhancement. This also helps in reducing porosity within the blended mortar matrix which leading the long-term strength of the GGBS blended mortar (Shahas et al., 2022). On the other hand, fly ash is primarily a pozzolanic material which requires the presence of calcium hydroxide to react and form another C-S-H.

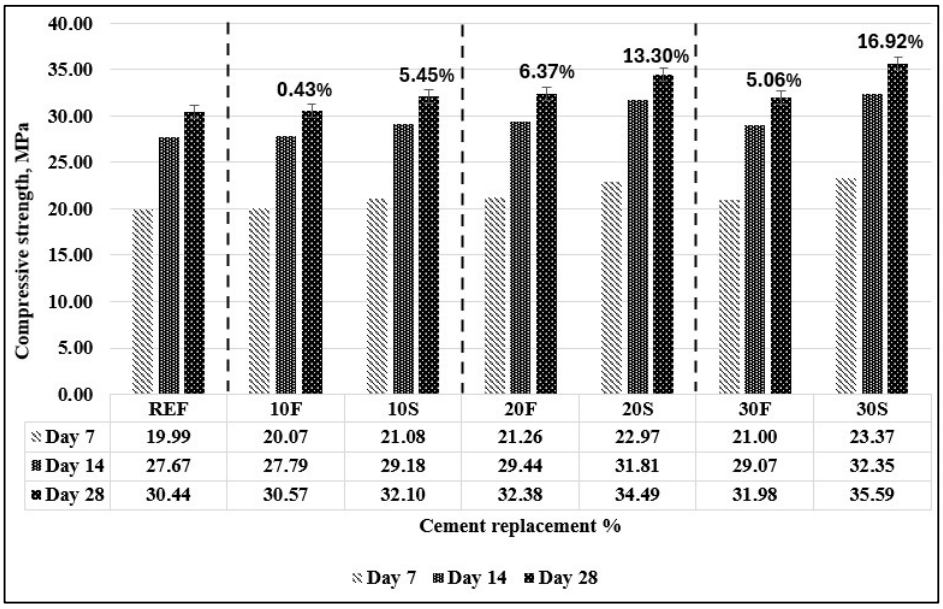


Figure 4.20 Compressive Strength of Binder Formulation

4.3.2.2 Split Tensile Strength

The tensile strength development for blended mortar containing fly ash (F) and GGBS (S) is presented in Figure 4.21. The data consistently depicted a linear increase in strength relative to curing age across all specimens when compared to the reference specimen, which recorded tensile strengths of 1.96 MPa, 2.72 MPa, and 2.99 MPa at 7, 14, and 28 days, respectively.

At the 10% cement replacement level, GGBS exhibited a slightly improved performance pattern compared to fly ash. On day 7, 10S recorded 2.02 MPa, whereas 10F achieved 2.00 MPa. This trend continued through the final curing stage, where at day 28, 10S reached 3.07 MPa with a 2.68% increment over reference specimen. Similarly, with 10F results where it achieved 3.04 MPa by 1.67% increment compared to reference specimen. Upon increasing the cement replacement to 20%, a slight shift in the performance pattern was observed whereby 20F recorded 2.08 MPa at day 7, slightly exceeding the 2.04 MPa provided by 20S. By day 28, 20F managed to achieve a tensile strength of 3.17 MPa, representing a 6.02% increase compared to the reference specimen, while 20S reached 3.11 MPa, a 4.01% increment. This shift suggests that at this specific replacement level, fly ash contributes effectively to early tensile strength by initiating a more robust pozzolanic reaction.

However, at the 30% cement replacement level, the 30S specimens outperformed 30F across all curing periods. On day 7, 30S recorded 2.09 MPa compared to the 2.06 MPa observed in 30F. By the end of the 28-day curing period, 30S demonstrated a tensile strength of 3.19 MPa, which constitutes the highest observed improvement at a 6.69% increment over the reference. In comparison, 30F reached 3.14 MPa, representing a 5.02% increase over reference specimen. While it is evident that both supplementary cementitious materials (SCMs) contribute to the formation of secondary C-S-H, the latent hydraulic reaction of GGBS appears to consume calcium hydroxide (CH) produced by cement hydration more continuously and for a longer duration than fly ash at higher replacement volumes (Munjal et al., 2021).

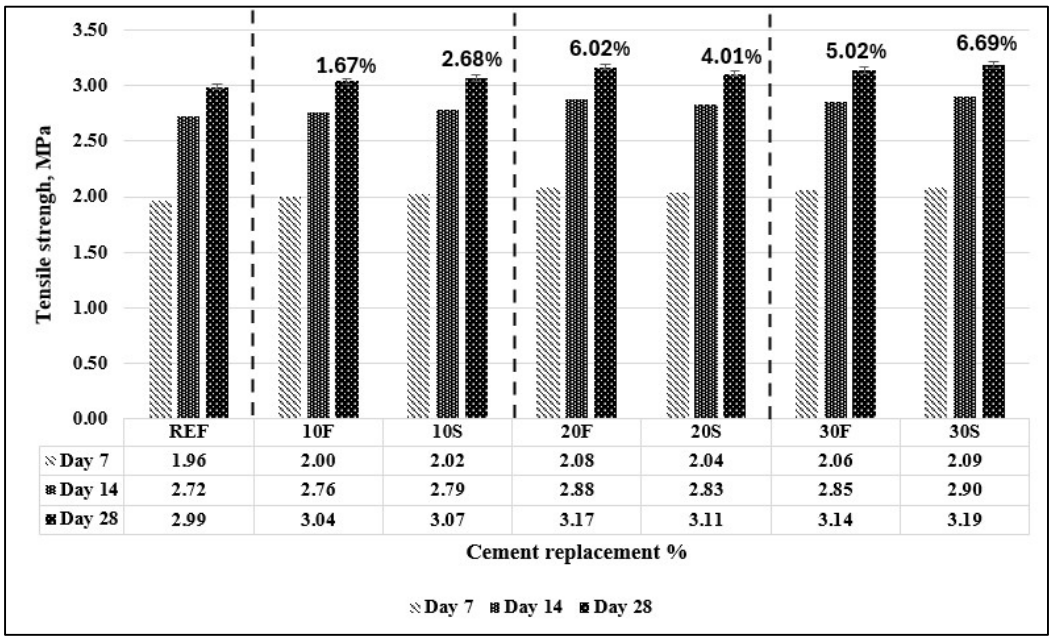


Figure 4.21 Tensile Strength of Binder Formulation

4.3.3 Durability Properties

4.3.3.1 Water Absorption

The Figure 4.22 represents the water absorption for the binder formulation whereby it consists of SCM material of fly ash and GGBS with three constant replacement percentages of 10%, 20% and 30%. It can be seen that the water absorption of blended mortar generally decreased with the increment of cement replacement

compared to reference specimen, indicating the significance of SCMs in creating denser mortar. At the 10% replacement level, both fly ash and GGBS showed a close reading of water absorption value with 1.79% and 1.78%. Nevertheless, at 30% of the replacement level, the 30S recorded the lowest water absorption among all specimens by 1.64%. This demonstrates the effectiveness of GGBS in refining pore structure and reducing water absorption compared to fly ash.

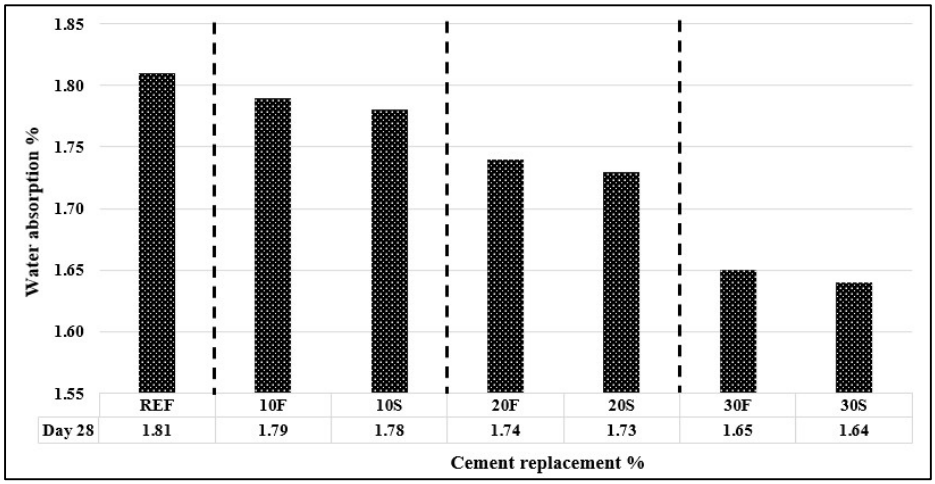


Figure 4.22 Water Absorption for Binder Formulation

4.4 Summary of Binder Formulation

A comprehensive binder formulation study has been conducted in order to determine the optimal cement replacement sources and also the percentage for the blended mortar. This binder formulation stage consisted of physical properties of density, mechanical properties, as well as the durability properties incorporating two supplementary cementitious materials of fly ash and GGBS. Moreover, each SCM was consistently used within a range of 10%, 20% and 30% of cement replacement. Nevertheless, the experimental results led to the optimum percentage of SCM, whereby 30% of GGBS managed to exhibit dominance across all parameters. Hence, this formulation shall be continued for further stages of the research, named as binder modification, which involves the incorporation of graphene oxide (GO). From this binder modification, in-depth testing was conducted to observe the optimum performance of GO within all parameters for use as a corrosion inhibitor.

4.5 The Properties of Binder Modification

This sub-section focused on binder modification. It incorporated the optimal percentage of supplementary cementitious material (SCMs) from the previous section, specifically the 30% GGBS replacement that was nominated as the optimal binder formulation. This modified binder then included graphene oxide (GO), and the properties of each resulting mixture were thoroughly studied and analysed.

4.5.1 Physical Properties

4.5.1.1 Density

Figure 4.23 depicted the influence of GO in blended mortar with various percentages. Initially, the control (30SG0) specimen exhibited a density of 1.860 g/cm^3. Upon the inclusion of 0.02% GO (30SG2), a slight increase in density, achieving the highest density of 1.890 g/cm^3 was observed. This can be attributed to several factors the first one would be the optimal dispersion of 0.02% GO found to be effective compared to other specimens. At low percentages of GO (0.02%), a well dispersed within the cement matrix, effectively generates an efficiency of C-S-H gel which acted as the primary strength phase. This eventually facilitates more hydration process leading to a denser hydration product and higher density. Not only that but due to the filling effect of GO, it also helps to reduce the porosity of the specimen (30SG2). However, a subsequent decrease of density beyond optimal percentages of 0.02% was observed. This is a very common phenomenon in nanomaterial inclusion in cementitious-based material as uniform dispersion can become challenging at times. This could lead to agglomeration products where clusters were formed as defects rather than effective fillers within the cement matrix. Thus, this consequently reduces the overall density as it creates localized voids and interrupts the homogeneity of the blended mortar (L. Zhao et al., 2018). Lastly, this also might happen due to excessive GO tends to adsorb more water during the mixing process resulting in a more porous microstructure and less dense.

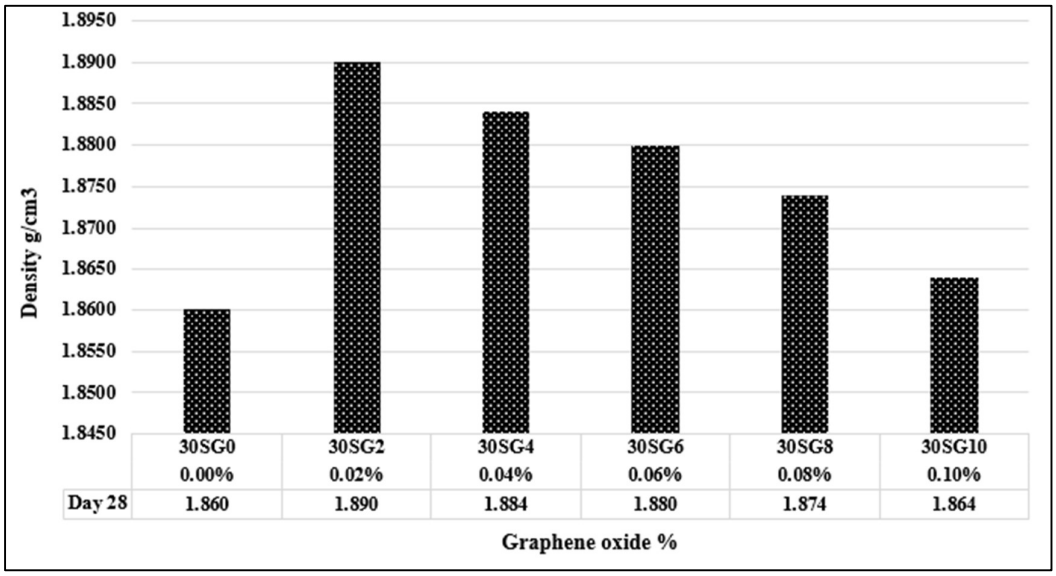


Figure 4.23 Density of Binder Modification

4.5.2 Mechanical Properties

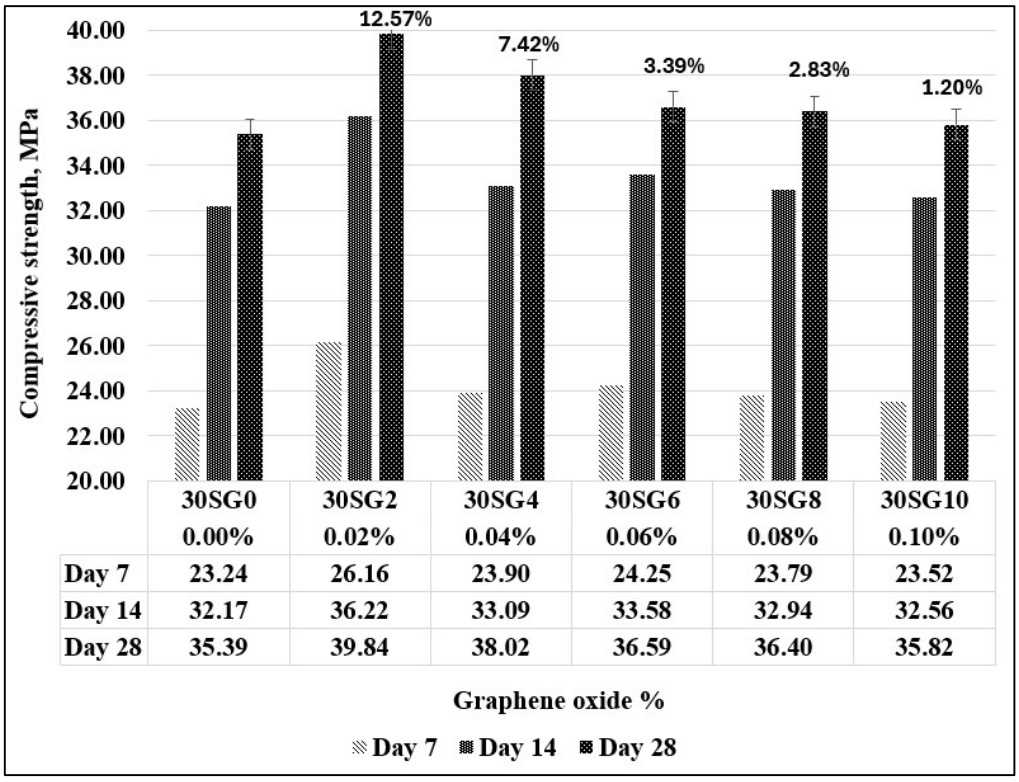
4.5.2.1 Compressive Strength

The compressive strength results are presented in the Figure 4.24. Technically, the compressive strength of each specimen was varied with the inclusion of GO of 0.02%, 0.04%, 0.06%, 0.08% and 0.10%. Moreover, at 28 days, the compressive strength tends to show the predicted strength of mature blended mortar. The compressive strength of the tested specimen ranged from 23.24 MPa to 23.52 MPa, 32.17 MPa to 32.56 MPa and 35.39 MPa and 35.82 MPa for 7, 14 and 28 days respectively. However, better results were achieved with the combination of 0.02% GO whereby it managed to obtain the highest compressive strength value of 39.84 MPa. In detail, the data illustrates a 12.57% difference of compressive strength enhancement compared to control specimen. This indicates that an adequate amount of GO can effectively improve the overall strength. The significant improvement of GO in the specimen can be explained as due to the functional group of oxygen in the graphene surface, it tends to provide greater bonding strength between GO and other cementitious matrix material. By all means, this shows with an adequate amount of GO, it perfectly balanced dispersion movement can be achieved during the mixing process leading to a homogenous mixture. This eventually causes higher stiffness properties to be embedded in the specimen and directly increases the load-transfer efficiency from the cement

matrix to the reinforcement. This also can be related towards the "bridging effect" which is possessed by GO whereby due to the hydrophilic features of GO, it significantly enhanced interaction between layers of cement matrix material (Akarsh et al., 2022). This shall lead to a greater load-bearing capacity enhancement for the mixture when loads are being applied. On top of that, the increment of compressive strength in the mixture also can be discussed due to the specific surface area of GO itself as a nanomaterial. This can be explicated as GO has been devoted as one of the biggest surface areas compared to other nano materials. This creates beneficial traits for the GO to enhance the chemical reaction with the cement matrix even better for the strength development stage. To be more specific, for a quicker and more effective chemical reaction, the surface area of the nanomaterial is compulsory and crucial. Therefore, GO has the ability to quickly react with hydration products such as Calcium Hydroxide to form C-S-H gel. Moreover, the high surface area of GO itself consequently helps the C-S-H particles to bond perfectly with GO which acts as nucleation sites that continuously promote C-S-H growth along the GO flakes. This ultimately leads to an increment in strength in the bond strength of the cement matrix. This eventually causes higher stiffness properties to be embedded in the specimen and directly increases the load-transfer efficiency from the cement matrix to the reinforcement. Finally, the growth of efficient C-S-H tends to provide denser microstructure and even micro pores within any transition area of the cement matrix to be filled perfectly. Hence, this leads towards a higher quality of mixture with greater strength capacity. On top of that, the chemical interaction between polycarboxylate superplasticizer and GO also enhanced the hydration products during cement hydration process (Bheel et al., 2023).

However, the decline pattern in compressive strength with the increment of GO percentages also presents a crucial point in this study. At 0.04% GO (30SG4), the improvement strength was exhibited only at 7.42% and at 0.06% GO (30SG6) even lower at 3.39% of strength enhancement with reference to those of control specimens. Beyond these percentages, the improvements were marginal where 2.83% and 1.20% improved strength has been recorded for 0.08% GO (30SG8) and 0.10% GO (30SG10). There is no doubt that the incorporation of GO often enhanced the mechanical properties but exceeding beyond the optimal concentration appears to lead to a detrimental effect. This can be attributed to the challenge of achieving a homogenous dispersion of GO

within the cement matrix. In detail, as the GO concentration increases, the van der Waals forces between GO's bonding become visible and stronger, leading to agglomeration (Vantadori et al., 2022). Consequently, it weakens the overall structural integrity within the cement matrix and diminishes the desired bonding between cementitious material.



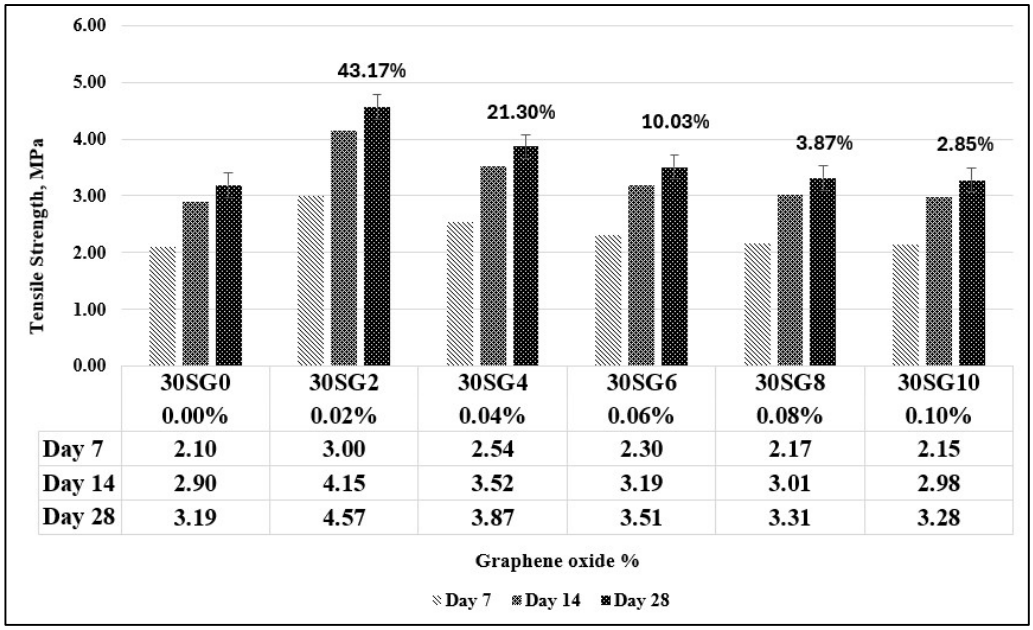
	30SG0 0.00%	30SG2 0.02%	30SG4 0.04%	30SG6 0.06%	30SG8 0.08%	30SG10 0.10%
Day 7	23.24	26.16	23.90	24.25	23.79	23.52
Day 14	32.17	36.22	33.09	33.58	32.94	32.56
Day 28	35.39	39.84	38.02	36.59	36.40	35.82

Figure 4.24 Compressive Strength of Binder Modification

4.5.2.2 Split Tensile Strength

The Figure 4.25 reveals a non-linear pattern of the graph between GO percentages and the tensile strength of blended mortar. The tensile strength of GO-blended mortar was discovered to improve ranging from 2.10 MPa to 2.15 MPa at 7 days, 2.90 MPa to 2.98 MPa at 14 days, and 3.19 MPa to 3.28 MPa at 28 days. Generally, the strength enhancement dependent to the consistency of its typical cement hydration and also in inclusion of GO, particularly at the optimal concentration. It is clear that 0.02% of GO (30SG2) resulted in the most significant strength enhancement and exhibited a 43.17% increase in tensile strength compared to the control specimen. This can be explained due to the high surface area of GO which promotes an improved

bonding between GO and the cement matrix. This also means that the reactivity between GO and other cementitious materials increased tremendously with 0.02%, resulting in higher tensile strength. Not only that but the filling effect of GO also tends to reduce the crack propagation and improve the overall strength of the specimens (Janavika & Prakash Thangaraj, 2023). This can be explained as carbon-based material such as GO continues to provide a sheet-like microstructural configuration whereby it helps in terms of prevention guidance for any crack when load is applied. In addition, GO also contributes towards the densification of the specimen due to the filling effect. The filling effect can be explained as nano-size particles of GO tend to interlock and fill available pores in the specimen. Consequently, it enhances a denser specimen compared to others. Nevertheless, beyond 0.02% of GO, the tensile strength indicated a decline pattern as shown in the figure. At 0.04% of GO (30SG4), the tensile strength improved only by 21.30% at 28 days. The pattern continues for other GO percentages (30SG6, 30SG8 and 30SG10) as it shows progressively smaller improvement. This might happened due to the tendency of GO agglomeration where it acted as defects within the cement matrix. This directly causes a reduction in strength and the effectiveness of stress transfer.



	30SG0 0.00%	30SG2 0.02%	30SG4 0.04%	30SG6 0.06%	30SG8 0.08%	30SG10 0.10%
Day 7	2.10	3.00	2.54	2.30	2.17	2.15
Day 14	2.90	4.15	3.52	3.19	3.01	2.98
Day 28	3.19	4.57	3.87	3.51	3.31	3.28

Figure 4.25 Tensile Strength of Binder Modification

4.5.3 Durability Properties

4.5.3.1 Water Absorption Test

The experimental results can be observed on day 28 as shown in Figure 4.26, where it is clear that GO influenced the water absorption of blended mortar. As an overview observation, the control specimen (30SG0) exhibited a water absorption of 1.63%. However, as the GO percentages increased to 0.02% (30SG2), the water absorption significantly decreased to 1.47%, devoted to the lowest absorption among all specimens. This indicates that 0.02% GO managed to imply the densest among the series of specimens. This can be attributed to GO's high surface area where it effectively acts as a nucleation site for the growth of C-S-H gels. This enhanced nucleation promotes a more homogenous and even compact formation of hydration products, leading to greater microstructure refinement. This also may happen due to the filing effect owned by GO itself which helps to reduce the overall void content and tortuosity of the pores within the cement matrix (Sai et al., 2025). Not only that but this also happened due to GO facilitates the pozzolanic reaction and cement hydration started by GGBS in the blended mortar. This creates a higher volume of solid hydration products and reduces the volume of interconnected pores to water absorption. In contrast, the increase in GO percentages (0.04% to 0.10%), tends to be attributed to the negative effect of agglomeration and poor dispersion. These defects within the cement matrix, create larger voids rather than filling pores. Not only that but this also leads to the entrapment of air voids resulting in a higher total porosity and increased water absorption. Last but not least, this potentially hinders the growth of C-S-H leading to a less dense specimen of blended mortar.

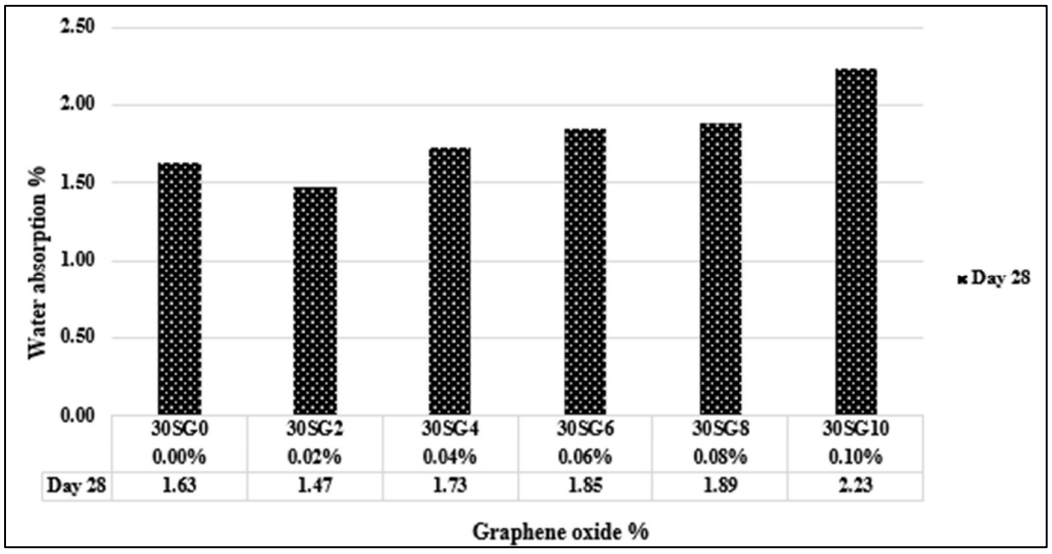


Figure 4.26 Water Absorption for Binder Modification

4.6 Corrosion Assessment of GO-Blended Mortar

4.6.1 Rapid Chloride Penetration Test (RCPT)

The RCPT results, as shown in the Table 4.6, clearly prove the significance of GO towards the chloride ion permeability of the blended mortar. This can also be explained as the pattern of results indicating that adequate percentages of GO tend to show a low chloride permeability. The control specimen of 30SG0 exhibited a total charge passed of 2500 coulombs, which included moderate chloride permeability according to ASTM C1202 (2022). This also explained the presence of 30% of GGBS as supplementary cementitious material, which provides a significant pore refinement and chloride resistance due to its pozzolanic reaction. This refers to the alumina content introduced by GGBS itself as it delivers a critical chemical defence known as Chloride Binding. Chloride binding happens when the chloride ion migrates through the pores, it is being "captured" by the high alumina content to form Friedel's salt. This automatically locks the movement of chloride ions into a stone-like matrix within the blended mortar (Aydoğan et al., 2025).

Nevertheless, the results continued to mark a significant improvement in chloride permeability as 0.02% GO (30SG2) demonstrated the lowest total charge passed by 800 coulombs. This directly puts 30SG2 as a "very low" chloride permeability rating, with a difference of 68% compared to the control specimens (30SG0). It tends to refine the microstructure and initiates a barrier against chloride ion

penetration into the cement matrix. This can also be explained by GO's filling effect, which effectively fills the left voids properly within the cement matrix, leading to stiffer blended mortar. This also proves that GO does not merely fill voids, but it tends to maximize the efficiency of chloride binding formation. This can be described as GO to ensure the GGBS hydration is evenly distributed by creating a dense network where the chloride ion is more likely to encounter the reactive alumina. This ended up with more formation of Friedel's salt within the GO-blended mortar. This hydration reaction significantly enhances the pore-blocking mechanism, leading to higher strength and lower permeability (Munjal et al., 2021). More discussion can be added as two-dimensional GO can also deliver the bridge micro-cracks effect and indirectly increase the tortuosity path for chloride ion diffusion within the cement matrix (Hulagabali et al., 2023). This hardens the movement of the penetrated ions to push through the cement matrix.

Nevertheless, as the percentage of GO beyond 0.02%, the favourable influence of chloride permeability gradually decreased. This can be attributed to the potential early agglomeration of GO. As an example, 30SG4 with 0.04% showed a slight total charge passed by 1200 Coulombs, projecting the chloride permeability rating to be low. Even though it still offers considerable advantages, such as chloride resistance and pore refinement, it still indicates a reduction compared to 0.02% GO. As the results continue, 0.06% of GO in 30SG6 started to lead to a higher total charge passed by 1800, placing the rating as moderate. The results for GO percentages of 0.08% and 0.1% also increase at a gradual rate by 2200 and 2800 coulombs. The discussion for the results can be described due to the agglomeration of GO itself. This is because GO tends to possess very strong van der Waals forces, which hold a high potential for clumping within the cement matrix if not properly dispersed. This agglomeration can be localised at any weak zones, leaving a pathway for chloride ions to penetrate easily. Therefore, an overall view of RCPT data also can be shown in Figure 4.27.

Table 4.6
Rapid Chloride Test Results for GO-Blended Mortar

Mixtures	Graphene Oxide (%)	Total Charge Passed (Coulombs)	Chloride Permeability Rating (ASTM C1202)
30SG0	0.00	2500	Moderate
30SG2	0.02	800	Very Low
30SG4	0.04	1200	Low
30SG6	0.06	1800	Moderate
30SG8	0.08	2200	Moderate
30SG10	0.10	2800	Moderate

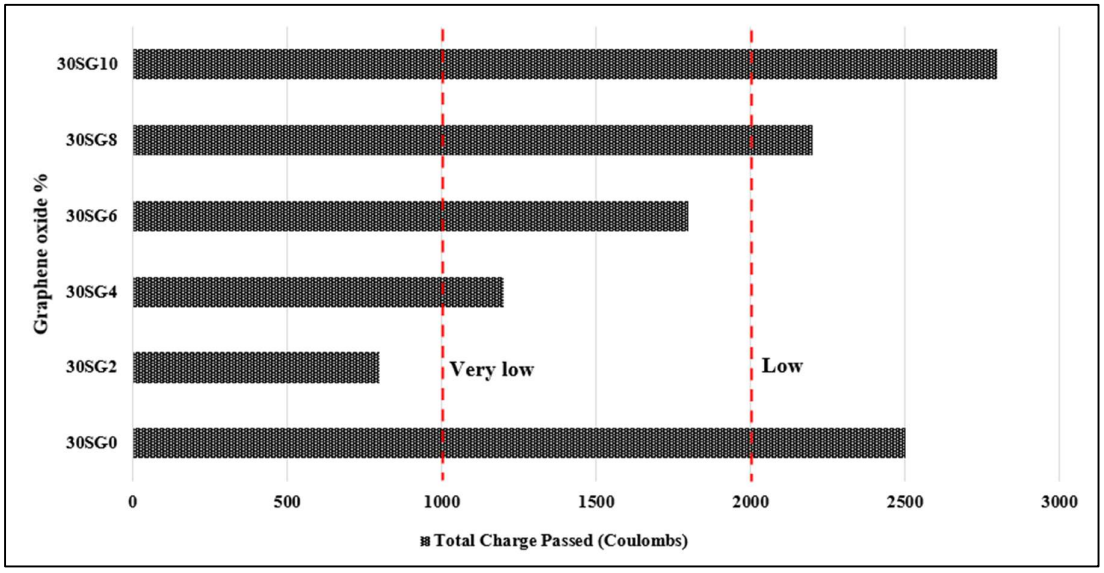


Figure 4.27 Total Charged Passed in RCPT for GO-Blended Mortar

4.6.2 Half Cell Potential (HCP)

This sub-section discussed the Half-Cell Potential test (HCP) whereby the results were obtained for each GO-blended mortar under two conditions which are normal curing and saltwater curing (Sodium Chloride, NaCl). This test also followed the guidelines of ASTM C876 (2015) as shown in Table 4.7, followed by Table 4.8 where the measurement was recorded at 30, 60 and 90 days. Therefore, as presented in a Figure 4.28 and Table 4.8, portrayed a relevant trends of data related to GO-blended mortar to different exposure.

Firstly, it can be seen that a consistent trend of data for all exposed specimens under both exposure conditions as HCP values tend to become negative over time. This is an expected occurrence as a longer time is conceded, with a higher tendency of corrosion initiation and propagation. Moreover, it is crystal clear that different exposures influenced the reading of HCP. This drives the contrast of the highly corrosive nature of chloride ions found in the saltwater solution. This aligns with the existing literature review regarding the impact of chloride-rich environments on reinforcement in concrete. Under normal curing conditions, 30SG2 mix with 0.02% of GO consistently revealed the lowest negative potential of corrosion occurrence. The data obtained shows a reading of -215 mV found in 30SG2 resulting in the lowest corrosion possibility compared to other specimens on 90 days. This proves that the potential benefits of GO can only be achieved by maintaining a low percentage of blended mortar. This can also be shown in saltwater conditions where 0.02% GO is pronounced as the lowest probability of corrosion. This can be shown at 90 days, the control mix of 30SG0 depicted the highest probability of corrosion with a -390mV reading. In contrast, 30SG2 exhibited a significantly lower potential corrosion by -275 mV underlying the optimum GO percentage in mitigating corrosive penetration.

Generally, it can be concluded that 0.02% GO-blended mortar (30SG2) consistently demonstrated the lowest HCP reading under both exposure conditions. The improved corrosion resistance portrayed by 0.02% of GO can be attributed to several major mechanisms. As mentioned in the previous chapter, GO owns a well-dispersed two-dimensional structure that acts as a protective barrier which consequently enhances the penetration resistance of corrosive media such as oxygen, water and chloride ions to the steel reinforcement (Rezakhani et al., 2023). Not only that but GO also tends to contribute to an adequate amount of microstructure refinement due to the filling effect.

This ultimately produces a denser and less permeable GO-blended mortar. On top of that, 0.02% of GO also leads to a more torturous pathway for corrosive penetration (Qureshi & Panesar, 2019). Nevertheless, as the GO percentages increased, it seemingly led to a reduction of corrosion resistance ability. This may happened due to the agglomeration of GO resulting in the disruption of the cement hydration process and poor protective barrier. Based on the HCP reading for both conditions, it is noticeable that the highest probability of corrosion was obtained in the control mix (30SG0) with readings of -280 mV in normal condition and -390 mV for saltwater condition. This exposed the vulnerability of conventional mortar when exposed to chloride-rich environment conditions. However, it is also crucial to take note that GO percentage beyond 0.02% as seen in 30SG4, 30SG6, 30SG8 and 30SG10 did not show any significant improvement in corrosion resistance. The reading for this specimen revealed more negative values of HCP compared to 30SG2 highlighting the critical observation of adequate GO percentage in blended mortar.

In conclusion, this test comprehensively provides clear evidence of how corrosive penetration leads to corrosion probability in embedded steel of blended mortar. Nevertheless, it is also worth noticing that the inclusion of GO specifically 0.02% helps in improving the durability of the blended mortar under these exposed conditions. This shall lead to more potential utilization of GO as an effective additive in cementitious material to ensure the durability of reinforced cementitious-based material.

Table 4.7
Corrosion Condition According to Half Cell Potential (ASTM C876-15)

E_{corr} vs CSE	Corrosion Condition
$E_{corr} > -200$	Low (10% of risk corrosion)
$-200 > E_{corr} > -350$	Intermediate corrosion risk
$-350 > E_{corr} > -500$	High (<90% of risk corrosion)
$E_{corr} < -500$	Severe Corrosion

Table 4.8
Half Cell Potential Reading for GO-Blended Mortar

	Normal condition			Saltwater condition		
Mix	30 days	60 days	90 days	30 days	60 days	90 days
30SG0	-70	-140	-280	-98	-195	-390
30SG2	-54	-108	-215	-69	-138	-275
30SG4	-67	-134	-267	-73	-145	-290
30SG6	-69	-138	-275	-78	-155	-310
30SG8	-72	-144	-288	-87	-173	-346
30SG10	-72	-145	-289	-92	-184	-367

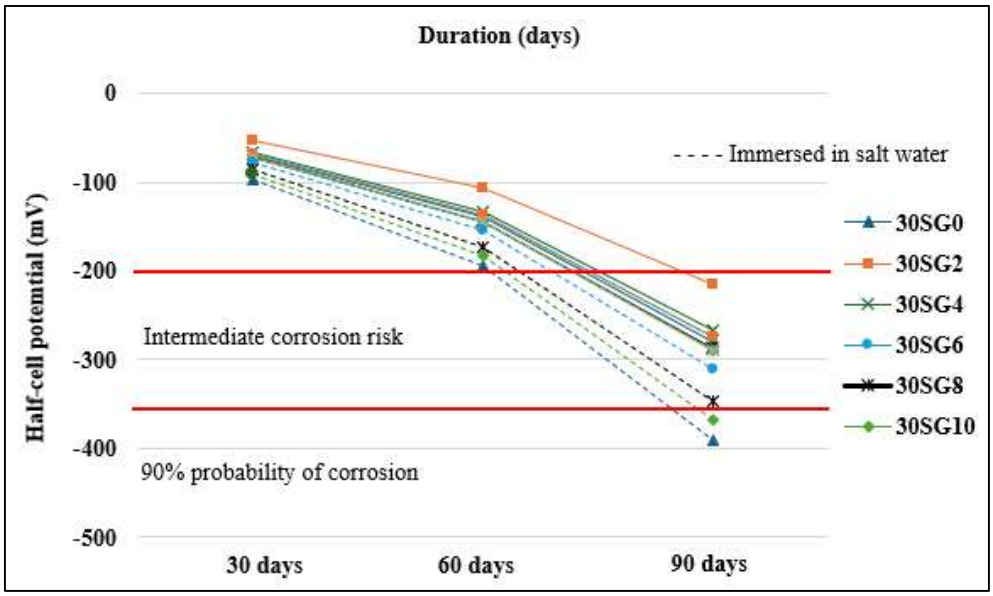


Figure 4.28 Influence of Various GO to Corrosion Probability in Blended Mortar

4.7 Porosity and Microstructure Properties

This section focussed on the morphology and size distribution of GO-blended mortar through SEM and MIP tests.

4.7.1 Scanning Electron Microscopy (SEM)

This section focussed on the microstructural analysis of the GO-blended mortar through SEM. The findings from this test shall reveal the influence of GO percentages

on the morphology and microstructure of blended mortar. Henceforth, every SEM micrograph for each sample can be presented in the Figure 4.29. Firstly, it is essential to consider control mortar (30SG0) as depicted in the figure as it portrayed the typical microstructure of blended mortar specifically GGBS. The cement matrix exhibited a relatively porous structure with the presence of a needle-like crystal representing the calcium silicate hydrate (C-S-H) formation. It is also noticeable some crystalline phases indicate the calcium hydroxide (CH) crystal which is commonly observed as a larger plate structure. Overall observation concluded that the control sample of blended mortar resulted in moderate density but was not fully optimized by the hydration product. However, a different observation can be seen with the incorporation of 0.02% GO (30SG2) within the blended mortar as shown in Figure 4.30. This can be explained as it demonstrated a significant microstructure refinement compared to the control sample (30SG0). The SEM images reveal a compact and even denser microstructure formation indicating GO's filling mechanism performed significantly with the cement hydration product.

This aligns with Wang et al. (2019) findings who confirmed that adding an adequate dosage of GO facilitates the formation of calcium silicate hydrate (C-S-H). Not only that but GO also helps in forming a lamellar structure and numerous oxygen functional groups when it reacts with cementitious material. In detail, the formation of C-S-H is observed within the cement matrix as the needle-like contributes to filling the void spaces which ultimately enhances the hydration product. The inclusion of GO in the blended cement matrix demonstrates the formation of hydration crystal that significantly improves the pattern of the microstructural composite. Not only that but it also can be seen as the growth of crystalline flower-like floral shape pattern appears to gradually thinner blended well with C-S-H formation which eventually leads to denser cement matrix. The findings in the study align with the microstructural observation by Akarsh et al., (2022), where it has been concluded that at a low dosage of GO below 0.03%, a flower-like structure has formed within the cement matrix. Moreover, with an adequate of GO percentages (0.02%), it also appears that a homogenous dispersion has been achieved due to low signs of agglomeration. This occurs due to the nucleation effect of GO as it facilitates the cement hydration process, leading to robust microstructure. This additional Figure 4.30 presents a close-up SEM image offering a detailed analysis of the 0.02% GO (30SG2) sample. Align with the previous discussion, the image specifically reveals the development of column-shaped hydration crystals

blooming into interlinked polyhedral pattern hydration crystals. These formations of polyhedral pattern act as pores and crack fillers, preventing any crack propagation to the blended microstructure (Alla & Asadi, 2023). Moreover, it also can be reported that, in the cavity and openings of the blended cement matrix, the floral hydration crystal established a cross-connection structure leading to strength enhancement of the GO-blended mortar. This close-up also suggested the GO's bridging effect as it enhanced crack resistance by hindering multiple-scale propagation. Nevertheless, as the percentage of GO increases higher than 0.02%, it can be seen that the SEM images started to portray linear deterioration of microstructure. This can be explained as 0.04% GO (30SG4) displaying inconsistent refinement as some areas are localized with hydration product, but some indicate an early sign of GO agglomeration. The close up image shown in Figure 4.30, it can be seen that the irregular polyhedral crystal started to form within the GO-blended mortar, which eventually leads to agglomeration or clumping of GO. The formation of agglomeration happened due to stress concentration points with the cement matrix leading to random spots left un-filled. Not only that but it also can stated that as further increase in GO percentage (0.06%, 0.08%, and 0.10%), the degree of GO agglomeration becomes more visual and worse. This can be proved as SEM images illustrate larger and irregular clusters of GO scattered within the cement matrix. Moreover, these agglomerate particles continue to disturb the C-S-H gel network resulting in poor bonding effectiveness and decrease in mechanical performance (Wang et al., 2015). Consequently, the formation of ettringite needle appears to be less significant and the porous started to form vigorously. This also hinders the desired nucleation sites for hydration products and stagnates the development of interconnected microstructure.

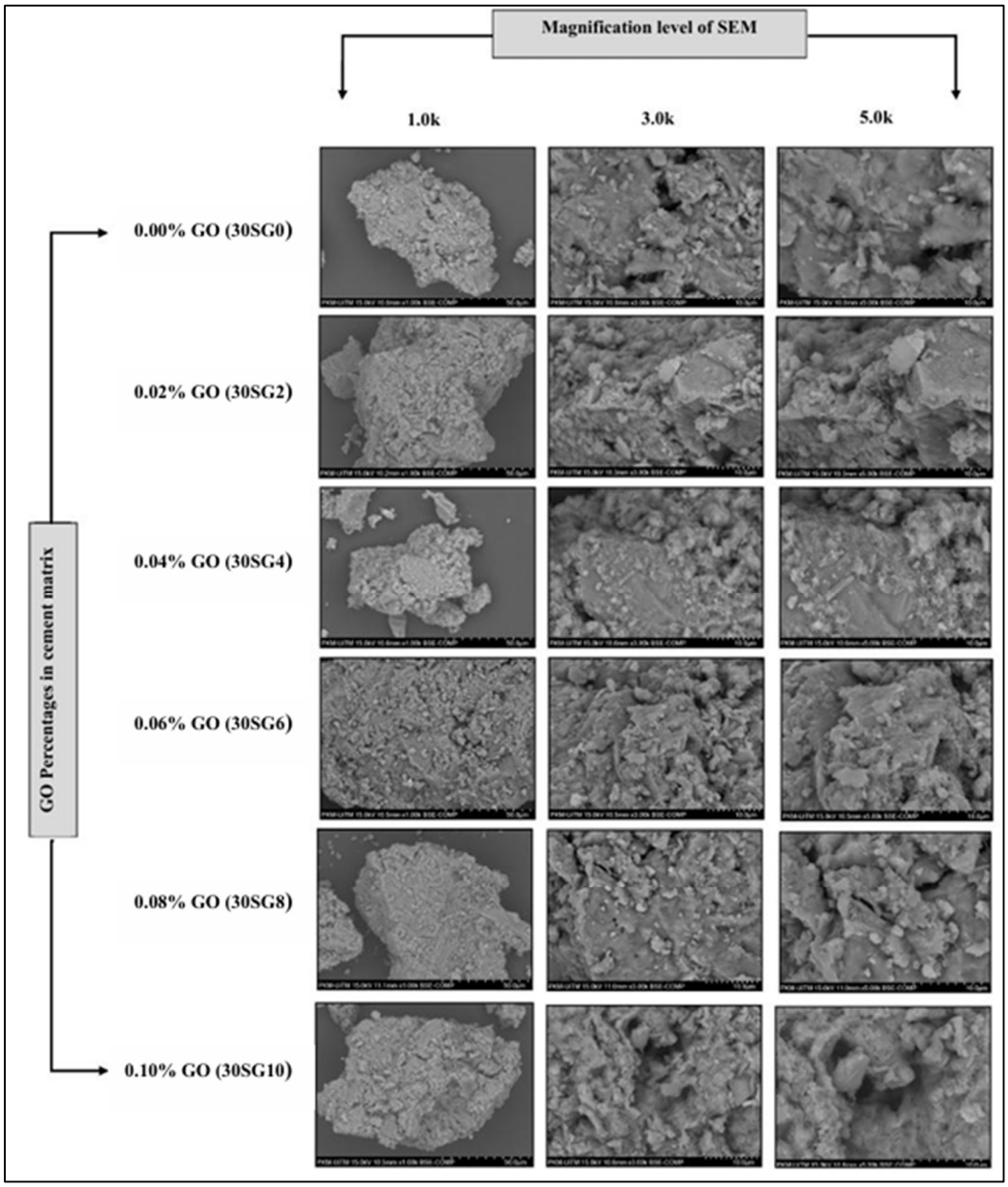


Figure 4.29 SEM Images of Cement Hydration Crystals in a Cementitious Matrix at Varying Dosages of GO at Different Magnification Level

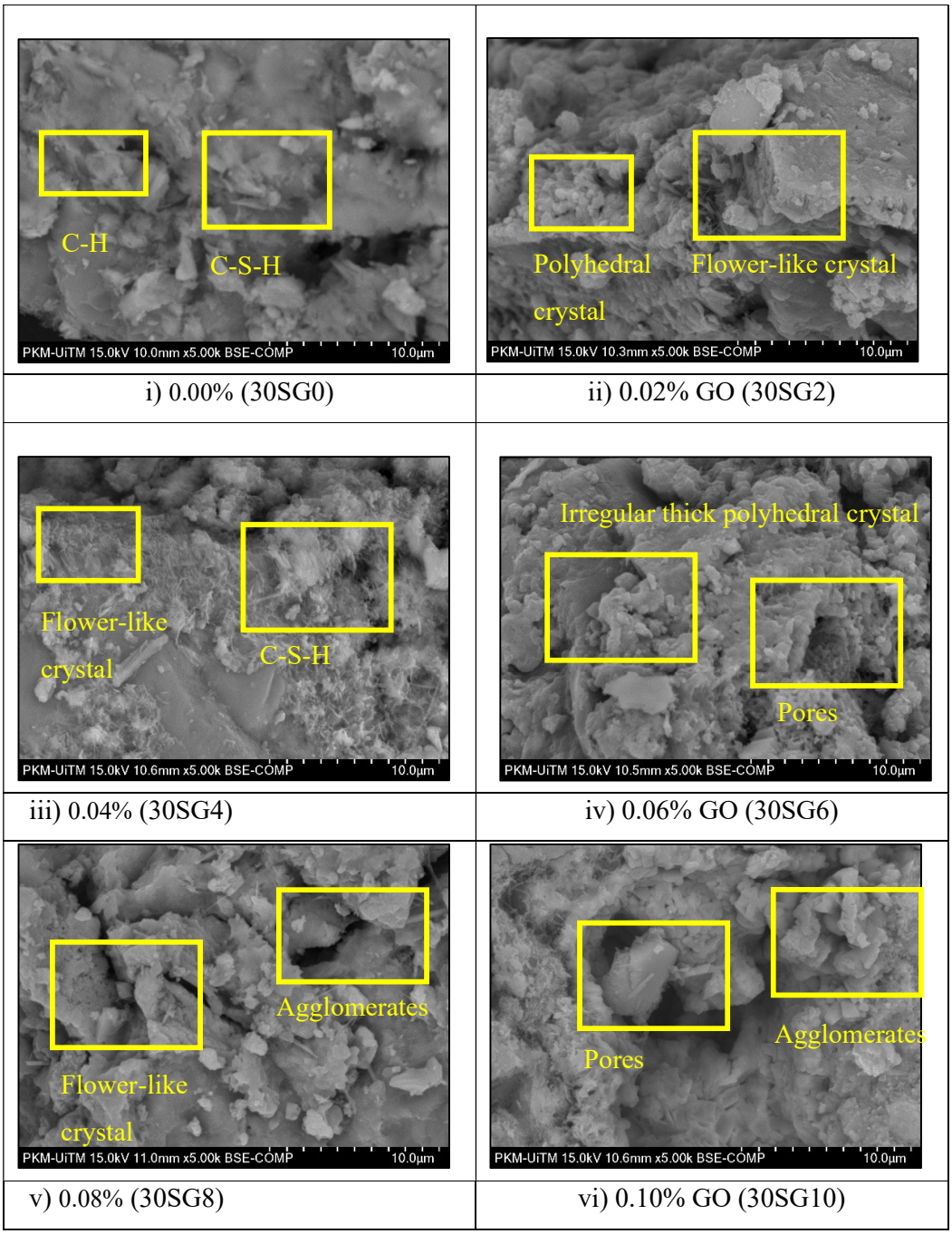


Figure 4.30 Close-Up Magnification SEM Image of GO-Blended Mortar Samples

4.7.2 Mercury Intrusive Porosimetry (MIP)

The discussion of results and analysis continues with the provided Mercury Intrusion Porosimetry (MIP) results. Generally, the pores in the hardened cement paste can be categorised into several scales of nano scale gel (<10 nm), micro scale (10-10,000 nm), as well as macro scale (>10,000 nm). Therefore, Figure 4.31 visualised the pore structure characteristics of various GO inclusions in the blended mortar samples. The designed curves from the figure represent the cumulative pore volume along with pore diameter for each mix. This shall give an insight into the microstructure of the samples and the potential impact on the application of corrosion resistance. Therefore, it can be seen that 0.02% of GO in 30SG2 is profound to be the lowest cumulative pore volume compared to all samples. The black line representing 30SG2 is consistently located below all other line curves from each scale. This explained the utilisation of GO even at small and controlled percentages, effectively delivering the best result in pore refinement. This can be explained as 0.02% GO tends to lead to a denser, yet compact microstructure compared to other samples. This may have happened due to the GO nucleation sites, as it facilitates the formation of C-S-H gel, which consequently promotes a more homogenous cement matrix. Not only that, but due to the exceptionally high surface area of GO, it helps to adsorb free water and effectively fasten the reactivity with other cementitious material during mixing. This shall foster a more compact arrangement of hydration products within the cement matrix (Meng et al., 2021). On top of that, the utilization of GO also leads to more compacted microstructure by acting as effective pore-filling agent. This allows the physical occupying mechanism within the matrix leading to greater bridging effect.

Nevertheless, as the percentage of GO increases beyond 0.02%, the detrimental effect, such as agglomeration, begins to dominate the samples, leading to an increase in overall porosity. As an overall observation, a progressive increase in the cumulative pore volume was shown in samples of 0.04% GO (30SG4), 0.06% GO (30SG6), and 0.08% GO (30SG8). The highest curve line has also been nominated by the 30SG10 sample with 0.10% GO. This can be explained as a higher percentage of GO, which tends to agglomerate due to the van der Waals forces and its own high specific surface area. This agglomeration defect disturbed the formation of a proper dense cement matrix by creating larger voids, which directly acted as weak zones within the hardened cement matrix (Long and Gu, et al., 2018). This can also lead to air entrapment during the

mixing process, resulting in even larger pores and voids. Furthermore, the poor dispersion of GO can also lead to greater air entrapment during mixing, stunting the growth of the hydration product.

To summarise, the MIP results demonstrate the influence of GO on the microstructure of the blended mortar, which is highly dependent on the included percentages. This led to the addition of 0.02% of GO, which significantly proves the best pore refinement within the pore structure, resulting in denser material with the lowest cumulative pore volume recorded compared to other samples. This also justifies the importance of a proper compact and dense sample towards enhanced durability of the blended mortar. By the MIP results, it can be shown that 30SG2 managed to reduce the risk of penetration potential, especially the corrosive penetration media. However, a higher GO percentage results in porosity, leading to a long-term performance defect. Based on the mercury intrusion porosimetry (MIP) test results, the porosity of each sample was determined to evaluate the pore size distribution within the graphene oxide (GO)-blended mortar matrix. The experimental report provided the necessary parameters for this computation, specifically the bulk density and total intrusion volume for each mixture. Utilizing these values within the governing equation establishes a clear correlation between GO content and pore volume. The computed porosity values are summarized in Table 4.9.

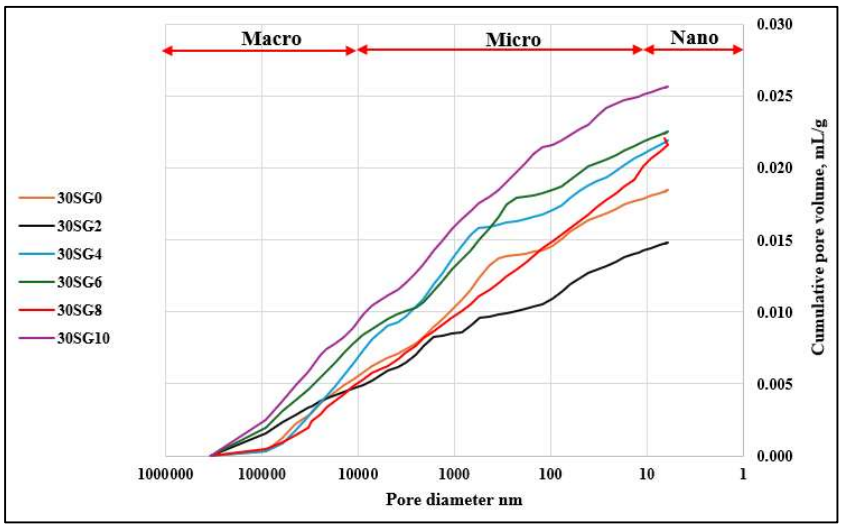


Figure 4.31 MIP Results for Various GO in Blended Mortar

Table 4.9
Calculated Porosity Value for Each Samples Based on MIP Test Report

Mixture	Density (g/mL)	Total Intrusion volume (mL/g)	Porosity (%)	Reduction Difference (%)
30SG0	2.4510	0.0920	18.40	-
30SG2	2.4500	0.0801	16.41	10.82
30SG4	2.4507	0.0803	16.44	10.65
30SG6	2.4509	0.0855	17.32	5.87
30SG8	2.4510	0.0875	17.66	4.02
30SG10	2.4510	0.0882	17.78	3.37

Therefore, the analysis of porosity begins with a baseline of 30SG0 acted as the control sample with 0.00% of GO as shown in Figure 4.32. It can be seen that the control sample portrayed a 18.40% of porosity indicating a plain sample with non-nano-modification. Nonetheless, an obvious observation was determined as a sharp decrease in porosity value by 16.41% by 30SG2, which contains 0.02% of GO. This shows a drop of 10.82% compared to the control sample. This reduction of porosity highlighted the influence of GO as pore-modifying material due to its filling effect as well as the nucleation sites for C-S-H growth. This also shows that how GO enhanced the pore network within the cement matrix and reducing the potential of external penetration. The discussion continues for the 30SG40 with 0.04% GO as it indicated slight increase in porosity by 16.44%. Beyond this percentages, an additional GO in the blended mortar does not lead to any expected low porosity as the potential detrimental effect begins to dominate. This explains on the porosity trend gradually increases with the percentage of GO content specifically from 0.04% GO (16.44%), the porosity rises to 17.32% at 0.06% GO, then to 17.66% at 0.08% GO, and finally to 17.78% at 0.10% GO. While these porosity values are still considered to remain lower than the control sample but the upward trend through GO's influence in the blended mortar should not be neglected. The increase in porosity at higher percentage of GO primarily attributed by the non-homogeneous mixture of the samples. This leads to the fundamental of GO itself as high surface area exhibited a stronger tendency to agglomerate (Li et al., 2017). This shall lead to a larger void being formed in the cement matrix and ultimately increase the total porosity. Not only that but the poor dispersion of excessive GO also contributed as the major factor in the context (Zhao et al., 2018). As an example, even though sample of 30SG10 with 0.10% GO observed to remains lower than control sample by 17.78% of total porosity, it still indicates that the challenge of agglomeration remains still.

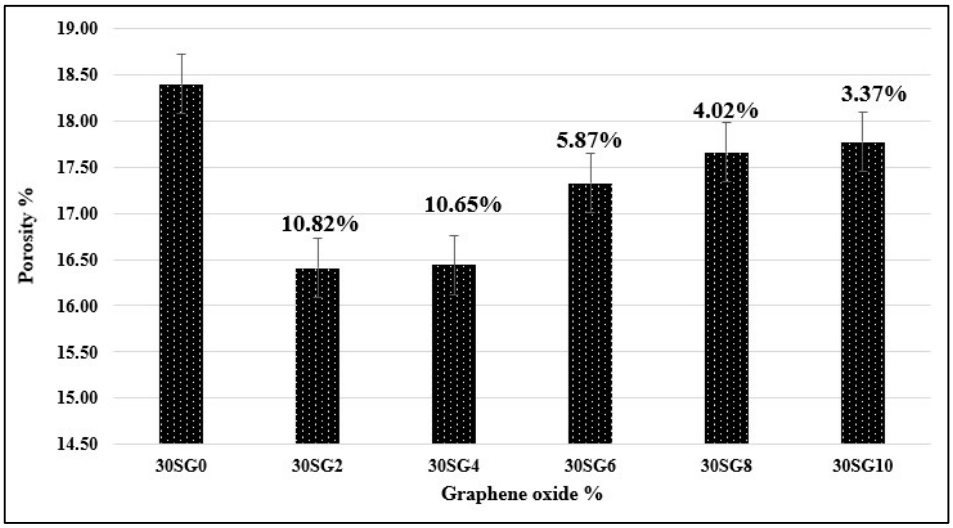


Figure 4.32 Pore Structure of GO-Blended Mortar

4.7.3 X-Ray Diffraction (XRD) Analysis for GO-Blended Mortar

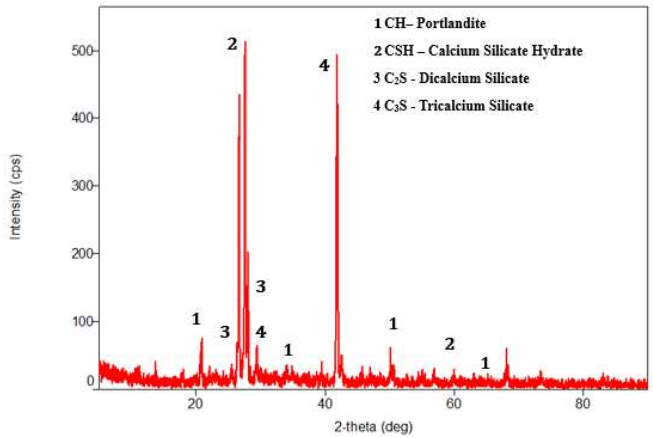
This sections analysed on the crystalline phases of the GO-blended mortar which notably on Portlandite (Calcium Hydroxide), and the formation of the amorphous Calcium Silicate Hydrate (CSH) gel. Therefore, by establishing a comparative baseline between each specimens, the role of GO in promoting pore refinement densification and nucleation effect can be effectively justified.

Based on Figure 4.33, it can be seen that the control specimens contain 30% of GGBS serves as the fundamental baseline in this analysis. The control specimen can be characterized as high and sharp diffraction peaks reaching intensities of 500 count per seconds (cps). The figure also shows the existence of Portlandite and CSH gel at the 18° and 34° at 2 theta. This high intensity reflections are common indicative formation found in crystalline structure of GGBS within blended cementitious based system. Not only that but, based on the control sample also the left over product were observed such as C_2S and C_3S. This leads to lesser pore refinement and redundant product of cement hydration.

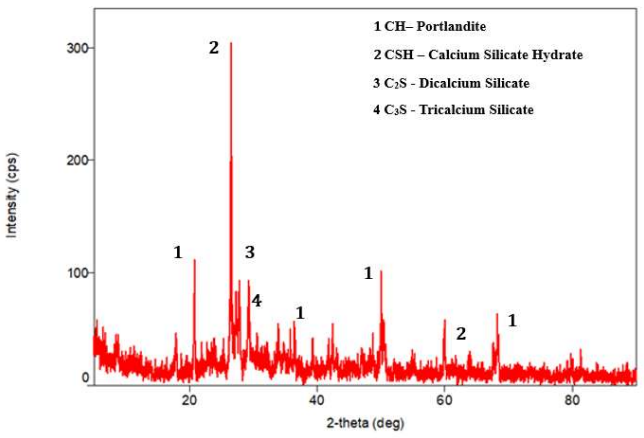
Further evidence indicates that the addition of 0.02% GO (30SG2) marks a significant improvement in the microstructure of the mortar. This improvement is characterized by a substantial drop in the intensity of crystalline peaks from the control baseline to approximately 300 CPS. This reduction justifies the conclusion that the nucleation effect of GO was effectively initiated during the cement hydration process.

This is because GO provides a high surface area with oxygen-containing functional groups that facilitate the creation of growth sites for hydration products. This is further supported by the diminished presence a few of C_2S and C_3S peaks in the XRD patterns, which correlates with the accelerated formation of C-S-H gel. Consequently, a higher degree of nucleation and a greater volume of hydration products are observed even at this low dosage of GO. This process eventually optimizes the pore refinement of the blended mortar, aligning with the mechanical and microstructural findings observed elsewhere in this study. Not only that but as a comparison to control specimen, the amount of CH was more in GO-blended mortar specifically at 0.02% GO. This is known as CH can be used as an indicator for a degree for hydration. This also align with Ur Rehman et al., (2018) where the CH intensity was observed increased with an adequate amount of GO dosage in cement composite specimens.

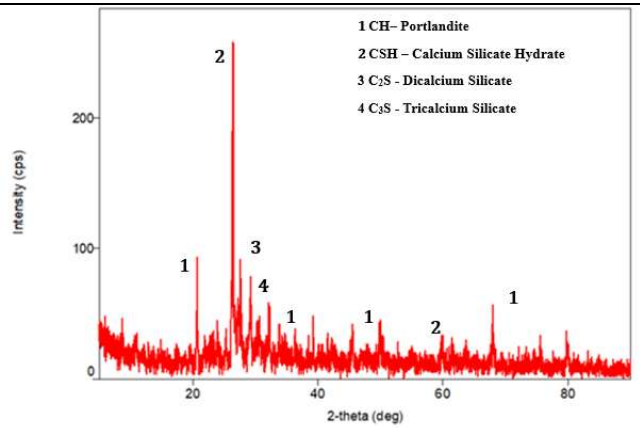
As the analysis continues, the range of 0.04% to 0.08% continues to exhibit similar findings, where it indicates the availability of the GO surface area continues to facilitate as a nucleation site for hydration growth. However, as the result approached to 0.10% of GO, a significant shift in the diffraction pattern can be observed. The XRD pattern started to a notable increase in background noise, which signifies the onset of the GO agglomeration process. This can be explained as at high dosage, the dispersive forces within the GO stated to deteriorated and restacking. These eventually lead to agglomeration defects, creating disordered amorphous zones (X. Li et al., 2017). This also provides strong evidence of a critical limit to the nucleation benefits of GO.



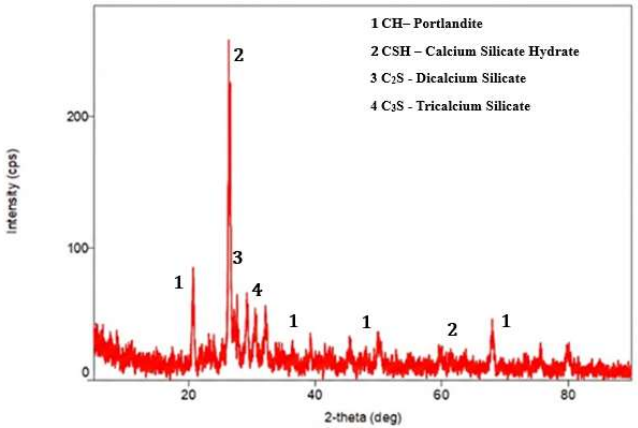
i) 0.00% (30SG0)



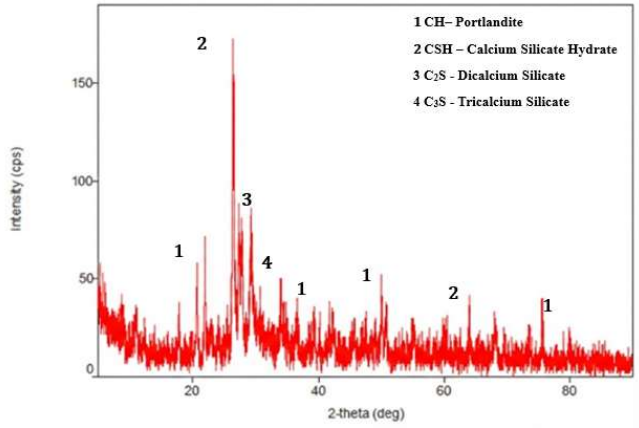
ii) 0.02% (30SG2)



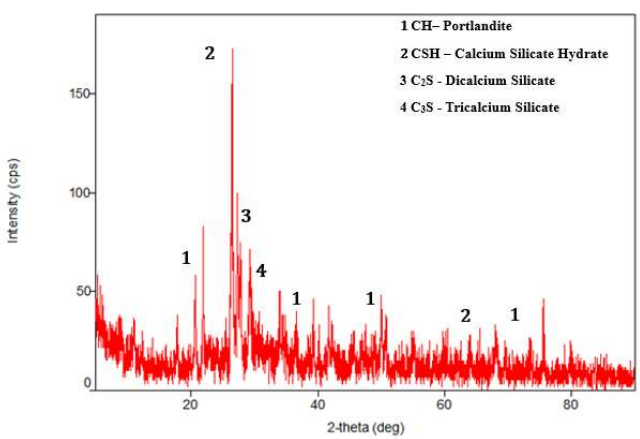
iii) 0.04% (30SG4)



iv) 0.06% (30SG6)



v) 0.08% (30SG8)



vi) 0.10% (30SG10)

Figure 4.33 XRD Pattern for GO-Blended Mortar Specimens

4.8 Summary of Binder Modification

Upon establishing the 30% GGBS as the baseline , the binder modification was performed to evaluate the performance of GO as nanomaterial additive. The experimental results dominated by 30SG2 mix, containing 0.02% GO, as the optimum threshold of nanomaterials additive. This is because it managed to demonstrate a significant influence on the mechanical as well as durability properties as GO-blended mortar. To be more precise, an adequate dosage of GO delivers three major mechanism of filling, bonding as well as the nucleation effect to the mortar system. This demonstrates the influenced of GO as active sites for accelerating growth of C-S-H gel which indirectly enhance the pore refinement mechanism within the blended mortar. This structural densification was further proved in the durability parameters where 30SG2 mix achieved a “very low” chloride permeability rating in RCPT. Not only that but HCP monitoring a significant results as 0.02% GO increased the tortuosity of the matrix by delay the onset of active corrosion. Not only that but based on the MIP results, 0.02% of GO managed to extend to pore filling effect as it modulates the cement hydration product resulting in more resistant blended mortar. Furthermore, through XRD analysis also it can be stated that the additional of GO influenced to the growth of CSH which justifies the nucleation mechanism within the blended matrix. This significantly facilitates the hydration product into a denser microstructure and high degree of pore refinement. Thus, this proves that the 30SG2 formulation represents the peak synergistic balance between supplementary cementitious materials and nanomaterials.

CHAPTER 5
MASS LOSS CALCULATION

5.1 Introduction

This chapter discussed the experimental results that can define the corrosion performance resistance of GO-blended mortar, with the analytical approach of Mass loss. This section delivers the final phase of the study where it measures several of critical parameters of Mass Loss (m) including Time to Depassivation (T_{HCP}), Active Corrosion Time (t) and Total Corrosion Current (I). Generally, the value of T_{HCP} was derived from the existing data of Half Cell Potential (HCP), which serves as the time factor within the corrosion period. The data itself purposely defined the duration of non-corroding Initiation Period and consequently established the Active Time Corrosion (t) for every sample in the study. Moreover, the Mass Loss (m) can be considered as the final outcome, derived from integrating the calculated active time (t) and rate factor of current (I) into Faraday's Law. This serves specifically as the measurement of structural damage due to the corrosion itself. Therefore, it reveals the quantitative value in grams, which can validate the enhancement of various GO percentages performance within the blended mortar. It is also worth noting that this section extends the discussion of the Half Cell Potential (HCP) results. While HCP provides a durability properties of GO-blended mortar against corrosion, the mass loss data quantifies an analysis of physical degradation of the steel rebar. Henceforth, Figure 5.1 depicted the main parameters required for the Faraday's law to calculate the mass loss of rebar due to corrosion. This chapter also focussed on using specifically 30SG2 sample as calculation example to ensure continuity of the discussion.

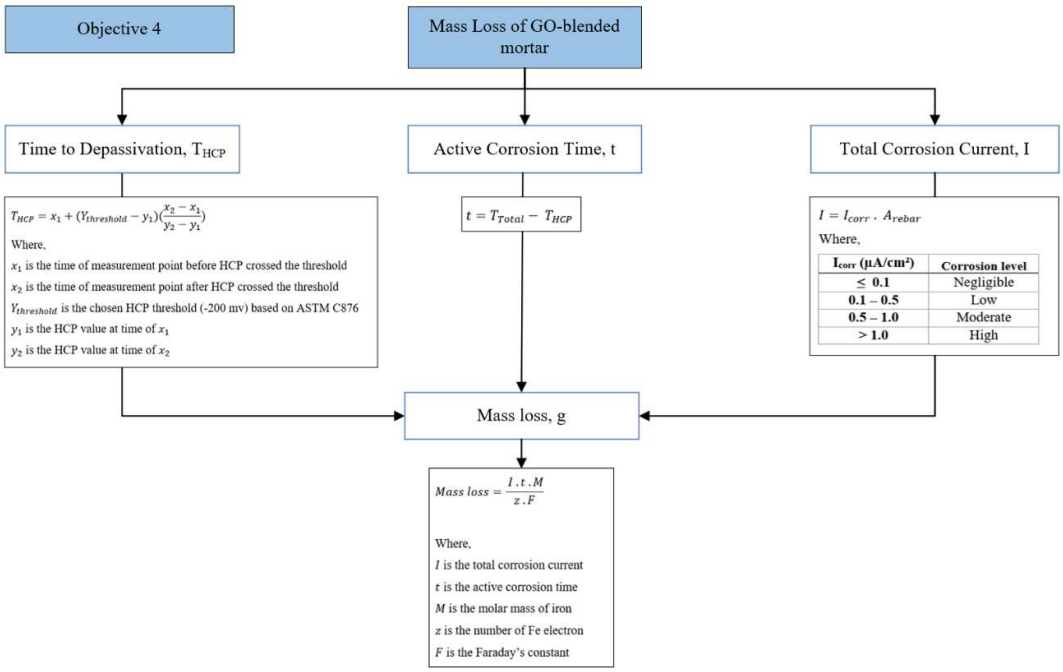


Figure 5.1 Framework for Mass Loss Calculation

5.2 Time to Depassivation (T_{HCP})

As mentioned in the previous subsection, the Half Cell Potential (HCP) served as a crucial factor for experimental observation, which can define the passive protection stage against corrosion. The fundamental theory of corrosion relates the Time to Depassivation (T_{HCP}), which precisely defines the passive phase, explaining the existence of a protective film that remains intact. This also shows that the value of Mass Loss (m) is still zero. As provided by the standard of ASTM C876 (2015), the HCP measurement helps to reveal the probability of corrosion rate whenever the potential drops below -200 mV. This indicates a 10% probability that active corrosion has been chemically compromised, which explains why the T_{HCP} has ended. Therefore, a linear interpolation equation has been derived in order to obtain the required T_{HCP} in this study.

As for the study, the HCP measurement has been tested under two conditions, which were the normal condition and the saltwater condition as shown in Table 5.1. As an example for the normal condition, shows that the control sample (30SG0) has crossed the critical threshold of passivation by 73 days. This establishes a baseline for the protective period provided by the control blended mortar without GO. Nevertheless, the optimal sample of 30SG2 has successfully delayed the depassivation up until 86 days,

indicating an additional 13 days of extension compared to the control sample. Therefore, the calculation for these measurements can be shown below.

Not only that, but as for the saltwater condition, due to a greater chloride concentration and exposure to corrosion, the T_{HCP} were predicted to be low across all mixes compared to normal condition samples. Nevertheless, an absolute protective benefit has been portrayed by 30SG2, reaching up to 74 days, which is higher compared to the control mix. Based on the results, it can be concluded that the consistency of 0.02% in 30SG2 for both conditions significantly forms a greater protective barrier against corrosive media penetration. Henceforth, the full calculated T_{HCP} for 30SG2 in normal condition has been determined. Moreover, the results of T_{HCP} for all samples and tabulated in Table 5.2.

Table 5.1
Half Cell Potential Reading for GO-Blended Mortar

	Normal condition			Saltwater condition		
Mix	30 days	60 days	90 days	30 days	60 days	90 days
30SG0	-70	-140	-280	-98	-195	-390
30SG2	-54	-108	-215	-69	-138	-275
30SG4	-67	-134	-267	-73	-145	-290
30SG6	-69	-138	-275	-78	-155	-310
30SG8	-72	-144	-288	-87	-173	-346
30SG10	-72	-145	-289	-92	-184	-367

$$T_{HCP} = x_1 + (Y_{threshold} - y_1)(\frac{x_2 - x_1}{y_2 - y_1}) \quad (5.1)$$

Where,

x_1 is the time of measurement point before HCP crossed the threshold

x_2 is the time of measurement point after HCP crossed the threshold

$Y_{threshold}$ is the chosen HCP threshold (-200 mv) based on ASTM C876 (2015)

y_1 is the HCP value at time of x_1

y_2 is the HCP value at time of x_2

$$T_{HCP} = 60 + (-200 - (-108))(\frac{90}{-215-(-108)})$$

$$T_{HCP} = 85.79$$

$$T_{HCP} \approx 86\ days$$

Table 5.2
Time to Depassivation, T_{HCP} For Every Mix in Normal and Saltwater Condition

Mix	Normal Condition	Saltwater Condition
	T_{HCP}, days	T_{HCP}, days
30SG0	73	61
30SG2	86	74
30SG4	75	71
30SG6	74	69
30SG8	72	65
30SG10	72	63

5.3 Active Corrosion Time (t)

One of the major parameters in the study was also the Active Corrosion Time (t), which represents the total duration during which the steel rebar is actively corroding. This parameter can be a direct consequence of T_{HCP}, which is defined as the after effect of the passive film that has been fully deteriorated due to penetration of corrosive media. Therefore, the Active Corrosive Time can be calculated by knowing the difference between the total days of 90 days of exposure, known as T_{total} and the determined time to Depassivation of T_{HCP}. The formula used for this parameter followed as below with an example of 30SG2 in a normal condition:

$$\begin{aligned} t &= T_{Total} - T_{HCP} \\ &= 90 - 86 \\ &= 4\ days \end{aligned} \tag{5.2}$$

As an example for the normal conditions, 30SG2 portrayed the longest T_{HCP} by 86 days, successfully reducing the active corrosion time (t) to the lowest at 4 days. This result also justifies that the inclusion of an adequate percentage of GO (0.02%) significantly reduced the probability of the formation of corrosion. Moreover, Table 5.3 indicated the calculated active corrosion time for every sample in the study for both conditions. Following the previous Table 5.2, it can be seen that in normal conditions, 30SG8 and 30SG10 are the shortest T_{HCP} of 72 days. This leads to the longest active time calculated compared to all samples by 18 days. The longer the active corrosion time recorded, the higher the tendency of corrosion formation on the steel bar within

the GO-blended mortar. Similarly, in the saltwater condition, 30SGO depicted the shortest day of T_{HCP}, resulting in the longest active time of 29 days.

Table 5.3
Active Corrosion Time (t) for Every Mix in Normal and Saltwater Condition

Mix	Normal Condition		Saltwater Condition	
	T_{HCP} (days)	t (days)	T_{HCP} (days)	t (days)
30SG0	73	17	61	29
30SG2	86	4	74	16
30SG4	75	15	71	19
30SG6	74	16	69	21
30SG8	72	18	65	25
30SG10	72	18	63	27

5.4 Total Corrosion Current (I)

The purpose of the Total Corrosion Current (I) was to identify the speed at which iron atoms are converted electrochemically into the expansive rust product. To be more precise, the lower the current density being recorded, the lower the accumulated mass loss of the rebar. However, a corrosion current density or also known as I_{corr} must be determined in the first place which refers to the corrosion rate exhibited on the exposed surface area of the steel bar. In definition, I_{corr} is the current generated due to the corrosion reaction per unit area of the exposed area of steel bar. Hence, in this study, I_{corr} was determined by using the interference method, whereby the corrosion rate was reliably inferred through the Rapid Chloride Permeability test (RCPT) results. The major principle of the interference method relies on the fundamental principle that the denser the mortar, the lower the permeability and the higher the electrical resistivity. This is because the higher resistivity of the electrical means it restricts the charge carrier mobility of the corrosive media, preventing a lower risk of corrosion (Kaur et al., 2020). According to Matilla et al., (2024), the corrosion current density can be established by correlating the electrochemical rate and the expected structural permeability. Therefore, Table 5.4 shows the relevant range proposed as the interference method used to determine the corrosion current density (I_{corr}).

Table 5.4
Range of Corrosion Current Value Related to Corrosion Level (Matilla et al., 2024)

I_{corr} (µA/cm²)	Corrosion level
≤ 0.1	Negligible
0.1 – 0.5	Low
0.5 – 1.0	Moderate
> 1.0	High

Therefore, based on the RCPT results in Table 4.6, it acts as an indicative superior barrier, which allowed to infer proportionally the corrosion current density (I_{corr}). Thus, Table 5.4 indicates the categorized I_{corr} based on RCPT data as primary indicator. It can be concluded that most of the mixes fall into the moderate and high categories, which confirms the corrosive penetration media. Nevertheless, 30SG2 portrayed different results by achieving 0.5 µA/cm², placing the category as a low corrosion level. As for the correlation discussion with the RCPT data, the higher the RCPT results, the higher the I_{corr}. This directly shows the possession of the lowest electrical resistivity, which eventually facilitates the rapid ion flow for corrosion reaction. However, as for the optimal mix for 30SG2, it successfully visualised the inclusion of an adequate amount to provide a denser microstructure with high electrical resistivity. Nevertheless, in order to obtain the total corrosion current, the value of I_{corr} were multiplied by the total area of the steel rebar, A_{rebar} embedded in the GO-blended mortar. In conclusion, this corrosion current density results explain the potential of GO in providing a protective barrier against corrosion propagation. Hence, the corrosion current density for each GO-blended mortar mixes has been tabulated in Table 5.5.

Table 5.5
Corrosion Current Density for Every Mix

Mix	I_{corr} (µA/cm²)	Corrosion level
30SG0	1.0	Moderate
30SG2	0.5	Low
30SG4	1.0	Moderate
30SG6	1.5	High
30SG8	1.5	High
30SG10	1.5	High

5.5 Mass Loss (m)

The final outcome from the previous parameters leads to the theory concept of Mass Loss (m). The mass loss can be defined as the quantitative measure of structural damage due to corrosive-induced corrosion. To be more specific, it helps in providing material performance by quantifying the grams of steel rebar consumed due to the active corrosion process. This mass loss is a direct consequence of the electrochemical reaction, which is being calculated using Faraday's Law equation.

$$Mass\ loss = \frac{I\ .t\ .M}{z\ .F} \tag{5.3}$$

where,

I is the total corrosion current

t is the active corrosion time

M is the molar mass of iron

z is the number of Fe electron

F is the Faraday's constant

The mass loss requires an additional constant parameter, such as the Molar mass of iron (M). The mass of one mole of iron is equal to 55.845 g/mol. Moreover, the valence value also represents the number of electrons exchanged during the anodic reaction, which is 2. Finally, Faraday's constant revealed the charge carried by one mole of electrons, which is 96485 C/mol. In order to provide a solid evidence on the influence of GO as a protective barrier in the blended mortar, a complete calculation of mass loss was determined using 30SG2 in normal condition as an example. This calculation tends to combine all collected parameters achieved by 30SG2 including the time of depassivation T_{HCP}, corrosion current density (I_{corr}) and active time corrosion (t). Therefore, Table 5.6 indicates the provided variable and constant for this calculation to ensure a more comprehensive understanding of the mass loss calculation.

Table 5.6
Mass Loss Variables for Mix 30SG2

Constant	Value	Unit
Diameter of steel rebar, ⌀	12	mm
Exposed Length, L	175	mm
Total exposure time, T_{total}	90	days
Steel surface area, A_{rebar}	65.97	cm^2
Molar mass	55.845	g/mol
Valence	192970	C/mol
Variable	**Value**	**Unit**
Time to Depassivation, T_{HCP}	86	days
Current Corrosion Density, I_{corr}	0.5	µA/cm²
Active Corrosion Time, t	4	days

The calculation started with establishing the Total Corrosion Current (I) where it is one of the major parameters within the mass loss equation derived from I_{corr} and the exposed surface area, A_{rebar}. Therefore, the total corrosion current can be calculated as:

$$A_{rebar} = \pi d \; x \; L \tag{5.4}$$
$$= \pi(12) \; x \; (175)$$
$$= 6597.34 \text{ mm}^2$$
$$= 65.97 \text{ cm}^2$$

$$I = I_{corr} \; . \; A_{rebar} \tag{5.5}$$
$$= 0.5 \; \mu \frac{\text{A}}{\text{cm}^2} . \; 65.97 \text{cm}^2$$
$$= 3.30 \text{ x } 10^{-5} \; A$$

Note : 1µ is equivalent to $1\text{x}10^{-6}A$

After determining the total corrosion current, the calculation continued with active corrosion time parameter as per discussed in the previous sub section of 5.3 in this chapter. Therefore, the active corrosion time has been determined by derived total exposure day and the time of depassivation, T_{HCP}.

$$t = T_{total} - \; T_{HCP}$$

$$= 90 - 86$$
$$= 4\ days$$
$$= 345{,}600\ s$$

Finally, the calculation of mass loss using the Faraday's Law has been determined in the study. The calculation continues as follows;-

$$Mass\ loss = \frac{I\ .t\ .M}{z\ .F}$$

$$= \frac{(3.30 \text{ x } 10^{-5}\ A).\ (345,600\ s).\ (55.845\ \frac{\text{g}}{\text{mol}})}{2\ \left(96485\ \frac{\text{C}}{\text{mol}}\right)}$$
$$= 0.0033\ g$$

5.6 Average Nominal Area Loss, A_{loss}

According to the mass loss, the calculation also leads to even wider discussion, which is the average nominal-sectional area loss (A_{loss}). A_{loss} was one of the major findings that can link the bridge between practical engineering damages and GO as a protective barrier additive within the blended mortar. This is because the greater the A_{loss} recorded, the higher the risk of premature failure of the structure. Not only that, but to calculate the A_{loss}, the exposed length of the steel has also been determined. The exposed length (L) refers to the segment of the steel that is embedded within the GO-blended mortar. This also defines an actual length for the corrosive penetration potential in the study. Moreover, the steel density has also been determined as a constant by 0.00758 g/mm^3. Henceforth, as the continuity calculation example from sample 30SG2, the area of loss was determined and recorded in the study. Therefore, the equation of the A_{loss} can be calculated as below:

$$A_{loss} = \frac{Mass\ loss}{Exposed\ Length} \tag{5.6}$$

where,

Mass loss is the total mass that has been converted into rust

Exposed length is the 175 mm steel bar segment embedded in blended mortar
Density of steel has been standardized as 0.00785 g/mm^3

$$A_{loss} = \frac{\frac{0.0033\ g}{0.00785\ \mathrm{g}/mm^3}}{175\ mm}$$
$$= 0.0024\ mm^2$$

Note : The value of mass loss was divided by the density of steel to obtain the volume of mass loss on steel

$$\rho = \frac{m}{v}$$
$$v = \frac{0.0033\ g}{0.00785\ \mathrm{g}/mm^3}$$
$$= 0.4203\ mm^3$$

Therefore, the complete performance data of GO in blended mortar as corrosion resistance additive is tabulated and presented in Table 5.7 and Table 5.8 for normal condition and saltwater condition. These tables also focussing on the major parameters such as time to depassivation (T_{HCP}), active corrosion time (t), total corrosion current (I), mass loss (m) as well as the average nominal-sectional area loss (A_{loss}).

Table 5.7
Derived Mass Loss (M) And Nominal Area Loss (A_{loss}) For GO-Blended Mortar in Normal Condition

Mix	Time to Depassivation (T_{HCP}), days	Active Corrosion Time (t), days	Total Corrosion Current, I	Mass Loss, g	Average nominal area loss, A_{loss}
30SG0	73	17	6.06 x $\mathbf{10^{-5}}$	0.0280	0.0204
30SG2	86	4	3.30 x $\mathbf{10^{-5}}$	0.0033	0.0024
30SG4	75	15	6.60 x $\mathbf{10^{-5}}$	0.0247	0.0180
30SG6	74	16	9.90 x $\mathbf{10^{-5}}$	0.0396	0.0288
30SG8	72	18	9.90 x $\mathbf{10^{-5}}$	0.0445	0.0324
30SG10	72	18	9.90 x $\mathbf{10^{-5}}$	0.0445	0.0324

Table 5.8
Derived Mass Loss (M) And Nominal Area Loss (A_{loss}) For GO-Blended Mortar in Saltwater Condition

Mix	Time to Depassivation (T_{HCP}), days	Active Corrosion Time (t), days	Total Corrosion Current, I	Mass Loss, g	Average nominal area loss, A_{loss}
30SG0	61	29	6.06 x $\mathbf{10^{-5}}$	0.0478	0.0348
30SG2	74	16	3.30 x $\mathbf{10^{-5}}$	0.0132	0.0096
30SG4	71	19	6.60 x $\mathbf{10^{-5}}$	0.0313	0.0228
30SG6	69	21	9.90 x $\mathbf{10^{-5}}$	0.0520	0.0378
30SG8	65	25	9.90 x $\mathbf{10^{-5}}$	0.0619	0.0450
30SG10	63	27	9.90 x $\mathbf{10^{-5}}$	0.0668	0.0486

5.7 Comprehensive Discussion

5.7.1 Mass Loss in Normal Condition

Figure 5.2 depicts the performance of GO-blended mortar, as it visualises the structural damage of mass loss as well as the time to depassivation T_{HCP}. There is no doubt that the inclusion of GO within the blended mortar influences the results as it acts as a protective barrier due to three distinct mechanisms of filling, bonding and nucleation effect. This can be discussed as 30SG2 managed to fulfil the full potential of GO, where it delivered the optimal mass loss under a longer set of time to depassivation. The optimal mix of 30SG2 was visibly the best formulation compared to others, as it reaches 86 days of time to depassivation. This indicates the maximum service life extension with an adequate amount of 0.02% of GO. This validates the filling effect of the GO as it tends to densify the sample, reducing its permeability to any sort of corrosive media to penetrate to the surface. Not only that, but this also explains a concept of the Labyrinth Effect, which holds to the uniqueness of GO as a protective barrier in the cement matrix. This leads to a complex and tortuous network, which remarkably increases the diffusion path for the corrosive media, eventually slowing down their penetration to the substrate. The diffusion can also be highlighted as a "tortuous diffusion path" among researchers in this discussion. This tortuous path ultimately leads to the reduction of potential corrosion media to penetrate and offer a greater penetration resistance compared to other materials (R. Zhang et al., 2021).

The existence of this mechanism can be justified further with the evidence discussed in section 4.7, specifically the SEM images. It has been confirmed that the filling effect managed to occupy the cracks within the GO-blended mortar at 0.02% GO. This amplifies the protective forces towards the surface of the cement matrix, which navigates a longer and even more complex route for the corrosive to reach the rebar. This increase in path length of penetration causes an even longer time to depassivation (T_{HCP}), serving as solid proof of the Labyrinth Effect specifically in mix 30SG2. In addition, GO also consist of a high aspect ratio and surface area, which amplifies the quality barrier in the cement matrix (Abdalla et al., 2022). In addition, the minimal mass loss portrayed by 30SG2 is also secured by the nucleation effect of the GO itself. This can be explained by the presence of oxygen functional groups, which tend to promote a faster hydration process of C-S-H growth, which eventually promotes

a denser, well-structured microstructure. In addition, the bonding effect of GO also provides the third layer of defence in the cement matrix. This can be described as the crack-bridging effect of GO, which tends to deliver the interlocking mechanism which prevents the propagation of micro-cracks and ensures higher resistance against corrosive penetration (Khalid et al., 2023).

In contrast, the failure of excessive dosage of GO in other samples (30SG6, 30SG8, 30SG10) shows that the time to depassivation drops tremendously, similar to the control sample of 73 days. This indicates the failure of GO to fulfil its purpose as a protective barrier, which likely happened due to the agglomeration of GO. Therefore, this explains the high mass loss recorded for the last three samples by 0.0396g and 0.0445g. This confirmed higher damage results compared to the control sample, as high doses of GO can disrupt and accelerate structural degradation.

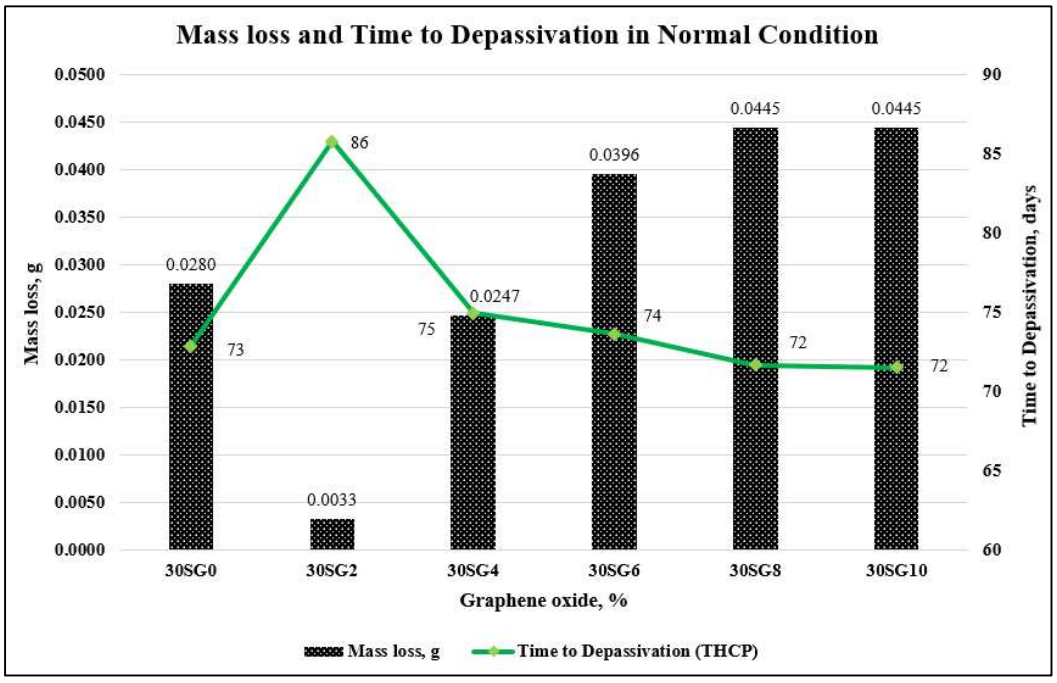


Figure 5.2 Mass Loss and Time to Depassivation in Normal Condition

5.7.2 Mass Loss in Saltwater Condition

The data presented in Figure 5.3 indicated the mass loss in saltwater conditions as a counterpart to a normal condition analysis. This because under aggressive saltwater condition, the corrosive role of NaCl becomes obvious and evident. This defence mechanism of the GO-blended mortar was pushed to the limit as the chloride ion vigorously attempt to penetrate the steel rebar and causing internal expansion. The discussion in this section also refers the exposure class of XS2 in the Euro-code. Nevertheless, a similar finding can be seen in the optimal mix of 30SG2, where it remains as the lowest mass loss compared to other samples. This can be discussed as the time to depassivation reaches 74 days, extending the service life by 13 days compared to the control sample (30SG0) at 61 days. As a control and high percentages of GO comparison, the destructive process due to the excessive chloride ion ingress known as calcium leaching. This is because the reaction between NaCl with by-product of blended mortar hydration which is calcium hydroxide to form Calcium Chloride ($CaCl_2$). The chemical equation can be shown as below:

$$Ca(OH)_2 + 2NaCl \rightarrow CaCl_2 + 2NaOH \quad (5.7)$$

Unlike the formation of the Friedelt's salt, the $CaCl_2$ is highly soluble, making its move freely capturing the alkalinity from the blended mortar causing more porosity and acidic matrix. This shall gradually reduce the compactness and load-bearing capacity of the blended mortar (Liu et al., 2026). This explains perfectly on the deterioration of passive layer of the steel rebar. However, the 30SG2 formulation managed to delay the process by a significant labyrinth effect of the GO, where it tends to create a torturous path for the corrosive media before it can penetrate to the blended mortar. Not only that, but the filling effect portrayed by GO also successfully provides a pore-blocking mechanism by making a denser sample. Not only that but due to the bonding effect of GO, it created this cross-linked and linear structure. Chu et al.,(2019) described these interactions can also be known as the "bricks and mortar" structure, where it tends to strengthen the bonding force (Jena & Philip, 2022). This consequently restricts a higher amount of corrosive penetration to the GO-blended mortar. Thus, corresponding to the highest T_{HCP}, the mass loss recorded was 0.0132g. This outcome

also confirms that densification promoted by GO's nucleation effect significantly reduces the potential of penetration and mass loss.

Nevertheless, as for the high percentages of GO, such as 30SG8 and 30SG10, they tend to exhibit a failure of the protective system under high chloride exposure. This can be explained by the T_{HCP} line declining sharply to 63 days for 30SG10. Not only that, but the mass loss data also spike tremendously to the highest points to 0.0668g, even higher than the control sample. This severe failure was caused by GO agglomeration formation, as discussed in the normal condition analysis, which consequently creates defects of high chloride absorption. These clumps created an express lane for the chloride ions to bypass the Labyrinth effect (PZhao et al., 2025). At this point, the salt's movement were actively destroys the chemical protective around the rebar and leads to severe mass loss.

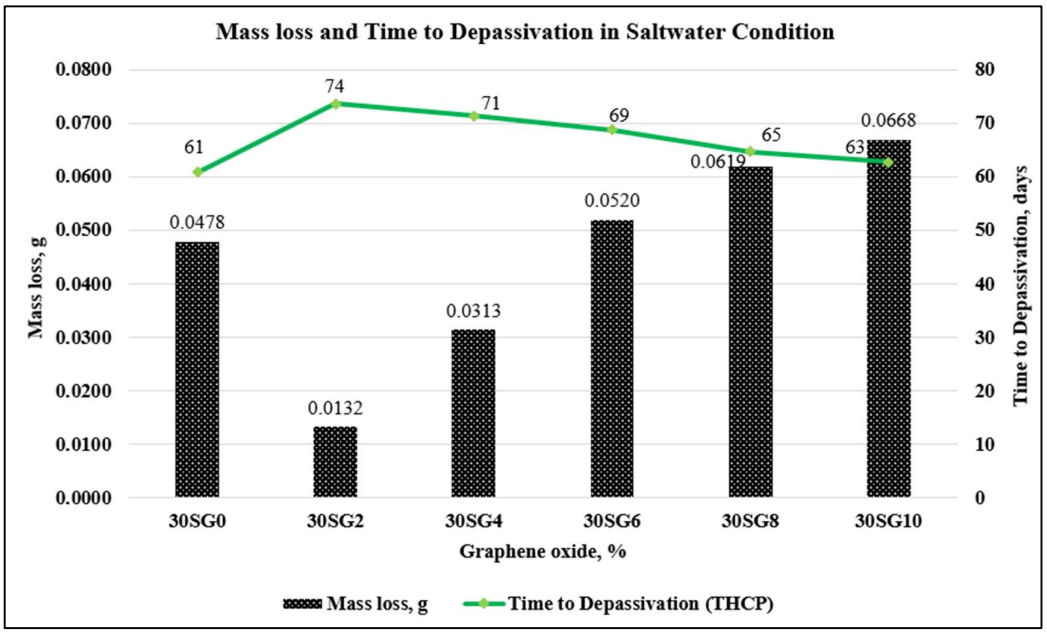


Figure 5.3 Mass Loss and Time to Depassivation in Saltwater Condition

5.7.3 Average Nominal Area Loss

This section discusses the analysis of the average nominal area loss (A_{loss}) for both conditions, revealing a non-linear relationship between GO percentages and structural resilience. Generally, Figure 5.4 indicated an obvious rise in A_{loss} for all mixes when transitioning from normal conditions to the saltwater condition. This happened due to the aggressive nature of the concentrated chloride environment in the saltwater. First and foremost, it can be seen that for the control sample, 30SG0, the average nominal area loss increased from 0.0204 mm^2 in normal conditions to 0.0348 mm^2 in saltwater condition. This confirmed a significant passive film failure when it was penetrated in another concentrated chloride curing.

The optimal mix for both conditions can be portrayed in 30SG2, which tends to demonstrate an exceptional ability of GO as a protective barrier. Although the A_{loss} recorded for the normal condition was 0.00024 mm^2, it increased to 0.0096 mm^2 in the saltwater condition, and both of these data remain as the lowest compared to all samples. This sustained performance can be explained similarly to the previous discussion related to the labyrinth effect of GO. This is significantly engaging for a fully dispersed GO within the cement matrix, which eventually creates these densified samples. This finding also can be related to the utilization of PCE-based superplasticizer as well where the polymer chains from PCE tends to adsorb onto the GO (Zhao et al., 2018). This enhances the repulsive forces within the cement matrix, creating a successful steric hindrance effect and preventing potential agglomeration. Not only that, but it also shall minimise the rate of A_{loss} by maintaining 88.24% and 72.41% of reduction for both conditions. This finalised the value of 0.02% of GO as the optimal percentage in the cement matrix.

However, an excessive GO percentage of samples, which were already losing their structural resilience in normal conditions, exhibits an even worse failure due to GO agglomeration. As an example, in the 30SG10 sample, the A_{loss} increased from 0.0324 mm^2 to 0.0486 mm^2 from normal to saltwater conditions. The reduction percentages also show a negative value of -39.66% indicating a greater loss compared to the control sample (30SG0) for the saltwater condition. These agglomeration formations also localised the routes within the material to be penetrated more easily by the corrosive media. This eventually accelerates a faster depassivation process and higher corrosion rate. Therefore, it is noticeable to state that a high GO percentage

defects the material's defence, which consequently leads to greater exposure and penetration.

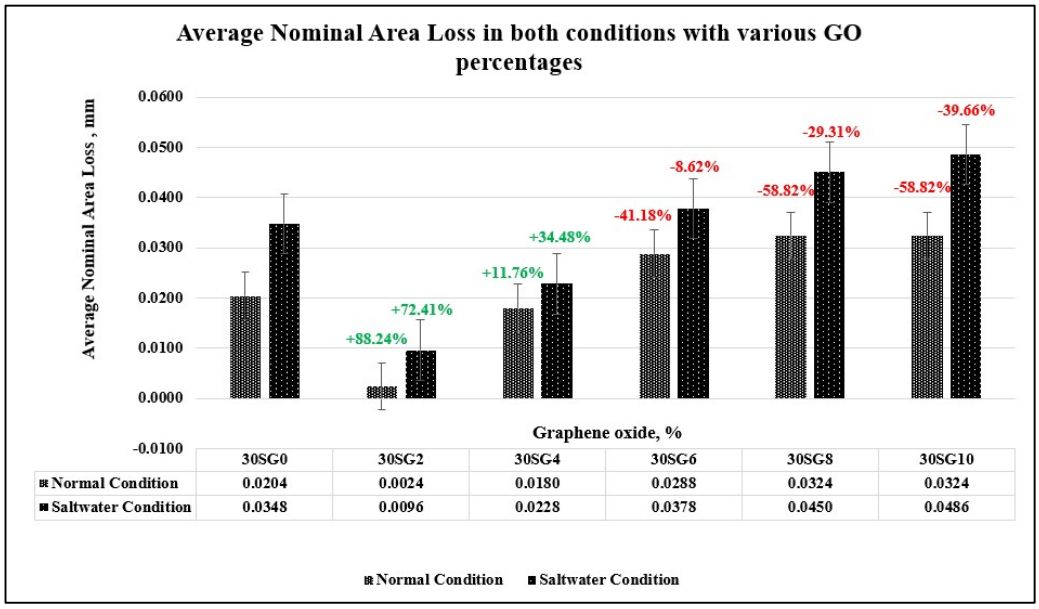


Figure 5.4 Average nominal Area Loss for Both Conditions of Curing

CHAPTER 6
CONCLUSION & FUTURE RECOMMENDATION

6.1 General Conclusion

This study successfully achieved all stated objectives by characterising and evaluating the full performance of GO in blended mortar. Not only that, but it is also worth mentioning that the experimental results significantly prove the four major mechanisms of GO in cementitious-based material, which include the filling effect, nucleation effect, bonding effect and labyrinth effect. The research framework also significantly progressed from initial material characterisation to the final phase of binder optimisation through mass loss quantification due to corrosion assessment.

6.1.1 Characterisation of Blended Material and Graphene Oxide, and to Evaluate Their Influence on the Physical, Mechanical, And Durability Properties for Binder Formulation

The first research objective was achieved through a systematic characterisation of raw materials which provided the fundamental basis for the subsequent binder formulation and modification phases. This initial stage focused on understanding the influence of two distinct cement replacements (fly ash and GGBS) including GO on chemical, phase and microstructure characterisation. XRD analysis revealed that GGBS exhibits a predominantly glassy, amorphous nature compared to the more crystalline profile of fly ash. These findings were further corroborated by morphological examination where the SEM imaging showed that GGBS particles possess an angular, irregular geometry, while fly ash was characterised by smooth, spherical particles. Simultaneously, the successful synthesis of GO from raw graphene through the simplified Hummer's method was validated through both chemical and structural evidence. Elemental analysis confirmed the effectiveness of the oxidation process, showing a significant rise in oxygen content within the carbon lattice. This chemical shift was physically manifested in the XRD patterns, where the interplanar d-spacing expanded from 4.94 A in the raw graphene to 12.54 A in the GO. This broad increase in d-spacing serves as definitive structural proof of the intercalation of oxygen-

containing functional groups between the carbon sheets. Furthermore, FESEM analysis of the synthesized GO revealed a characteristic wrinkled and multi-layered morphology, confirming its high surface area and suitability as a nano-filler. In this study, a fixed cement replacement strategy was implemented using 10%, 20%, and 30% concentrations. Results indicated that a 30% replacement of GGBS yielded the most significant improvements in the density, mechanical and water absorption properties of the blended mortar. The presence of calcium oxide in the GGBS accelerates the hydration process, leading to superior strength development. This occurs because GGBS produces a higher volume of Calcium Silicate Hydrate (C-S-H) gel compared to fly ash blended mortars. Furthermore, at the 30% threshold, the GGBS content facilitates hydration and pozzolanic reactions, resulting in optimal strength enhancement.

6.1.2 Investigation on the Optimum Ratio of Graphene Oxide in Producing Nano-Composite Mortar Under Physical, Mechanical and Durability Properties for Binder Modification

Following the optimization of the 30SG0 baseline, the 30SG2 mix (0.02% GO) exhibited the most significant mechanical enhancement, driven by three synergistic mechanisms of nucleation, filling, and bonding. The nucleation effect was facilitated by the oxygen-functional groups on the GO surface, which act as high-energy sites that attract calcium ions and accelerate the growth of C-S-H crystals. This results in a more uniform and rapid development of the hydration products throughout the binder. Simultaneously, the filling effect allowed the high-aspect-ratio GO to occupy the ultra-fine interstitial voids that are inaccessible to larger particles like GGBS, leading to a much denser microstructure. Finally, the bonding mechanism utilizes the oxygenated functional groups of GO which referred to the wrinkled morphology of the GO to arrest micro-cracks at their inception. By stopping crack tips, the GO prevents micro-cracks from coalescing into macro-fractures, thereby significantly increasing the overall compressive strength and structural integrity of the 30SG2 blended mortar.

6.1.3 Evaluation of the Microstructure and Durability of GO-Blended Mortar Against Corrosion Resistance

The third research objective was successfully addressed by correlating the microstructural evolution of GO-modified mortars with their long-term durability and corrosion resistance. Analytical techniques including Scanning Electron Microscopy (SEM) and Mercury Intrusion Porosimetry (MIP) provided critical validation of the nano-filling effect induced by GO at the optimal 0.02% dosage (30SG2). While SEM imaging visually confirmed a denser matrix with fewer micro-cracks, the MIP results quantified this improvement through a significant reduction in cumulative pore volume and a shift toward finer, non-connected pores. This structural refinement was essential, as it physically obstructs the pathways typically used by aggressive ions to penetrate the mortar. This microstructural densification served as the fundamental basis for the enhanced durability observed during Rapid Chloride Permeability (RCPT) and Half-Cell Potential (HCP) testing.

6.1.4 Investigation of the Mass Loss of the Steel Rebar Within The GO-Blended Mortar Using Faraday's Law Equation

Finally, the last objective was achieved by investigating the mass loss of the steel rebar within the GO-blended mortar using Faraday's Law equation. This phase also successfully designed one of the parameters of Time to Depassivation (T_{HCP}) by using linear interpolation from HCP results and the standard. Moreover, the Active Time Corrosion (t) and Total Current Corrosion (I) were also achieved as parameters for the mass loss. The calculated mass loss confirmed that mix 30SG2 obtained the lowest results of mass loss in both conditions of curing (normal and saltwater). Furthermore, the calculated mass loss was then converted into an average nominal area loss (A_{loss}), which serves as the final outcome in this study. This analysis revealed that the critical dosage of GO was crucial in defining greater dispersion within the blended mortar. This confirmed that the 30SG2 mix functions as a superior protective barrier against corrosive media. By increasing the tortuosity of the cementitious matrix, the inclusion of GO significantly inhibited chloride ion diffusion and oxygen transport, thereby delaying the initiation of the corrosion process.

6.2 Future Recommendation

Based on the findings of this study, it is highly recommended that the optimized Graphene Oxide (GO) modified blended mortar be utilized as an advanced structural patching mortar specifically engineered for marine environment infrastructure rehabilitation. The combination of a targeted 30 MPa compressive strength and a highly refined microstructure make this material ideal for localized repairs in tidal and splash zones, where high early-strength development and strong substrate interfacial bonding are critical to withstand cyclic wave actions. Future investigations should therefore focus on evaluating the physical performance of this material in marine repair configurations, specifically assessing its slant shear bond strength, volume stability, and long-term drying shrinkage behaviour when applied directly to degraded coastal concrete elements.

In terms of future prospects, this nano-engineered mortar holds significant potential to be developed into a high-performance, microstructural corrosion inhibitor for critical offshore and coastal infrastructure. Expanding upon the Half Cell Potential Test (HCPT) and Rapid Chloride Permeability Test (RCPT) data obtained in this research, future work should explicitly quantify its capacity to shield embedded steel reinforcement from marine chemical degradation. Long-term electrochemical monitoring and accelerated chloride ingress testing should be conducted under cyclic saltwater wet-and-dry simulations to evaluate how effectively the tortuous transport paths created by GO prevent chloride-induced corrosion. This will provide a comprehensive pathway toward commercializing these sustainable, GO-blended systems as heavy-duty, corrosion-resistant patching solutions for jetties, ports, and harsh marine environments.

REFERENCES

Abdalla, J. A., Thomas, B. S., Hawileh, R. A., & Syed Ahmed Kabeer, K. I. (2022). Influence of nanomaterials on the workability and compressive strength of cement-based concrete. *Materials Today: Proceedings*, *65*, 2073–2076. https://doi.org/10.1016/j.matpr.2022.06.429

Akarsh, P. K., Shrinidhi, D., Marathe, S., & Bhat, A. K. (2022). Graphene oxide as nano-material in developing sustainable concrete – A brief review. *Materials Today: Proceedings*, *60*, 234–246. https://doi.org/10.1016/j.matpr.2021.12.510

Alla, S., & Asadi, S. S. (2023). Investigation on fluidity, microstructure, mechanical and durability properties of snail shell based graphene oxide cement composite material. *Construction and Building Materials*, *362*. https://doi.org/10.1016/j.conbuildmat.2022.129767

Alterary, S. S., & Marei, N. H. (2021). Fly ash properties, characterization, and applications: A review. In *Journal of King Saud University - Science* (Vol. 33, Number 6). Elsevier B.V. https://doi.org/10.1016/j.jksus.2021.101536

Alvi, I. H., Li, Q., Hou, Y., Onyekwena, C. C., Zhang, M., & Ghaffar, A. (2023). A critical review of cement composites containing recycled aggregates with graphene oxide nanomaterials. *Journal of Building Engineering*, 105989. https://doi.org/10.1016/j.jobe.2023.105989

Andrade, C., Alonso, C., Gulikers, J., Polder, R., Cigna, R., Vennesland, Salta, M., Raharinaivo, A., & Elsener, B. (2004). Test methods for on-site corrosion rate measurement of steel reinforcement in concrete by means of the polarization resistance method. *Materials and Structures/Materiaux et Constructions*, *37*(273), 623–643. https://doi.org/10.1617/13952

Anish, V., Logeshwari, J., & Samson, S. (2025). Evaluation of Durability Characteristics on Hybrid Fibre Reinforced High-Performance Concrete Incorporated with Graphene Oxide. *Iranian Journal of Science and Technology - Transactions of Civil Engineering*, *49*(4), 3881–3904. https://doi.org/10.1007/s40996-024-01637-w

Anwar, A., Liu, X., & Zhang, L. (2023). Nano-cementitious composites modified with Graphene Oxide – a review. In *Thin-Walled Structures* (Vol. 183). Elsevier Ltd. https://doi.org/10.1016/j.tws.2022.110326

Anwar, A., Mohammed, B. S., Wahab, M. A., & Liew, M. S. (2020). Enhanced

properties of cementitious composite tailored with graphene oxide nanomaterial - A review. In *Developments in the Built Environment* (Vol. 1). Elsevier Ltd. https://doi.org/10.1016/j.dibe.2019.100002

Asen, F., & Dehestani, M. (2021). Influence of concrete mix proportions on lifetime flexural load-bearing capacity of RC beams under chloride corrosion of rebars. *Structures*, *29*, 2017–2027. https://doi.org/10.1016/j.istruc.2021.01.009

ASTM C109. (2016). *Standard Test Method for Compressive Strength of Hydraulic Cement Mortars (Using 2-in. or [50-mm] Cube Specimens)*. West Conshohocken: ASTM International.

ASTM C138. (2017). *Standard Test Method for Density (Unit Weight), Yield, and Air Content (Gravimetric) of Concrete*. West Conshohocken: ASTM International.

ASTM C496. (2017). *Standard Test Method for Splitting Tensile Strength of Cylindrical Concrete Specimens*. West Conshohocken: ASTM International.

ASTM C642. (2021). *Standard Test Method for Density, Absorption, and Voids in Hardened Concrete*. West Conshohocken: ASTM International.

ASTM C876. (2015). *Standard Test Method for Corrosion Potentials of Uncoated Reinforcing Steel in Concrete*. West Conshohocken: ASTM International.

ASTM C1202. (2022). *Standard Test Method for Electrical Indication of Concrete's Ability to Resist Chloride Ion Penetration*. West Conshohocken: ASTM International.

ASTM D4404. (2018). *Standard Test Method for Determination of Pore Volume and Pore Volume Distribution of Soil and Rock by Mercury Intrusion Porosimetry*. West Conshohocken: ASTM International.

Aydoğan, O. G., Dilber, A. A., & Özyurt, N. (2025). Friedel's salt stability and sulfate durability of seawater mixed cement-based materials. *Journal of Building Engineering*, *110*. https://doi.org/10.1016/j.jobe.2025.113124

Baomin, W., & Shuang, D. (2019). Effect and mechanism of graphene nanoplatelets on hydration reaction, mechanical properties and microstructure of cement composites. *Construction and Building Materials*, *228*. https://doi.org/10.1016/j.conbuildmat.2019.116720

Bellum, R. R., Muniraj, K., Indukuri, C. S. R., & Madduru, S. R. C. (2020). Investigation on Performance Enhancement of Fly ash-GGBFS Based Graphene Geopolymer Concrete. *Journal of Building Engineering*, *32*. https://doi.org/10.1016/j.jobe.2020.101659

Bheel, N., Ali, M. O. A., Kırgız, M. S., Shafiq, N., & Gobinath, R. (2023). Effect of graphene oxide particle as nanomaterial in the production of engineered cementitious composites including superplasticizer, fly ash, and polyvinyl alcohol fiber. *Materials Today: Proceedings*. https://doi.org/10.1016/j.matpr.2023.03.010

Bhojaraju, C., Mousavi, S. S., & Ouellet-Plamondon, C. M. (2023). Influence of GGBFS on corrosion resistance of cementitious composites containing graphene and graphene oxide. *Cement and Concrete Composites*, *135*. https://doi.org/10.1016/j.cemconcomp.2022.104836

Burgos, D. M., Guzmán, Á., Torres, N., & Delvasto, S. (2017). Chloride ion resistance of self-compacting concretes incorporating volcanic materials. *Construction and Building Materials*, *156*, 565–573. https://doi.org/10.1016/j.conbuildmat.2017.09.017

Chetty, K., Watson, M., Raine, T., McGurgan, T., Ladislaus, P., Chen, J., Zhang, S., Lin, L., & Jiang, G. (2022). Enhancing Concrete and Mortar Properties and Durability Using Pristine Graphene Particles. *Coatings*, *12*(11), 1703. https://doi.org/10.3390/coatings12111703

Chintalapudi, K., & Pannem, R. M. R. (2020). The effects of Graphene Oxide addition on hydration process, crystal shapes, and microstructural transformation of Ordinary Portland Cement. *Journal of Building Engineering*, *32*. https://doi.org/10.1016/j.jobe.2020.101551

Chu, J. H., Tong, L. B., Zhang, J. B., Kamado, S., Jiang, Z. H., Zhang, H. J., & Sun, G. X. (2019). Bio-inspired graphene-based coatings on Mg alloy surfaces and their integrations of anti-corrosive/wearable performances. *Carbon*, *141*, 154–168. https://doi.org/10.1016/j.carbon.2018.09.047

Chuah, S., Pan, Z., Sanjayan, J. G., Wang, C. M., & Duan, W. H. (2014). Nano reinforced cement and concrete composites and new perspective from graphene oxide. In *Construction and Building Materials* (Vol. 73, pp. 113–124). Elsevier Ltd. https://doi.org/10.1016/j.conbuildmat.2014.09.040

Cui, H., Yan, X., Tang, L., & Xing, F. (2017). Possible pitfall in sample preparation for SEM analysis - A discussion of the paper “Fabrication of polycarboxylate/graphene oxide nanosheet composites by copolymerization for reinforcing and toughening cement composites” by Lv et al. *Cement and Concrete Composites*, *77*, 81–85.

https://doi.org/10.1016/j.cemconcomp.2016.12.007

Dideikin, A. T., & Vul', A. Y. (2019). Graphene oxide and derivatives: The place in graphene family. In *Frontiers in Physics* (Vol. 6, Number JAN). Frontiers Media S.A. https://doi.org/10.3389/fphy.2018.00149

Divya, S., Praveenkumar, S., & Tayeh, B. A. (2022). Performance of modified nano carbon blended with supplementary materials in cement composite – An interpretive review. In *Construction and Building Materials* (Vol. 346). Elsevier Ltd. https://doi.org/10.1016/j.conbuildmat.2022.128452

Dong, L., Yang, J., Chhowalla, M., & Loh, K. P. (2017). Synthesis and reduction of large sized graphene oxide sheets. In *Chemical Society Reviews* (Vol. 46, Number 23, pp. 7306–7316). Royal Society of Chemistry. https://doi.org/10.1039/c7cs00485k

Du, H., Gao, H. J., & Pang, S. D. (2016). Improvement in concrete resistance against water and chloride ingress by adding graphene nanoplatelet. *Cement and Concrete Research*, *83*, 114–123. https://doi.org/10.1016/j.cemconres.2016.02.005

Firouzi, A., Abdolhosseini, M., & Ayazian, R. (2020). Service life prediction of corrosion-affected reinforced concrete columns based on time-dependent reliability analysis. *Engineering Failure Analysis*, *117*. https://doi.org/10.1016/j.engfailanal.2020.104944

Ganesh, S., Thambiliyagodage, C., Perera, S. V. T. J., & Rajapakse, R. K. N. D. (2023). Influence of Laboratory Synthesized Graphene Oxide on the Morphology and Properties of Cement Mortar. *Nanomaterials*, *13*(1). https://doi.org/10.3390/nano13010018

Ghazizadeh, S., Duffour, P., Skipper, N. T., & Bai, Y. (2018). Understanding the behaviour of graphene oxide in Portland cement paste. *Cement and Concrete Research*, *111*, 169–182. https://doi.org/10.1016/j.cemconres.2018.05.016

Ghulam, A. N., Dos Santos, O. A. L., Hazeem, L., Backx, B. P., Bououdina, M., & Bellucci, S. (2022). Graphene Oxide (GO) Materials—Applications and Toxicity on Living Organisms and Environment. In *Journal of Functional Biomaterials* (Vol. 13, Number 2). MDPI. https://doi.org/10.3390/jfb13020077

Gong, J., Qian, Y., Xu, Z., Chen, C., Jin, Y., Zhang, J., Li, Z., & Shi, X. (2024). Effect of graphene oxide on the properties of ternary limestone clay cement paste. *Nanotechnology Reviews*, *13*(1). https://doi.org/10.1515/ntrev-2023-0222

Guo, K., Miao, H., Liu, L., Zhou, J., & Liu, M. (2019). Effect of graphene oxide on chloride penetration resistance of recycled concrete. *Nanotechnology Reviews*, *8*(1), 681–689. https://doi.org/10.1515/ntrev-2019-0059

Han, B., Zheng, Q., Sun, S., Dong, S., Zhang, L., Yu, X., & Ou, J. (2017). Enhancing mechanisms of multi-layer graphenes to cementitious composites. *Composites Part A: Applied Science and Manufacturing*, *101*, 143–150. https://doi.org/10.1016/j.compositesa.2017.06.016

Han, Y., Shao, S., Fang, B., Shi, T., Zhang, B., Wang, X., & Zhao, X. (2023). Chloride ion penetration resistance of matrix and interfacial transition zone of multi-walled carbon nanotube-reinforced concrete. *Journal of Building Engineering*, *72*. https://doi.org/10.1016/j.jobe.2023.106587

Hong, X., Lee, J. C., Ng, J. L., Md Yusof, Z., He, Q., & Li, Q. (2023). Effect of Graphene Oxide on the Mechanical Properties and Durability of High-Strength Lightweight Concrete Containing Shale Ceramsite. *Materials*, *16*(7). https://doi.org/10.3390/ma16072756

Horszczaruk, E., Mijowska, E., Kalenczuk, R. J., Aleksandrzak, M., & Mijowska, S. (2015). Nanocomposite of cement/graphene oxide - Impact on hydration kinetics and Young's modulus. *Construction and Building Materials*, *78*, 234–242. https://doi.org/10.1016/j.conbuildmat.2014.12.009

Hosseini, P., Hosseinpourpia, R., Pajum, A., Khodavirdi, M. M., Izadi, H., & Vaezi, A. (2014). Effect of nano-particles and aminosilane interaction on the performances of cement-based composites: An experimental study. *Construction and Building Materials*, *66*, 113–124. https://doi.org/10.1016/j.conbuildmat.2014.05.047

Hulagabali, M. M., Vesmawala, G. R., & Patil, Y. D. (2023). Synthesis, characterization, and application of graphene oxide and reduced graphene oxide and its influence on rheology, microstructure, and mechanical strength of cement paste. *Journal of Building Engineering*, *71*. https://doi.org/10.1016/j.jobe.2023.106586

Janavika, K. M., & Prakash Thangaraj, R. (2023). Graphene and its application: A review. *Materials Today: Proceedings*. https://doi.org/10.1016/j.matpr.2023.05.446

Jena, G., & Philip, J. (2022). A review on recent advances in graphene oxide-based composite coatings for anticorrosion applications. In *Progress in Organic*

Coatings (Vol. 173). Elsevier B.V. https://doi.org/10.1016/j.porgcoat.2022.107208

Johari, M., Allahkaram, S. R., Teymouri, F., Azamian, I., & Shekarchi, M. (2021). The effect of carboxylate compounds on controlling nitrite's environmental side effects for carbon steel corrosion protection in the simulated concrete pore solution. *Construction and Building Materials*, *308*. https://doi.org/10.1016/j.conbuildmat.2021.125037

Kai, M. F., Zhang, L. W., & Liew, K. M. (2019). Graphene and graphene oxide in calcium silicate hydrates: Chemical reactions, mechanical behaviors and interfacial sliding. *Carbon*, *146*, 181–193. https://doi.org/10.1016/j.carbon.2019.01.097

Kaur, R., Kothiyal, N. C., & Arora, H. (2020). Studies on combined effect of superplasticizer modified graphene oxide and carbon nanotubes on the physico-mechanical strength and electrical resistivity of fly ash blended cement mortar. *Journal of Building Engineering*, *30*. https://doi.org/10.1016/j.jobe.2020.101304

Khalid, M. Y., Kamal, A., Otabil, A., Mamoun, O., & Liao, K. (2023). Graphene/epoxy nanocomposites for improved fracture toughness: A focused review on toughening mechanism. In *Chemical Engineering Journal Advances* (Vol. 16). Elsevier B.V. https://doi.org/10.1016/j.ceja.2023.100537

Kobayashi, K., Shinozaki, R., & Onoda, M. (2025). Repassivation of corroded rebar by early supply of high corrosion protection current using hybrid galvanic anode. *Construction and Building Materials*, *493*. https://doi.org/10.1016/j.conbuildmat.2025.143099

Konsta-Gdoutos, M. S., Batis, G., Danoglidis, P. A., Zacharopoulou, A. K., Zacharopoulou, E. K., Falara, M. G., & Shah, S. P. (2017). Effect of CNT and CNF loading and count on the corrosion resistance, conductivity and mechanical properties of nanomodified OPC mortars. *Construction and Building Materials*, *147*, 48–57. https://doi.org/10.1016/j.conbuildmat.2017.04.112

Kumar, N., Salehiyan, R., Chauke, V., Joseph Botlhoko, O., Setshedi, K., Scriba, M., Masukume, M., & Sinha Ray, S. (2021). Top-down synthesis of graphene: A comprehensive review. In *FlatChem* (Vol. 27). Elsevier B.V. https://doi.org/10.1016/j.flatc.2021.100224

Lee, J. C., Shafigh, P., & Bahri, S. (2019). Comparative study of mechanical properties

for substitution of normal weight coarse aggregate with oil-palm-boiler clinker and lightweight expanded clay aggregate concretes. In *Journal of Design and Built Environment* (Vol. 19, Number 3).

Li, S., Jiang, J., Geng, Y., Hu, J., Sui, S., Liu, A., Hu, M., Shan, Y., & Liu, Z. (2024). Application of silane protective materials in the concrete durability improvement in recent years: A review. In *Engineering Failure Analysis* (Vol. 160). Elsevier Ltd. https://doi.org/10.1016/j.engfailanal.2024.108140

Li, X., Liu, Y. M., Li, W. G., Li, C. Y., Sanjayan, J. G., Duan, W. H., & Li, Z. (2017). Effects of graphene oxide agglomerates on workability, hydration, microstructure and compressive strength of cement paste. *Construction and Building Materials*, *145*, 402–410. https://doi.org/10.1016/j.conbuildmat.2017.04.058

Li, Z., Wang, H., He, S., Lu, Y., & Wang, M. (2006). Investigations on the preparation and mechanical properties of the nano-alumina reinforced cement composite. *Materials Letters*, *60*(3), 356–359. https://doi.org/10.1016/j.matlet.2005.08.061

Lin, C., Wei, W., & Hu, Y. H. (2016). Catalytic behavior of graphene oxide for cement hydration process. *Journal of Physics and Chemistry of Solids*, *89*, 128–133. https://doi.org/10.1016/j.jpcs.2015.11.002

Lin, Y., & Du, H. (2020). Graphene reinforced cement composites: A review. In *Construction and Building Materials* (Vol. 265). Elsevier Ltd. https://doi.org/10.1016/j.conbuildmat.2020.120312

Liu, C., Chen, F., Wu, Y., Zheng, Z., Yang, J., Yang, B., Yang, J., Hui, D., & Luo, Y. (2021). Research progress on individual effect of graphene oxide in cement-based materials and its synergistic effect with other nanomaterials. In *Nanotechnology Reviews* (Vol. 10, Number 1, pp. 1208–1235). De Gruyter Open Ltd. https://doi.org/10.1515/ntrev-2021-0080

Liu, C., Huang, X., Wu, Y. Y., Deng, X., Liu, J., Zheng, Z., & Hui, D. (2020). Review on the research progress of cement-based and geopolymer materials modified by graphene and graphene oxide. In *Nanotechnology Reviews* (Vol. 9, Number 1, pp. 155–169). De Gruyter. https://doi.org/10.1515/ntrev-2020-0014

Liu, C., Huang, X., Wu, Y. Y., Deng, X., & Zheng, Z. (2021). The effect of graphene oxide on the mechanical properties, impermeability and corrosion resistance of cement mortar containing mineral admixtures. *Construction and Building Materials*, *288*. https://doi.org/10.1016/j.conbuildmat.2021.123059

Liu, Q., Xu, Q., Yu, Q., Gao, R., & Tong, T. (2016). Experimental investigation on mechanical and piezoresistive properties of cementitious materials containing graphene and graphene oxide nanoplatelets. *Construction and Building Materials*, *127*, 565–576. https://doi.org/10.1016/j.conbuildmat.2016.10.024

Liu, Y., Zhong, T., Li, W., Li, Y., Jin, L., Qiu, L., Gu, L., & Ling, Y. (2026). Calcium leaching resistance and mechanism of early-age mortar with combined incorporation of glass powder and nano-silica under leaching conditions. *Case Studies in Construction Materials*, *24*, e05681. https://doi.org/10.1016/j.cscm.2025.e05681

Long, W. J., Gu, Y. cun, Xing, F., & Khayat, K. H. (2018). Microstructure development and mechanism of hardened cement paste incorporating graphene oxide during carbonation. *Cement and Concrete Composites*, *94*, 72–84. https://doi.org/10.1016/j.cemconcomp.2018.08.016

Long, W. J., Li, H. D., Fang, C. Le, & Xing, F. (2018). Uniformly dispersed and re-agglomerated graphene oxide-based cement pastes: A comparison of rheological properties, mechanical properties and microstructure. *Nanomaterials*, *8*(1). https://doi.org/10.3390/nano8010031

Lu, L., & Ouyang, D. (2017). Properties of cement mortar and ultra-high strength concrete incorporating graphene oxide nanosheets. *Nanomaterials*, *7*(7). https://doi.org/10.3390/nano7070187

Lv, S. H., Deng, L. J., Yang, W. Q., Zhou, Q. F., & Cui, Y. Y. (2016). Fabrication of polycarboxylate/graphene oxide nanosheet composites by copolymerization for reinforcing and toughening cement composites. *Cement and Concrete Composites*, *66*, 1–9. https://doi.org/10.1016/j.cemconcomp.2015.11.007

Lv, S., Liu, J., Sun, T., Ma, Y., & Zhou, Q. (2014). Effect of GO nanosheets on shapes of cement hydration crystals and their formation process. *Construction and Building Materials*, *64*, 231–239. https://doi.org/10.1016/j.conbuildmat.2014.04.061

Lv, S., Ma, Y., Qiu, C., & Zhou, Q. (2013). Regulation of go on cement hydration crystals and its toughening effect. *Magazine of Concrete Research*, *65*(20), 1246–1254. https://doi.org/10.1680/macr.13.00190

Lv, S., Ting, S., Liu, J., & Zhou, Q. (2014). Use of graphene oxide nanosheets to regulate the microstructure of hardened cement paste to increase its strength and toughness. *CrystEngComm*, *16*(36), 8508–8516.

https://doi.org/10.1039/c4ce00684d

Lv, S., Zhang, J., Zhu, L., & Jia, C. (2016). Preparation of cement composites with ordered microstructures via doping with graphene oxide nanosheets and an investigation of their strength and durability. *Materials*, *9*(11). https://doi.org/10.3390/ma9110924

Maglad, A. M., Zaid, O., Arbili, M. M., Ascensão, G., Șerbănoiu, A. A., Grădinaru, C. M., García, R. M., Qaidi, S. M. A., Althoey, F., & de Prado-Gil, J. (2022). A Study on the Properties of Geopolymer Concrete Modified with Nano Graphene Oxide. *Buildings*, *12*(8). https://doi.org/10.3390/buildings12081066

Manikanta, D., Ravella, D. P., M., S. R. C., & M., J. Y. (2020). Mechanical and durability characteristics of high performance self-compacting concrete containing flyash, silica fume and graphene oxide. *Materials Today: Proceedings*, *43*, 2361–2367. https://doi.org/10.1016/j.matpr.2021.01.684

Mashhadani, A., & Pershin, V. (2020). Concrete Modification Using Graphene and Graphene Oxide. *Advanced Materials & Technologies*, (2(18)), 046–056. https://doi.org/10.17277/amt.2020.02.pp.046-056

Matilla, A. L., Barrio, M. I. P., Escamilla, A. C., Ferrer, J. P., & Prieto, T. G. (2024). Analysis of the Effectiveness of the Application of Corrosion Inhibitors to Steel Re-Bars Embedded in Concrete. *Applied Sciences (Switzerland)*, *14*(8). https://doi.org/10.3390/app14083364

Meng, S., Ouyang, X., Fu, J., Niu, Y., & Ma, Y. (2021). The role of graphene/graphene oxide in cement hydration. *Nanotechnology Reviews*, *10*(1), 768–778. https://doi.org/10.1515/ntrev-2021-0055

Mohammed, A., Sanjayan, J. G., Duan, W. H., & Nazari, A. (2015). Incorporating graphene oxide in cement composites: A study of transport properties. *Construction and Building Materials*, *84*, 341–347. https://doi.org/10.1016/j.conbuildmat.2015.01.083

Munjal, P., Hau, K. K., & Hon Arthur, C. C. (2021). Effect of GGBS and curing conditions on strength and microstructure properties of oil well cement slurry. *Journal of Building Engineering*, *40*. https://doi.org/10.1016/j.jobe.2021.102331

Nascimento, D. O. Do, Silva, D. R., Antunes, R. A., Souza, T. C. C., Reis, T. M. C. Dos, Capelossi, V. R., & Lins, V. de F. C. (2024). The beneficial effect of graphene oxide on the corrosion resistance of reinforced concrete. *REM* -

International Engineering Journal., *77*(3). https://doi.org/10.1590/0370-44672023770011

Pan, Z., He, L., Qiu, L., Korayem, A. H., Li, G., Zhu, J. W., Collins, F., Li, D., Duan, W. H., & Wang, M. C. (2015). Mechanical properties and microstructure of a graphene oxide-cement composite. *Cement and Concrete Composites*, *58*, 140–147. https://doi.org/10.1016/j.cemconcomp.2015.02.001

Qureshi, T. S., & Panesar, D. K. (2019). Impact of graphene oxide and highly reduced graphene oxide on cement based composites. *Construction and Building Materials*, *206*, 71–83. https://doi.org/10.1016/j.conbuildmat.2019.01.176

Qureshi, T. S., Panesar, D. K., Sidhureddy, B., Chen, A., & Wood, P. C. (2019). Nano-cement composite with graphene oxide produced from epigenetic graphite deposit. *Composites Part B: Engineering*, *159*, 248–258. https://doi.org/10.1016/j.compositesb.2018.09.095

Raki, L., Beaudoin, J., Alizadeh, R., Makar, J., & Sato, T. (2010). Cement and concrete nanoscience and nanotechnology. In *Materials* (Vol. 3, Number 2, pp. 918–942). https://doi.org/10.3390/ma3020918

Ren, J., Luo, X., Bai, R., Pan, C., & Zhang, J. (2022). Pore characteristics of different phase in nano-modified concrete and their influences on the compressive strength. *Journal of Building Engineering*, *46*. https://doi.org/10.1016/j.jobe.2021.103784

Rezakhani, D., Jafari, A. H., & Hajabassi, M. (2023). Durability, mechanical properties and rebar corrosion of slag-based cement concrete modified with graphene oxide. *Structures*, *49*, 678–697. https://doi.org/10.1016/j.istruc.2023.01.149

Sai T, Y., & P, J. (2025). Efficacy of graphene oxide-based nanomaterials in customized cement mixtures, a review of recent research trends. In *Hybrid Advances* (Vol. 10). Elsevier B.V. https://doi.org/10.1016/j.hybadv.2025.100428

Schwarz, W., Pichlhöfer, A., Van Den Hondel, A., & Esteves, H. (2018). Maintenance and repair of steel reinforced concrete structures by galvanic corrosion protection-field experiences over 10 years. *MATEC Web of Conferences*, *199*. https://doi.org/10.1051/matecconf/201819905005

Shahas, S., Girija, K., & Nazeer, M. (2022). Evaluation of pozzolanic activity of ternary blended supplementary cementitious material with rice husk ash and GGBS. *Materials Today: Proceedings*. https://doi.org/10.1016/j.matpr.2023.01.073

Siddique, R., & Bennacer, R. (2012). Use of iron and steel industry by-product (GGBS)

in cement paste and mortar. In *Resources, Conservation and Recycling* (Vol. 69, pp. 29–34). https://doi.org/10.1016/j.resconrec.2012.09.002

Singh, K. R., Nayak, V., Sri, S., Singh, J., Solanki, P. R., & Singh, R. P. (2022). Introduction: zero-dimensional carbon nanomaterials. In *Zero-dimensional Carbon Nanomaterials*. IOP Publishing. https://doi.org/10.1088/978-0-7503-4048-9ch1

Singh, R. K., Kumar, R., & Singh, D. P. (2016). Graphene oxide: Strategies for synthesis, reduction and frontier applications. In *RSC Advances* (Vol. 6, Number 69, pp. 64993–65011). Royal Society of Chemistry. https://doi.org/10.1039/c6ra07626b

Son, D. H., Hwangbo, D., Suh, H., Bae, B. Il, Bae, S., & Choi, C. S. (2023). Mechanical properties of mortar and concrete incorporated with concentrated graphene oxide, functionalized carbon nanotube, nano silica hybrid aqueous solution. *Case Studies in Construction Materials*, *18*. https://doi.org/10.1016/j.cscm.2022.e01603

Suo, Y., Guo, R., Xia, H., Yang, Y., Zhou, B., & Zhao, Z. (2022). A review of graphene oxide/cement composites: Performance, functionality, mechanisms, and prospects. In *Journal of Building Engineering* (Vol. 53). Elsevier Ltd. https://doi.org/10.1016/j.jobe.2022.104502

Tay, C. H., & Norkhairunnisa, M. (2021). Mechanical Strength of Graphene Reinforced Geopolymer Nanocomposites: A Review. In *Frontiers in Materials* (Vol. 8). Frontiers Media S.A. https://doi.org/10.3389/fmats.2021.661013

Tong, T., Fan, Z., Liu, Q., Wang, S., Tan, S., & Yu, Q. (2016). Investigation of the effects of graphene and graphene oxide nanoplatelets on the micro- and macro-properties of cementitious materials. *Construction and Building Materials*, *106*, 102–114. https://doi.org/10.1016/j.conbuildmat.2015.12.092

Ur Rehman, S. K., Ibrahim, Z., Memon, S. A., Aunkor, M. T. H., Javed, M. F., Mehmood, K., & Shah, S. M. A. (2018). Influence of graphene nanosheets on rheology, microstructure, strength development and self-sensing properties of cement based composites. *Sustainability (Switzerland)*, *10*(3). https://doi.org/10.3390/su10030822

Vantadori, S., Magnani, G., Mantovani, L., Pontiroli, D., Ronchei, C., Scorza, D., Sidoli, M., Zanichelli, A., & Riccò, M. (2022). Effect of GO nanosheets on microstructure, mechanical and fracture properties of cement composites.

Construction and Building Materials, *361*, 129368. https://doi.org/10.1016/j.conbuildmat.2022.129368

Vitharana, M. G., Paul, S. C., Kong, S. Y., Babafemi, A. J., Miah, M. J., & Panda, B. (2020). A study on strength and corrosion protection of cement mortar with the inclusion of nanomaterials. *Sustainable Materials and Technologies*, *25*. https://doi.org/10.1016/j.susmat.2020.e00192

Wang, Q., Li, S., Pan, S., Cui, X., Corr, D. J., & Shah, S. P. (2019). Effect of graphene oxide on the hydration and microstructure of fly ash-cement system. *Construction and Building Materials*, *198*, 106–119. https://doi.org/10.1016/j.conbuildmat.2018.11.199

Wang, Q., Wang, J., Lu, C. X., Cui, X. Y., Li, S. Y., & Wang, X. (2016). Rheological behavior of fresh cement pastes with a graphene oxide additive. *Xinxing Tan Cailiao/New Carbon Materials*, *31*(6), 574–584. https://doi.org/10.1016/S1872-5805(16)60033-1

Wang, Q., Wang, J., Lu, C. X., Liu, B. W., Zhang, K., & Li, C. Z. (2015). Influence of graphene oxide additions on the microstructure and mechanical strength of cement. *Xinxing Tan Cailiao/New Carbon Materials*, *30*(4), 349–356. https://doi.org/10.1016/s1872-5805(15)60194-9

Wei, Z., Wang, Y., Qi, M., Bi, J., Yang, S., & Yuan, X. (2021). The role of sucrose on enhancing properties of graphene oxide reinforced cement composites containing fly ash. *Construction and Building Materials*, *293*. https://doi.org/10.1016/j.conbuildmat.2021.123507

Wu, Y. Y., Que, L., Cui, Z., & Lambert, P. (2019). Physical properties of concrete containing graphene oxide nanosheets. *Materials*, *12*(10). https://doi.org/10.3390/MA12101707

Xie, Z., zhou, H., li, Q., he, C., zhang, S., & li, D. (2020). Effects of colloidal nanosilica/polycarboxylate ether superplasticizer nanocomposite and graphene oxide on properties of fly ash blended cement. *Construction and Building Materials*, *262*. https://doi.org/10.1016/j.conbuildmat.2020.120767

Xu, G., Du, S., He, J., & Shi, X. (2019). The role of admixed graphene oxide in a cement hydration system. *Carbon*, *148*, 141–150. https://doi.org/10.1016/j.carbon.2019.03.072

Xu, Y., Zeng, J., Chen, W., Jin, R., Li, B., & Pan, Z. (2018). A holistic review of cement composites reinforced with graphene oxide. In *Construction and Building*

Materials (Vol. 171, pp. 291–302). Elsevier Ltd. https://doi.org/10.1016/j.conbuildmat.2018.03.147

Ying, G. G., Song, C., Ren, J., Guo, S. Y., Nie, R., & Zhang, L. (2021). Mechanical and durability-related performance of graphene/epoxy resin and epoxy resin enhanced OPC mortar. *Construction and Building Materials*, *282*. https://doi.org/10.1016/j.conbuildmat.2021.122644

Yuan, X., Zhang, L., Chen, X., & Liu, F. (2022). Study on the mechanical properties and frost resistance of multiple modified concrete. *Materials Research Express*, *9*(4). https://doi.org/10.1088/2053-1591/ac3951

Yuvaraj, S., Nirmalkumar, K., Rajesh Kumar, V., Gayathri, R., Mukilan, K., & Shubikksha, S. (2022). Influence of corrosion inhibitors in reinforced concrete – A state of art of review. *Materials Today: Proceedings*, *68*, 2406–2412. https://doi.org/10.1016/j.matpr.2022.09.118

Zhang, M., Sun, S., Liu, K., Li, T., & Yang, H. (2023). Research on the critical chloride content of reinforcement corrosion in marine concrete — A review. In *Journal of Building Engineering* (Vol. 79). Elsevier Ltd. https://doi.org/10.1016/j.jobe.2023.107838

Zhang, R., Long, Z., Long, G., Wang, J., Wang, X., Zhang, X., & Jiang, Y. (2024). Mechanism of graphene oxide concrete macro-micro properties evolution under large temperature difference freeze-thaw action. *Construction and Building Materials*, *415*. https://doi.org/10.1016/j.conbuildmat.2024.135019

Zhang, R., Yu, X., Yang, Q., Cui, G., & Li, Z. (2021). The role of graphene in anti-corrosion coatings: A review. In *Construction and Building Materials* (Vol. 294). Elsevier Ltd. https://doi.org/10.1016/j.conbuildmat.2021.123613

Zhang, S. P., & Zong, L. (2014). Evaluation of relationship between water absorption and durability of concrete materials. *Advances in Materials Science and Engineering*, *2014*. https://doi.org/10.1155/2014/650373

Zhang, Y., Cui, M., Chen, G., & Han, W. (2022). Experimental study of the effects of graphene nanoplatelets on microstructure and compressive properties of concrete under chloride ion corrosion. *Construction and Building Materials*, *360*. https://doi.org/10.1016/j.conbuildmat.2022.129564

Zhao, L., Guo, X., Liu, Y., Ge, C., Chen, Z., Guo, L., Shu, X., & Liu, J. (2018). Investigation of dispersion behavior of GO modified by different water reducing agents in cement pore solution. *Carbon*, *127*, 255–269.

https://doi.org/10.1016/j.carbon.2017.11.016

Zhao, L., Guo, X., Song, L., Song, Y., Dai, G., & Liu, J. (2020). An intensive review on the role of graphene oxide in cement-based materials. In *Construction and Building Materials* (Vol. 241). Elsevier Ltd. https://doi.org/10.1016/j.conbuildmat.2019.117939

Zhao, P., Si, Z., Huang, L., He, Y., Liu, X., & Zhang, Y. (2025). A review of the repair measures for reinforced concrete affected by chloride ion corrosion. In *Journal of Building Engineering* (Vol. 102). Elsevier Ltd. https://doi.org/10.1016/j.jobe.2025.112028

Zhao, W., Chen, Y., Liu, Z., Wang, L., & Li, X. (2023). Effects of surface-modified coal-bearing metakaolin and graphene oxide on the properties of cement mortar. In *Construction and Building Materials* (Vol. 372). Elsevier Ltd. https://doi.org/10.1016/j.conbuildmat.2023.130796

Zhao, Z., Qi, T., Zhou, W., Hui, D., Xiao, C., Qi, J., Zheng, Z., & Zhao, Z. (2020). A review on the properties, reinforcing effects, and commercialization of nanomaterials for cement-based materials. In *Nanotechnology Reviews* (Vol. 9, Number 1, pp. 349–368). De Gruyter. http3s://doi.org/10.1515/ntrev-2020-0023

Zhou, A., Wu, Y., Li, H., Li, J., Sun, T., & Yang, Y. (2025). Experimental study of graphene oxide modified ultrafine cement properties and grouting model. *Journal of Building Engineering*, *99*. https://doi.org/10.1016/j.jobe.2024.1116

AUTHOR'S PROFILE



Khairul Nazhan Khairul Izwan holds a Bachelor of Engineering (Hons) Civil (2023) from Universiti Teknologi MARA (UiTM) and is a PhD candidate in Civil Engineering (2026) at the same university. His research specialization lies in the development of nanomaterial specifically on carbon based material, with a PhD thesis centred on the utilization of Graphene Oxide (GO) to enhance the properties of blended mortars. This work includes a rigorous analytical assessment of mass loss to evaluate the durability particularly towards corrosion resistance characteristic of nano-reinforced cementitious materials.

LIST OF PUBLICATION

Izwan, K., Apandi, N., Zailani, W. Shamsol, A. (2026). From morphology to mechanics: correlating graphene oxide properties with compressive strength enhancement in cement paste. *IOP Conference Series: Earth and Environmental Science*, 1619(1), 012014. https://doi.org/10.1088/1755-1315/1619/1/012014

Adesina, A. (2025). Recent Trends in the Sustainability Improvement and Use of Wastes in Cementitious Materials. Woodhead Publishing.

Izwan, K. N. K., Mohd Apandi, N., Zailani, W. W. A., Shamsol, A. S., & Chee, W.-K. (2025). A review of Graphene Oxide (GO) performance on cementitious application. *Advances in Concrete Construction*, 199–221.https://scholar.kyobobook.co.kr/article/detail/4040070883598

Shamsol, A. S., Apandi., Zailani, W.W.A., & Izwan, K. N. K. (2024). Characterization and Properties of Binder and Nano-Filler in Geopolymer Paste with Graphene Oxide. *Jurnal Kejuruteraan*, 36(4), 1677-1688. https://doi.org/10.17576/jkukm-2024-36(4)-30

Shamsol, A. S., Apandi., Zailani, W.W.A., & Izwan, K. N. K., Zakaria, M., &Zulkarnain, N. N. (2024). Graphene oxide as carbon-based materials: A review of geopolymer with addition of graphene oxide towards sustainable construction materials. In Construction and Building Materials. *In Construction and Building Materials* (Vol. 411). Elsevier Ltd. https://doi.org/10.1016/j.conbuildmat.2023.134410